Generation and Detection of Short Optical Pulses

David Antony Barrow

A thesis submitted to the University of Glasgow for the degree of Ph.D.

September 1995

ProQuest LLC.
789 East Eisenhower Parkway
P.O. Box 1346
Ann Arbor, MI 48106 – 1346

Generation and Detection of Short Optical Pulses

by

David A. Barrow

Abstract

Two-photon induced conductivity is observed in a reverse biased p-i-n GaAs/AlGaAs optical waveguide. When this waveguide was used as a the non-linear detection element of an autocorrelator, an autocorrelation trace of a passively Q-switched semiconductor laser at 1.3 μm and a passively Q-switched two-section semiconductor laser at 980 nm was successfully obtained.

Self-pulsation is observed in a two-section strained GaAs/InGaAs quantum well laser with an observed pulse width of 25 ps, at frequencies up to 11 GHz. Self-pulsating frequencies up to 18 GHz have been observed in GaAs/AlGaAs QW two-section lasers. A non-monotonic relationship is seen between absorption in the saturable absorber and the applied reverse bias, in QW two-section lasers.

Optoelectronic mixing of very high-frequency amplitude-modulated signals using a semiconductor laser simultaneously as a local oscillator and mixer is proposed. Experimental verification using a two section GaAs/InGaAs quantum well laser is presented.

A monolithically integrated extended cavity modelocked laser fabricated by impurity free vacancy disordering of the quantum well structure is proposed. An extended cavity length of 2.25 mm is proposed giving a total cavity length of 2.5 mm, corresponding to a modelocked frequency of 17 GHz.

Acknowledgements

I would like to thank all those who have helped and expressed interest in my work, in particular my supervisor Professor John Marsh for his continual supervision and guidance throughout the course of this project.

I would also like to thank Professor Effim Portnoi of the Ioffe Institute for his advice and the encouragement he showed me during the initial year of my project.

Also the optoelectronics group, Catrina Bryce, Karen McIlveny and Steve Ayling who made the Monday morning group meetings so much more enjoyable.

The people who worked with me on some of the experiments, especially Dr Francis Laughton, Dr Eugene Avrutin, and Dr Ian Thayne.

All the technical staff especially Lois Hobbs and Joan Carson.

This project was funded by an SERC CASE studentship with BNR Europe.

To my parents

List of Contents

Chapter 7 Optoelectronic Frequency Mixing in Semiconductor Lasers

Chapter 8 Field Distribution Measurements in Q-Switched Semiconductor Lasers

Chapter 9. Modelocked and Extended Cavity Lasers

Chapter 1

Introduction

As demand increases for broader band services, such as high quality data transfer, high definition television and video conferencing, so the demand for reliable, compact, cheap sources of stable picosecond pulse trains at ultrahigh repetition rates, increases. Semiconductor lasers are ideal candidates for use in ultrahigh-bit-rate data processing systems and fibre optics telecommunications due to their small size and ease of large scale manufacture at a relatively low cost per laser. For these reasons there is a large commercial as well as academic interest in the fabrication of ultra-short pulsed lasers. This interest has been 'fuelled' by the advancements that have occurred in material design such as the use of multiple quantum wells and strained layer structures. With the decrease in pulse width and increase in repetition frequency there has also been a corresponding demand for accurate measurement of these optical pulses on a femtosecond timescale.

This thesis examines both the generation and detection of ultra-short pulses using some of the recent advances in semiconductor technology. The main body of the work carried out over the last three years can be divided into three areas of study. The first area of work was on two-photon absorption in GaAs/AlGaAs p-i-n waveguide structures, in which a GaAs/AlGaAs waveguide was designed, fabricated and demonstrated as a two-photon detector in an autocorrelation experiment. The autocorrelator was then used to measure ultra-short optical pulses. The second body of work involved the fabrication of self-pulsating and passively modelocked quantum well GaAs/AlGaAs and InGaAs/GaAs semiconductor lasers to produce high frequency ultra-short pulses. The high frequency repetition rates are achieved by fabricating both devices with intra-cavity saturable absorbers. These two areas were combined so that optical pulses produced from the self-pulsating laser were measured accurately using the two-photon autocorrelator. The third area of work demonstrated the optoelectronic frequency mixing of a high frequency electrical signal with an optical signal to produce an amplitude-modulated optical signal. The experiment illustrated the use of a self-pulsating semiconductor laser as a non-linear mixing element with the natural self-pulsating frequency of the laser diode providing the local-oscillating frequency.

Historical Background

The most commonly used method for measuring a train of pulses is autocorrelation by second harmonic generation in a non-linear crystal. The first group to observe that the second-harmonic conversion of the output of a Michelson interfereometer provides specific information about the pulsewidth of an optical pulse were Maier *et al* [1] in 1966, however this method was relatively slow. It was not until 1980 that interest was renewed in this measurement technique when Sala *et al* [2] showed an almost cw autocorrelation employing an audio loudspeaker driven at 30 Hz in one arm of the Michelson interferometer. Second harmonic generation using a non-linear crystal however requires relatively high optical power levels. Other non-linear processes such as two-photon-induced fluorescence [3] and two-photon-induced electron emission [4] have been used for pulse-width measurements. In 1991 Takagi *et al* [5] illustrated an autocorrelation based on two-photon conductivity in a commercial photodiode the advantage of this method being its inexpensive nature and simplicity in optical arrangement. However, the planer arrangement of the photodiode meant that the sensitivity of the device was low. In this thesis a novel method based on the same phenomenon is presented. A reverse biased p-i-n GaAs/AlGaAs optical waveguide is used as a nonlinear detection element of an intensity and interferometric autocorrelator with the longer interaction length of the waveguide providing greater measurement sensitivity.

The first self sustained pulsations from a semiconductor laser were observed by Basov *et al* in 1968 [6], using a double section homojunction GaAs laser operated at liquid nitrogen temperature. Self-sustained pulsations were seen at room temperature in degraded GaAs/AlGaAs double heterostructure lasers by E.S Yang *et al* [7] in 1974. By 1980 [8] pulses as short as 14 ps at a frequency up to 800 MHz were observed in a tandem-type laser with a transverse junction stripe junction driven by 300 ps current pulses. In 1982 Harder *et al* [9] observed cw self-pulsations at frequencies up to 2 GHz in GaAs/AlGaAs buried heterostructure semiconductor lasers with a split contact and inhomogeneous current injection. Increased interest in quantum well lasers in 1986 led to the demonstration of active q-switching in a GaAs/AlGaAs MQW laser with an electroabsorption monolithic loss modulator by Arakawa [10]. Optical pulses as narrow as 18 ps were generated with a bandwidth as high as 3 GHz. The highest self-sustained pulsations (7 GHz) to date have been recorded from a V-channeled substrate inner-stripe AlGaAs laser diode [11].

The thesis begins by reviewing the main techniques that are commercially used in measuring ultra-short optical pulses, discussing the advantages and disadvantages of each method. Chapter three then examines the theory behind ultra-short pulse

generation along with three techniques most commonly used to generate short pulses, direct modulation, Q-switching and mode-locking. Chapter four contains the device fabrication details of a passively Q-switched two-section laser and includes the design considerations made before device production. The results from this two-section laser are then presented in chapter five. The two-photon autocorrelator is examined in chapter six where fabrication and experimental results are presented. Chapter seven contains an experiment using a two-section laser as a local oscillator in which optical frequency mixing is performed within the device, both the experimental and theoretical work are presented. The dynamic behaviour of transverse modes in passively Q-switched lasers is examined in chapter eight. Chapter nine examines the work carried out on passive modelocked extended cavity lasers with a review of intermixing techniques and fabrication processes, and then results obtained from the device.

1.1 References

1. M. Maier, W. Kaiser, and J. A. Giordmaine, "Intense light bursts in the stimulated1 Raman effect," *Phys. Rev. Lett.*, vol. 17, pp. 1275-1277, 1966.

2. K. Sala *et al* ,"CW Autocorrelation measurement of picosecond laser pulses," *IEEE Journal of Quantum Electronics*, vol. 16, pp.990-996, 1980.

3. J. Giordmaine *et al,* "Two Photon excitation of flourescene by picosecond light pulses," *Appl. Phys. Lett.*, vol. 11, pp. 216-218, 1967.

4. W.R. Bennet, Jr., *Et al, IEEE Journal of Quantum Electronics*, vol. 10, pp.97-98, 1974.

5. Y. Takagi, T. Kobayashi, K. Yoshihara, and S. Imamura, "Multiple and single shot Autocorrelator based on two-photon conductivity in semiconductors," *Opt. Lett.*, vol. 17, pp. 658-660, 1992.

6. N. G. Basov, "0-1-dynamics of injection lasers," *IEEE J. Quantum Electron.*, vol. QE-4, pp. 855-964, 1968.

7. E. S. Yang, P. G. McMullin, A. W. Smith, J. Blum, and K. K. Shih, "Degradation-induced microwave oscillations in double heterostructure injection lasers," *Appl. Phys. Lett.*, vol. 24, pp. 324-327, 1974.

8. H. Ito *et al,* "Self-q-switched picosecond optical pulse generation with tandem-type AlGaAs TJS laser," *Electron. Lett,* vol.17, pp. 15-16, 1981.

9. Ch. Harder, K. Y. Lau, and A. Yariv, " Bistability and pulsations in semiconductor lasers with inhomogeneous current injection," *IEEE J. Quantum Electron.*, vol. QE-18, pp. 1351-1361, 1982.

10. Y. Arakawa, A. Larsson, J. Paslaski, and A. Yariv, "Active Q-switching in a GaAs/AlGaAs multiquantum well laser with an intracavity monolithic loss modulator," *Appl. Phys. Lett.*, vol. 48, pp. 561-563, 1986.

11. X. Wang, G. Li and C. Ih, "Microwave/Millimeter-wave frequency subcarrier lightwave modulations based on self-sustained pulsation of laser diode," *J. Lightwave Tech.*, vol. 11, pp. 309-315, 1993.

Chapter 2

Ultrashort pulse measurement techniques

2.1. Introduction

Recent rapid development in ultrashort pulsed-laser techniques has led to sub-picosecond pulsewidths and repetition frequencies in the terahertz range. With this advancement in technology also has come a need to observe these phenomena directly on a femtosecond timescale. Measurement of optical pulses at a sub-picosecond temporal resolution has become essential in the monitoring of pulsewidths of high performance systems such as ultrahigh-bit-rate fibre-optic transmission and scientific and industrial diagnostic measurements such as electrooptic sampling and impulse response testing of optical components.

It is the purpose of this chapter to review all the ultrashort pulse measurement techniques currently available, to discuss the advantages and disadvantages of each method and to examine under what circumstances each technique can be applied. Initially techniques such as a optical chronography and fast photodiodes that give a direct temporal profile of the pulse train are reviewed. Then indirect methods such as linear and non-linear correlation measurements are discussed. However, some of the pulse measuring techniques such as two-photon absorption-fluorescence are not reviewed here since they are rarely used at present. All the techniques discussed in this chapter have been used by myself to measure q-switched pulses from a semiconductor laser and will be mentioned further in later chapters. However before looking at pulse measurement techniques we must first examine the structure of ultra-short pulses.

2.2. Structure of ultrashort pulses

In order to understand how to measure ultrashort pulses, we must first consider their mathematical description.

The magnitude of the electric field vector of a plane wave optical pulse at a fixed point in space can be expressed as a Fourier integral

$$E(t) = \frac{1}{\sqrt{2\pi}} \int_{-\infty}^{+\infty} e(\omega) \exp(-i\omega t) d\omega. \qquad (2.1)$$

Which can be transform$E(t) = \frac{1}{\sqrt{2\pi}} \int_{-\infty}^{+\infty} e(\omega) \exp(-i\omega t) d\omega$.rem

$$e(\omega) = \frac{1}{\sqrt{2\pi}} \int_{-\infty}^{+\infty} E(t) \exp(i\omega t) dt. \tag{2.2}$$

In most applications of wave theory, it is convenient to use the real part of the complex function. This is achieved by omitting the negative frequency components of (2.1) and including a factor of 2 to ensure that E(t)=Re V(t)

$$V(t) = \frac{1}{\sqrt{2\pi}} \int_{0}^{\infty} 2e(\omega) e^{-i\omega t} d\omega$$

$$V(t) = \frac{1}{\sqrt{2\pi}} \int_{-\infty}^{\infty} v(\omega) e^{-i\omega t} d\omega \tag{2.3}$$

where V is the amplitude of the electric field vector. Taking the inverse transform again we get

$$\begin{aligned} v(\omega) &= \frac{1}{\sqrt{2\pi}} \int_{-\infty}^{+\infty} V(t) e^{i\omega t} dt \\ &= 2e(\omega) \qquad (\omega > 0) \\ &= 0 \qquad\quad (\omega < 0) \end{aligned} \tag{2.4}$$

The complex functions V(t) and v(ω) define an optical pulse in the time and frequency domains, respectively. These functions can be simply expressed in terms of their modulus and argument

$$v(\omega) = a(\omega) e^{i\phi(\omega)} \tag{2.5}$$

Where a(ω) and ϕ(ω) are the spectral amplitude and spectral phase respectively and in the time domain

$$V(t) = \tilde{V}(t) e^{-i\omega t} \tag{2.6}$$

where

$$\tilde{V}(t) = A(t) e^{i\phi(t)}. \tag{2.7}$$

The modulus and argument of $\tilde{V}$ are the temporal amplitude and phase, respectively. Equation (2.6) will frequently be used to describe the structure of a pulse in the time domain. In the quasi-monochromatic case, both A(t) and ϕ(t) are slowly varying functions of time and represent the amplitude and phase of the carrier wave. The instantaneous intensity of an optical signal in the time domain can therefore be defined as

$$I(t) = V(t)V^*(t) = \tilde{V}(t)\tilde{V}^*(t) = A^2(t) \tag{2.8}$$

In general, I(t) is not strictly equal to the square of the real field E(t), but in the quasi-monochromatic case, $\frac{1}{2}I(t)$ represents the time average of $E^2(t)$ over a few optical cycles. Taking the total energy of the pulse to be proportional to the area under the temporal or spectral intensity profile, we get by Parseval's theorem

$$\int_{-\infty}^{+\infty} I(t)dt = \int_{-\infty}^{+\infty} i(\omega)d\omega \tag{2.9}$$

Thus the structure of an optical pulse is completely defined by a phase and an intensity (or amplitude). A complete description of this structure in one domain, time or frequency, gives enough information to obtain a profile in the other, using Fourier transforms. However, there is no one-to-one correspondence between the intensity profiles of I(t) and i(ω) since each depend not only on each other but also on the associated phase function. The general relationship between the two is

$$\frac{\Delta\omega\Delta t}{2\pi} \geq K$$
$$or \quad \Delta\nu\Delta t \geq K \tag{2.10}$$

where $\Delta\omega(\Delta\nu)$ and Δt are the full widths half maximum (FWHM) of i(ω) (i(ν)) and I(t), respectively, and K is a constant of the order of unity. Importantly, the shortest pulse obtainable for a given spectral bandwidth is said to be transform limited where

$$\Delta t_{min}\Delta\nu = K \tag{2.11}$$

Values of a variety of shaped pulses for the transform limited case, K, are listed in appendix 1. Transform limited pulses are produced by lasers in a modelocked regime. The laser is described as modelocked because in the frequency domain it corresponds to correlating the spectral amplitudes and phases. An ideally modelocked situation is illustrated in Fig. 2.1. In this simulation, a laser operating in a number of discrete longitudinal modes equally spaced at intervals of $\delta\omega$ and with time independent amplitudes $a(\omega)$ are locked together so that the spectral phases $\phi(\omega)$ are zero.

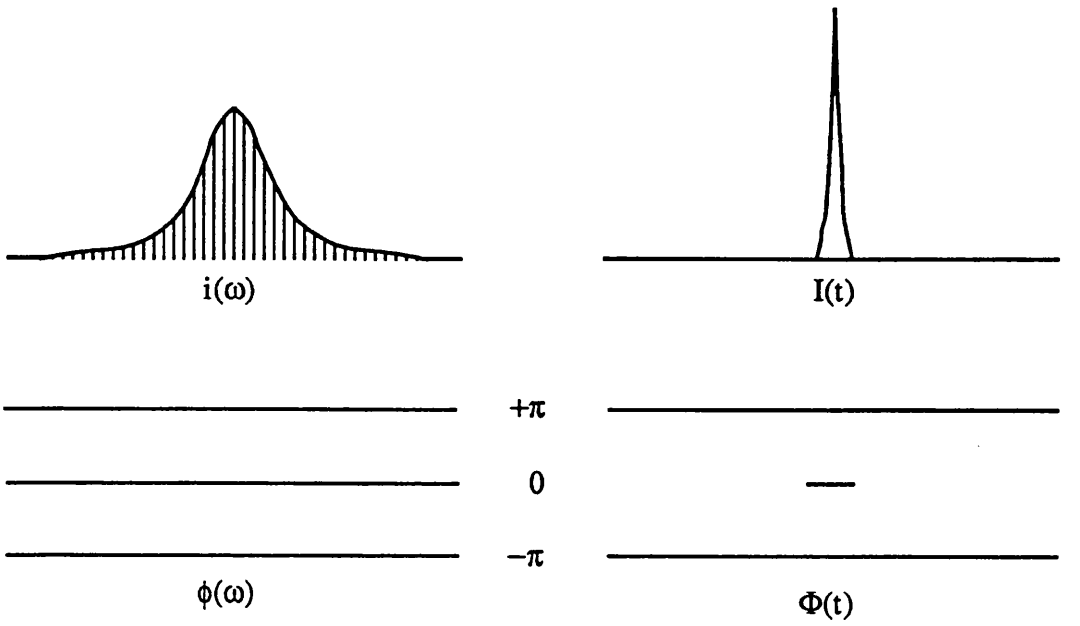

Fig. 2.1. Phase and intensity profiles in both the spectral and time domain for an ideal modelocked pulse, the temporal intensity should be scaled up by about x 20 to correspond with the spectral profile.

For simplicity, the spectral intensity is chosen to be a gaussian function in Fig. 2.1.

$$i(\omega) = e^{\frac{(\omega-\omega_0)^2}{\alpha}}. \tag{2.12}$$

From this we can then show that the temporal profile is the related Gaussian function

$$I(t) = \alpha\ e^{-\alpha(t-t_0)^2} \tag{2.13}$$

and K=2 ln 2 /π =0.441 in (2.11). Slightly different values of K apply for other pulse shapes. A table of pulse shapes against time-bandwidth product values is compiled in appendix 1.

2.3 Direct Measurements of ultra-short pulses

2.3.1. Fast photodiodes

The simplest and most direct method of measuring the intensity profile of ultrashort pulses is the photodiode oscilloscope combination. It is also one of the cheapest techniques, and easiest to arrange where the output from the laser diode is focused onto a fast photodetector which is connected to an oscilloscope which measures the resulting electrical signal. This method has the advantage of being able to measure any pulse train without the need of a triggering source, however, the main disadvantage to this technique is its time resolution, which depends on the risetime of both the photodetector and the oscilloscope. The limiting factor in this case is the oscilloscope, with the fastest commercially available real-time oscilloscope having a 10 GHz bandwidth.

If the pulses to be measured are repetitive, as from a cw modelocked laser for instance, and if real-time measurement is not required, pulse sampling techniques can be employed. This method uses a sampling head to sample the electrical pulse from a fast photodiode. The sampling head samples the electrical pulse at discrete intervals in time, using a trigger signal as a reference point, eventually forming the temporal profile of the pulse after the sampling and averaging of a number of pulses. The time resolution of this technique is better than a standard photodiode oscilloscope combination, with the fastest commercially available sampling head having a bandwidth of 50 GHz. However it is not a real-time measurement and a trigger signal is needed at the optical pulse repetition frequency.

The photodiode-pulse sampling technique was used to examine the self-pulsating frequency of two-section lasers. The time resolution of the system was too large to accurately measure the pulse width of individual pulses, the photodiode had a bandwidth of 18 GHz and the sampling heads bandwidth was 50 GHz which gave a total rise time of 30 ps. There was also an added timing jitter due to the triggering of the sampling scope which was measured to be 5 ps.

Recent developments in photodiodes with integrated bias tees and matched resistors have shown usable electrical bandwidths in excess of 100 GHz (a FWHM time response of 3.5 ps) along with high efficiencies[1]. However, a time resolution at least as short as 1 ps is required for adequate laser diagnosis which can only be realised by correlation or electron-optical chronography techniques.

The method of studying rapidly varying luminous phenomena by electron-optical cronography was first proposed by Zavoiskii and Fanchenko in 1956 [2]. The method as the name suggests involves the conversion of light into electrons by the use of a photocathode. Fig. 2.2. shows the operating principle of the streak camera. In this particular arrangement the camera gives intensity vs. time vs. position (or wavelength). For example, used in combination with a spectroscope, time variation of the incident light with respect to wavelength can be measured (time resolved spectroscopy).

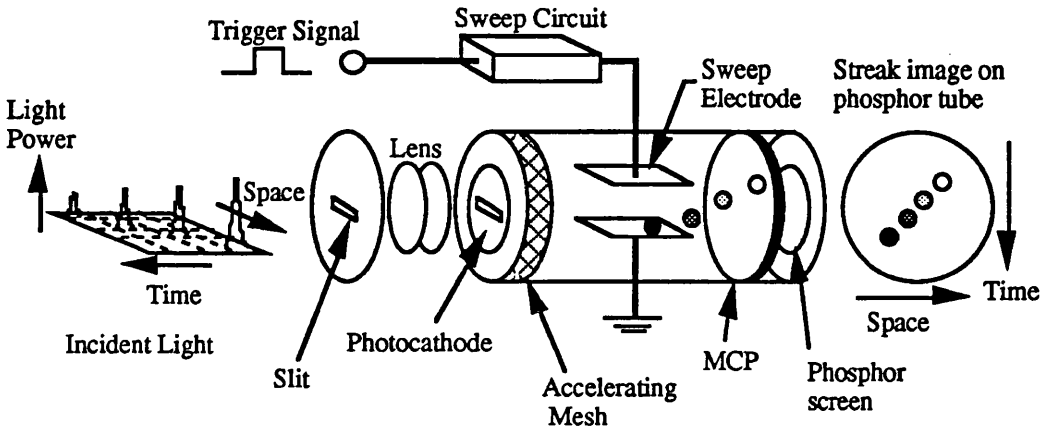

Fig. 2.2. Schematic showing the operating principles of a streak tube.

Operating principle

The light being measured passes through a slit and is focused into a slit image on the photocathode of the streak tube. The light is then converted by the photocathode into a number of electrons which is proportional to the intensity of the light. The electrons are then accelerated by an accelerating mesh through a pair of sweep electrodes until they bombard a phosphor screen at the other end of the streak tube. As the electrons pass through the pair of sweep electrodes, a high voltage is applied across the parallel plates. During the high speed voltage sweep, the electrons, which arrive at slightly different points in time corresponding to the position of the train of optical pulses, are deflected at different angles in the vertical direction. The electrons then enter a micro-channel plate where they are multiplied several thousands of times, after which they impact against a phosphor screen to be converted back into light.

The optical pulse is converted into a 'streak' like image formed on a phosphor screen, the phosphor image corresponding to the first pulse in the pulse train is placed in the uppermost position, with the others being arranged in sequential order from top to bottom where the vertical direction on the screen serves as the time axis. The horizontal

axis corresponds to the pulses position in space, and the brightness of the phosphor image corresponds to the intensity of the light. We can thus find the optical intensity of the pulse train from the phosphor image, and the time and incident light position from the location of the phosphor image.

Resolution

The time resolution is ultimately limited by the spread of photoelectron transit times in the streak tube. This spread is due to the variation of initial electron energies produced by the photocathode before acceleration. It can be shown [3] that, for any electron-optical arrangement, the distribution of photoelectron transit times through the image tube has a half width,

$$\Delta\tau_D = m\Delta U/eE \qquad (2.14)$$

where ΔU is the half-width of the initial electron velocity distribution (dependant on wavelength and type of photocathode) and e and m are the electronic charge and mass respectively. Therefore in order to minimise the spread of the photoelectron transit times the electric field strength E near the photo-cathode must be maximised. In other words the quicker the electrons are accelerated to a high velocity, the shorter the time they take to 'forget' their small initial differences in energy. Streak cameras with sub-picosecond resolution therefore have to have extraction fields in the region of 10 $KV \cdot cm^{-1}$.

System Configuration and Operation

In order to measure ultra-high speed phenomena using a streak camera, a trigger section and a readout section are required. The basic system configuration is shown in Fig. 2.3.

The trigger section controls the timing of the streak sweep, ensuring that the voltage applied to the sweep electrodes is synchronised to the incident light. For this purpose, we use a delay unit, which controls the time taken for the trigger pulse to reach the sweep circuit, hence altering the position of the phosphor image within the time frame of the streak camera. If the frequency of the external trigger signal is too high, a frequency divider is used to reduce the repetition rate. Also, in cases where there is no trigger signal from the device such as a cw modelocked laser, it has to be produced from the pulse train itself using a fast photodiode.

A high-sensitivity camera and a frame grabber are used to read the images into a computer which analyses the data and adds a scaling factor to the image to produce an accurate

reading of the pulse profile in time. The scaling factor differs from tube to tube and is normally calibrated in the factory.

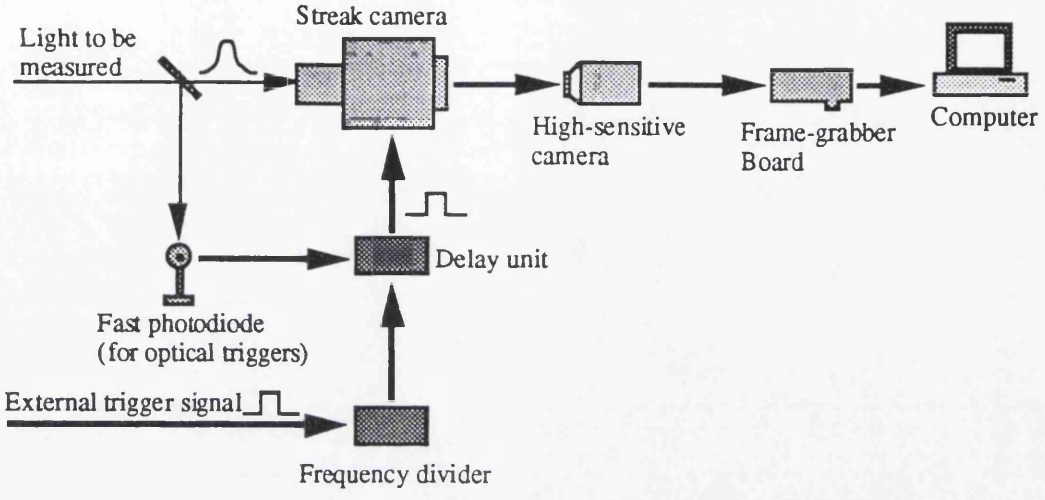

Fig. 2.3. Schematic of the basic system configuration of streak camera.

There are two main types of sweep method for measuring optical pulses, single sweep, and synchroscan. Single sweep, as the name implies, measures the temporal profile of the pulse with a single voltage sweep (single shot) . The pulse shape can then be made up from a number of sweeps giving an average temporal profile or, if the peak pulse intensity is high enough, a single shot will produce a temporal profile. A linear ramp voltage is applied to the deflection (sweep) electrodes during the sweep. This method is best suited to a laser with a high peak power that can produce a trigger signal, however, the maximum sweep frequency is limited to 10 kHz.

Syncroscan sweep measurement refers to a high speed repeated sweep in which a high frequency sine wave voltage is applied to the deflection electrodes. Synchronising the repetition rate of the optical pulse train to the sweep frequency, streak images can be accumulated (integrated) at a fixed position on the phosphor screen. The advantage of this method is that it allows very faint repetitive optical phenomena to be measured with a high signal to noise ratio. However, the trigger frequency which controls the sweep frequency must be exactly the same, an exact multiple, or an exact fraction of the repetition rate of the pulse train. This method is ideal for cw modelocked semiconductor lasers because of their fixed repetition rate and low peak pulse power.

The temporal resolution from the best commercially available streak cameras for both these sweep methods is about 1 ps [4]. The fluctuation in the operation timing of the sweep circuit or trigger jitter is another element that effects the temporal resolution of the system. For the synchroscan method it is less than the temporal resolution and is therefore negligible, for the single sweep technique the trigger jitter is about ± 5 ps. One problem

the streak camera has with measuring semiconductor lasers is the low sensitivity the streak tubes have at detecting 1.3 and 1.5 μm incident light. A standard S1 Borosilicate streak tube has a spectral response of between 300 and 1600 nm however, the radiant sensitivity of the tube drops from 2 mA/W to 0.2 μA/W between 850 nm and 1500 nm respectively.

2.4. Indirect Measurements

(Correlation Measurement)

It has been shown so far that direct measurement of the duration of relatively long optical pulses is most often made by either a fast photodetector or streak camera. Since it was not expected that direct electronic techniques would be capable of measuring time duration's down to 10^{-13} s, new measuring techniques had to be found for the measurement of the time duration of picosecond pulses. One indirect method which is commonly used to measure ultrashort pulses is concerned with the study of the temporal intensity profile through its correlation functions. In this section, we review the various experimental techniques for linear and non-linear correlations and the important information obtained from both methods.

2.4.1. Linear correlation

The simplest linear optical autocorrelator is the Michelson interferometer. First we will consider how the interferometer works and then show what optical information it supplies which, we will find, is the same information as a grating or prism spectrograph, although in a different form.

A Michelson interferometer configuration is illustrated in Fig. 2.4. An incident pulse with an amplitude V(t) is split into two pulses each with an amplitude $V(t)/\sqrt{2}$. Each of these pulses is made to traverse a separate orthogonal arm of the interferometer. After transversing their respective paths D_1 and D_2 the pulses are recombined and then incident onto a square law detector such as a photodetector

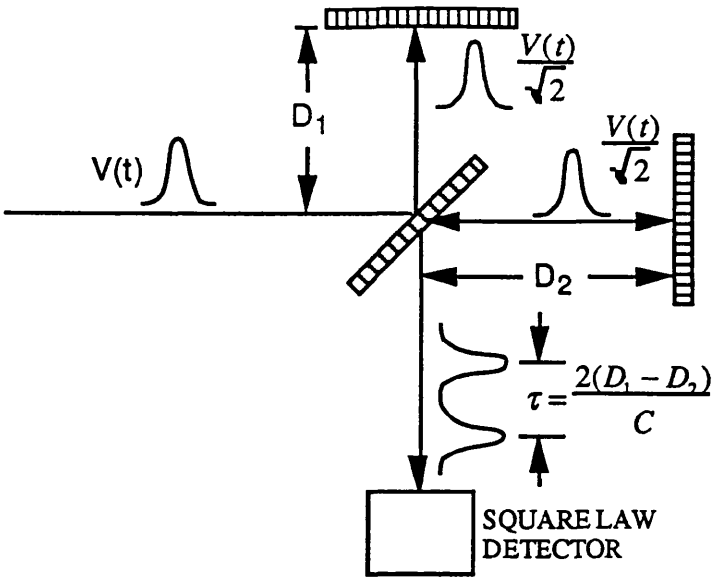

Fig. 2.4. Schematic of a Michelson interferometer.

If the path lengths are not equal, using equation (2.6), the pulses can be represented by

$$V_1(t) = \frac{\tilde{V}(t)}{\sqrt{2}} e^{-i\omega t} \tag{2.15}$$

and

$$V_2(t-\tau) = \frac{\tilde{V}(t-\tau)}{\sqrt{2}} e^{-i\omega(t-\tau)} \tag{2.16}$$

where $\tau = 2(D_2 - D_1)/c$ and $\tilde{V}(t)$ is the slowly varying envelope of the pulse with respect to ω. The intensity incident on the detector is given by

$$I(t,\tau) = \left(\left|V_1(t) + V_2(t-\tau)\right|\right)^2. \tag{2.17}$$

Assuming the response of the detector is slow compared to the pulse width or the time delay τ, the output signal of the detector, $S(\tau)$, is

$$\begin{aligned} S(\tau) &= \int_{-\infty}^{+\infty} I(t,\tau)dt \\ &= W(1 + A(\tau)) \end{aligned} \tag{2.18}$$

where W is the pulse energy and A(τ) is the autocorrelation function of the pulse amplitude,

$$W = \int_{-\infty}^{+\infty} \tilde{V}^2(t)dt \tag{2.19}$$

and

$$A(\tau) = \frac{\int_{-\infty}^{+\infty} \tilde{V}(t)\tilde{V}(t-\tau)e^{-i\omega\tau}dt}{\int_{-\infty}^{+\infty} \tilde{V}^2(t)dt} \tag{2.20}$$

We can see that when τ =0 then $S(\tau)$/W=2 and when the two pulses are not overlapped $S(\tau)/W = 1$. Again using the inverse Fourier transform we find

$$S(\tau) = \frac{1}{\sqrt{2\pi}} \int_{-\infty}^{+\infty} e^{i\omega\tau} |P(\omega)|^2 d\omega \tag{2.21}$$

where $|P(\omega)|^2$ is the power density spectrum of the original laser pulse. The power density spectrum is measured by a spectrometer and the amplitude autocorrelation measured with an interferometer. However, as can be seen, knowledge of one uniquely specifies the other. The two results are essentially equivalent and the equivalence arises from the fact that both instruments are linear optical systems.

It is clear that when the two pulses are recombined an interference pattern will be observed in the plane of the detector. The interference changes occur at set intervals in time, reaching a maximum at τ=0, 2L/c, 4L/c,....(where L is the difference in length of the arms of the interferometer), and gradually falling to zero in moving away from these points, Fig. 2.5. The difference in path lengths, ΔD over which the interference pattern is visible is called the coherence length. The coherence length and the spectral bandwidth of the pulse are related by

$$\frac{2\Delta D}{c} = \frac{2\pi}{\Delta\omega} = \Delta\tau_c \tag{2.22}$$

where $\Delta\tau_c$ is the coherence time.

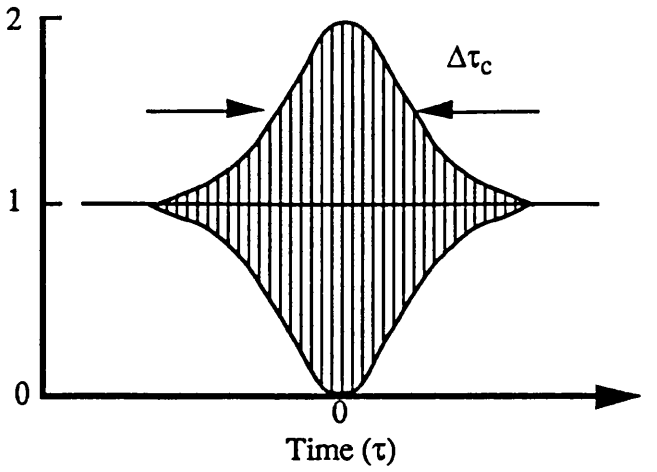

Fig. 2.5. Result of a measurements with a linear optical instrument, the vertical hatching represents closely spaced interference fringes.

The coherence time will equal the width of the pulse only when the entire spectral content of the pulse is due to the short duration of its envelope, $\Delta\tau_c = \Delta\tau = 1/\Delta\upsilon$. In other words, the relation $\Delta\omega\Delta t \geq 2\pi$ provides only a lower limit to the pulse duration and can be used to determine Δt only in the transform-limited case. The linear cross-correlation of an unknown pulse with one of known characteristics can provide specific information about the temporal intensity and is also useful in studying the structural similarity of different pulses. Therefore, it can be concluded that any measurement taken with a linear optical system can provide only information establishing a lower limit to the time duration of a pulse.

2.4.2. Nonlinear Correlation Methods

Introduction

Maier *et al* [5], in 1966, were the first to point out that second-harmonic conversion (SHG) of the output of the Michelson interferometer provides specific information about the pulse width through the second-order correlation function. The ability of a non-linear autocorrelation to measure the picosecond temporal profile of an optical pulse accurately, stems from the use of accurate, readily controlled increments in length to measure the spatial length of a pulse, and the effectively instantaneous electronic mechanism underlying SHG. The second-harmonic autocorrelation technique was later superseded by the two-photon fluorescence (TPF) method due mainly to the fact that TPF enabled single shot measurements whereas SHG autocorrelations requires several pulse shots while varying the path length. With the arrival of cw passive modelocking [6] and advances in calibrated stepper motors came a renewed interest in SHG autocorrelation, pulsewidth measurements could now be obtained in a few seconds. Then another advance came with the use of a commercial shaker assembly driven at 22 Hz [7] with such a large increase in "scan" rate an almost "cw" autocorrelation measurement could be made. This section presents a general review of "fast" and "slow" correlations with and without background contributions.

Slow Autocorrelation

The manner in which a nonlinear optical system can perform a slow correlation function measurement of a pulse can be explained as follows. Firstly it must be noted that a slow correlation function is calculated assuming a smooth, slowly varying envelope and phase perturbation for the optical pulse. We have already mentioned (2.6) that the optical pulse can be expressed in time by

$$V(t) = A(t)e^{i\phi(t)}e^{-i\omega t} \tag{2.23}$$

where A(t) and $\phi(t)$ are slowly varying functions of time and represent the amplitude and phase of the envelope wave. It must therefore be noted that slow correlation functions are determined solely by the time dependencies of the pulse envelope A(t); all information regarding the phase perturbations $\phi(t)$ is lost as a consequence of the failure of the slow correlations to resolve the much faster frequency variations $e^{-i\omega t}$.

To measure the pulsewidth of pulse the two output pulses from the Michelson interferometer, $V_1(t)$ and $V_2(t)$, are passed through a nonlinear optical crystal. The second harmonic output from the nonlinear optical crystal is given by

$$^{2\omega}A(t) = \left[A_1(t) + A_2(t-\tau)\right]^2 \tag{2.24}$$

neglecting the constant representing the second harmonic generation efficiency of the crystal. Again looking at the output signal S(τ) from a detector having a slow response time with respect to ω and τ is given by

$$S(\tau) = \int_{-\infty}^{+\infty} \left|{}^{2\omega}A(t)\right|^2 = {}^{2\omega}W(1+2G(\tau)) \tag{2.25}$$

where ${}^{2\omega}W$ is the second harmonic pulse energy and $G(\tau)$ is the autocorrelation function of the pulse intensity,

$${}^{2\omega}W = \int_{-\infty}^{+\infty} A^4(t)dt \tag{2.26}$$

and

$$G(\tau) = \frac{\int_{-\infty}^{+\infty} A^2(t)A^2(t-\tau)dt}{\int_{-\infty}^{+\infty} A^4(t)dt}. \tag{2.27}$$

When τ=0, $S(\tau)/{}^{2\omega}W = 3$, and when the two pulses are not overlapped, $S(\tau)/{}^{2\omega}W = 1$. Measurement of the variation of $S(\tau)/{}^{2\omega}W$ as a function of τ gives the time duration over which the energy of the pulse is distributed. Fig. 2.6 illustrates the results expected from a nonlinear crystal for two types of pulses a transform limited pulse, $\Delta\tau = \Delta\tau_c = 1/\Delta\upsilon$, and a pulse where $\Delta\tau >> 1/\Delta\upsilon$. The profiles show that in (a) the intensity ratio between the peak and wings is 3:1, in (b) the intensity ratio is closer to 3:2 this is due to the pulse being superimposed on a low intensity background. In the full autocorrelation function the side wings of the background show up, but in contrast to the central position, no fringe structure is detected. This is due to the background light not being phase locked.

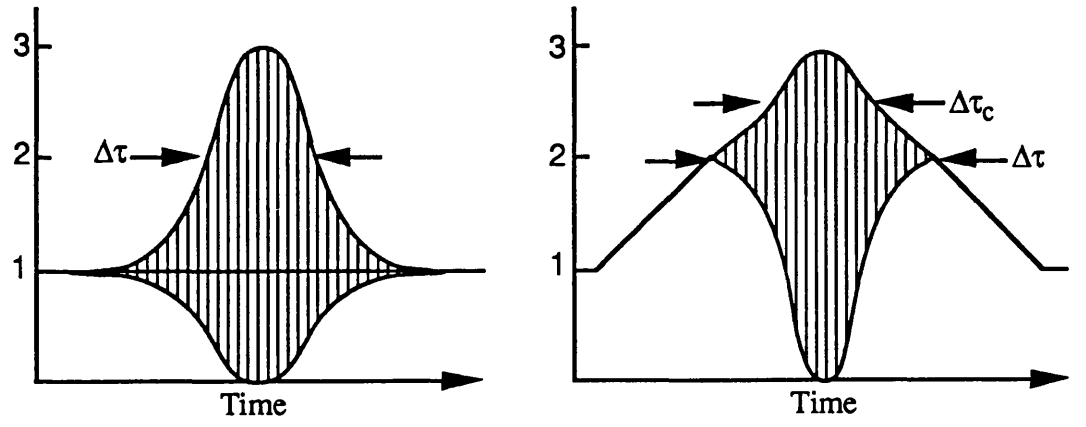

Fig. 2.6. Interference fringes from a nonlinear optical instrument. a) $\Delta\tau_c = 1/\Delta\upsilon$ and when b) $\Delta\tau > 1/\Delta\upsilon$

In this configuration as we have already said when the two pulses are not overlapped a single pulse is able to generate a harmonic signal which means that the correlation function is superimposed on a uniform background. There is however, a technique that reduces the background light to zero.

Zero Background "slow" Correlation

Weber [6], therefore, proposed to insert orthogonal polarizers in the two arms of the interferometer and to phase match the nonlinear crystal for SHG of the second kind. In this configuration, the orthogonally polarised pulses only generate harmonic radiation when they overlap hence the correlation profile obtained for an isolated pulse has zero background. The experimental arrangement is shown in Fig. 2.7.

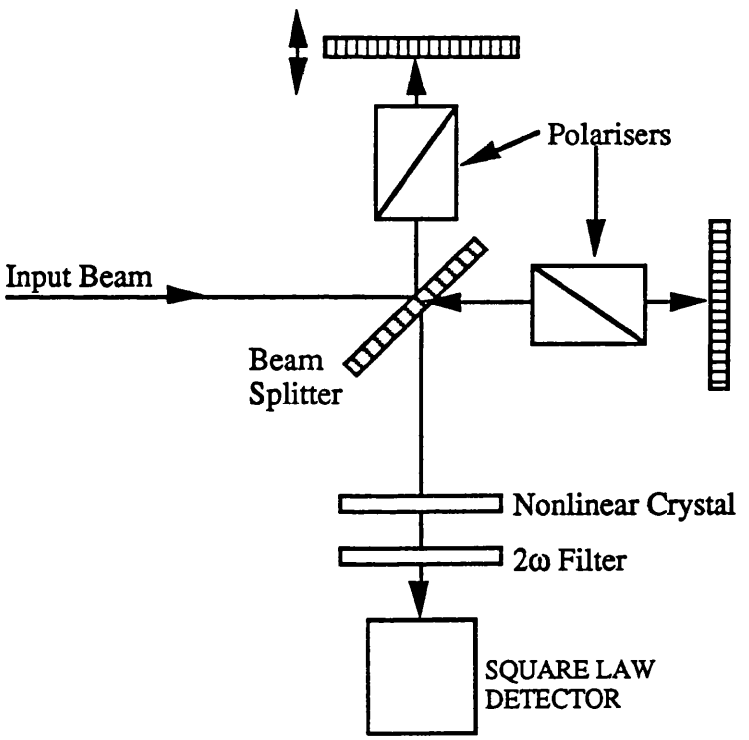

Fig. 2.7. The zero-background (ZB) technique for pulsewidth measurement devised by Weber [6], using polarisers in a Michelson arrangement to produce orthogonally polarised beams.

For the background-free second-order autocorrelation

$$S_0(\tau) = G(\tau) = \frac{\int_{-\infty}^{+\infty} A^2(t)A^2(t-\tau)dt}{\int_{-\infty}^{+\infty} A^4(t)dt} \qquad (2.28)$$

which gives a contrast ratio of 1:0 between the peak and wings. The autocorrelation trace is shown in Fig. 2.8.

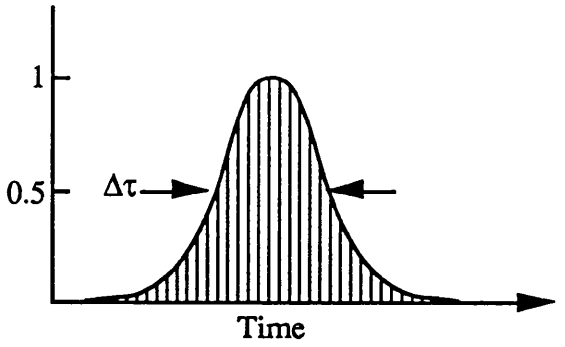

Fig. 2.8. Zero background autocorrelation trace.

Fast Autocorrelation

To resolve the fast variations ($e^{-i\omega\tau}$) inherent in the correlation function the mechanical stability and accuracy of the interferometer must be such, that the change in path length, chosen for each point of measurement, is small compared to the wavelength, i.e. spatial variations must be controlled on a scale of roughly $\frac{1}{10}$ that of the shortest wavelength of the pulse, ~100 nm. It is not surprising, therefore, that the "slow" correlation functions are measured in preference to the "fast" or fringe resolved correlation. The "fast" correlation function can be defined as

$$S^f(\tau) = 1 + \frac{2\int_{-\infty}^{+\infty} V^3(t)V(t+\tau)dt + 2\int_{-\infty}^{+\infty} V(t)V^3(t+\tau)dt + 3\int_{-\infty}^{+\infty} V^2(t)V^2(t+\tau)dt}{\int_{-\infty}^{+\infty} V^4(t)dt} \qquad (2.29)$$

The maximum peak to background ratio, which must be observed in a fringe resolved experiment is therefore 8:1. The fringe resolved "fast" autocorrelation trace for a Gaussian-shaped envelope is illustrated in Fig. 2.9. Fig. 2.9 (a) shows a fringe resolved correlation of a pulse with no background light intensity, the contrast ratio is 8:1. Fig. 2.9 (b) shows a fringe resolved correlation of the same Gaussian pulse superimposed onto a high intensity background. Due to the relatively high intensity background (~30 % of the pulse energy) the contrast ratio between the central peak and wings is less than 8:1. Again the background light is assumed to be "noisy" and no phase locking occurred in the outer wings. The width of the region where the correlation function shows interference, is proportional to the coherence length.

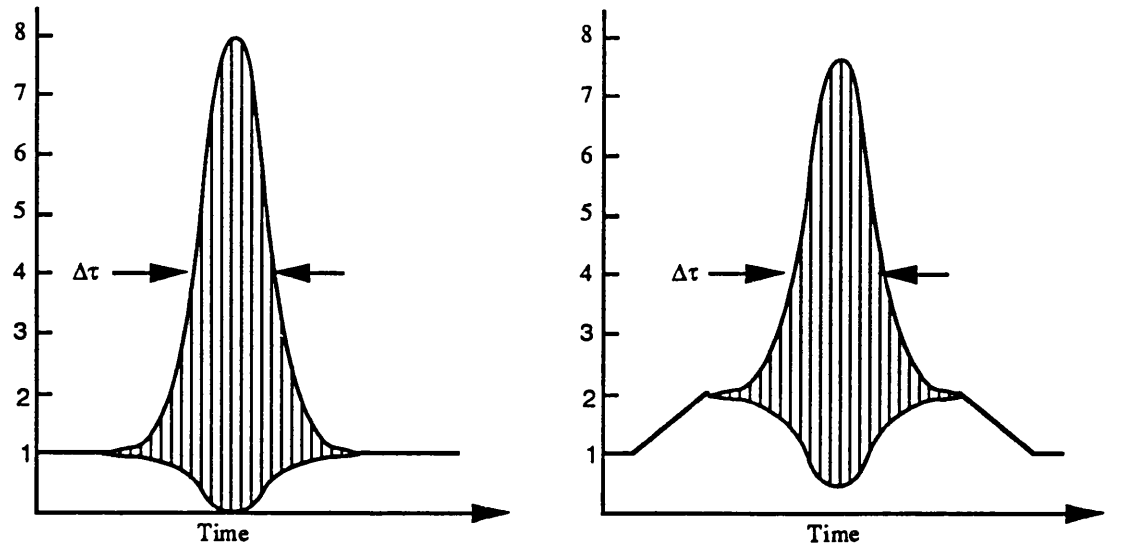

(a) (b)

Fig. 2.9. "Fast" autocorrelation traces with the pulse superimposed on :a) zero background light, b) a small level of background light.

If the delay time between the incident pulses is changed in increments which do not match the periodicity of the interference pattern, then the full autocorrelation function is sampled at various points along the interference curve. As a consequence an additional modulation pattern appears in the correlation function, whose periodicity depends on the mismatch. The accuracy of the envelope of the correlation function can be restored by decreasing the increments of the delay time.

Zero Background "fast" Correlation

The zero background (ZB) fringe resolved correlation is performed using the same experimental arrangement as the ZB "slow" correlation function, Fig. 2.5, combined with the small spatial variations of the interferometer used in the fringe resolved technique. The ZB fringe resolved correlation function can be described as

$$S_0^f = \frac{\int_{-\infty}^{+\infty} V^2(t)V^2(t-\tau)dt}{\int_{-\infty}^{+\infty} V^4(t)dt} \qquad (2.30)$$

which gives a contrast ratio of 1:0.

Pulse Shape Analysis

To give a full understanding of the difference between the various types of autocorrelation functions, it is instructive to adopt a specific model for V(t). In this way we can directly compare the information stored in each autocorrelation about the pulse shape. A Gaussian pulse having a linear chirp is chosen,

$$V(t) = A(t)\cos(\omega t + \phi(t)) = A_0 e^{-t^2/2T^2} \cos\left(\omega t + \frac{at^2}{T^2}\right). \tag{2.31}$$

From this description of a Gaussian pulse we get the corresponding fringe resolved autocorrelations,

$$S^f(\tau) = 1 + 4e^{-(3+4a^2)\tau^2/8T^2} \cos(\omega t)\cos\left[\frac{a^2\tau^2}{2T^2}\right] + e^{-(1+4a^2)\tau^2/2T^2} \cos(2\omega\tau) + 2e^{-\tau^2/2T^2} \tag{2.32}$$

and for the zero background case

$$S_0^f(\tau) = \tfrac{2}{3}e^{-\tau^2/2T^2} + \tfrac{1}{3}e^{-(1+4a^2)\tau^2/2T^2} \cos(2\omega t). \tag{2.33}$$

While the time-averaged slow autocorrelation functions are

$$S(\tau) = 1 + 2e^{-\tau^2/2T^2} \tag{2.35}$$

and for the zero background case

$$S_0(\tau) = e^{-\tau^2/2T^2} \tag{2.36}$$

It can be seen that the terms in the correlation functions get simpler and therefore easier to analyse as we progress from the fringe resolved autocorrelation to the slow ZB autocorrelation. This simplification, however, is gained at the cost of "loss of information" about the original pulse characteristics. The information contained on the linear chirp phase is lost in the slow correlation and appears only in the fringe resolved function. Although for the simple, Gaussian pulse with linear chirp, the two slow correlations functions $S(\tau)$ and $S_0(\tau)$ are effectively equivalent; subtle but important differences will exist in the nature of these two functions in those cases where the pulse is structured or "noisy".

Resolution

The resolution of the autocorrelation system depends mostly on the stability of the interferometer and its accuracy in being able to control the path difference between the two incident pulses. The resolution time is also found to be proportional to the reciprocal thickness of the SHG crystal. The decrease in resolution is due to dispersive effects in the crystal which broadens the detected autocorrelation peak. However, with decreasing crystal thickness, the second harmonic signal also decreases so that the sensitivity of the detector sets a limit to the resolution.

The main disadvantage to this method is that the correlation function is not recorded directly, the SHG technique requires several shots of pulses while varying path delays in order to produce the complete autocorrelation. However, this problem was solved by increasing this 'scan' rate to rates greater than 10 Hz to allow what could be termed as a 'CW' autocorrelation measurement. This technique was first reported by Fork and Beisser in 1978, who used a commercial shaker assembly driven at 22 Hz. Other disadvantages to using SHG optical crystals are that they have to be phased matched to the appropriate wavelength being measured and their conversion efficiencies are in the order of 5%. Recently however efficiencies of up to 30% has been recorded using optical gratings written in lithium niobate [8].

2.5 References

1. Y. Wey, K. Giboney, J. Bowers et al, "108-GHz GaInAs/InP p-i-n photodiodes with integrated bias tees and matched resistors," *IEEE Photonics Tech. Letters,* vol. 5, pp. 1310-1312, 1993.

2. E. K. Zavoiskii and S. D. Fanchenko, "Physical fundamentals of electron-optical chronography", *Sov. Phys.- Dokl.,* vol. 1, pp. 285-288, 1956.

3. E. K. Zavoiskii and S. D. Fanchenko, "Image converter high-speed photography with 10^{-9} to 10^{-14} sec. time resolution", *Appl. Opt..,* vol. 4, pp. 1155-1167, 1965.

4. Hamamatsu Photonics K. K., "Universal Streak Camera C5680", specifications catalogue, 1993.

5. M. Maier, W. Kaiser, and J. A. Giordmaine, "Intense light bursts in the stimulated Raman effect," *Phys. Rev. Lett.,* vol. 17, pp. 1275-1277, 1966.

6. A. Dienes, E. P. Ippen, and C. V. Shank, "A mode-locked CW dye laser," *Appl. Phys. Lett.,* vol. 21, pp. 348-350, 1972.

7. R. L. Fork and F. A. Beisser, "Real-time intensity autocorrelation interferometer," *Appl. Opt.,* vol. 17, pp. 3534-3535, 1978.

8. M. Fejer (Stanford University) Talk given at CLEO Europe, 1994.

Chapter 3

Short Pulse Generation using Semiconductor Lasers

3.1. Introduction

One of the most important applications for semiconductor lasers is in digital optical transmission systems. Within such an environment many demands are placed on the laser performance; it must operate over a wide temperature range, have high output power but at the same time must be able to couple into a monomode fibre, it must be capable of high modulation frequencies and have a stable spectral output. One of the key areas of development of semiconductor lasers is an increase in modulation bandwidth. In the future multigigahertz bandwidths and picosecond pulsewidths will make possible new areas of applications involving transmission of microwave signals through optical fibres.

Microwave transmission with large bandwidth capabilities becomes especially advantageous when the system requires a reduction of weight or data transmission over long distances. Early works on high frequency modulation were limited by the intrinsic properties of the laser diode to the lower gigahertz range. However, major interests in the higher frequency ranges such as the C (3.9-6.2 GHz) and X (5.2-10.9 GHz) bands have stimulated efforts to extend the modulation bandwidth of semiconductor lasers to these frequency ranges.

As well as in high-speed optical communications systems, ultrashort pulses are also being used for optoelectronic measurement applications such as electrooptic sampling [1], analogue to digital conversion [2], and impulse response testing of optical components. These applications require high power, short pulses with good spectral characteristics.

The demand for picosecond pulse technology of semiconductor lasers is therefore high, and used in a wide range of applications. In this chapter several of the most important methods of achieving ultrashort pulses at high frequency rates are investigated. The direct modulation of semiconductor lasers is examined, looking at the optimum parameters for high speed modulation. There is a review of self-pulsation in semiconductor lasers along with a physical and mathematical description of this ultra-short pulse generating technique. Finally there is an examination of modelocking in semiconductor lasers with the main part of the section concentrating on passive modelocking. The influence of material parameters on performance, in particular the transient behaviour and linewidth, are considered, with the advantages of quantum well

design also discussed. First, the relevant physics of rate equations and relaxation oscillations of semiconductor lasers are considered.

3.2. The Rate Equations

To understand the dynamic response of semiconductor lasers in either direct modulation, gain switching, self-pulsation or modelocking we must first look at the rate equations. The rate equations describe the interplay between stimulated emission and the injected carriers.

Due to the small physical size of the lasers, we treat the system as a circuit element whereby we ignore the spatial variations of carrier density and photons along the cavity length, z. First we look at the cross-sectional overlap between the optical mode and the inverted population, which can be described as,

$$\Gamma = \frac{\int_{-d/2}^{+d/2} E^2(x)dx}{\int_{-\infty}^{+\infty} E^2(x)dx} \tag{3.1}$$

In other words Γ is the optical confinement factor, where d is the width of the active region.

The first rate equation describes the temporal evolution of the carrier density. The density of the inverted population n is equal to the injected current, J, divided by the electronic charge and the active region thickness i.e.,

$$\frac{dn}{dt}(\text{production}) = \frac{J}{ed} \tag{3.2}$$

However, there is a loss of carriers through both radiative and nonradiative processes. The rate of this decay can be expressed in terms of the carrier lifetime, τ_s. The rate of decrease of the inversion is proportional to the inversion multiplying that rate.

$$\frac{dn}{dt}(\text{spontaneous}) = -\frac{n}{\tau_s} \tag{3.3}$$

Stimulated emission depletes the inversion in direct proportion to the intensity of the stimulating wave. Therefore, the stimulated recombination rate of carriers should account for the fact that the inversion density must be at least enough to make the cavity transparent (gain equals losses) before stimulated loss of carriers occurs. Furthermore, stimulated emission will clamp the carrier density at its transparency condition.

$$\frac{dn}{dt}(\text{stimulated emision}) = -A(n - N_{nom.})P \tag{3.4}$$

where $N_{nom.}$ is the carrier density that makes the material transparent and A is a constant that takes into account many factors. These are the gain coefficient per unit of inversion,

the group velocity of the wave, the optical confinement factor and the volume of the cavity.

Thus the total rate of change of the carrier density is,

$$\frac{dn}{dt} = \frac{J}{ed} - \frac{n}{\tau_s} - A(n - N_{nom.})P \tag{3.5}$$

This equation is simply a system of bookkeeping of the supply and use of the carriers and how they interact with the photons.

The rate of change of photons in the cavity mode have a separate rate equation that is coupled to the rate of change of the carrier density. The stimulated emission term is the same except for a sign change.

$$\frac{dP}{dt}(\text{stimulated emission}) = A(n - N_{nom.})P. \tag{3.6}$$

Next we look at the spontaneous emission term and find that only a fraction of the spontaneous recombination results in the production of a photon and only a fraction of that enters the cavity mode. This is due to the random direction of the emission of photons during spontaneous emission.

$$\frac{dP}{dt}(\text{spontaneous}) = \beta\frac{n}{\tau_s} \tag{3.7}$$

Where β is the fraction of spontaneous recombination that produces a photon in the cavity mode.

Finally there is a term that takes into account the losses due to the waveguide and any coupling loss. Here we use the photon lifetime, τ_p, to describe the change in photon density, P

$$\frac{dP}{dt}(\text{coupling, internal losses}) = -\frac{P}{\tau_p}. \tag{3.8}$$

Thus the rate equation for the photons becomes

$$\frac{dP}{dt} = A(n - N_{nom})P + \beta\frac{n}{\tau_s} - \frac{P}{\tau_p}. \tag{3.9}$$

Equations (3.5) and (3.9) are the simpler forms of the time-dependent behaviour of semiconductor lasers describing the transient development of electron concentration, n, and photon density, P. They will be used later as the base equations onto which more complex forms of transient behaviour can be derived.

3.3. Relaxation Oscillations

A large quantity of information concerning the dynamical behaviour of semiconductor lasers can be obtained from the small signal analysis of the rate equations. By linearizing equations (3.5) and (3.9) the resulting modulation response has the transfer characteristic of a second-order low-pass network. A resonance in the modulation response, known as relaxation oscillation in lasers, results from the interplay between the optical field and the population inversion. Fig. 3.1 illustrates the response of a semiconductor laser to a step current pulse; the pulse is biased below threshold and then a 2 ns pulse of amplitude twice threshold is applied. This may be understood qualitatively, as follows. The carrier concentration builds up steadily during a delay time, which is dependant on the magnitude of the current and other laser parameters. The carrier density reaches a value exceeding the value required for threshold, and lasing occurs. The lasing action causes a rapid depletion in carriers due to fast (stimulated) recombination. When there are no longer sufficient carriers to maintain lasing, the stimulated light output ceases and the entire process commences again. However, on each successive cycle the carrier and photon populations commence from somewhat higher values than the preceding cycle, and hence the periodic behaviour is damped by a damping factor (γ).

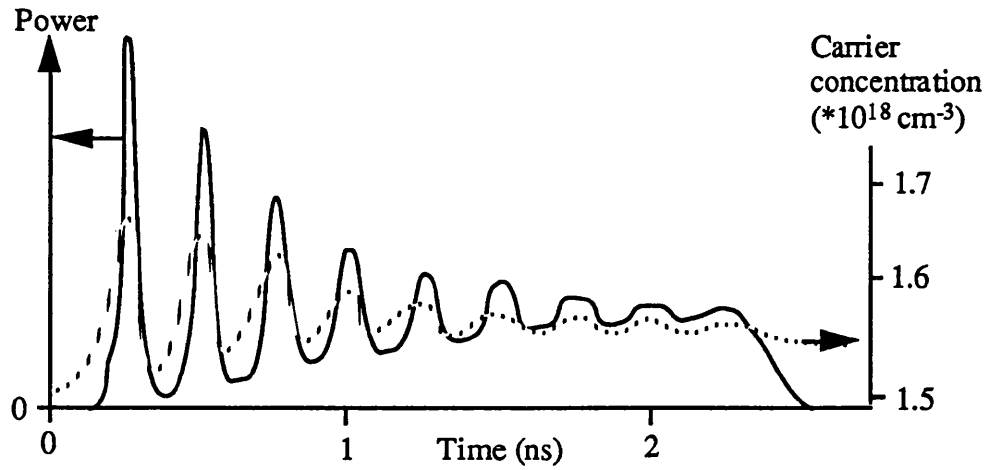

Fig. 3.1. Relaxation oscillations in output power and carrier concentration in response to a 2 ns current pulse.

The frequency and amplitude of the relaxation oscillations, is dependent on many factors, for example the spontaneous emission factor, lateral carrier diffusion, and presence of saturable absorbing defects. The relaxation oscillation frequency obtained from the small signal analysis [3] is

$$f_{res} = \frac{1}{2\pi}\sqrt{\frac{AP_o}{\tau_p}} \tag{3.10}$$

where τ_p is the photon lifetime which can be defined in terms of loss coefficients in the Fabry perot cavity and can be given by [4],

$$\tau_p = \frac{1}{v\left[\Gamma\alpha_{act} + (1-\Gamma)\alpha_{clad} + \frac{1}{2L}\ln(\frac{1}{R_1R_2})\right]} \tag{3.11}$$

where v is the group velocity of the light, α_{act} and α_{clad} are the losses due to the cladding and active regions respectively, L is the length of the device, and R_1 and R_2 is the reflectivity of both facets; P_0 is the steady-state photon density and A is the differential optical gain constant.

The damping rate of the relaxation oscillations is a function of the effective carrier lifetime in the laser active region τ_s and the relaxation frequency, as described by the following equation [5]:

$$\gamma = \frac{1}{\tau_s} + Kf_{res}^2. \tag{3.12}$$

where K is the damping factor. In order to model the damping behaviour of a semiconductor laser properly, it is necessary to take into account gain saturation at high photon densities. Therefore including non-linear gain in the expression for the damping factor:

$$K = \frac{(2\pi)^2}{v_g}\left(\frac{\varepsilon}{A} + \frac{1}{\alpha_i + \alpha_m}\right) \tag{3.13}$$

where ε is the non-linear gain coefficient, and α_i and α_m are the optical loss in the laser cavity and the mirror.

3.3.1. Increasing the modulation bandwidth.

The modulation bandwidth of semiconductor lasers is widely accepted to be equal to the relaxation oscillation frequency, although it is well recognised that the relaxation resonance, whose magnitude varies considerably amongst lasers, can limit the useful bandwidth to somewhat below the relaxation oscillation frequency.

The parameters of the relaxation oscillation frequency can be clearly seen if we rewrite (3.10) in an equivalent form, taking into account the pumping current of the device :

$$f_{res} = \frac{1}{2\pi}\sqrt{\frac{\Gamma N_{nom.} A\tau_p + 1}{\tau_s\tau_p}\left(\frac{J}{J_{th}} - 1\right)} \tag{3.14}$$

where J_{th} is the threshold current density. Equation (3.14) suggests a number of ways to increase the relaxation frequency - by increasing the optical gain coefficient or the pumping current, or by decreasing the photon lifetime or the threshold current. However the relaxation frequency cannot be increased by decreasing the spontaneous carrier lifetime, τ_s, since this also increases the threshold current.

The differential optical gain coefficient, A, can be increased roughly by a factor of 5 by cooling the laser down to 77 K or by using quantum confinement such as quantum well or wire structures. The use of multiple quantum wells (MQW) has been experimentally demonstrated by Uomi *et al* [6] and has been found to enhance the relaxation frequency by a factor of 2 at room temperature. This, along with a narrower gain spectrum producing fewer longitudinal modes under modulation, makes MQW material favourable for use in high speed semiconductor lasers.

Increasing the pumping current would also increase the relaxation frequency, however the photon density in the active region would also increase which simultaneously increases the optical output power density I_{out} according to [3]

$$I_{out} = \tfrac{1}{2} P_o h\omega v_g \ln\left(\frac{1}{R}\right) \tag{3.15}$$

where $h\omega$ is the photon energy and v_g is the group velocity. Catastrophic mirror damage occurs at a power density of $I_{out,cat} \approx 1$ MW/cm^2 for a GaAs/AlGaAs laser with a mirror reflectivity of R=0.3. This value sets an upper limit on the maximum permissible photon density and therefore, the maximum modulation frequency.

The final way of increasing the modulation bandwidth is to reduce the photon lifetime by shortening the length of the laser cavity. However, shorter lasers have to be driven at a higher current density which will cause thermal effects due to excessive heating and therefore limit the maximum attainable modulation bandwidth.

Strained Quantum Well Material

A reduction in the threshold current density is not the only advantage of using strained active layers in heterostructure injection lasers – predictions have also been made of significantly higher parameters. The high modulation frequencies that can be obtained in lasers with quantum well (QW) active layers are thought to be linked to an enhancement of the gain and its energy derivative near QW levels. For example, in QW lasers a two- or three-fold increase in the modulation bandwidth is expected compared to ordinary double heterostructure (DH) lasers [7], and with strained QW layers the modulation bandwidth can be increased further by a factor of three [8]. It has also been shown [5,9] that as well as the addition of strain in the active region, an increase in the number of quantum wells and the addition of p-doping in the barriers can increase the modulation response. The differential gain is increased both by the addition of strained

QW's and by an increase in the number of QW's however, in both cases, this is offset by corresponding increases in the non-linear gain coefficient ε, leading to relatively constant values of the damping factor K, and hence little variation in the maximum intrinsic modulation bandwidth. The addition of p-doping, on the other hand, leads simultaneously to an increase in differential gain and a decrease in K. As a result, the p-doped lasers demonstrate very efficient high speed direct modulation. The performance enhancements in the p-doped lasers are attributed predominately to a decrease in the non-linear gain coefficient, arising most likely from a decrease in the intraband relaxation time τ_{in}.

A combination of strained multiple quantum wells and p-doping in the QW barriers in the future will lead to higher frequency modulation not just in direct modulation of semiconductor lasers but also in other high speed applications such as gain switching and Q-switching.

3.4. Direct modulation

3.4.1. Introduction

Direct modulation of semiconductor lasers is a relatively simple technique for yielding pico-second pulses at gigahertz repetition rates, and work carried out by Lau *et al* [10] has shown modulation bandwidths in excess of 10 GHz under reliable room temperature continuous operation. We have already discussed the laser parameters of direct physical relevance that affect the modulation bandwidth of semiconductor lasers and seen how, by optimising them, we can increase the bandwidth. More recent studies of strained multiple quantum wells has shown that a modulation bandwidth of 30 GHz is possible [11] and intrinsic gain modulation at frequencies at up to 75 GHz has been observed in strained InGaAs/GaAs laser diodes [12]. However, even with these advances in technology, high speed direct modulation still remains "in the laboratory" because of the large drive currents which have typically been required. In the future the successful application of direct laser modulation for very high speed digital transmission or microwave optical links will require a) a reduction in drive current required to achieve high modulation bandwidths, b) an increase in the maximum intrinsic modulation bandwidth, and c) high speed laser structures which can be integrated with high speed transistors.

3.4.2. Description and Analysis of Direct Modulation

Direct modulation utilises combined dc and microwave current injection; the current bias I_o is normally maintained above threshold in order to reduce turn-on delay.

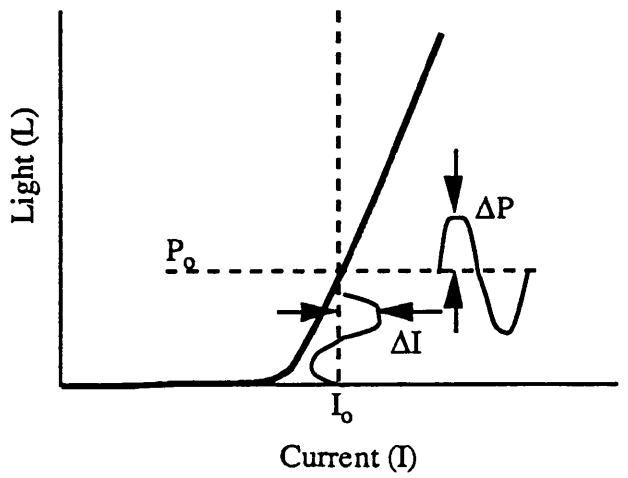

Fig. 3.2. Illustration of a directly modulated laser.

A typical light-out current-in (L-I) curve is shown in Fig. 3.2; from this illustration it is possible to see that, as the current is varied by ΔI about the bias current I_o, the light output will also vary in a similar synchronous manner.

A model of short pulse generation by direct modulation can be derived from the carrier (3.5) and photon (3.9) rate equations [13].

$$\frac{dN}{dt} = J_o + J_1 e^{j\omega t} - A(N - N_{nom})P - \frac{N}{\tau_s} \tag{3.16}$$

If spontaneous emission is disregarded, (3.14) can be integrated to give

$$g(t) = \frac{A}{N_{nom}}\tau_s\left[J_o + \frac{J_1 e^{(j(\omega t - \phi))}}{(1+\omega^2\tau_s^2)^{\frac{1}{2}}}\right] - A \tag{3.17}$$

This equation is represented by the dashed line in Fig. 3.3. The phase delay between the injected current and the carrier density is

$$\phi = \tan^{-1}(\omega\tau_s) \tag{3.16}$$

When the carrier density N_{th} is reached, corresponding to threshold, a short light pulse centred at $t = t_0$ is emitted. The light pulse, due to stimulated recombination, depletes the carriers as illustrated in Fig. 3.3(b) by the solid line.

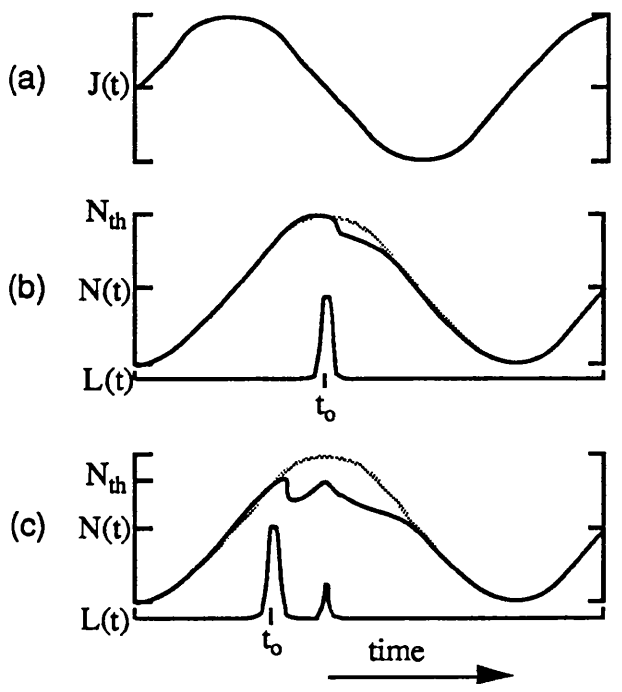

Fig. 3.3. Schematic of the time dependence of (a) the injected current density and (b) the gain and photon density near threshold. (c) At higher currents where the gain reaches threshold a second time, a second pulse is emitted.

The recovery of the gain in Fig. 3.3 is shown to be faster than the repetition period, however, in practice $\tau_s \approx 2ns$. For high repetition rates above 500 MHz, therefore, the gain should be summed over previous pulses to give an accurate value. As the direct and microwave current is increased we see a change in the phase position of the pulse, relative to the rf current. At particularly high currents above threshold, where the carrier density recovers sufficiently to reach threshold a second time, a second pulse is emitted, Fig. 3.3(c).

3.4.3. Electrical Parasitic Effects

Another concern which possibly limits the bandwidth of high frequency electronic devices is the adverse effects that parasitic elements might have. Poor modulation performance has often been observed and has been attributed to parasitic resistance and capacitance present in the semiconductor laser [14]. Fig. 3.4 shows a typical small signal circuit model for a laser and package.

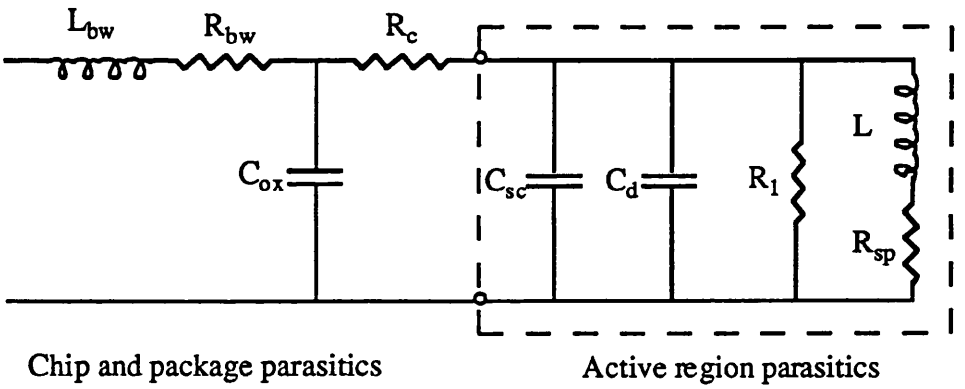

Fig. 3.4. Small signal circuit model for a ridge waveguide laser.

L_{bw} - bondwire inductance
R_{bw} - bondwire resistance
R_c - contact resistance
C_{ox} - parallel effective capacitance associated with an oxide isolation layer
C_{sc} - space charge capacitance of the p-n heterojunction
R - resistance of the active region
R_{sp} - resistance modelling the damping effect of spontaneous emission
L - inductance in the active region representing an exchange of energy between carriers and photons
C_d - diffusion capacitance of device

A number of parasitic elements are present, both external (bondwire inductance, resistance) and internal (parallel capacitance from oxide and p-n junction and the series resistance of the contact and p cladding layers). One can also include a submount capacitance by connecting a shunt capacitance to the entire circuit in Fig. 3.4, however this is normally negligible in well constructed mounts. The active region is modelled by a parallel *RLC* circuit [15] which can be used for small signal analysis. Charge storage in the active layer is modelled by the diffusion capacitance C_d and the small signal photon storage is modelled by the inductance L.

The combined effect of the chip and package parasitics is to reduce the risetime of the current pulse into the laser active region. The value of the bond wire inductance depends not only on the length of the wire but also its diameter and proximity to the ground plane. A good wire-bond should not constitute an inductance much larger than 1 nH. Parasitic capacitance is usually the major element of concern at high frequencies. This value normally depends on the laser material and also the thickness and quality of the silica that acts as a passivation layer. Normal values of capacitance should be around 5 pF. The parasitic capacitance, C_{ox} , can be reduced by using polyimide, which has a thicker layer thickness, as a passivation layer and by designing the p-type electrode so that it has minimal surface area [16].

One of the problems with parasitic elements, that is often observed at high modulation rates, is that of the laser output at any particular time being dependent upon the signal during the previous few bit periods. This sort of 'history' or 'memory' effect is known as patterning and can be clearly seen in eye patterns. It occurs when the modulation rate is such that the carrier density cannot return to steady state during the off or zero period. At particularly high modulation speeds >25 GHz the standard treatment of a laser diode as a lumped electrical element, Fig. 3.4, cannot be assumed for device lengths over 300 μm. This is because the microwave propagation of the electrical signal exhibits slow wave propagation characteristics, and loss effects. The frequency dependence of the microwave loss results in roll-off of the modulation response at high frequency [17].

3.4.4. Longitudinal mode dynamics

Control of the longitudinal mode spectrum is not an important concern in short haul (<1 km) applications where multimode fibre is used, since the primary dispersion of multimode fibres is intermodal instead of chromatic. For applications in a long transmission link where single-mode fibres are used, the spectrum of the laser becomes important especially in long-haul systems (>100 km). Continuous single mode operation under high-speed operation would be ideal, however, in practice no laser oscillates in a single mode especially at high data rates (> 1Gbit/sec). High modulation frequencies

cause an oscillation in the carrier density which is accompanied by a movement in the gain peak which, in Fabry-Perot lasers, often results in a switch in the longitudinal mode and hence operating wavelength. These spectral transients tend to disappear at higher modulation frequencies (> 500 MHz) where the spectrum does not have time to respond within a modulation cycle. However, it is observed that the width of the individual modes broadens at higher frequencies although the relative amplitudes of the modes do not change. This change in operating wavelength or 'chirp' arises from fluctuations in the refractive index of the cavity as a result of oscillations in the carrier density. As the modulation frequency increases so do the carrier density fluctuations, and consequently, the line broadening effect is more pronounced at higher frequencies. The equation for the linewidth is [18]

$$\Delta\upsilon = \frac{gN_{sp}v_g^{\,2}E_g}{8\pi P}\left(1+\alpha^2\right)\alpha_m \tag{3.17a}$$

where N_g is the group refractive index, P is the power output per facet from the laser, L is the cavity length and α is the linewidth enhancement factor α_m is the normalised end-loss which for a Fabry-Perot laser is given by $\alpha_m = -L^{-1}\ln(R)$. N_{sp} is the ratio of spontaneous to stimulated emission given by

$$N_{sp} = \left[1 - e^{\frac{E-eV}{kT}}\right]^{-1} \tag{3.17b}$$

where eV is the separation of the quasi-Fermi levels at lasing. From the expression we can predict that the spectral linewidth can be reduced by increasing the cavity length through the use of external cavity lasers or an extenal cavity mirror. The spectral linewidth is also inversely proportional to the output optical power. Another approach for reducing the linewidth is to modify the density of states through the use of quantum wells [19]. It has been found that there is a ten-fold decrease in the laser linewidth in a thin QW laser compared to a conventional double heterostructure laser. Work on strained QW lasers [20] has theoretically shown that α can be reduced to zero by p-type doping compressive-strained quantum wells and appropriately detuning the lasing wavelength.

3.5. Self-pulsating Semiconductor lasers

3.5.1. Introduction

The first successful demonstration of a semiconductor laser took place in 1962. It is therefore remarkable that two years later Lasher [21] proposed a two-section bistable laser consisting of a Fabry-Perot injection laser with two electrically isolated p-contacts. One contact has an injection current passed through it the other biased in such a way that it '*acts as a nonlinear absorber of light.*' Basov [22] in 1968 investigated two optically connected GaAs homojunction diodes, and observed self- sustained pulsations under conditions that one of the diodes absorbed and another amplified. Self sustained pulsations were observed in aged and degraded GaAs/AlGaAs semiconductor lasers [23]. In 1979 Dixon and Joyce [24] suggested a possible model for sustained oscillations found in GaAs/AlGaAs double heterostructure lasers. They proposed the observed pulsations arise from near-band-edge absorption in localised regions of strong carrier depletion caused by nonradiative recombination at the cleaved facets or internal defects in the cavity. They calculated that the depleted regions occurred at ≈ 5 μm from the mirror facets (carrier diffusion length). Their model helped to explain the increased tendency to pulsate following a relatively small amount of ageing. They found that the decrease in light output during the first few hours of cw testing was due to optical loss near the mirror which results, in turn, from an increase in surface-recombination current. Thus the laser can move from a region where the end loss is too small to satisfy the instability criterion, to a region where pulsations are allowed.

Shortly after this, in 1982, Harder *et al.* [25] observed bistability and pulsations at microwave frequencies in cw GaAs semiconductor lasers with inhomogeneous current injection, over fifteen years after Lasher first proposed such a device. Inhomogeneous current injection was achieved by using a twin segment contact. They showed experimentally that, depending on the electrical bias conditions, the negative differential resistance across the absorber leads either to a narrow hysteresis loop with self-sustained pulsations or to bistability with a large hysteresis loop without self-sustained pulsations.

There are two types of Q-switching that are generally used and are reported here, active and passive Q-switching.

3.5.2. Active Q-switching

The normal configuration used for active Q-switching consists of a two-section laser with the long section forward biased to produce gain in the device, Fig. 3.5(a). The short section is reverse biased to suppress lasing in the structure. An rf modulated electrical signal is also applied to the short section so that the section acts as an intracavity

electroabsorption loss modulator. When an electrical pulse is applied to the short section, the peak of the pulse forward biases the section resulting in a narrow time window of low loss in the cavity for the optical pulse being emitted. The timing jitter of the emitted pulse train is lower than passive Q-switching due to the presence of a high stability driving source.

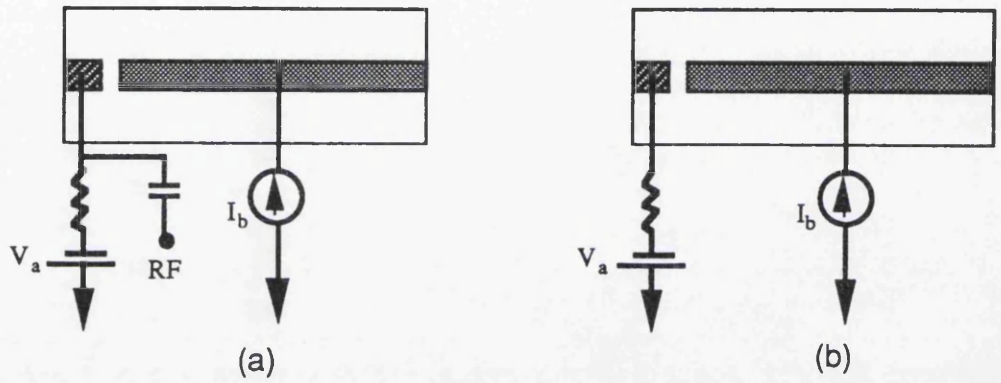

Fig. 3.5. Schematic of two types of Q-switched laser. a) Active Q-switching b) Passive Q-switching or self-pulsation.

One report of active Q-switching in a GaAs/AlGaAs MQW laser has produced pulse widths as narrow as 18.6 ps FWHM at a repetition rate of 3 GHz [26]. Derickson *et al* reported a standard double heterostructure GaAs/AlGaAs two section laser producing actively Q-switched pulses of 15 ps FWHM wide at a repetition frequency of 1 GHz. The measured pulse energy was 4 pJ and the spectral width was 2.4 THz which gave a high time-bandwidth product of 36.

3.5.3. Self-Pulsation

Passive Q-switching or self-pulsation in laser diodes is caused by instabilities induced by regions of saturable absorption coupling with regions of high gain. A standard configuration for a two-section self-pulsating laser is shown in Fig. 3.5(b). The short section of the two-section laser is reverse biased and acts as a saturable absorber, and the long section is forward biased to provide the gain. The self-pulsating repetition rate is controlled by varying the current to the gain section of the device and has been found experimentally to vary approximately as $1/I^{1/2}$[27, 28] as predicted by Peterman [29]. This shows a similar dependence as the repetition rate of relaxation oscillations against drive current. Other methods of self-pulsation have been reported by Barnsley *et al* [27]. Instead of reverse biasing the short section of the laser the absorber region is left open circuit and is selectively doped with Zn using MOVPE. The Zn ions act as centres for

non-radiative recombination which reduces the carrier lifetime. Strong pulsations using this method have been seen at frequencies up to 5 GHz at a gain section current of 200 mA and operating temperature of 17 °C; a pulse width of 20 ps FWHM was also measured. The self-pulsating lasers also showed a strong dependence of repetition frequency against operating temperature. For the same value of drive current the repetition frequency changed from 5 GHz to 3.6 GHz with a temperature change from 17 °C to 30 °C.

3.5.4. Description of self-pulsation

It is well known that saturable absorption introduced into the semiconductor laser cavity plays an important role in the dynamic behaviour of a semiconductor laser, and can cause bistable operation or self-pulsations. The effect on the dynamic stability is due to the nonlinear relationship between the gain and the carrier density. If the gain were, for example, linearly dependent on the carrier density, then even 100% efficient transfer of excited carriers from the gain to the absorbing region via the intermediary of stimulated emission, would not increase the net gain of the laser. Therefore, with an insufficient nonlinearity, the absorption of the saturable absorber raises the threshold current but does not result in pulsations.

In 1976 Stern [30] proposed a calculated gain-loss curve for GaAs, Fig. 3.5. The region B describes the situation in the gain section and the region A describes the situation in the saturable absorber. As the optical emission builds up, the gain at B decreases by an amount Δg. Simultaneously the loss decreases by an amount $\Delta\alpha$.
The necessary condition for lasing then takes the form

$$r_2\Delta\alpha > r_1\Delta g \tag{3.18a}$$

where r_1 is the length of the gain section and r_2 is the length of the absorber section. Since the gain decreases less than the absorption decreases, for a given transfer of excitation, the net remaining gain after "saturation" is larger than that needed for steady state lasing, and the system emits a pulse. To achieve instability, the slope of the absorber curve at A must be sufficiently greater than the slope of the gain region at B.

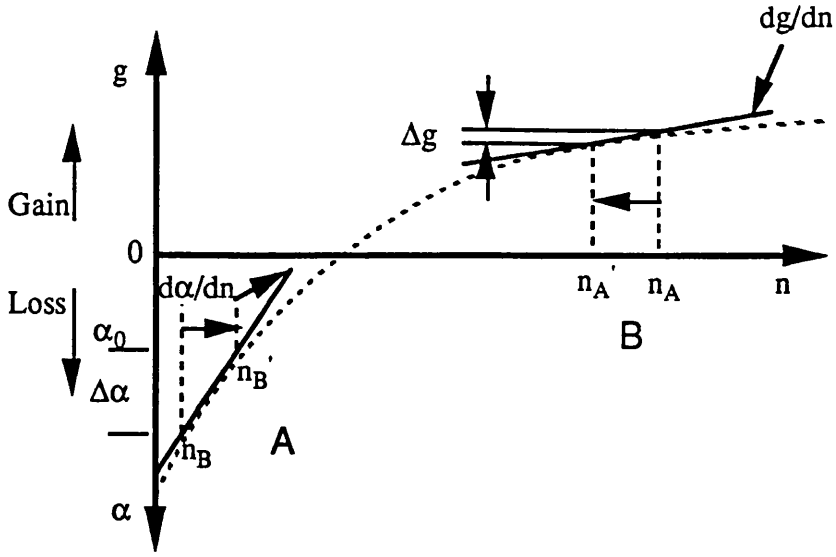

Fig. 3.5. The schematic of the generalised gain-loss curve for GaAs. The region in B depicts the change in the gain region of the laser which occurs when the carrier density changes from n_A (just before the laser emits a pulse) to n_A' (just after the emitted pulse). The region in A depicts the analogous situation in the saturable absorber region.

We can regard the absorptivity $\alpha = \Delta\alpha + \alpha_0$ as a composite of the saturating or bleaching absorptivity $\Delta\alpha$ and a fixed absorptivity α_0. Increases in α_0 arise from local heating, increased surface recombination and impurity absorption effects. The increase in α_0 also increases α and makes the pulsation criterion (3.18) easier to satisfy. Estimates can be made of the amount by which the loss slope has to be greater than the gain slope to satisfy the instability criterion. The loss due to free carrier absorption and scattering is estimated to be $\alpha_s \approx 10\text{cm}^{-1}$ and the distributed loss due to the mirror reflectivity $\alpha_m = -L^{-1}\ln R \approx 30\text{cm}^{-1}$. The absorption in the saturable absorber is also estimated α=200 cm^{-1}, therefore the distributed loss due to a 400 μm cavity and a 30 μm absorber is $\alpha_E = r_2\alpha/L = 15\text{cm}^{-1}$. Thus, of the photons generated within the laser, a fraction η_E is absorbed in the saturable absorber where

$$-\frac{d\alpha/dn_A}{dg/dn_B} > \eta_E = \frac{\alpha_E}{(\alpha_s + \alpha_m + \alpha_E)} \qquad (3.18b)$$

From this equation we find that the loss slope $-d\alpha/dn_A$ must therefore be $1/\eta_E \approx 3.7$ times steeper than the gain slope dg/dn_B for pulsations to occur for the case when α=200 cm^{-1}.

Fig. 3.6 illustrates the time dependence of the gain and loss in the laser cavity and shows how self-sustained pulsations are formed. Initially, before the formation of the pulse, section (a) of Fig. 3.6, the loss is greater than the gain. Any spontaneous emission

produced in the laser cavity is absorbed by the saturable absorber. The gain builds up and eventually exceeds the unsaturated loss (a). At this point the leading edge of a pulse is formed from noise; at the same time the saturable absorber bleaches and the loss drops to the unsaturable loss (b), the loss due to mirror transmission, free carrier absorption, waveguide loss etc. As the intensity of the pulse increases, the gain drops, however because the loss saturates faster than the gain, the central part of the pulse is amplified. When the gain reaches saturation below the unsaturable loss, the trailing edge of the pulse experiences net loss.

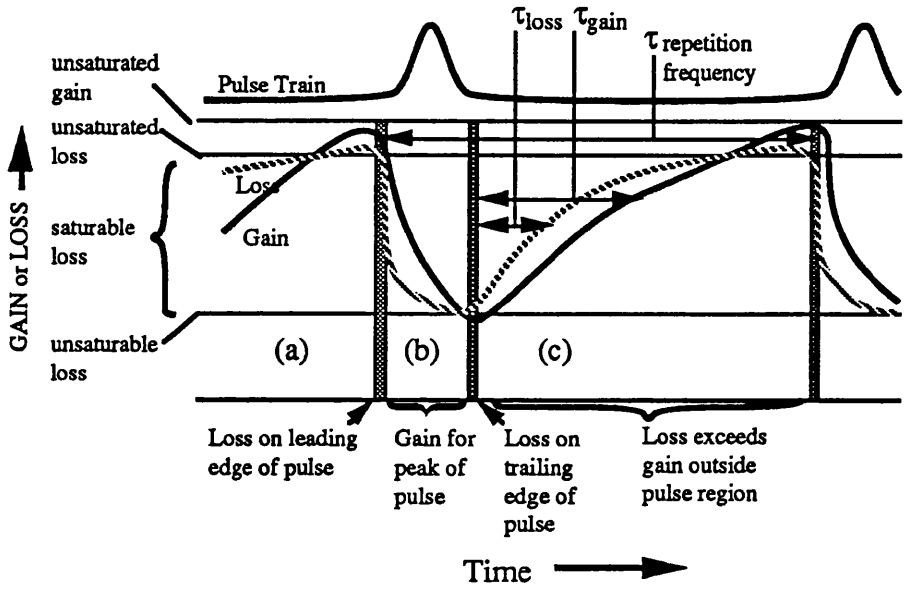

Fig. 3.6. Gain and loss dynamics for self pulsation.

Although the formalism is very similar, the physics of self-pulsing is very different from modelocking. In the case of modelocking, which will be described later, the pulse is shorter than the cavity round trip time and travels back and forth being repetitively shaped by the action of the gain and absorber. The repetitive shortening of the pulse is limited by dispersive pulse broadening which occurs as the pulse travels through the cavity. Passive Q-switching produces pulses that are longer than the cavity round trip time, which means the laser can be treated as a lumped element. The pulse builds up from noise and is shaped by the action of the gain and absorber, however, unlike modelocking, it is not repetitively shaped. Therefore, it is not required to include dispersion when determining the equilibrium pulse shape. All these factors are considered when forming a mathematical model of self-pulsation.

3.5.5. Self pulsation model

To give a mathematical description of self pulsation in a semiconductor laser, the rate equations are slightly modified to describe the rate of change of carriers in the absorbing section. Also, in using the rate equations, it is implicit that the results are applicable only on a time scale longer than the round trip transit time of the laser diode, which is typically 10 ps or shorter. The rate equation describing the gain section is the same as (3.5) in section 3.2

$$\frac{dn_1}{dt} = \frac{J}{ed} - \frac{n_1}{\tau_1} - a_1(n_1 - N_1)P \qquad 3.19$$

A modified version, used previously by Haus [31], describes the rate of change of carriers in the absorbing unpumped region

$$\frac{dn_2}{dt} = -\frac{n_2 - N_2}{\tau_2} - a_2 n_2 P \qquad 3.20$$

where n_2 is the population difference between the lower and upper transition levels of the saturable absorber. The rate of change of photon flux (in which the spontaneous recombination term is negligible and therefore ignored) is given by:

$$\frac{dP}{dt} = v_g\left[r_1 a_1(n_1 - N_1) - r_2 a_2 n_2 - \frac{1}{v_g \tau_{ph2}}\right]P. \qquad 3.21$$

a_1 and a_2 are the gain and absorber cross sections, N_1 is the gain carrier concentration at transparency, N_2 is the equilibrium absorber population density in the absence of light, P is the photon flux in the cavity (photons per unit time), v_g is the group velocity of light, τ_2 is the absorber relaxation time and r_1 and r_2 are the fractions of the total cavity length occupied by the gain and absorber media. τ_{ph2} is the photon lifetime due to output coupling and linear loss. The spontaneous emission term has been neglected in (3.21), as is often done in treating laser dynamics above threshold. The light intensity is related to the photon flux P by $I = \hbar\omega P$.

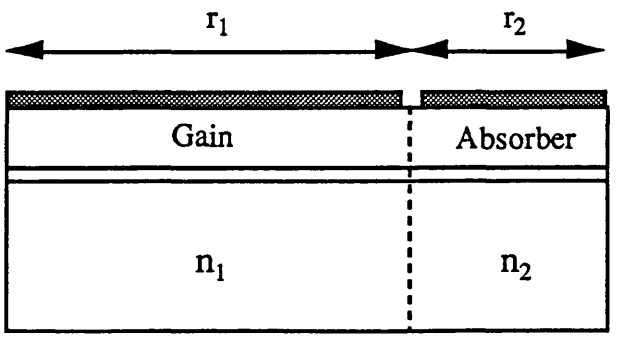

Fig. 3.6. Schematic of the model used in the self-pulsation calculation.

In this model we consider the total photon flux P neglecting the multimode characteristic of semiconductor laser emission. The phases between the different longitudinal modes is in fact random, and therefore the emitted pulse is just an envelope of an optical "noise" burst. The incoherent nature of the self pulsating laser diode pulse is observed in second harmonic autocorrelation traces, in which random coherence spikes are seen. The pulse is therefore not transform limited.

(3.19)-(3.21) can be solved for a repetitive pulse solution by a method analogous to that used by Haus [31, 32] in the theory of modelocking and subsequently used here by Kuznetsov [33] for self-pulsations of a semiconductor laser. Firstly a dynamic equation for the flux is obtained by finding the gain and absorber populations. The non-linear saturation terms are expanded to low orders so as to facilitate a closed form solution. We then assume a pulse shape and obtain the pulsation parameters from the dynamic equation.

Assuming the absorber follows the photon flux quasistatically, we solve for the absorber population (3.20) and obtain

$$n_2 = \frac{N_2}{1+\frac{P}{P_0}} \qquad 3.22$$

where $P_0 \equiv 1/a_2\tau_2$ is the absorber saturation flux. Assuming a pulse-like solution, we can describe the gain population during and between the pulses. We can also assume, since the pulsewidth is much shorter than the gain relaxation time (~5ns), that

$$\frac{dn_1}{dt} \equiv -a_1(n_1 - N_1)P \qquad 3.23$$

with the solution

$$n_1(t) = N_1 + m_o e^{-E/E_s} \qquad 3.24$$

where we have defined $E_s = 1/a_1$ and

$$E(t) = \int_{-\infty}^{t} P(t')dt' \qquad 3.25$$

E (t) is the accumulated "energy" of the pulse (energy in units of $\hbar\omega$ per unit cross section area) and E_g is the gain saturation "energy." Just before the pulse $n_1 = N_1 + m_0$, where m_0 is a constant to be determined from the analysis. Between the pulses, where the photon flux should be approaching zero, from (3.19) the derived expression is

$$n_{(1)}(t) = \frac{J\tau_1}{ed} - m_1 e^{\frac{-t}{\tau_1}}. \qquad 3.26$$

Before the pulse, the carrier density should have recovered to its unsaturated value $J\tau_1/ed$ and, just after the pulse, the carrier density should have dropped to the value $J\tau_1/ed - m_1$. Where m_1 is a constant to be determined by the analysis.

To obtain the dynamic equation for pulse formation we have to use gain (3.24) and absorber (3.22) population expressions in (3.21) for the photon flux. Assuming weak saturation during the pulse, n_1 and n_2 are expanded to low orders in the saturation parameters

$$n_1 \equiv N_1 + m_o\left[1-\left(\tfrac{E}{E_g}\right)+\tfrac{1}{2}\left(\tfrac{E}{E_g}\right)^2\right]. \qquad 3.27$$

$$n_2 \equiv N_2\left(1-\tfrac{P}{P_o}\right) \qquad 3.28$$

Since the gain is energy saturated it is expanded to a second order, whereas the absorber is power saturated and expanded to a first order, since the saturation power is very high. Substituting these equations into (3.21), the obtained pulse dynamics equations are

$$\frac{dP(t)}{dt} = v_g\left[\left(g_o - \alpha_2 - \frac{1}{v_g\tau_{ph1}}\right)+\alpha_2\left(\frac{P}{P_o}\right)-g_o\left(\frac{E}{E_g}\right)+\tfrac{1}{2}g_o\left(\frac{E}{E_g}\right)^2\right]P(t) \qquad 3.29$$

$$= v_g g_T(t)P(t) \qquad 3.30$$

Where $g_o \equiv r_1 a_1 m_o$ is the gain coefficient before the pulse, $\alpha_2 \equiv r_2 a_2 N_2$ is the unsaturated absorber loss and the quantity in square brackets is $g_T(t)$ the net gain.

Solution to the Self-Pulsating Model

If we assume a hyperbolic secant shape for the pulse amplitude, the photon flux is

$$P(t) = V\,\mathrm{sech}^2\left(t/\tau\right) \qquad 3.31$$

Substituting the pulse shape into (3.29), we obtain three characteristic equations which become, after some manipulation,

$$v_g\left(g_o - \alpha_2 - \frac{1}{v_g\tau_{ph1}}\right)\tau = 2 \qquad 3.32$$

$$\left(\frac{g_o}{\alpha_2}\right)P_o V\tau^2 = 2E_g^2 \qquad 3.33$$

$$\left(\alpha_2 v_g \tau\right)\frac{V}{P_o} = \left(\frac{\alpha_2 v_g E_g}{P_o} - 1\right) \qquad 3.34$$

Here we have three equations and three unknowns: pulse amplitude V, pulse width τ, and initial gain g_o. Since all the variables in (3.32)-(3.34) are positive, a meaningful solution requires that

$$\left(g_o - \alpha_2 - \frac{1}{\upsilon_g \tau_{ph1}}\right) > 0 \qquad 3.35$$

as implied by (3.32). Also, the net gain before the pulse must be positive,

$$\frac{\alpha_2 \upsilon_g E_g}{P_o} > 1 \qquad 3.36$$

as implied by (3.34). Both these equations are conditions for self-pulsation.

Further definitions of some of the terms used are: the photon lifetime of the saturable absorber

$$\tau_{ph2} = \frac{1}{\upsilon_g \alpha_2} = \frac{1}{r_2 a_2 N_2 \upsilon_g} \qquad 3.37$$

the total photon lifetime

$$\frac{1}{\tau_{ph}} = \frac{1}{\tau_{ph1}} + \frac{1}{\tau_{ph2}} \qquad 3.38$$

The effective absorber saturation energy is :

$$E_A = \frac{P_o}{\upsilon_g \alpha_2} = \frac{1}{a_2}\left(\frac{\tau_{ph2}}{\tau_2}\right), \qquad 3.39$$

and the p parameter, the gain saturation energy over the absorber saturation energy,

$$p = \left(\frac{E_g}{E_A}\right) = \frac{a_2}{a_1}\frac{\tau_2}{\tau_{ph2}} \qquad 3.40$$

solving (3.32)-(3.34) for the unknowns we obtain for the pulse width

$$\tau = 2\tau_{ph}\left[\frac{p^2 - p + 1}{p - 1}\right] \qquad 3.41$$

the pulse amplitude

$$V = \frac{1}{2}\frac{E_A}{\tau_{ph}}\left[\frac{(p-1)^2}{p^2 - p + 1}\right], \qquad 3.42$$

the initial gain

$$g_o = \frac{1}{\upsilon_g \tau_{ph}}\left[\frac{p^2}{p^2 - p + 1}\right], \qquad 3.43$$

The accumulated energy of the pulse is

$$E(t) = V\tau\left[\tanh\left(\frac{t}{\tau}\right)+1\right] \qquad 3.44a$$

and the total pulse energy E_o is

$$E_o = E(t\to\infty) = 2V\tau = 2E_g\left(1-\frac{1}{p}\right). \qquad 3.44b$$

The consistency of the solution is determined by looking at the net gain before $g_t^{(b)}$ and after $g_t^{(a)}$ the pulse

$$g_t^{(b)} = g_o - \alpha_2 - \frac{1}{v_g\tau_{ph1}} = \frac{1}{v_g\tau_{ph}}\left(\frac{p-1}{p^2-p+1}\right) \qquad 3.45$$

$$g_T^{(a)} = \left(g_o - \alpha_2 - \frac{1}{v_g\tau_{ph1}}\right) - g_o\left(\frac{E_o}{E_g}\right) + \frac{1}{2}g_o\left(\frac{E_o}{E_g}\right)^2 = -g_T^{(b)} \qquad 3.46$$

Considering these two equations, we conclude that the pulsation condition p>1 assures a positive net gain before the pulse and a net loss after the pulse. Since there is no stored pulse in the cavity, as in modelocking, positive net gain before the pulse is required for self starting. In this analysis it is worth noting that, from (3.31), the leading edge of the pulse is exponential, as expected for a signal building up from noise. Also we can see that there is net loss after the pulse due to dynamic gain saturation; this condition is required to terminate the pulse. The net gain at the peak of the pulse, that is $g_T(t=0)$, is zero which is characteristic of Q-switching and relaxation oscillations. As illustrated in the previous section (3.5.4.) it appears from these equations that the pulse is shaped by gain saturation, while absorber saturation brings about instability and ensures sustained pulsation's.

Calculating the Repetition Period

For sustained pulsation the gain must recover before the start of the following pulse between the values given by (3.45) and (3.46). From (3.27) we find the gain carrier concentration before (n_{1b}) and after (n_{1a}) the pulse

$$n_{1b} = N_1 + m_o \qquad 3.47$$

$$n_{1b} = N_1 + m_o\left(1-2\frac{p-1}{p^2}\right) \qquad 3.48$$

where m_o is easily obtained from g_o. The recovery of the gain proceeds according to (3.26), such that $n_1(t=0)=n_{1a}$ and $n_1(t=T)=n_{1b}$, where T is the pulsation period.

$$J_{th} = \frac{ed}{\tau_1}(N_1+m_o) = \frac{ed}{\tau_1}\left[N_1 + \frac{g_o}{r_1 a_1}\right] \qquad 3.49$$

From (3.47)-(3.49) with (3.26) we obtain the pulse period T:

$$T = \tau_1 \ln\left[1 + \frac{B}{(J/J_{th} - 1)}\right] \qquad 3.50$$

where

$$B = 2\left(\frac{p-1}{p^2}\right)\left(1 + \frac{r_1 a_1 N_1}{g_o}\right)^{-1}. \qquad 3.51$$

We can see that as $J \to J_{th}$, the repetition rate goes to zero. At high values above threshold ($(J/J_{th} - 1) >> B$) the repetition rate is linear in J

$$\frac{1}{T} = \frac{1}{B\tau_1}\left(\frac{J}{J_{th}} - 1\right) \qquad 3.52$$

but near threshold the dependence is more complicated. Such linear dependence at high currents has to be reconciled with the square root dependence observed experimentally [27, 28] and predicted by Dixon and Joyce [24] in their small signal analysis. The linear dependence at high currents is said [24] to be derived from the carrier refilling time. It is worth noting from this analysis that the pulse parameters such as pulse width and amplitude do not change with increasing bias; only the pulsation period changes with bias.

3.5.6. Passively Q-switched Laser with Ion Implanted Saturable Absorber

As mentioned previously, ageing and degradation of the end facets of a laser diode can cause nonradiative recombination and produce strong carrier depletion at either end of the device. This in turn produces self-pulsation in the output of the laser diode. Similar double heterostructure GaAs/AlGaAs lasers with a saturable absorber produced by deep implantation of heavy ions into the facets have been fabricated [34] . In such an absorber, deep absorption modulation may be obtained along with high recovery rates. The saturable absorber of this type utilises the idea of spatial separation of charge carrier generation and recombination regions. This may be obtained by means of creating local amorphized regions with very high carrier recombination rates in the crystalline material. If the dimensions of the of the amorphized regions are smaller than the area in between these regions then the material characteristics, such as the steep edge of the absorption spectrum are unchanged, whereas the effective lifetime of nonequilibrium carriers is drastically reduced. Hence, deep absorption modulation is possible due to the dynamic Burstein-Moss (band filling) effect, as in a normal direct-gap bulk semiconductor. However, the recovery time of this effect is now defined by the rate of carrier capture by the amorphized regions and thus may be several orders of magnitude faster than the interband recombination time. Calculated values of absorber recovery times are around 6 ps, and oxide stripe heterostructure lasers with this type of saturable absorber have produced passive Q-switched pulses less than 10 ps in duration and more than 1 W in

peak power. Pulsation frequencies up to 20 GHz have also been observed. However, because of the high threshold current of these devices due to the material structure and the high absorption from the ion implanted saturable absorbers, the lasers have to be driven in a quasi-cw regime-with short pulses of ~ 5 ns duration.

Such lasers were supplied to the optoelectronics group by Prof. E. L. Portnoi from the Ioffe institute, St Petersburg and were used in a number of ultra-short pulse experiments which are discussed later.

3.5.7. Multiple Quantum Well Two-section Lasers

Quantum well lasers with tandem electrodes have numerous applications in optical communications. By biasing both sections above transparency the modulation bandwidth can be increased and the wavelength can be tuned over a wide range due to the so-called gain lever effect [35]. By reverse biasing one section as a saturable absorber and the other section forward biased to produce gain, bistability and self-pulsation can be induced. The mechanism of self-pulsation in multiple-contact laser diodes arises from instability in the continuous wave operation of a laser with an intra-cavity saturable absorber. These instabilities are caused by certain physical factors, the differential gain in the absorbing region must be greater than the differential gain in the gain region, described in 3.5.4, and also the lifetime of the carriers in the absorber must be less than the carrier lifetime of the gain section. The lifetime of the carriers in the absorber is dependent on the electric field applied across the QW, (see section 3.5.8). As the carrier lifetime is decreased with increased applied reverse bias the two-section laser goes from the regime of bistability to self-pulsation.

The self-pulsation in a two-section laser is enhanced by the use of a multiple quantum well structure. This increased efficiency is due to two mechanisms: a large loss change, and a high differential gain resulting in a narrow pulse width. A large loss change is realised with the quantum confined stark effect in the absorber section and the band shrinkage effect in the optical amplifier. A high differential gain is expected in the quasi-two-dimensional electronic system of a MQW structure. Therefore the use of a MQW structure satisfies the requirements for the generation of narrow optical pulses.

3.5.8. Intracavity Saturable Absorbers

Introduction

Electroabsorption in semiconductor multiple quantum wells is one of the most efficient processes for making optical intensity modulators and hence has attracted a great deal of interest [36], [37]. Using the reverse biased MQW structure as an intra-cavity saturable absorber or electroabsorption loss modulator in self-pulsating and mode-locked lasers has increased their performance considerably, producing pulses of 0.6 ps, at rates up

to 350 GHz [38]. In order to produce a stable train of short pulses at these microwave and millimetre repetition rates, the absorption recovery must be fast enough to recover before the next pulse is produced. Understanding the dynamics of the saturable absorber is necessary for laser design optimisation. It is also important to understand the mechanisms of the non-linear absorption properties of waveguide structures and the inherent limits to their recovery times.

Much experimental and theoretical work has been carried out on the optical characteristics of GaAs/AlGaAs MQW material [39]. It has been found that in these structures there are prominent room-temperature exciton resonance's near the band edge, Fig. 3.7 and that the exciton absorption saturates at optical intensities ~10X lower than those required to saturate the GaAs band-to-band transition. The MQW sample exhibits enhanced

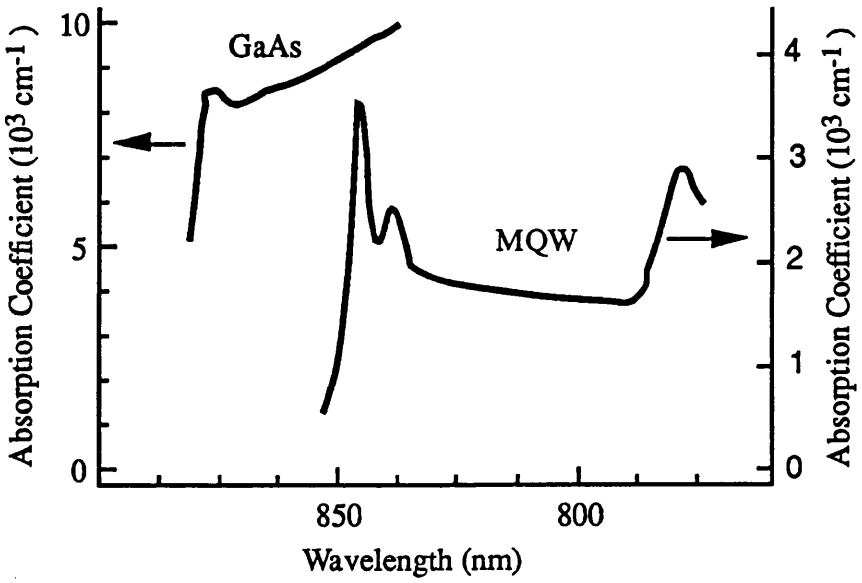

Fig. 3.7. Room-temperature linear-absorption spectra for bulk GaAs and GaAs/AlGaAs MQW samples near the band edge [39].

absorption at the band-edge, and the double peaked structure is caused by excitons whose binding energy is enhanced by the two-dimensional confinement. When an electric field is applied to the quantum wells perpendicular to the layers, the exciton absorption peak shifts to a lower energy. This phenomenon is called the quantum confined Stark effect and is much larger than the Franz-Keldysh effect seen in bulk material. The dominant mechanism is the decrease in confinement energies, resulting in a red shift of the excitonic absorption energy. The band discontinuities prevent the ionisation of the exciton, allowing exciton resonances to be observed at room temperature with large applied fields ($> 10^5$ V/ cm), Fig. 5.19. Also, the carrier induced band shrinkage effect is enhanced in

MQW lasers compared to a conventional double heterostructure lasers, resulting in a decrease of the lasing photon energy by about 20 meV compared to the intrinsic absorption edge. Consequently, the effect of the band-gap shrinkage in the amplifier section and the enhanced electroabsorption in the modulator section, result in extremely large loss changes which are induced by the application of an electric field to the saturable absorber.

Quantum Well Carrier Sweep Out

Absorption of light leads to the creation of electron-hole pairs inside the quantum well. These created carriers, if allowed to build up, change the performance of the saturable absorber through essentially two mechanisms: excitonic saturation and electric field screening. Electric field screening is a mechanism by which the photogenerated carriers screen the applied electric field. In order to avoid these effects and increase the recovery time of the saturable absorber, the carriers must be swept out of the quantum well where they were created. The two main mechanisms thought to be responsible for the carrier sweep out are thermionic emission and tunneling [37], however recent studies have concluded that the emission mechanism is normally dominated by thermionic emission [36]. It has been found that;

1) the sweep out time decreases with increasing applied electric field because both the thermal emission and tunneling lifetimes decrease due to the reduction in barrier height.

2) The sweep out times increase with barrier thickness due to the increase in the tunneling time.

3) The sweep out times increase with increasing ΔE_g (the energy difference between the QW and barrier) due to the increase in both the thermal emission and tunneling times.

4) The sweep out time decreases with an increase in temperature due to a decrease in thermal emission time.

The recovery time of the saturable absorber has a monotonic decrease with increasing reverse bias, but is also dependent on the pulse energy which is attributed to the screening effects of the escaped carriers [38]. An absorption recovery time of 4 ps has been measured at a reverse bias of 5 V which translates to a maximum repetition rate in excess of 250 GHz. Recent pump-probe experiments [39] have found the existence of an ultrafast absorption dynamic. This initial transient, with a rise and fall time of less than 150 fs, is followed by a slower rise that peaks after a few picoseconds, and finally an exponential recovery that depends on the reverse bias. It is thought that this transient may be responsible for some of the high speed mode-locking results.

3.6. Modelocking of semiconductor laser diodes

3.6.1. Introduction

Recent advances in technologies such as high bit rate time division multiplexed communication systems and ultralong distance soliton fiber transmission have required very short optical pulses at high repetition rates with pure spectral properties. Direct modulation, gain switching and Q-switching all have their limitations: all three methods of short pulse generation produce pulses generated from noise and switched on from below threshold. This causes significant fluctuations in both carrier density and the time delay between the excitation and optical pulse, which results in significant frequency chirp and timing jitter. These methods also have a modulation bandwidth limitation which depends on material design considerations. Recently 30 GHz direct modulation has been achieved by Ralston *et al* [5] using strained $In_{0.35}Ga_{0.65}As/GaAs$ quantum wells, however realistic modulation bandwidths do not look like they will exceed this value by much in the future.

Short optical pulses with very pure spectral properties, low timing jitter and high repetition rates can be obtained from modelocked semiconductor lasers. This technique utilises the fact that a semiconductor laser can oscillate at more than one optical frequency corresponding to more than one mode. These longitudinal modes of the laser can be phase locked by the use of a saturable absorber or by a microwave oscillator whose repetition frequency is equal to the round trip frequency of the laser cavity.

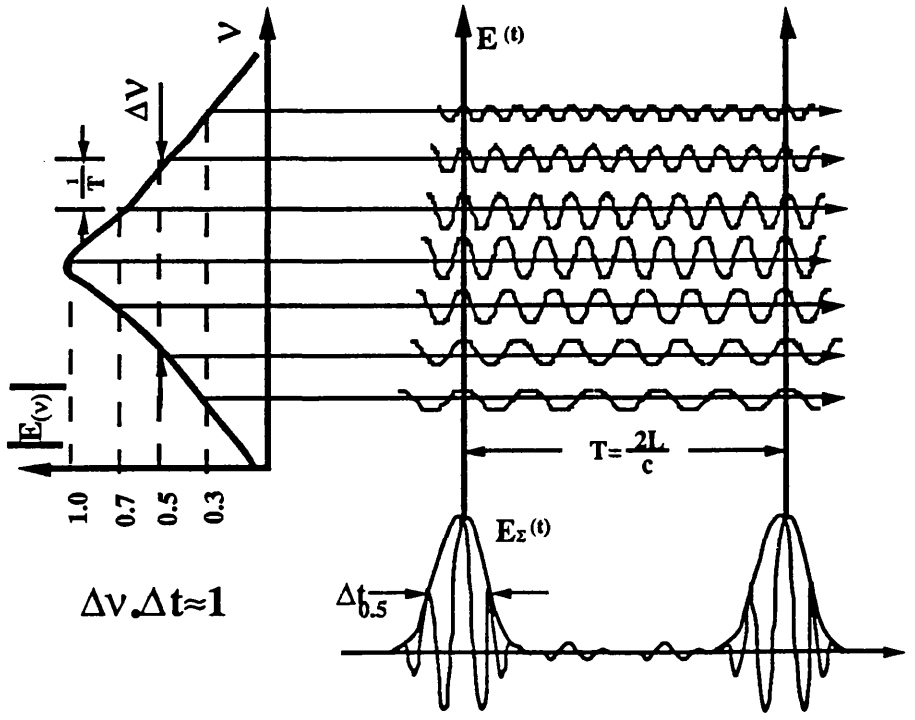

Fig. 3.8. Schematic illustrating the phase locking of modes in a mode-locked laser.

To produce short pulses, longitudinal modes over a wide frequency range have to be locked together. The width of the pulses is ultimately limited by the overall laser bandwidth and the unevenness in mode spacing caused by variations of the effective index with frequency (dispersion).

3.6.2. Actively mode-locked external-cavity lasers

The first successful active modelocking of a c.w. GaInAsP laser diode was achieved by Glasser in 1978 [42]. Fig. (a) shows the simple external configuration for modelocking used by Glasser. It consists of a semiconductor diode laser with a single pumping electrode and an antireflection coated facet coupled to an external cavity. The external cavity contains a collimating lens, a feed back mirror, and possibly a wavelength control filter.

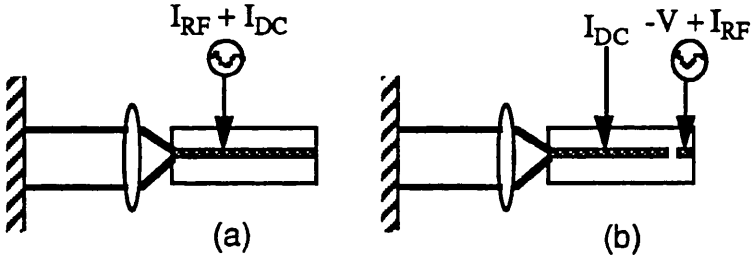

Fig. 3.9. Modelocked laser configurations. (a) Single-segment external cavity active modelocking. (b) Two-segment external cavity active modelocking.

During the active modelocking process, the gain of the laser is modulated with electrical pulses that have a period very close to the round trip time in the laser cavity.

$$T = \frac{1}{f_{rep}} = \frac{2Ln_{eff}}{c} \qquad 3.53$$

is the equation giving the repetition frequency, where T is the round trip time, L is the length of the cavity, n_{eff} is the effective refractive index of the whole laser cavity, and c is the speed of light. Large amplitude, short pulses are used to create a very narrow time window of net gain in the device which will then produce short optical pulses. Pulses as short as 600 fs with 0.024 pJ of energy have been generated using active modelocking of single segment semiconductor lasers [43].

However, one of the main problems of external cavities is secondary pulse formation due to imperfect anti reflection coatings on the external cavity facet. The reflected pulse is amplified because the main pulse does not fully deplete the gain and the modulated current pulse may still be creating new carriers. These secondary pulses can build up over many round trips to significant energy values compared to the main pulse. Schell *et al.* [44] have calculated that even a good antireflection coating, 10^{-5}, will cause multiple pulse formation at the round trip time of the laser diode cavity.

In Fig. 3.9(a), the gain and gain modulation are incorporated in the same section of the device. By separating the gain and gain modulation into two separate sections as in Fig. 3.9(b), the multiple pulsation problem can be suppressed. One section is forward biased with a DC current to provide the gain for the device while the other section acts like a reverse biased saturable absorber driven by a modulated current (electroabsorption loss modulator). Since the modulated section is reverse biased, only the peak of the modulation cycle actually injects charge into the short section resulting in an even shorter effective pumping interval. At the end of the modulation pulse, the short section is reverse biased and sweeps out any carriers left in the active region, resulting in a very high loss condition for any secondary pulses in between the main pulses.

3.6.3. Passively mode-locked external cavity lasers

The passive mode locking technique is the most commonly used form of modelocking since its first reports by Morozov *et al* [45] and Bogdankevich *et al.* [46]. The technique, which requires no external high speed modulation, can supply a simple, reliable, and compact source of picosecond optical pulses. The key component necessary for passive modelocking is a suitable saturable absorber. In most cases the saturable absorber used is slow, that is to say the recovery time of the absorber is longer than the pulse length but must be shorter than the repetition frequency. The slow saturable absorber absorbs the leading edge of the pulse leaving the trailing edge unattenuated. Slow saturable absorption along with gain saturation during the trailing edge of the optical pulse leads to net pulse narrowing on each successive passage through the modelocked cavity.

The first reported stable passive mode-locking of a diode laser with an external saturable absorber element was made by Silberberg *et al* in 1984 [47]. The set up used, illustrated in fig. 3.10, consisted of a saturable absorber and a mirror arranged in an external cavity. The saturable absorber consisted of 47 GaAs/AlGaAs quantum wells with antireflection coatings on both the exposed surface of the saturable absorber and the external cavity facet of the laser diode.

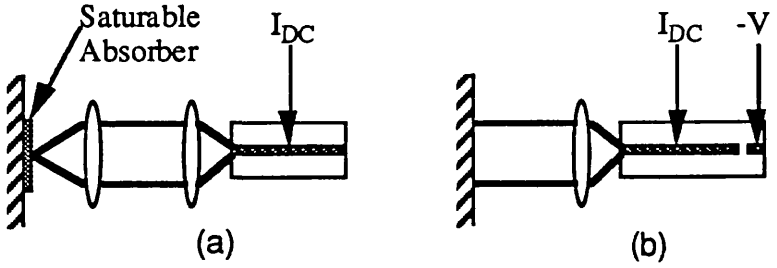

Fig. 3.10. Schematic of two passively modelocked arrangements.

In his analysis of the conditions necessary for modelocking a homogeneously broadened laser with a saturable absorber [32], Haus showed that the relaxation of the absorber must be faster than that of the gain and that one must have

$$\sigma_A/A_A > \sigma_G/A_G \qquad 3.54$$

and

$$\tau_A < \tau_G \qquad 3.55$$

Where σ_A and σ_G are the effective optical cross sections of the absorbing particles and gain medium, respectively, and A_A and A_G are the cross sectional areas of the laser beam in the absorber and gain media. τ_A and τ_G are the lifetimes of the absorber and gain saturation effects. As discussed in the previous section, MQW structures have absorption characteristics which make them ideal as saturable absorbers. It has been found that, in these structures, there are prominent room temperature exciton resonances near the band edge. Due to the screening effect of optically created carriers, the exciton absorption saturates at optical intensities ≈ 10 times lower than those required to saturate the GaAs band to band transition. Therefore, in a MQW absorber $\sigma_A >> \sigma_G$. To decrease the recovery time of photoexcited carriers in the MQW saturable absorber, the incident light from the arrangement in Fig. 3.10 (a) was tightly focused onto the MQW sample. The tight focusing of the light beam effectively causes the generated carriers to diffuse laterally out of the interaction region in times comparable with the recombination time. A beam focused down to 2 μm produces an absorber recovery time < 400 ps. Pulses as short as 1.6 ps have been obtained with this method, however the repetition frequency was only 2 GHz [47]. This method therefore has a limited repetition rate; a more ideal method is illustrated in Fig. 3.10 (b). The long section is forward biased to provide gain for the laser. By reverse biasing the short segment of the laser, a saturable absorber is formed. The reverse biased section acts basically like a waveguide photodetector. The incoming optical pulse saturates the band-to-band absorption and bleaches the short segment. After the passage of the optical pulse through the absorber section, the electric field in the photodetector sweeps the carriers out of the active region and returns the segment to the high attenuation state. Reverse bias intracavity waveguide saturable absorbers in passively modelocked systems, as mentioned previously, can produce saturable absorber recovery times of less than 4 ps. Single pulses as short as 2.5 ps with 0.7 pJ of energy have been achieved in two-section passively mode-locked structures [48].

3.6.4. Monolithic Cavity Mode-locked Semiconductor Lasers

The previous discussion of multisegment external-cavity mode-locked lasers illustrated that both the gain and absorbing section can be implemented on the same chip. This section will examine the integration of an extended waveguide cavity to replace the

external cavity resulting in an integrated monolithic cavity mode-locked laser structure. Monolithic cavity devices can be designed to be very small and do not have the mechanical instabilities associated with the optical elements in an external cavity.

Monolithic Hybrid Mode-locked Laser

There are two main types of monolithic mode-locked laser. Fig. 3.11 (a) shows a monolithic hybrid mode-locked laser: the device has a reverse biased saturable absorber (section a), a gain region (section c) which is forward biased with a dc current plus an rf modulation at the cavity round trip frequency. In between the gain and absorbing regions is an active waveguide (section b) which is biased with a dc current so that the cavity is transparent.

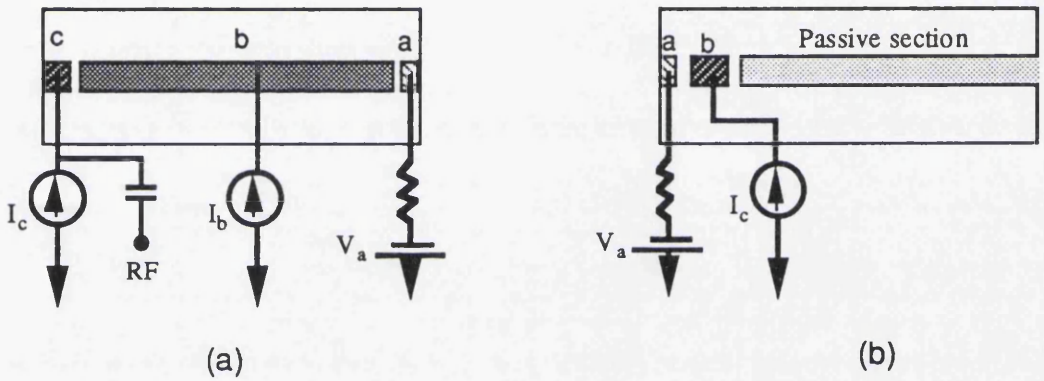

Fig. 3.11. Schematic of two monolithic modelocked lasers. a) With an active extended cavity. b) With a passive extended cavity.

Pulse widths as short as 1.4 ps at a repetition rate of 15 GHz have been obtained from this device with peak energies of about 0.03 pJ [49]. Active waveguides however, are susceptible to high levels of timing jitter due to the spontaneous emission created when the pulse travels through the active waveguide. The spontaneous emission causes gain, index of refraction and photon density variations. Index of refraction noise can directly lead to timing jitter by introducing a randomness in the round trip time. Gain and photon density fluctuations can also lead to timing jitter through an amplitude to timing jitter conversion process. The amplitude to timing jitter process occurs because variations in the gain and saturable absorber saturation levels lead to variations in the round trip time. Monolithic cavity devices which incorporate long sections of low-loss passive waveguide should give comparable timing jitter to their external cavity counterparts.

Monolithic Passive Waveguide Mode-Locked Laser

Monolithically integrated extended cavity lasers with passive waveguides have only recently been reported compared to the other methods [50],[51]. This is due to the difficulty of forming low loss passive waveguides. Fig. 3.11 (b) shows a schematic of passively mode-locked extended cavity laser: the device has a reverse biased saturable absorber (section a), and a forward biased gain section (section b). The passive waveguide can be fabricated using a number of methods; the fabrication processes used in [50] and [51] involve the growth of a 1.5 μm (lasing wavelength) active layer on top of a 1.3 μm (absorption wavelength) passive layer. The pulse train then couples from the active section into the passive section with an estimated coupling efficiency of better than 90 %. The propagation loss of the waveguide is 3 to 4 dB/cm. Pulse widths as short as 5 ps at a repetition rate of 8.57 GHz have been obtained using such a device passively modelocked [51]. Similarly pulses 4 ps wide at a repetition rate of 40 GHz have been obtained from an actively mode-locked device [50].

Other methods of low-loss waveguide fabrication include impurity induced disordering and dielectric cap annealing both of which methods intermix the QWs with the barriers and hence increase the effective bandgap. These methods are discussed in full in chapter 9.

3.6.5. Colliding Pulse Mode-locked lasers

Passive mode-locking can be improved with colliding pulse effects in saturable absorbers. Reports using dye lasers have shown [52] that the interaction of the counterpropagating pulses creates a transient grating in the population of absorber molecules, which synchronises, stabilises, and shortens the pulse in both counter-propagating trains. In the semiconductor device, the saturable absorber is located in the middle of the waveguide so that the two pulses time themselves to collide in the centre saturable absorber, Fig. 3.12(a). Compared to a single pulse travelling in the cavity, the pulse shaping is more effective with the colliding pulse mode-locked (CPM) configuration because there are two pulses adding coherently to saturate the absorber and only one pulse to saturate the gain section. The transient grating generated by the colliding pulses further reduces the saturation energy of the absorber and limits the necessary spectral bandwidth. Transform limited optical pulses with a duration of 0.64 ps have been achieved with a passively modelocked laser at repetition rates up to 350 GHz[53].

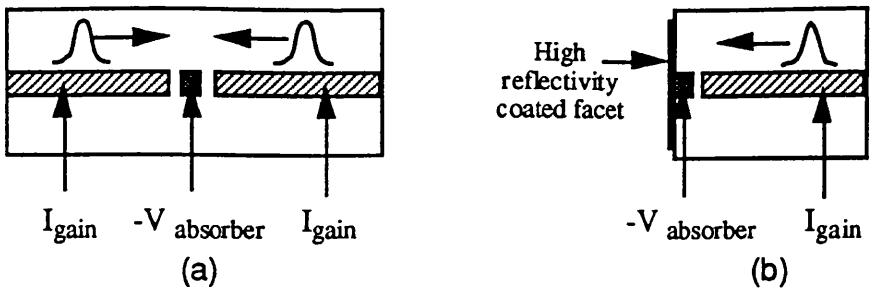

Fig. 3.12. Schematic of two saturable absorber configurations. a) Colliding pulse configuration. b) Self-colliding pulse configuration.

Another configuration based on the same effect is self-colliding pulse mode-locking (SCPM), Fig. 3.12(b). A highly reflective coating is deposited onto the facet adjacent to the saturable absorber, so that the pulse collides with itself in the saturable absorber. The pulse in the SCPM configuration has the same effect on the saturable absorber as the counter-propagating pulses in the CPM laser, however, it does not have the advantage of two gain sections. To date the longest CPM fabricated is 2.5 mm corresponding to 32 GHz repetition rate [36]; because of its length the device was designed with an active waveguide. Since the CPM has to be twice as long as a standard mode-locked laser, future problems may arise when lower repetition frequencies are required (X-band). The CPM device would have to be over 7 mm long for a repetition rate corresponding to 10 GHz. Active waveguides this length would seriously degrade the counter-propagating pulses, therefore CPM devices with passive waveguides could be a solution to the generation of low frequency transform, limited mode-locked pulses.

3.7 References

1. J. Wiesenfeld, "Electrooptic Sampling of high speed devices and integrated circuits," *IBM J. Res Develop.*, vol. 34, pp. 141-161, 1990.

2. R. A. Becker, *et al*, "Wide band electrooptic guided wave analogue to digital converters," *Proc. IEEE*, vol. 72, pp. 802-819, 1994.

3. K. Y. Lau, and A. Yariv, "Ultra high speed semiconductor lasers," *IEEE J. Quantum Electron.*, vol. QE-21, pp. 121-137, 1985.

4. M. Adams and I. D. Henning, "Optical fibres and sources for optical communications," Plenum press, 1990.

5. J. D. Ralston, S. Weisser, *et al*, "Control of differential gain, nonlinear gain, and damping factor for high speed application of GaAs-based MQW lasers," *IEEE J. Quantum Electron.*, vol. QE-29, pp. 1648-1659, 1993.

6. K. Uomi, N. Chinone, T. Ohyoshi, and T. Kajimura, "High relaxation oscillation frequency (beyond 10 GHz) of GaAlAs multiquantum well lasers," *Japan Appl. Phys.*, vol. 24, pp. L539-L541, 1985.

7. K. W. Wakao, *et al* , "," *Appl. Phys. Lett.*, vol. 41, pp. 1113-1115, 1982.

8. Y. Arakawa, K. Valhala, and A. Yariv, "Quantum noise and dynamics in quantum well and quantum wire lasers," *Appl. Phys. Lett.*, vol. 45, pp. 950-952, 1984.

9. L. F. Lester, *et al*, "Comparison of the teoretical and experimental differential gain in strained layer InGaAs/GaAs quantum well lasers," *Appl. Phys. Lett.*, vol. 59, pp. 1162-1164, 1991.

10. K. Y. Lau, *et al*, "Direct amplitude modulation of short-cavity GaAs lasers up to X-band frequencies," *Appl. Phys. Lett.*, vol. 43, pp. 1-3, 1983.

11. S. Weisser, J. D. Ralston, *et al*, "Efficient high-speed direct modulation in p-doped InGaAs/GaAs MQW lasers," *Electron. Lett.*, vol. 28, pp. 2141-2143, 1992.

12. E.L. Portnoi, Yu. M. Shernjakov, G.B. Venus, B.S. Yavich, J.H. Marsh and D.A. Barrow : "Gain modulation at millimeter wave frequencies in strained QW lasers"— International Symposium on Nanostructures: Physics and Technology, St Petersburg, Russia, 3-18 June 1993.

13. J. P. Van Der Ziel and R. Logan, "Generation of short optical pulses in semiconductor lasers by combined dc and microwave current injection," *IEEE J. Quantum Electron.*, vol. QE-18, pp. 1340-1350, 1982.

14. R. S. Tucker and D. J. Pope, "Circuit modeling of the effect of diffusion on damping in a narrow-stripe semiconductor laser," *IEEE J. Quantum Electron.*, vol. QE-19, pp. 1179-1183, 1982.

15. J. Katz *et al*, "The intrinsic electrical equivalent circuit of a laser diode," *IEEE J. Quantum Electron.*, vol. QE-17, pp. 4-7, 1981.

16. R. S. Tucker and I. Kaminow, "High frequency characteristics of directly modulated InGaAsP ridge waveguide and buried heterostructure lasers," *J. Lightwave Tech.* vol. 2, pp. 385-393, 1984.

17. D. A. Tauber, *et al,* "Inherent bandwidth limits in semiconductor lasers due to distributed micriowave effects," *Appl. Phys. Lett.* vol. 64, pp. 1610-1612, 199

18. C. Henry, "Theory of the linewidth of semiconductor lasers," *IEEE J. Quantum Electron.,* vol. QE-18, pp. 259-264, 1982.

19. Y. Arakawa, A. Yariv, "Theory of gain, modulation response, and spectral linewidth in AlGaAs Quantum well lasers," *IEEE J. Quantum Electron.,* vol. QE-21, pp. 1666-1674, 1985.

20. Takayuki Yamanaka, Yuzo Yoshikuni, Wayne Lui, *et al,* "Theoretical analysis of extremely small linewidth enhancement factor and enhanced differential gain in modulation doped strained quantum-well lasers," *Appl. Phys. Lett.* vol. 62, pp. 1191-1193, 1993.

21. G. J. Lasher, "Analasyis of a proposed bistable injection laser," *Solid-State Electron.,* vol. 7, pp. 707-716, 1964.

22. N. G. Basov, "0-1-dynamics of injection lasers," *IEEE J. Quantum Electron.,* vol. QE-4, pp. 855-964, 1968.

23. E. S. Yang, P. G. McMullin, A. W. Smith, J. Blum, and K. K. Shih, "Degradation-induced microwave oscillations in double heterostructure injection lasers," *Appl. Phys. Lett.,* vol. 24, pp. 324-327, 1974.

24. R. W. Dixon, and W. B. Joyce, "A possible model for sustained oscillations (pulsations) in (Al, Ga)As double-heterostructure lasers," *IEEE J. Quantum Electron.,* vol. QE-15, pp. 470-474, 1979.

25. Ch. Harder, K. Y. Lau, and A. Yariv, " Bistability and pulsations in semiconductor lasers with inhomogeneous current injection," *IEEE J. Quantum Electron.,* vol. QE-18, pp. 1351-1361, 1982.

26. Y. Arakawa, A. Larsson, J. Paslaski, and A. Yariv, "Active Q-switching in a GaAs/AlGaAs multiquantum well laser with an intracavity monolithic loss modulator," *Appl. Phys. Lett.,* vol. 48, pp. 561-563, 1986.

27. P. E. Barnsley, H. J. Wickes, G. E. Wickens, and D. M. Spirit, "All-optical clock recovery from 5 Gb/s RZ data using a self-pulsating 1.56 μm Laser diode," *IEEE Photon. Technol. Lett.,* vol. 3, pp. 942-945, 1991.

28. S. Olvadia *et al,* "Low- frequency relative intensity noise in self-pulsating ridge waveguide quantum well lasers," *IEEE Photon. Technol. Lett.,* vol. 4, pp. 336-338, 1992.

29. K. Peterman, *Laser diode modulation and noise.* London: Kluwer, 1988.

30. F. Stern, "Calculated spectral dependance of gain in excited GaAs," *J. Appl. Phys.,* vol. 47, pp. 5382-5389, 1976.

31. H. A. Haus, "Theory of modelocking with a fast saturable absorber," *J. Appl. Phys.*, vol. 45, pp. 3049-3058, 1975.
32. H. A. Haus, "Theory of modelocking with a slow saturable absorber," *IEEE J. Quantum Electron.*, vol. QE-11, pp. 736-746, 1975.
33. Mark Kuznetsov, "Pulsations of semiconductor lasers with a proton bombarded section" *IEEE J. Quantum Electron.*, vol. QE-21, pp. S87-S92, 1985.
34. E. L. Portnoi, N. M. Stel'makh, and A. V. Chelnokov,"Non linear effects in high powered Q-switched diode lasers," *Sov. Tech. Phys. Lett.*, vol. 15, pp. 865-867, 1989.
35. K. Y. Lau, "The inverted gain-levered semiconductor laser–direct modulation with enhanced frequency modulation and suppressed intensity modulation," *IEEE Photon. Technol. Lett.*, vol. 3, pp. 703-705, 1991.
36. A. M. Fox, *et al,* "Quantum well carrier sweep out: Relation to electroabsorption and exciton saturation," *IEEE J. Quantum Electron.*, vol. QE-27, pp. 2281-2294, 1991.
37. J. A. Cavailles, *et al* , "Simultaneous measurements of electron and hole sweep out from quantum wells and modeling of photoinduced field screening dynamics," *IEEE J. Quantum Electron.*, vol. QE-28, pp. 2486-2497, 1991.
38. Y. K. Chen, and M. C. Wu, "Subpicosecond monolithic colliding-pulse mode-locked quantum well lasers," *Appl. Phys. Lett.*, vol. 58, pp. 1253-1255, 1991.
39. P. W. Smith, Y. Silberberg, and D. A. B. Miller, "Modelocking of semiconductor diode lasers using saturable excitonic nonlinearities," *J. Opt. Soc. Am.*, vol. 2, pp. 1228-1235, 1985.
40. L. R. Brovelli, *et al,* "Optical pulse mixing measurement of carrier lifetime and absorption recovery time in reverse-biased GaAs/AlGaAs single quantum well laser structures," *J. Appl. Phys.*, vol. 76, pp. 7713-7719, 1994.
41. J. R. Karin, R. J. Helkey, *et al,* "Ultrafast dynamics in field-enhanced saturable absorbers," *Appl. Phys. Lett.*, vol. 64, pp. 676-678, 1994.
42. L. A. Glasser, "C.W. modelocking of a GaInAsP diode laser," *Electron. Lett.*, vol. 14, pp. 725-726, 1978.
43. D. J. Derickson, P.A. Morton, J. E. Bowers, and R. L. Thornton," Short pulse generation using multisegment mode locked semiconductor lasers," *IEEE J. Quantum Electron.*, vol. QE-28, pp. 2186-2201, 1991.
44. M. Schell, A. Weber, E. Schol, and D. Bimberg, "Fundamental limits of subpicosecond pulse generation by active modelocking of semiconductor lasers: The spectral gain width and the facet reflectivities," *IEEE J. Quantum Electron.*, vol. QE-27, pp. 1661-1669, 1991.
45. V. N. Morozov, V. V. Nikitin, and A. A. Sheronov, "Self-synchronisation of modes in a GaAs semiconductor laser," *JETP Lett.*, vol. 7, pp. 256-258, 1968.
46. O. V. Bogdankevich, *et al,* "Modelocking in a semiconductor laser with electronic excitation of an internal nonlinear active medium," *JETP Lett.*, vol. 12, pp. 128-129, 1970.

47. Y. Silberberg, P. W. Smith, *et al,* "Passive modelocking of a semiconductor diode laser," *Optics Lett.,* vol. 9, pp. 507-509, 1984.

48. D. J. Derickson, P.A. Morton, J. E. Bowers, and R. L. Thornton, "Comparison of timing Jitter in external and monolithic cavity mode-locked lasers," *Appl. Phys. Lett.,* vol. 59, pp. 3372-3374, 1991.

49. P. A. Morton, J. E. Bowers, *et al,* "Monolithic hybrid mode-locked 1.3 μm semiconductor lasers," *Appl. Phys. Lett.,* vol. 56, pp. 111-113, 1990.

50. R. S. Tucker, *et al,* "40 GHz Active mode-locking in a 1.5 μm monolithic extended cavity laser," *Electron. Lett.,* vol. 25, pp. 621-622, 1989.

51. P.B. Hansen, *et al,* "InGaAsP monolithic extended cavity laser with integrated saturable absorbers for active, passive , and hybrid mode-locking at 8.6 GHz," *Appl. Phys. Lett.,* vol. 62, pp. 1445-1447, 1993.

52. R. L. Fork, B. I. Greene, and C. V. Shank, "Generation of optical pulses shorter than 0.1 ps by colliding pulse mode locking," *Appl. Phys. Lett.,* vol. 38, pp. 671-672, 1981.

53. 25. M. C. Wu, Y. K. Chen, *et al,* "Transform limited 1.4 ps optical pulses from a monolithic colliding-pulse mode-locked quantum well laser," *Appl. Phys. Lett.,* vol. 57, pp. 759-761, 1990.

54. Y. -K. Chen, and M. C. Wu, "Monolithic colliding-pulse mode-locked quantum well lasers," *IEEE J. Quantum Electron.,* vol. QE-28, pp. 2176-2185, 1992.

Chapter 4

Two-Section Laser Diodes

4.1. Introduction

One of the simplest techniques of obtaining picosecond optical pulses is passive Q-switching or self-pulsation of multi-contact diode lasers. The fabrication technique for producing such lasers is relatively simple and involves few additional fabrication steps than those used to produce a standard ridge waveguide laser.

This chapter reviews the fabrication process of a ridge waveguide two-section laser. Each process is examined from material design right through to heatsink mounting and wire bonding. After fabrication an explanation of the test processes that are made on the two-section lasers are given. First, the standard device characterisation procedures that each two-section lasers go through, such as light-current characteristics and near and far field profiles, are explained. Then the test procedures for characterisation of self pulsation of the devices are described. The description of the pulse measurement systems used on these devices, such as autocorrelation and optical chronography, have been covered already in chapter two.

4.2. Design

4.2.1. Material

Two-section lasers were made in both GaAs/AlGaAs and strained InGaAs/GaAs material. Two 860 nm semiconductor material structures were grown by metal organic chemical vapour deposition (MOCVD) at the EPSRC III/V facilities in Sheffield, which contained two and four quantum wells respectively. The device structure was sequentially grown on a (100) n^+-GaAs substrate orientated 3 degrees off and doped to 2 x 10^{18} cm^{-3}; a 0.1 μm n^+-GaAs buffer layer (4 x 10^{18} cm^{-3}); a 1.5 μm n-$Al_{0.42}Ga_{0.58}As$ cladding layer (Si- 5.5 x 10^{17} cm^{-3}); a 0.1 μm $Al_{0.20}Ga_{0.80}As$ undoped waveguide layer; an undoped active region consisting of two (or four) 100 Å GaAs quantum wells separated by 100 Å $Al_{0.20}Ga_{0.80}As$ barriers; a 0.1 μm $Al_{0.20}Ga_{0.80}As$ undoped waveguide layer; a 1.3 μm p-$Al_{0.42}Ga_{0.58}As$ upper cladding layer (C- 3.3 x 10^{17} cm^{-3}); and a 0.1 μm p^+ -GaAs contact layer (Zn- 8 x 10^{18} cm^{-3}).

A strained 980 nm structure, OC 1586, was grown by MOCVD at Plessey Caswell also. The layers consisted of a 1 μm n^+-GaAs buffer layer; a 1.5 μm n-$Al_{0.60}Ga_{0.40}As$ cladding layer (Si-doped 2 x $10^{18}cm^{-3}$); a 0.15 μm graded $Al_xGa_{1-x}As$ waveguide region,

with $0.6 \geq x \geq 0.2$ (undoped); two 60 Å $In_{0.2}Ga_{0.8}As$ wells separated by 250 Å GaAs barriers, a 0.15 μm graded $Al_xGa_{1-x}As$ upper waveguide region, with $0.2 \leq x \leq 0.6$ (undoped); a 0.1 μm p-$Al_{0.60}Ga_{0.40}As$ upper cladding region (C doped 2 x $10^{18}cm^{-3}$); a 500 Å p-$Al_{0.30}Ga_{0.70}As$ etch stop layer (C doped 2 x $10^{18}cm^{-3}$); a 0.87 μm p-$Al_{0.60}Ga_{0.40}As$ upper cladding region (C doped 2 x $10^{18}cm^{-3}$) and a 0.32 μm p^+-GaAs contact layer (Zn doped 1 x $10^{19}\,cm^{-3}$). Both associated energy-band diagrams are illustrated in appendix 2.

4.2.2. High speed material design.

Improvements in modulation frequency are possible through the use of strained Quantum Wells, an increase in the number of QW's, and p-doping of the barriers. The mechanisms that produce these high values of intrinsic modulation bandwidth are discussed in full in chapter 3. The improvements in direct modulation demonstrated by J. Ralston *et al* [1] were hoped to be copied in self-pulsating lasers. By using a high speed material structure similar to Ralston's it was proposed that a decrease in pulse width and an increase in repetition frequency would be seen. As well as strained multiple quantum wells with p-doped barriers, the material structure was designed with a an effective Al mole fraction of x = 0.8 in the cladding layers. The use of such a high Al mole fraction allows an increase in the waveguide vertical confinement factor Γ_v, leading both to an increase in relaxation frequency at a given current, due to an increase in photon density, and a substantial decrease in core and cladding layer thickness. This shortens MBE growth time and on the whole serves to simplify fabrication by reducing vertical etch depths. The material structure was grown in the department by the MBE group.
The layers consisted of a 1 μm n^+-GaAs buffer layer; a 0.1 μm graded $Al_xGa_{1-x}As$ region, with $0.8 \geq x \geq 0$ (undoped); a 0.8 μm graded $Al_{0.8}Ga_{0.2}As$ lower cladding region (Si-doped 3 x $10^{18}cm^{-3}$) SPSL;a 480 Å lower core region; two 57 Å $In_{0.2}Ga_{0.8}As$ wells separated by 200 Å GaAs barriers, a 480 Å upper core region ; an 0.8 μm graded $Al_{0.8}Ga_{0.2}As$ upper cladding region; an 0.1 μm graded $Al_xGa_{1-x}As$ upper cladding region, with $0 \leq x \leq 0.8$ (Be-doped, 5 x $10^{18}cm^{-3}$); and a 0.2 μm p^+-GaAs contact layer (Be- doped, 1 x $10^{19}\,cm^{-3}$).

The $Al_{0.80}Ga_{0.20}As$ cladding layers were implemented using binary short-period super-lattices (two-monolayer (ML) thick GaAs layers alternating with eight-ML-thick AlAs layers). Such binary SPSL layers, in conjunction with the use of As_2, have been shown to enhance both the QW luminescence properties and lasing performance of MQW laser structures. This, proposedly, is due to the SPSL trapping contaminants between layers and stopping them from entering the active region. The material structure was grown but was unfortunately found not to lase, another wafer has since been grown but there was no time to fabricate two-section lasers with it.

4.2.3. Mask Design.

The mask sets were designed on computer and written on to chrome masks using an electron beam writer. The first mask defined the width of the waveguides, which were 3.5 μm written periodically every 600 μm. The second mask defined the opening for the contact window above the waveguides; this was designed to be slightly smaller than the width of the waveguide, 2.5 μm. The final mask defined the metal contacts of both segments of the two-section laser. The saturable absorber was designed with a number of fixed lengths between 35 μm and 7 μm, and the cavity length of the laser was arranged so that it could be scribed between 200 and 600 μm. The mask designs for each stage of photolithography are illustrated in appendix 3.

Before starting fabrication the depth to which the ridge waveguide was to be etched was calculated using F-Wave, a vector finite difference computer program. The depth was calculated so that 860 nm light would propagate along the waveguide in a zero order optical mode.

4.3. Fabrication

4.3.1. Cleaning

The wafer was scribed into 8 x 8 mm pieces and then cleaned in a reflux condenser using solvents. The first cleaning stage refluxed the sample in trichloroethane for one hour, to remove any grease deposits. The sample was then refluxed in ethanol for an hour to remove any traces of trichloroethane and then cleaned in acetone for 20 minutes in an ultrasonic bath. Finally the sample was washed in deionised water for five minutes to remove any deposits of acetone and then blown dry.

4.3.2. Photolithography

The sample was then coated with a thin mask layer of silica (2000 Å) in a plasma enhanced chemical vapour deposition machine (PECVD), at 300 °C, fig. 4.1(a). At this stage, for ease of handling and photolithography, the sample was mounted onto a glass slide. Using photoresist as an adhesive, the sample was stuck onto the glass slide and baked for half an hour at 110 °C.

In the next stage, a layer of photoresist was deposited onto the sample. Primer was first spun onto the sample to remove any surface moisture and so aid adhesion of the photoresist, then positive photoresist, Shipley S1400-17, was spun onto the samples at 3000 rpm for 40 seconds. The thickness of the photoresist at this speed was 0.8 μm,

however, because the sample was square and relatively small, it was found that photoresist collected at the corners to a thickness of about 1.5 μm. Mounting the sample on a glass slide and spinning it off-axis reduced this build up and gave better photolithographic reproduction. The sample was pre-baked at 90 °C for 30 minutes, and then exposed for 5 seconds in the mask aligner, making sure that the waveguides were parallel with the edge of the sample, fig. 4.1(b). The sample was developed and washed in deionised water, then postbaked at 120 °C, to harden the resist, fig. 4.1(c).

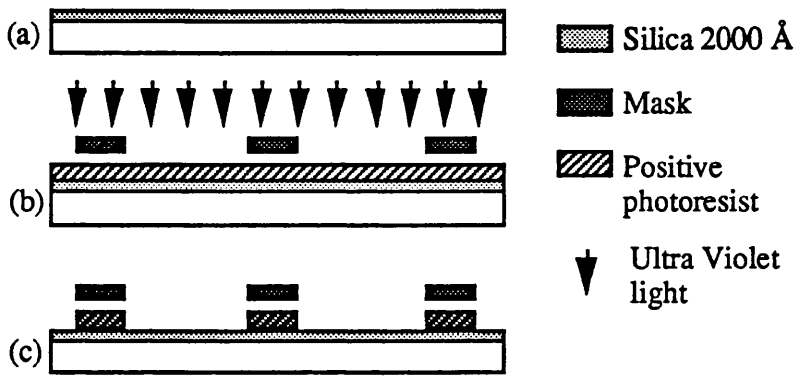

Fig. 4.1. First photolithography stage.

4.3.3. Dry Etching

The silica was etched in a Plasmatech 80 reactive ion etch machine for 3 minutes, using C_2F_6, fig. 4.2(a). The sample was then ultrasonically cleaned in acetone for 10 minutes and washed in RO water. The silica pattern left on the sample acted as a mask and was used to produce sharp edge definition of the etched waveguide. To produce clean vertical sidewalls, the sample was dry etched in a Plasmatech 80 reactive ion etch machine using $SiCl_4$, fig. 4.2(b). The best results were obtained at a forward rf power of 100 W and gas flow of 9 sccm, which has an etch rate of about 1600 Å/min, depending on the aluminium fraction content of the AlGaAs material. The etch rate of the silica was around 150 Å/min. Finally the silica mask was removed in buffered hydrofluoric acid, fig. 4.2(c).

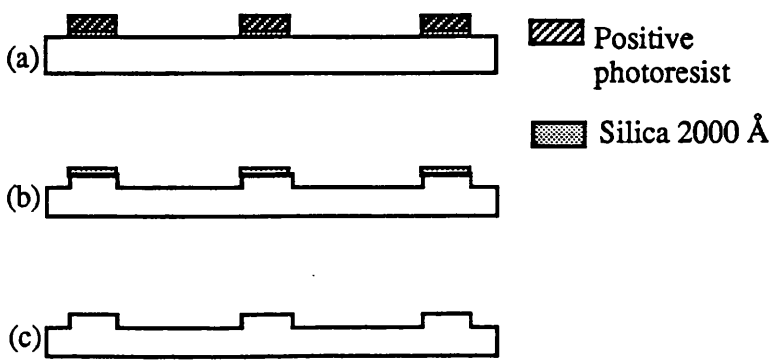

Fig. 4.2. RIE of the waveguide

4.3.4. Second Photolithography stage

A layer of silica (2000 Å) was deposited onto the sample, fig. 4.3(a), and then another layer of photoresist, S1400-17, was spun over the sample. The sample was baked at 90 °C for 30 minutes and then aligned in the mask aligner The sample was exposed for 7 seconds, then developed to open up a window in the resist above the waveguides, fig. 4.3(b+c).

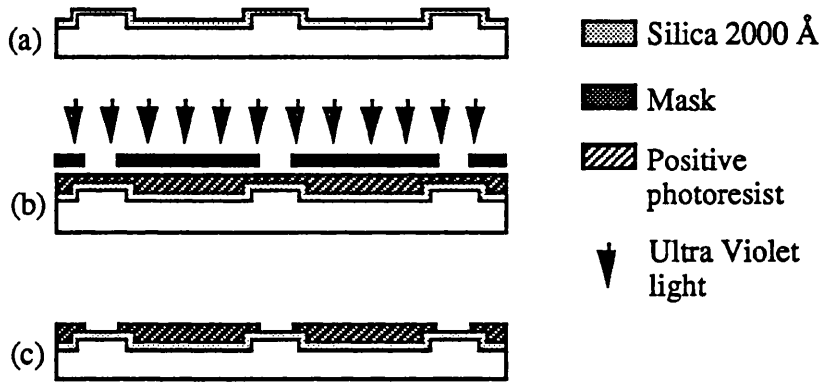

Fig. 4.3. Second photolithography stage, defining the contact windows.

4.3.5. Metalisation

The sample was post-baked at 120 °C for 30 minutes and then wet etched in buffered HF for 20 seconds immediately followed by a quench in RO water to halt the chemical reaction. If the window is etched for too long, severe undercutting occurs which can increase the threshold current of the laser. At this stage a window had been opened in the silica above the waveguide mesa, Fig. 4.5(a), where a metal contact could be formed. The resist was removed in acetone and the sample washed. A new layer of photoresist, S-1400-31, was spun onto the sample and baked at 90 °C for 15 minutes. Then the sample was soaked in chlorobenzene for 15 minutes and baked at 90 °C for another 15 minutes. The chlorobenzene soak, in the middle of the pre-bake, forms a hard layer on the surface of the resist so that when the sample is developed an overhang is formed which aids the lift-off process, as illustrated in Fig. 4.4.

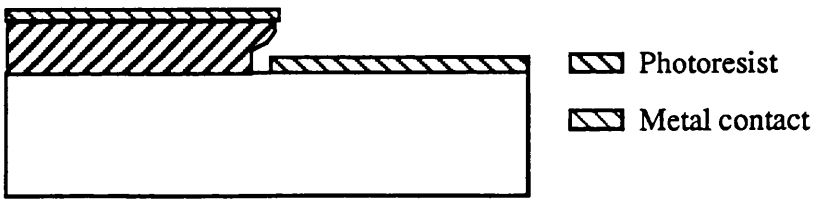

Fig. 4.4. Schematic illustrating the lift off technique.

The sample was aligned and exposed for 12 seconds and then developed and washed, Fig. 4.5(b). Before the p-type contact was deposited, the sample was etched in ammonia solution for one minute to remove any surface oxidation of the P^+ GaAs contact layer. A Ni/Au contact layer was evaporated onto the sample at a vacumn pressure of $2x10^{-6}$ torr. During the evaporation the sample was rotated through 30° to ensure that the side walls of the waveguide were coated but not coating the overhang so that lift off was still possible. The sample was then soaked in acetone until all the metal on top of the photoresist had lifted off, Fig. 4.5(c). Ni/Au was used because it formed an ohmic contact with the p-type material, allowing the carriers to be swept out of the saturable absorber with minimal electrical resistance.

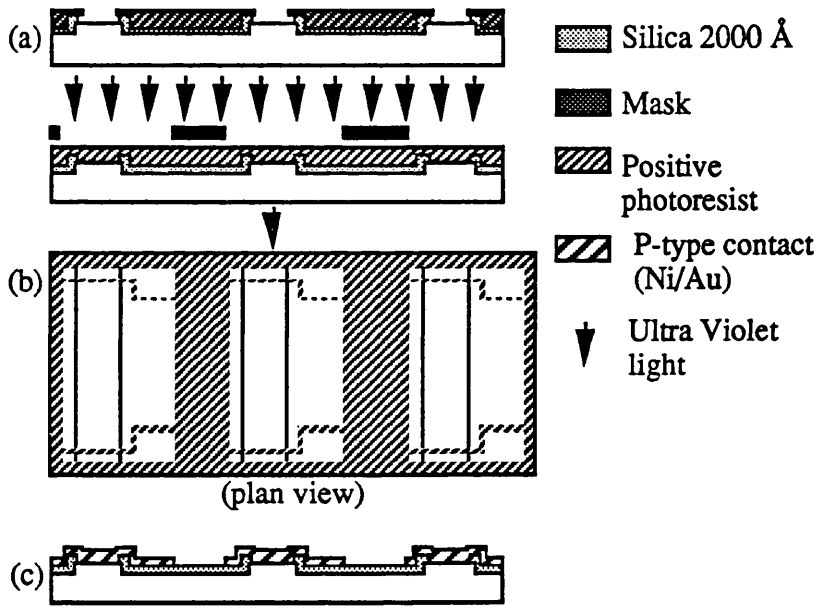

Fig.4.5. Final photolithographic stage, metalisation and lift off.

The backside of the sample was thinned down to to reduce the substrate thickness to ~150 μm. The sample was mechanically hand polished using 3 μm Al_2O_3 grit and then refluxed in trichloroethane. The n-type contact was then deposited, using a standard mikohm recipe, appendix 4. The final step was the selective etch of the P^+-GaAs contact layer between the two segments for electrical isolation. The GaAs was selectively dry etched using $SiCl_4$ gas at low power. The sample was etched at an overpressure of 12 mtorr, a flow rate of 6 sccm, a reverse dc bias of less than 70 V and an rf power of 15 W. The etch rate selectivity of GaAs/AlGaAs under these conditions was found to be about 5000:1. Due to the low power used, the ion etching was found to leave very little damage.

4.4. Testing

The two-section lasers were initially tested in a pulsed regime with a mark space ratio of 2000:1 before selecting the ones with the best characteristics for mounting onto heatsinks and wire bonding both sections. The unmounted lasers were tested pulsed so that adverse heating affects, due to poor heatsinking, were negligible.

4.4.1. LI test

Light current (*L-I*) characteristics were taken of all the lasers before the best devices were mounted onto heatsinks. From the *L-I* graph, the threshold current and quantum efficiency of the laser were found. The linearity of the *LI* graph above threshold was also examined. 'Kinks' in the curve normally imply that the laser, at a certain current, is switching from one transverse mode to a different one.

The sample was scribed into individual devices, of various cavity lengths, for testing and assessment. The accuracy of the scribe along the saturable absorber facet was found to be within ± 3 μm and the laser cavity lengths varied between 500 μm and 200 μm.

The lasers light-current characteristics were analysed under a pulsed regime using 500 ns pulses at 1 kHz, which gave a mark space ratio of 2000:1. The electrical contacts to the device were made by clamping the laser in a clip, so that both sections of the p-side were forward biased. A large area silicon photodiode, connected to a box car integrator, was used to monitor the output signal from the device. The box car integrator was used to recover the pulsed analogue signal from the photodetector. It works by opening a gate 100 ns long during the current pulse then integrating the signal, using a fast gated integrator, over the 100 ns. The output from the integrator is then normalised by the gate width to provide a voltage which is proportional to the average of the input signal.

The test rig was automated using a Macintosh computer running a program called Lab View, which controlled the current to the laser, received the data and produced an input current against output power graph.

4.4.2. Near and Far Fields

Near field and far field scans were taken to examine the mode profile of the laser. Lasers with a strong single transverse mode usually correlated with a linear *L-I* curve. The near field mode profile was taken with a Hammamatsu infra-red camera and the image produced was read into a computer through a frame grabber. The far field profiles were recorded by mounting the laser to be tested on a rotational stage while a fixed Si p-i-n photodetector measured the power of the incident light. As the stage rotated values of

light intensity were taken against degrees of rotation; these were again recorded using Labview.

4.4.3. Electrical Isolation of the Two Segments

Before the device was mounted onto a heatsink, the electrical isolation between the two sections was tested. The two sections were probed and an HP semiconductor parameter analyser was used to calculate the electrical resistance between them. A typical result is illustrated in Fig. 4.6, showing a measured resistance between the segments of 5 kΩ which corresponds to a segment separation of 30 μm. The plot in Fig. 4.6 shows the voltage/current curve (left hand axis); the other curve (right hand axis) illustrates the dynamic resistance against voltage calculated from the voltage/current curve. Both curves are linear indicating that both p-type contacts are ohmic.

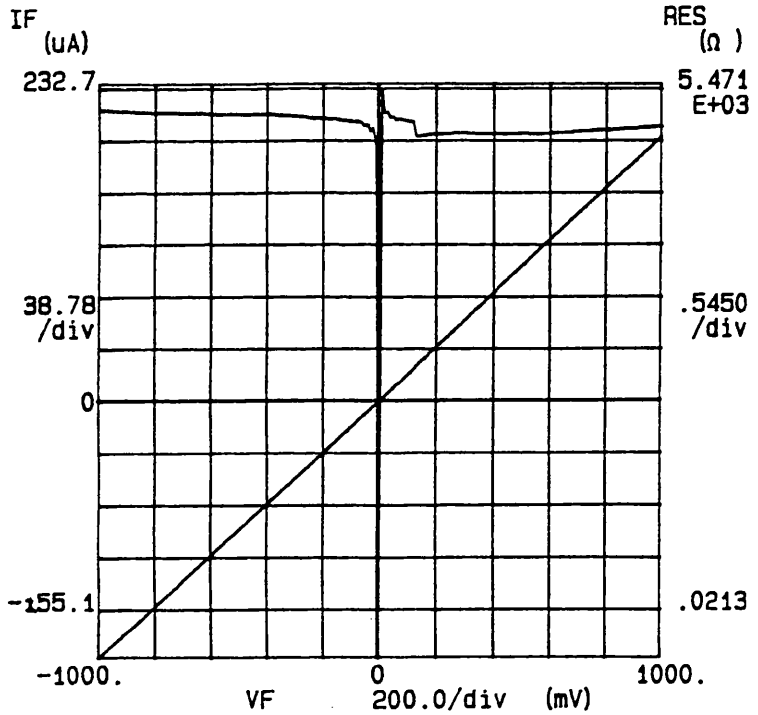

Fig. 4.6. Forward and reverse measurements of current/voltage and resistance/voltage between the two segments.

4.4.4. Mounting onto Heatsinks

A copper heatsink was designed for simplicity of production and ease of interchange in the cw test rig. The surface of the copper block, onto which the device was mounted, was polished to a 3 μm finish, using diamond paste. The highly polished surface ensured maximum heat transfer from the device to the copper. The mount was then coated, under vacuum, with 100 nm of nickel then 150 nm of gold. The copper block

was coated to stop the copper oxidising in the indium flux and because indium on copper forms an alloy which can cause strain and lead to degradation of the device.

The devices with the lowest threshold current and a high quantum efficiency were mounted onto the heatsinks. The heatsink was heated to 172 °C, just above the melting point of indium, and indium flux was applied to the area onto which the device was to be bonded. A ball of indium, 100 μm diameter, was used to bond the device onto the heatsink. Bond pads (3x1 mm^2) were also indium bonded onto the heatsink. The heatsink was then refluxed in trichloroethane for 30 minutes to remove the indium flux. The two sections of the device were gold wire bonded using an ultrasonic wire bonder.

4.4.5. Quasi-cw passive q-switching.

With both sections electrically bonded, the device could be tested for self pulsation. The first experimental setup is illustrated in Fig. 4.7 where the laser was driven by a pulse generator. The advantage of this method was that the sampling oscilloscope was triggered directly from the pulse generator.

In this arrangement, the output from the laser diode was collected by a collimating lens and focused onto a fast photodetector. The output from the detector was connected to the sampling head of a sampling oscilloscope. The area of the photodetector was relatively small, 30 μm diameter, therefore a beamsplitter and infra-red camera arrangement were used to examine the reflected image of the photodiode, Fig. 4.7, and aid alignment.

The sampling oscilloscope was triggered from the pulse generator via a delay line so that, by varying the delay, the pulse appeared on the sampling oscilloscope. The main disadvantage of this method was its poor time resolution, which depends on the rise time of the photodetector and the sampling head. The GaAs photodetector's bandwidth was 18 GHz and the sampling head has a bandwidth of 50 GHz, therefore the best resolution expected from this arrangement was around 60 ps. The gain section was pumped using an Avtech CV pulse generator which supplied a 2 ns pulse with a rise time of 300 ps driven at 5 kHz. A reverse bias of between 0 and 7 V was supplied to the saturable absorber.

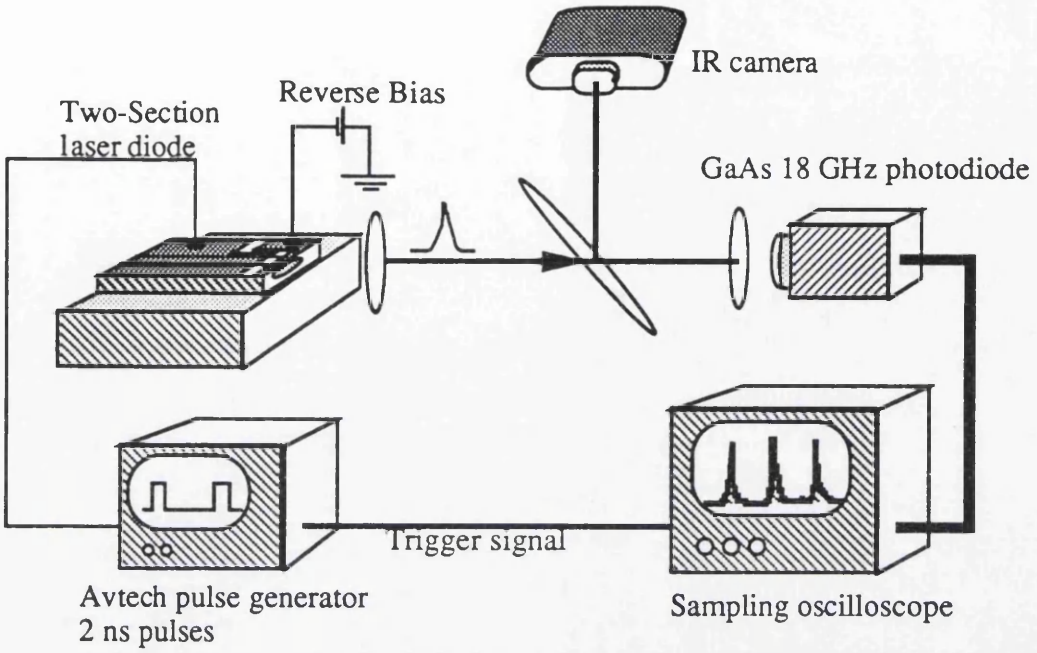

Fig. 4.7. Schematic of an experimental arrangement to measure the quasi-cw pulses from a two-section laser.

4.4.6. CW test.

The two-section devices were tested with a constant current source in a peltier cooled sample holder. The holder was designed so that the laser could be accessed from either facet, and RF signals could be applied to the laser if necessary. The constant current source was designed to be stable with less than 5 μA fluctuation.

Passive Q-switching was obtained by applying a constant current to the gain section and a reverse bias to the saturable absorber. The reverse bias circuit had a 1 kΩ resistor in series to limit the current from the saturable absorber and protect it from break down. During the experiment, the peltier cooler was set to 15 °C. The optical pulse from the laser was collected by a collimating lens (x40 magnification) and focused onto a 18 GHz GaAs *p-i-n* photodiode (GEC Marconi). The 980 nm two-section laser was tested using an InGaAs *p-i-n* photodiode. An infra red camera was again used to aid alignment, Fig. 4.8. The detector output was connected to an RF spectrum analyser for observation of the repetition rate and higher order harmonics (Tektronix 492).

The optical pulses were also observed in real time as well as in the frequency domain. The output from the detector was divided into two equal signals using a RF spliter. One signal was connected to the head of a sampling oscilloscope (Tektronics CSA 402), the other electrical signal was used to trigger the scope. The optical pulses could then be monitored in time.

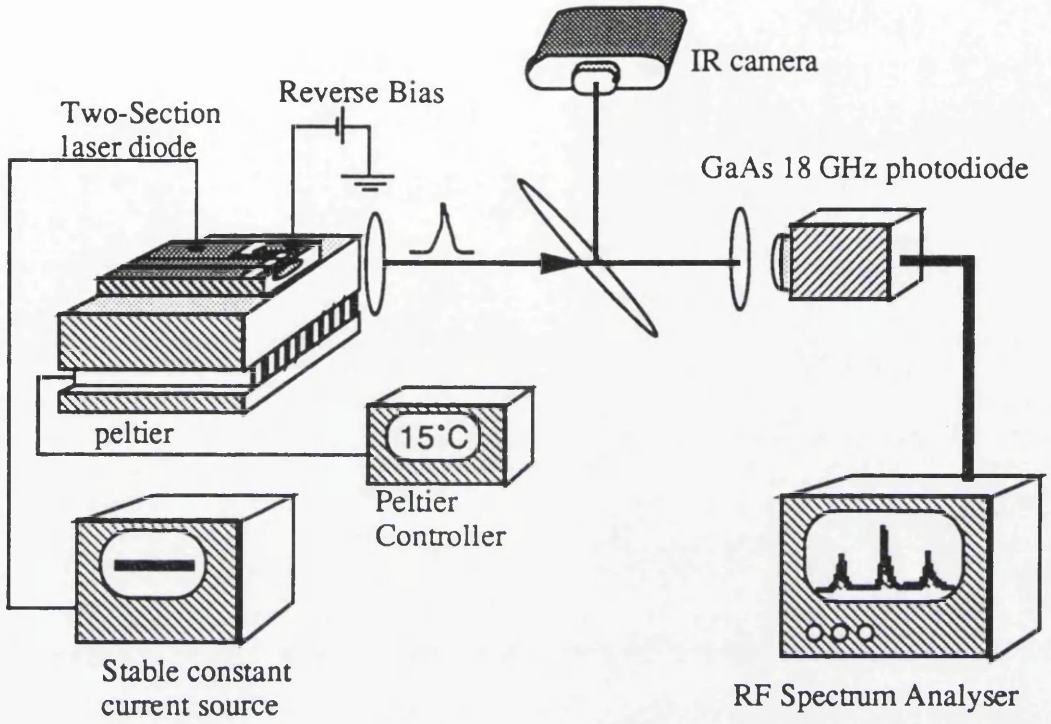

Fig. 4.8. Schematic of an experimental setup to measure cw passive q-switching.

4.5. Reference

1. J. D. Ralston *et al,* "Control of differential gain, nonlinear gain. and damping factor for high speed application of GaAs based MQW lasers," *IEEE J. Quantum Electron.,* vol. 29, pp. 1648-1658, 1993.

Chapter 5

Two-Section Laser Results.

5.1. Introduction

In this chapter the results from the two-section lasers are described along with an analysis of these results. The results of the device characterisation are given showing low threshold currents and high quantum efficiencies. Then the results of the two-section lasers self-pulsating are examined. The devices are first tested in a pulsed 'quasi cw' regime to examine their self-pulsation behaviour at high currents. Then the lasers self-pulsating characteristics are examined in a cw regime. These results show a close accordance with the best results of self-pulsating lasers published so-far, with very high self-pulsation frequencies and short pulse widths.

5.2. Device Characterisation.

The current light characteristics of all the lasers fabricated were taken after scribing. The lasers were tested using the laser test rig described previously, with both sections of the p-contact forward biased. Typical results for material QT 546, the double quantum well structure grown by MOCVD at Sheffield, are shown in Fig. 5.1. The material has a current density of 450 A/cm^2. The threshold current of this laser, I3, was 14 mA with a quantum efficiency of 34 % per facet.

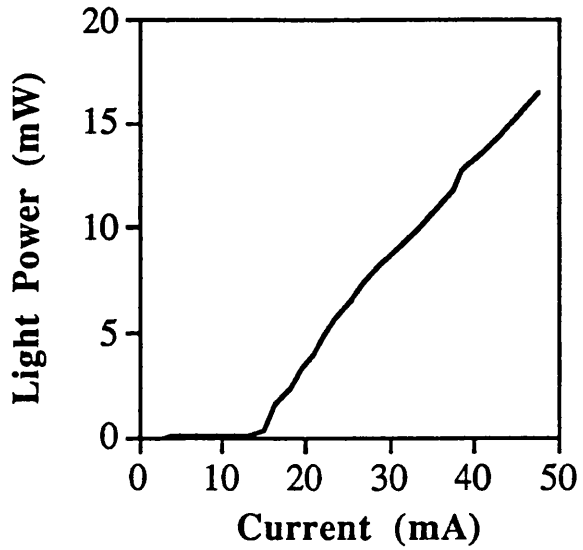

Fig. 5.1. Light current curve for material QT 546 laser I3.

Light current characteristics for material QT 418 a four quantum well structure with a current density of 400 A/cm,^{2} are shown in Fig. 5.2. From the graph the threshold current

was found to be 12 mA and the quantum efficiency 27 % per facet. From the graph the threshold current was found to be 12 mA and the quantum efficiency 27 % per facet.

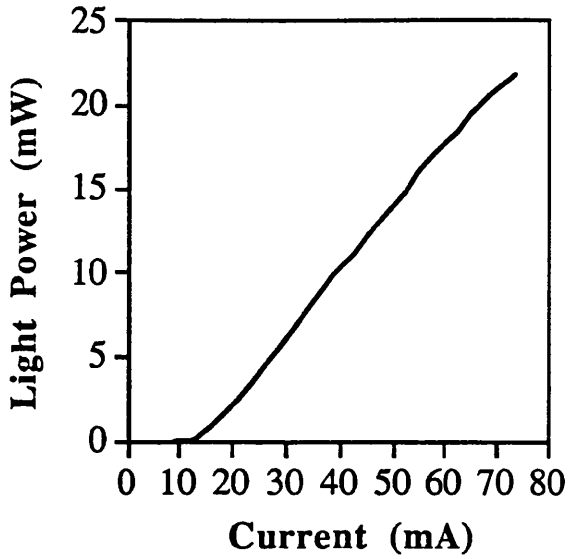

Fig. 5.2. Light current curve for material QT 418 laser A3.

The final devices tested were fabricated in strained GaAs/InGaAs double quantum material OC 1586. This material has a low current density of 190 A/cm^2, due to the fact that under a biaxial compressive strain, the heavy-hole band is raised above the light-hole band and the effective mass of the material in the plane of the heterojunction is reduced [1]. A lighter effective mass reduces the density of states, and the laser achieves the threshold condition at a smaller carrier density.

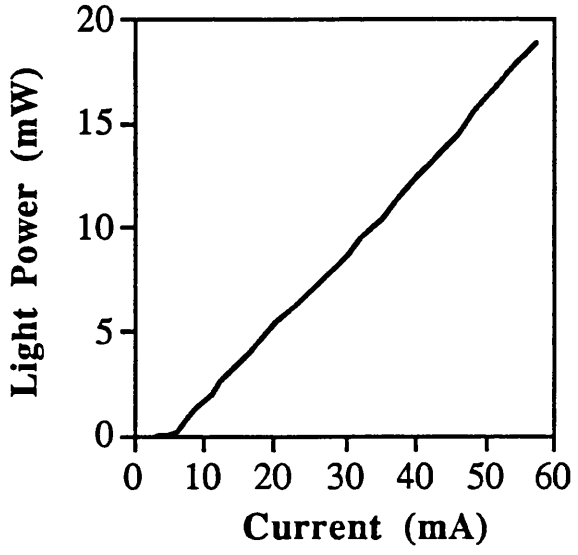

Fig. 5.3. Light current curve for material OC 1586 laser H3.

A typical light-current result is illustrated in Fig. 5.3; the threshold current is 6 mA and the quantum efficiency is 26 % per facet. The spectrum of one of the lasers is also shown in Fig. 4.12, the spectrum being taken using an Anritsu spectrometer with a resolution of 1 Å. The laser is driven in this case with a cw current of 18 mA, and the temperature is maintained by a peltier cooler at 20 °C. The lasing wavelength at this drive current and temperature is centered at 961 nm. The longitudinal mode spacing for this device can be clearly resolved as 3.3 Å which coresponds to the cavity length which is 350 μm.

$$\delta\lambda = \frac{\lambda^2}{2LN_g} = \frac{.961^2}{2\times 350\times 4} = 3.29\text{Å}, \tag{5.1}$$

where $\delta\lambda$ is the longitudinal mode separation, L is the cavity length and N_g is the group refractive index.

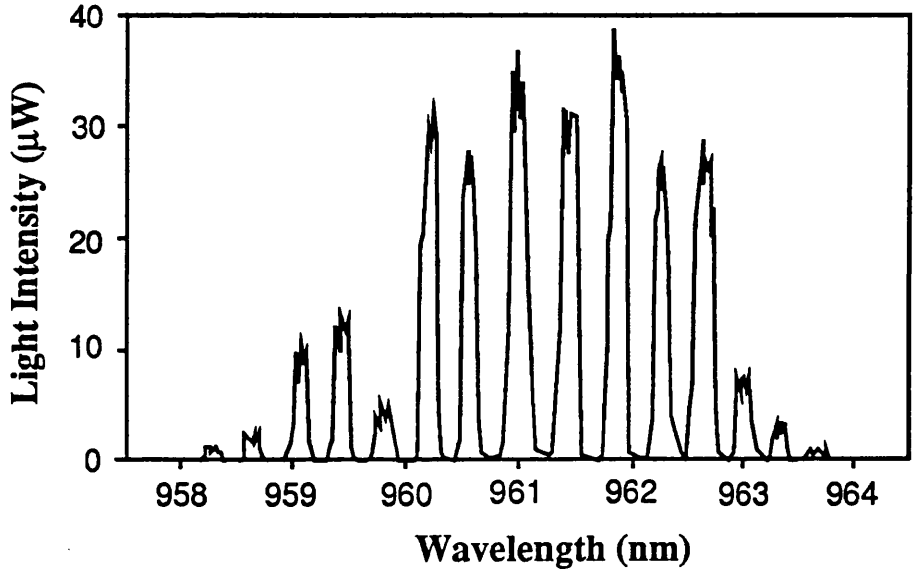

Fig. 5.4. Wavelength spectrum from material OC 1586

5.2. Testing the Devices under Self Pulsation

5.2.1. Quasi C.W. Measurements

The two-section lasers were initially tested in a quasi cw regime using the experimental arrangement in section 4.4.5. Using short high powered pulses to drive the gain section the laser could be driven at much higher currents than in a cw regime. Heating effects due to high currents were therefore negligible.

Spectral Behaviour under Self Pulsation

The light spectrum of a two-section GaAs /AlGaAs laser was examined at different values of saturable absorber voltage. This experiment shows what impact an increase in reverse bias has on the lasing characteristics of the self-pulsating laser diode, and gives a better understanding of the physical effects the saturable absorber has on the gain of the device.

The laser was tested under a quasi-cw pulsed regime. The gain section of the laser was driven with 2 ns pulses of ≈ 100 mA whose amplitude was kept constant while the saturable absorber voltage was varied between 0 and 2.1 V. Fig. 5.5 shows the optical spectra for various absorber voltages.

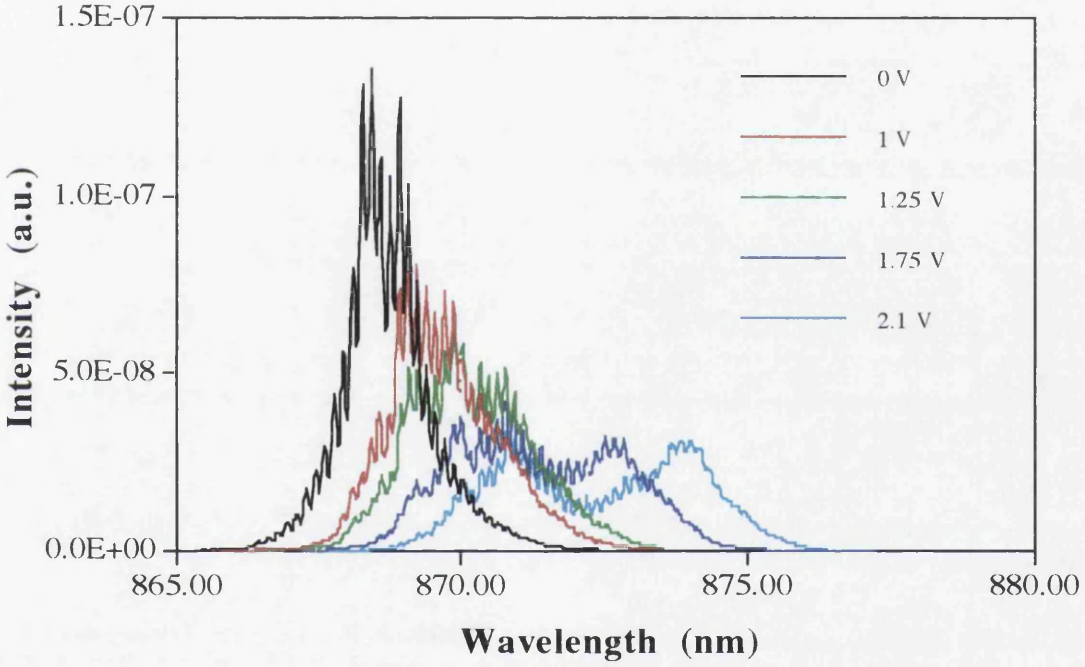

Fig. 5.5. Optical spectra for various absorber voltages.

As the reverse bias was increased, a broadening of the spectra could be seen and the peak of the spectrum moved to a higher wavelength. With this particular device, self-pulsation was observed at a reverse bias of 1.75 V, which resulted in a typical "rabbit's ear" shape to the spectrum. This broadening of the spectrum is due to the effect of self-pulsations in the laser; as the reverse bias is increased the self-pulsations become clearly defined and the pulses narrow. As the temporal profile of the pulse narrows a corresponding increase in the spectral width occurs. This relationship is described by the inverse Fourier transform theorem (eqn. 2.10), therefore, to form a shorter pulse more longitudinal modes are needed. The spectral width for a 20 ps pulse, assuming a good time-bandwidth product, 30, for a Q-switched laser, is calculated to be 3.7 nm. Which is in close agreement with the recorded results.

The shift in wavelength can be attributed to the movement of the compound gain which is strongly affected by excitonic absorption in the passive section. Due to the Stark effect, the absorption peak of the saturable absorber shifts to a longer wavelength. Increasing the reverse bias of the absorber leads to a red shift of the absorption peak and, also, to a flattening of the peak.

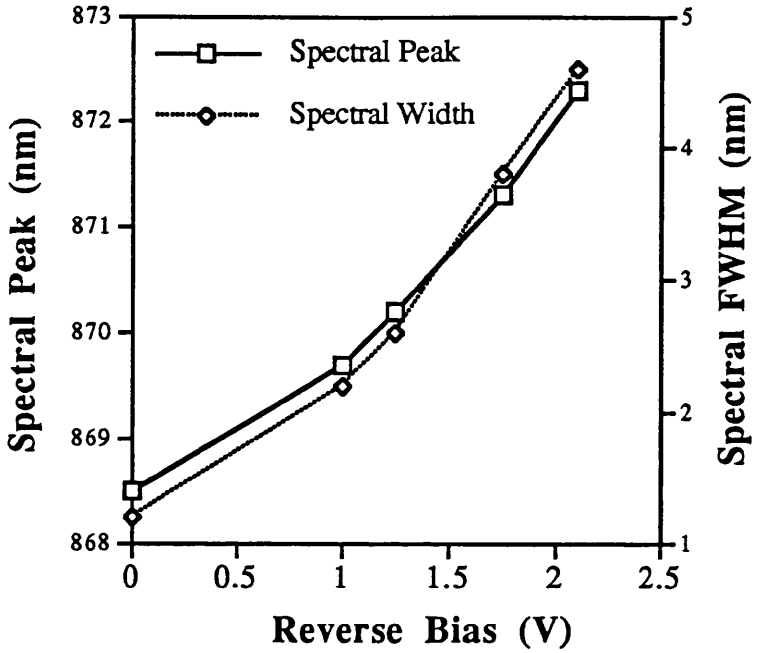

Fig. 5.6. A plot of the spectrum peak and spectrum width against reverse bias .

From Fig. 5.6 it can be seen that there is an almost quadratic relationship between the position of the spectral peak and the reverse bias across the saturable absorber, and that the laser has a spectral tuning range of 4 nm between 0 and 2.1 V. It can also be seen that the spectral width increases monotonically with an increase in reverse voltage.

Temporal Behaviour under Self-Pulsation

Initially the bonded lasers were measured under a pulsed (quasi-cw) regime using the laser test rig illustrated in Fig. 4.7. The pulses detected by a photodetector, with a frequency response of 18 GHz, were then sampled using a communication signal analyser (Tektronics CSA 402). A result is shown in Fig. 5.7 from a strained layer InGaAs MQW two-section device self-pulsating at 11 GHz with a reverse bias of 2.5 V across the saturable absorber. By varying the drive current between ~50 and ~250 mA the self pulsation frequency of this particular device was found to tune between 3 and 11 GHz. Another sampling oscilloscope measurement of a two-section laser is shown in Fig. 5.8, the repetition frequency is 8 GHz. The device has a drive current of ~200 mA applied to the gain section and a reverse bias of 2.5 V to the saturable absorber. The same laser with

the same reverse bias and a drive current of ~50 mA is shown in Fig. 5.9, the repetition frequency is 3 GHz.

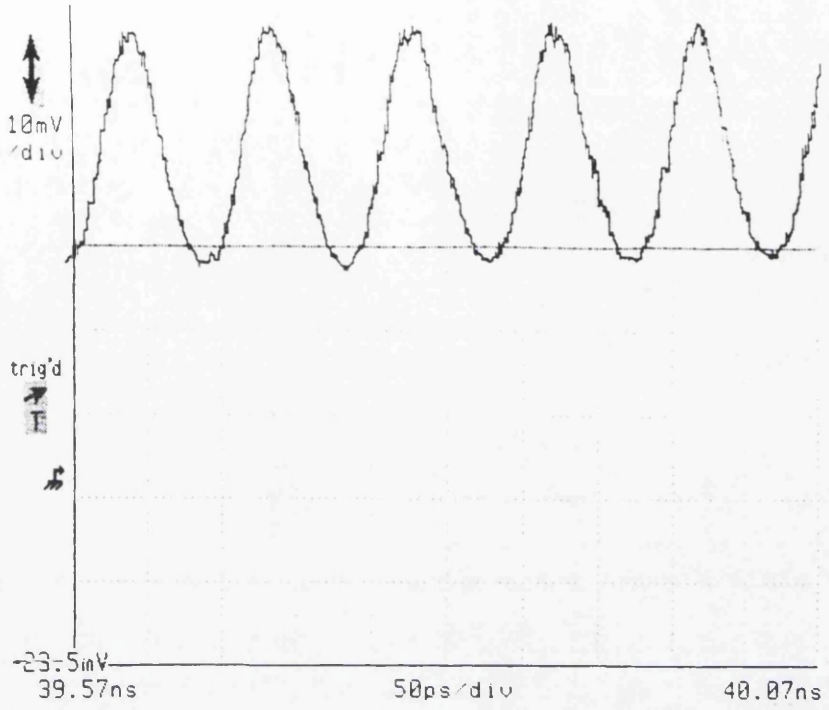

Fig. 5.7. Trace from a communications signal analyser showing a self-pulsating frequency of 11 GHz

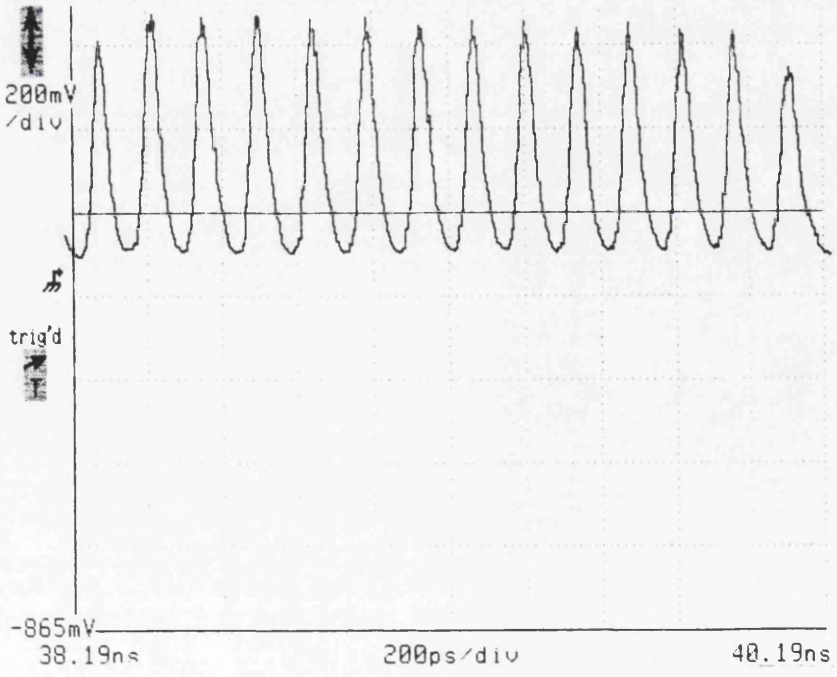

Fig. 5.8. Trace from a communications signal analyser showing a self-pulsating frequency of 8 GHz

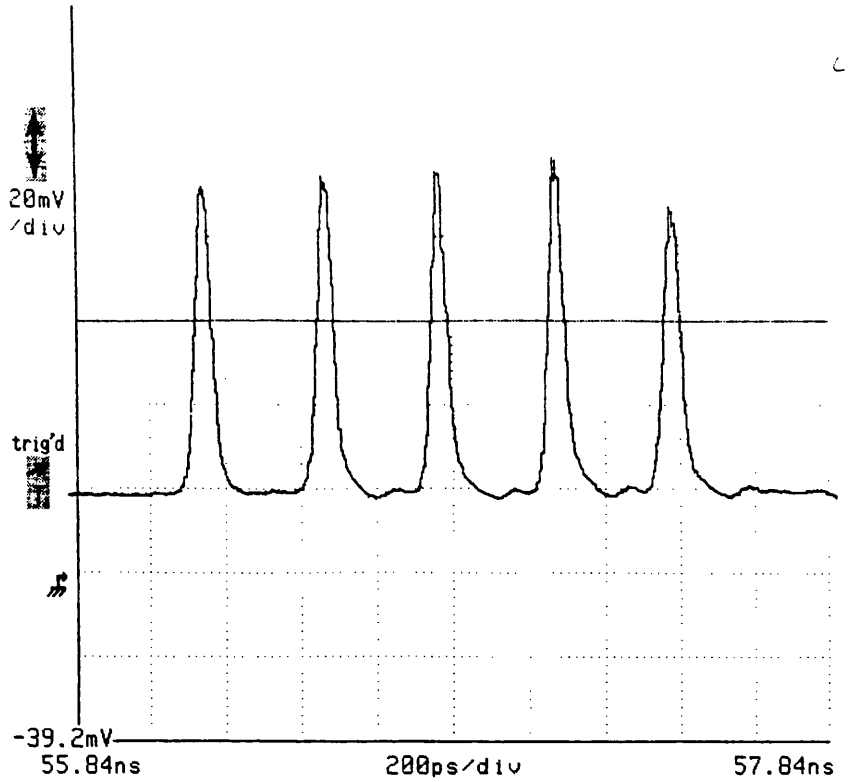

Fig. 5.9. Trace from a communications signal analyser showing a self-pulsating frequency of 3 GHz

A number of self-pulsating laser diodes (SP-LD), with a range of cavity and saturable absorber lengths, was tested using the quasi-cw method. Various saturable absorber lengths were examined, ranging from 30 μm down to 7 μm, to monitor the effect the amount of absorption has on self-pulsation characteristics.

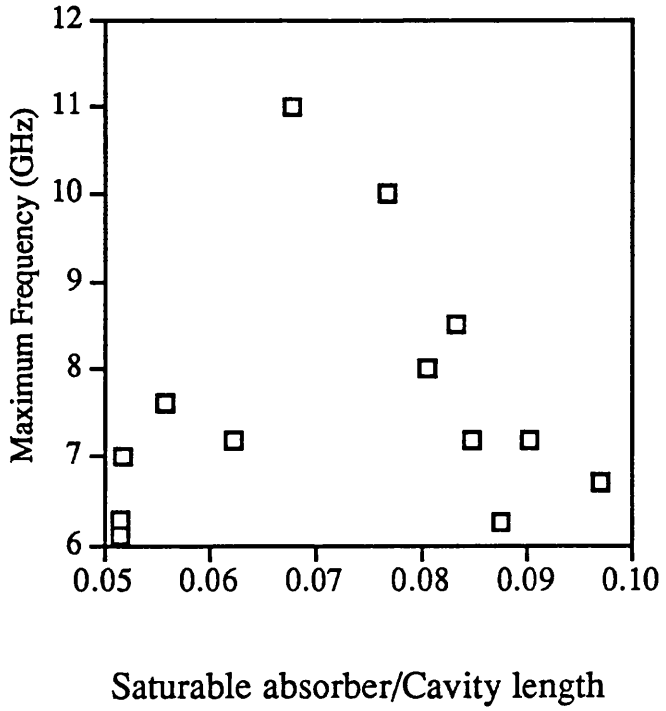

Fig. 5.10. Maximum repetition frequency against saturable absorber / cavity length.

GaAs/InGaAs 980 nm devices were used to determine the values of peak self-pulsating frequency against the ratio of saturable absorber/cavity length. The reverse bias, across the saturable absorber of the device, was kept constant at 2.5 V while the injected current was increased until the maximum repetition rate was found. The correlated data generally follow a Gaussian shape with a maximum occurring at 11 GHz corresponding to a saturable absorber to cavity length ratio of 0.07. Either side of this optimum value the maximum repetition rate decreases illustrating that there are possibly two physical mechanisms responsible for reducing the self-pulsation frequency, one at high absorber/cavity length ratio and one at low absorber/cavity length ratio. The scatter in the data points, in fig 5.10, from a Gaussian profile shape can be explained by variations in the slope efficiencies and current thresholds between each device. This variation is probably due to fabrication and wafer inconsistencies.

Streak Camera Results

Devices were taken to the Ioffe institute in St Petersburg, Russia and analysed there using a streak camera. The SP-LD was driven in a quasi-cw regime using a 3 ns pulse with an approximate Gaussian temporal variation. The output from the device was collimated and then focused onto the slit of the camera. The amplitude of the current pulse was difficult to measure because of its high frequency components which made any direct temporal measurement such as a current probe technique change the shape of the pulse due to the inductance induced. A non intrusive method of measurement had to be used. The current pulse amplitude was estimated by comparing it to a known current value, the threshold current; the output of the pulse generator was kept at a constant amplitude and a number of fixed electrical attenuators were inserted before the laser, by changing the attenuation and therefore the amplitude of the current pulse the threshold current was found the value of the current coming directly from the pulse generator could be calculated. The current pulse amplitude before the attenuators was found to be 550 mA.

The sync line from the pulse generator was used to trigger the sweep unit of the streak camera which was used in a fast single sweep mode at a sweep repetition frequency of 10 kHz. The delay between the pulse generator and the camera was increased until the pulse appeared in the time window of the camera. The trigger timing jitter of the experimental system seemed to be negligible, as the pulse width of the laser measured in multiple shot mode, an averaging of many measurements, was within ± 1 ps of the pulse width of a single shot measurement. The streak camera technique gave a temporal

resolution of less than 2 ps with both the pulse width and the repetition frequency of the Q-switched pulse train observed accurately.

The results showed high repetition rates. One GaAs/AlGaAs device with a cavity length of 630 μm and saturable absorber length of 20 μm was observed to self-pulsate at 14 GHz with a measured pulse width of 23 ps (FWHM). The energy in each pulse was measured to be 1.6 pJ. The drive current to the gain section was 165 mA and the reverse bias during the self-pulsations was kept at 3 V. However, on increasing the reverse bias to between 3 and 5 V mode-locking was observed at a frequency of 63 GHz. This value of repetition frequency corresponded to a laser cavity length of .

$$L = \frac{c}{2nf} = \frac{2.99 \times 10^8}{2 \times 3.8 \times 63 \times 10^9} = 625 \mu m \qquad (5.2)$$

the same cavity length as the two-section device confirming that modelocking took place. The highest self-pulsation rate observed was from a GaAs/AlGaAs device with a cavity length measuring 420 μm and a saturable absorber length of 12 μm. This device passively Q-switched at a frequency of 16 GHz with a reverse bias of 3 V across the saturable absorber and a drive current of 160 mA.

The effect of current injection on self-pulsation

The effect of an injected current on the Q-switched pulse train from a two-section laser was observed while the reverse bias across the saturable absorber was kept constant. Streak camera results were taken from a device with a 640 μm cavity length and a 35 μm saturable absorber. As the injected current was increased, the reverse bias across the saturable absorber was monitored at 4.4 V. The streak camera results are shown in Fig. 5.11, *a)*, illustrates relaxation oscillations at 87 mA injected current ; *b)*, is taken at a current of 100 mA and corresponds to 2.2 GHz repetition rate ;*c)*, shows a pulse train with a self-pulsation rate just below 4 GHz and an injected current of 138 mA ; the streak camera trace, *d)*, has an injected current of 173 mA and the initial pulses have a repetition rate of 5 GHz the later pulses, however, stop pulsating resulting from the high current probably due to heating effects.

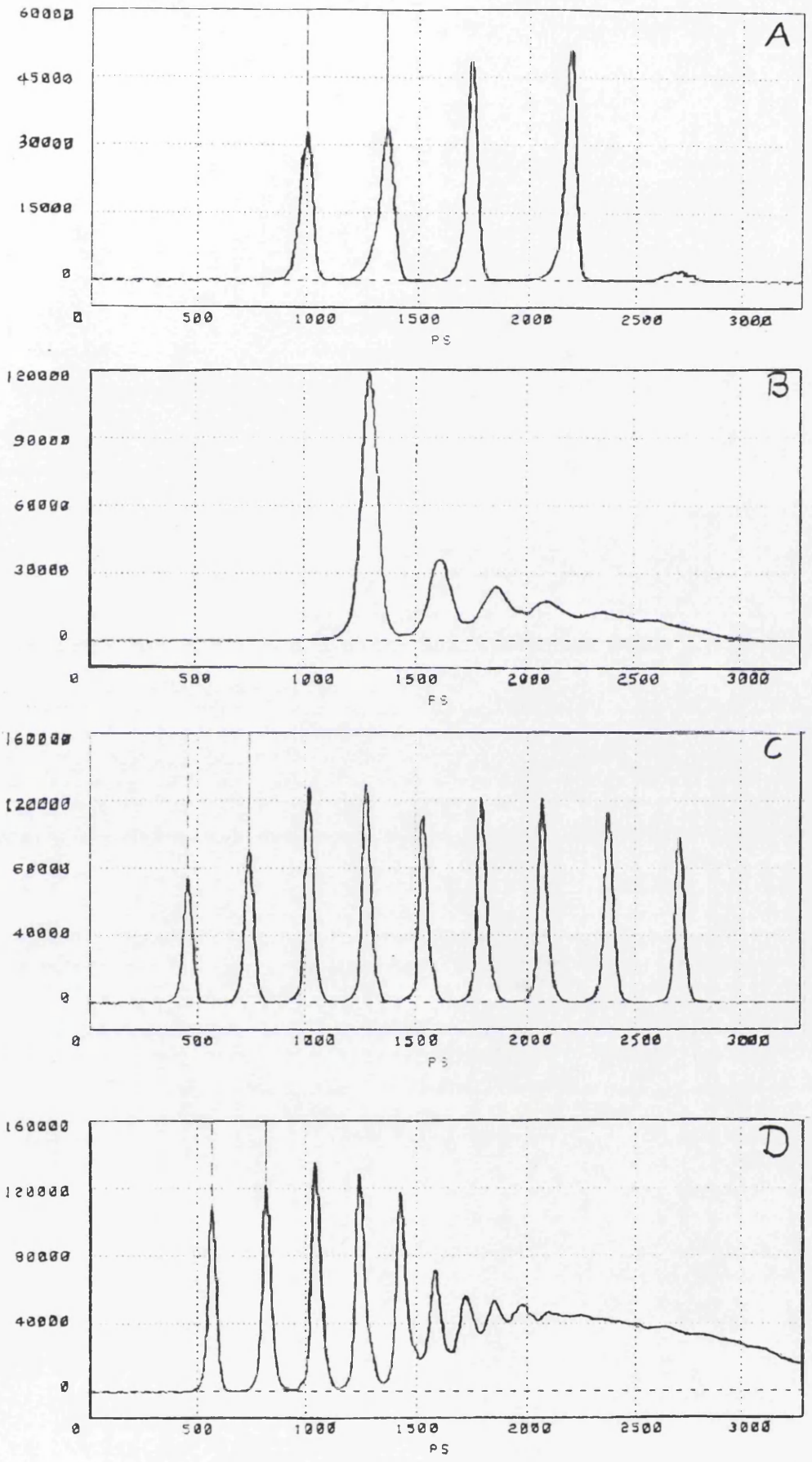

Fig. 5.11. Streak camera results from a self-pulsating two-section laser with a constant 4.4 V reverse bias, driven at varying currents. a) 87 mA, b) 100 mA, c) 138 mA, d) 173 mA.

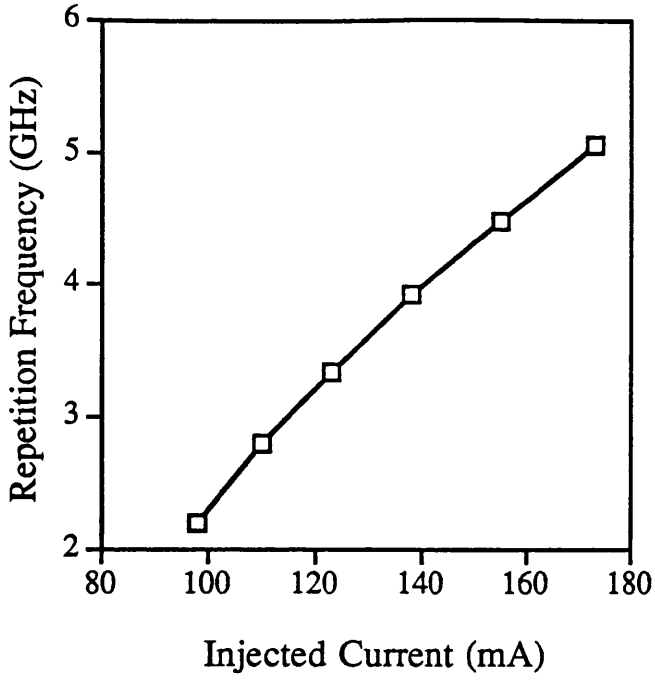

Fig. 5.12. Repetition frequency against current, taken from streak camera results.

The results were collected from the streak traces, and a graph of repetition frequency against injected current was formed, Fig. 5.12. The results show that there is a quadratic relationship between the injected current and the self-pulsating frequency. This relationship has been observed observed experimentally [2, 3] and predicted by Dixon and Joyce[4] in their small signal analysis which describes the self-pulsation repetition frequency dependence on gain current. The plot of frequency against $\sqrt{\text{Current}}$ is in Fig. 5. 13.

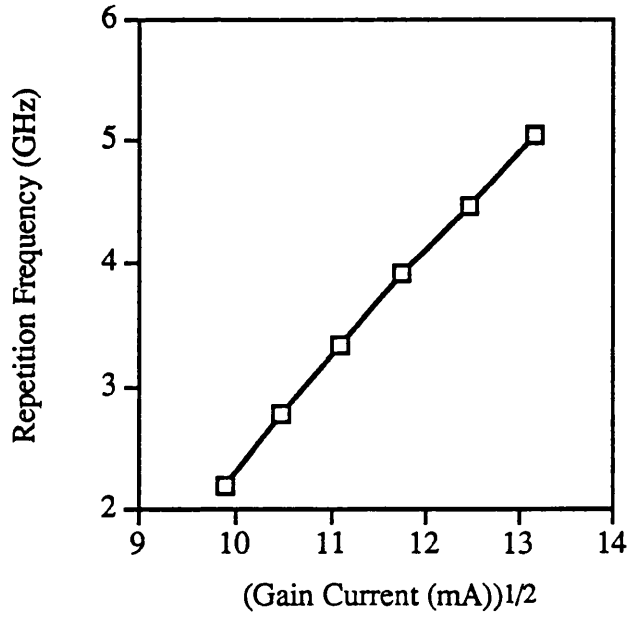

Fig. 5.13. Repetition frequency against $\sqrt{\text{Current}}$, taken from streak camera results.

The effect of reverse bias on self-pulsation

The effect of reverse bias voltage on the self-pulsation of a two-section GaAs/AlGaAs laser device was observed and recorded using the streak camera. The streak camera was used because it gave a direct temporal response of the pulse width and repetition frequency.

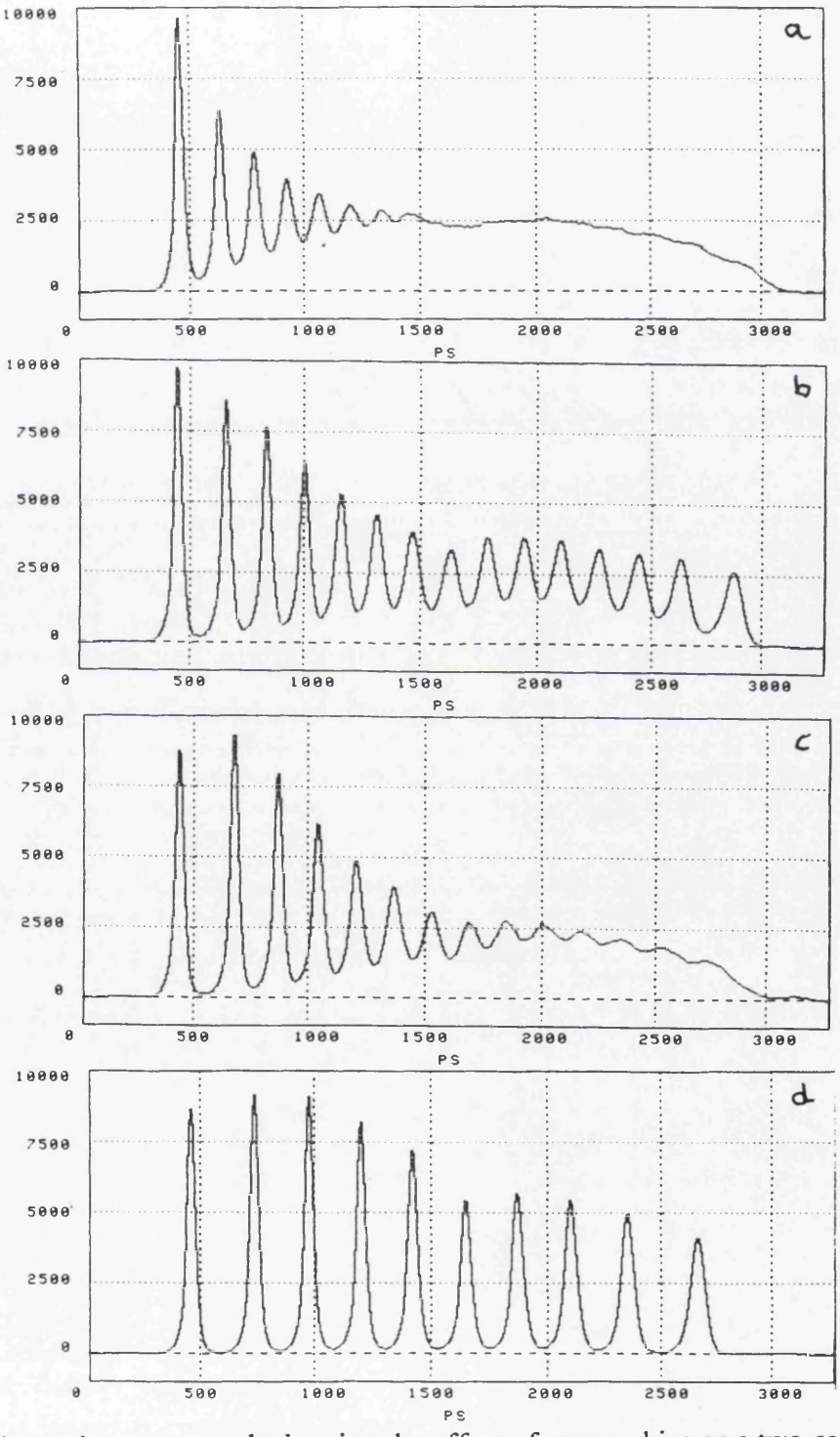

Fig. 5.14. A streak camera result showing the effect of reverse bias on a two-section laser driven by a constant current, 155 mA. a) 0 Vreverse bias, b) 1.25 V reverse bias, c) 2.5 V reverse bias, d) 5V reverse bias.

Fig. 5.14 shows the evolution of the pulse train observed while an increasing reverse bias voltage was applied to the saturable absorber. The laser was pumped using the 'bell' shaped current pulse described previously, with a constant peak current of 155 mA, while the absorption of the saturable absorber was increased. The first figure (a) shows the effect of the bell shaped pulse on the SP-LD with zero reverse bias on the saturable absorber. The unpumped region still produces enough absorption and enough instability along the laser cavity to produce relaxation oscillations in the light output which are observed for the first nanosecond, after which the laser runs cw. These oscillations are stronger than the relaxation oscillations normally observed in a standard laser, this is due to the unpumped region being able to produce enough absorption to cause instability and photon and carrier fluctuations in the cavity. The second figure (b) shows the effect of a reverse bias of 1.25 V across the saturable absorber. The streak camera trace shows clearly resolved pulses at the start of the pulse train, and, as the current amplitude of the 'bell' shaped pulse increases the self-pulsations become superimposed onto a 'bell' shaped cw trace. An explanation of this is that the loss in the cavity, due mainly to the saturable absorber, is not large enough to produce complete extinction of stimulated emission in between the pulses.

As the reverse bias increased, the pulse train becomes less resolved indicating a decrease in absorption until, at 2.5 V (c) the trace looks similar to (a). The pulse train then starts to become resolved again indicating an increase in absorption until, at 5 V the pulses are fully resolved (d). This implies that the absorption of the saturable absorber has a non monotonic dependance on the bias voltage applied. The absorption increases until it reaches a peak at 1.25 V then decreases to its lowest value at 2.5 V after which it increases again to reach a second maximum at 5 V reverse bias.

This effect is seen more clearly from data that was collected from another GaAs/AlGaAs two section device, Fig. 5.15. The cavity length of this device was 640 μm and saturable absorber length was 35 μm. The threshold current with the saturable absorber short circuited was 55 mA. During the experiment the injected current was kept constant at 98 mA while the reverse bias was increased. The maximum repetition frequency of this device was 5.1 GHz which occured at an injected current of 173 mA and reverse bias of 4.4 V.

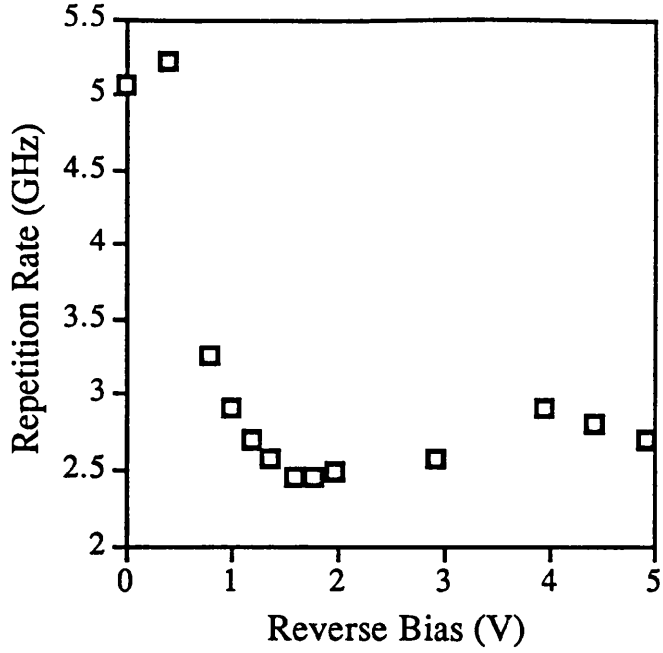

Fig. 5.15. Repetition rate against reverse bias taken from streak camera results.

If we first compare repetition frequency against reverse bias we can see that a maximum is reached at 0.4 V corresponding to 5.2 GHz, (192 ps) between the first and second pulse. At this reverse bias voltage, the device is not properly Q-switching and these values are the result of relaxation oscillations. As the reverse bias is increased to 1.6 V the repetition frequency decreases to a minimum of 2.5 GHz (408 ps). The repetition frequency then increases to another maximum at about 4 V corresponding to a self-pulsating frequency of 2.9 GHz after which the repetition frequency decreases again.

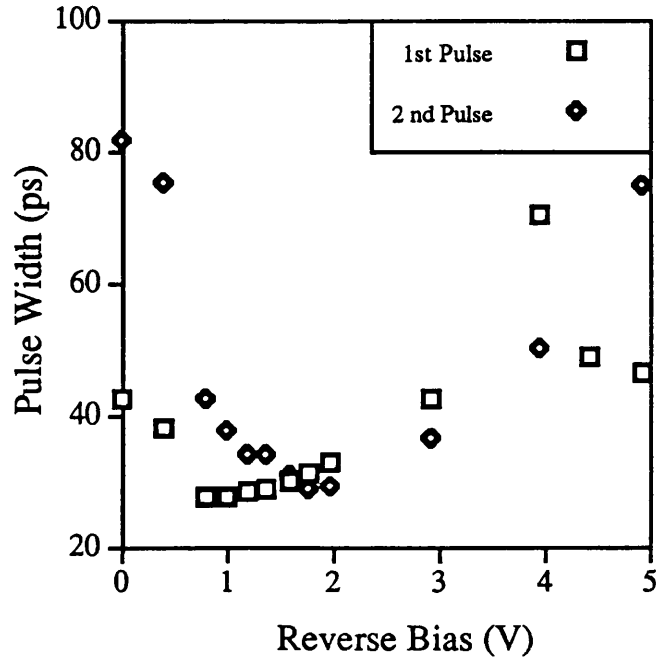

Fig. 5.16. Graph of pulse width against reverse bias.

Examining the results, from Fig. 5.16, for pulse width against reverse bias for the same device, we see that again the pulse width of the first and second pulses also reach their minimum widths at about 1.6 V. The pulse width of the first pulse then widens to a maximum at 4 V and then decreases in width again.

A second set of similar results was taken for a different device, and it can be seen that the same trend follows the previous device. The device length was 530 μm and saturable absorber length was 35 μm. Examining the results in Fig. 5.16, the repetition frequency reaches a minimum at 1.3 V then increases until 2.6 V beyond which the repetition frequency decreases again. The results below 0.5 V can be ignored, since they are due to relaxation oscillations before the laser is self pulsating.

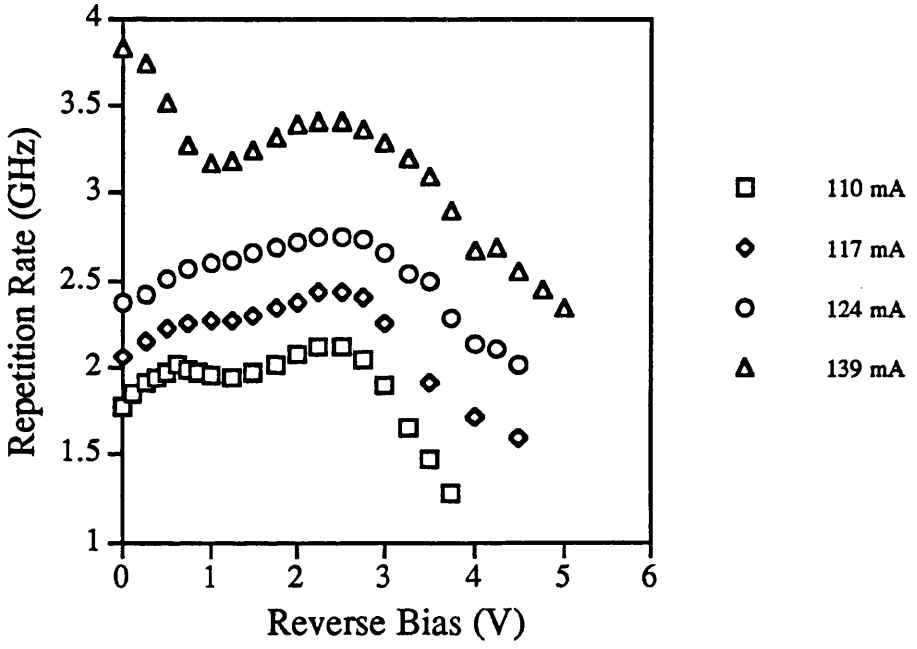

Fig. 5.17. Repetition rate against reverse bias under various injected currents.

The same pattern occurs for the pulse width against reverse bias, Fig. 5.18 . The pulse width reaches a minimum at around 1.4 V then increases to a maximum at 3 V when the pulse width begins to decrease again to another minimum at 5.2 V. It can also be seen from the graph that an increase in current leads to an increase in pulse width.

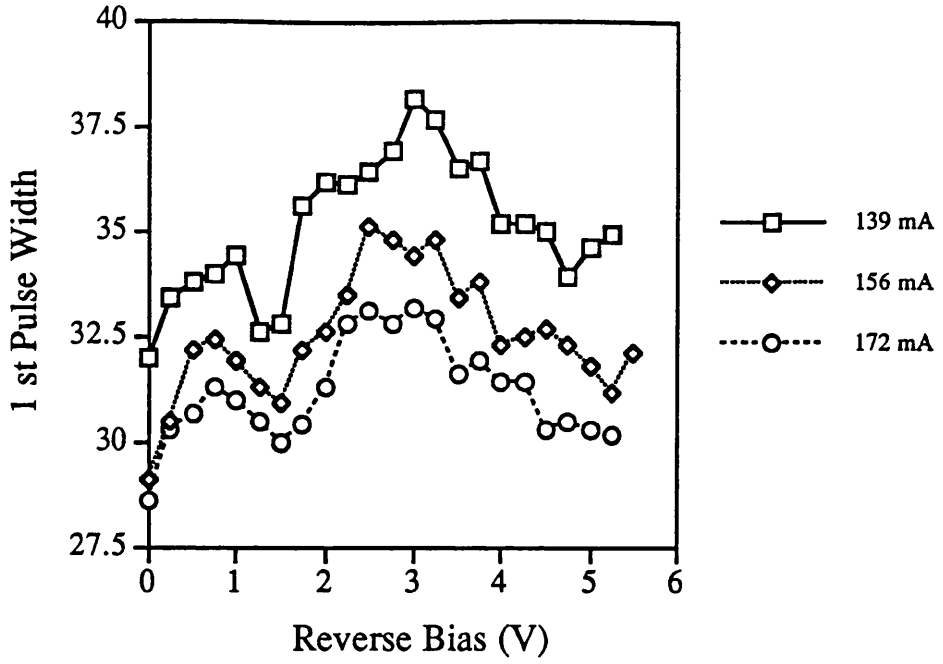

Fig. 5.18. Pulse width against reverse bias under various injected currents.

From the data that has been collected it can be seen that the repetition frequency does not decrease linearly with an increase in reverse bias as might be expected. It has already been stated that the sweep-out time of carriers decreases with an increase in electric field, which is due to the reduction in effective barrier height of the quantum well (pg 52). Therefore an increase in reverse bias should lead to a decrease in the carrier sweep out time and therefore an increase in absorption of the saturable absorber. However the non monotonic increase and decrease in repetition rate and pulse width, with reverse bias, indicates that the absorption does not have a direct linear relationship with the saturable absorber voltage.

The increase and decrease in the absorption can be explained by the quantum confined Stark effect, in which the excitons red-shift when an electric field is applied perpendicular to the quantum well layers, fig. 5.19a. The two peaks in absorption (i.e. the two minima in pulsewidth at 1.5 aand 4.5 V, fig. 5.18) can be accounted for by the red shift of the absorption edge of the saturable absorber from the first exciton peak (heavy hole) when the reverse bias is 1.5 V (6.2×10^4 V cm^{-1}) to the second exciton peak (light hole) at 4.5 V (1.8×10^5 V cm^{-1}). The electric field strength is calculated across the undoped waveguide layers and the wells and barriers, (0.24 μm).

From analysis of work carried out by Fox *et al* [5], we can roughly predict the red shift induced by a given electric field for a GaAs/AlGaAs material with 100 Å wells and barriers. We can then compare this shift in energy of the exciton peak at the two values of reverse bias to see if it is the same as the difference in energy between the heavy hole peak and the light hole peak.

The exciton shift in energy from a field strength of $6.2x10^4$ V cm^{-1} (1.5 V), the first peak in absorption, to $1.8x10^5$ V cm^{-1} (4.5 V), the second peak in absorption, is calculated to be ~37 nm (0.03 eV) [5]. There is also a lasing wavelength shift, from the movement of the compound gain, in the same direction which is ~ 7 nm (taken from the graph Fig. 5.6) corresponding to an increase in reverse bias from 1.5 Vto 4.5 V. This gives a total shift, relative to the change in lasing wavelength of ~ 30 nm (0.024 eV). This change in wavelength is equal to the difference in energy between the first exciton peak and the second, ~25 meV calculated from the data reported by Fox *et al* [5]. From these calculations it can be seen that the two peaks in absorption corresponds to the red shift of the exciton peaks, where the first peak in absorption corresponds to the first exciton peak (heavy hole), and the second peak in absorption corresponds to the second exciton peak (light hole), as illustrated in fig. 5.19b.

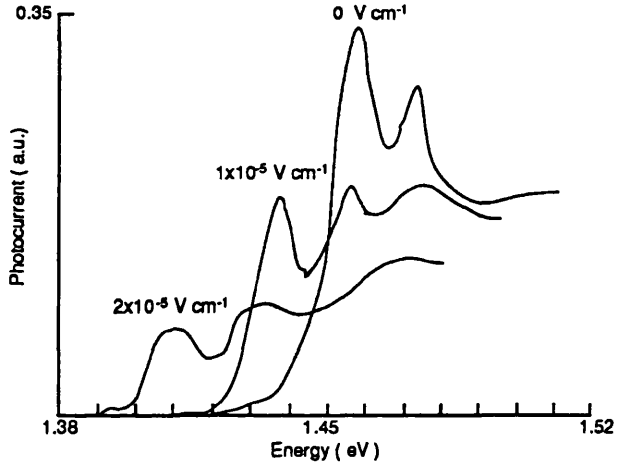

Fig. 5.19a. Electroabsorption model illustrating the quantum confined Stark effect at different electric field strengths.

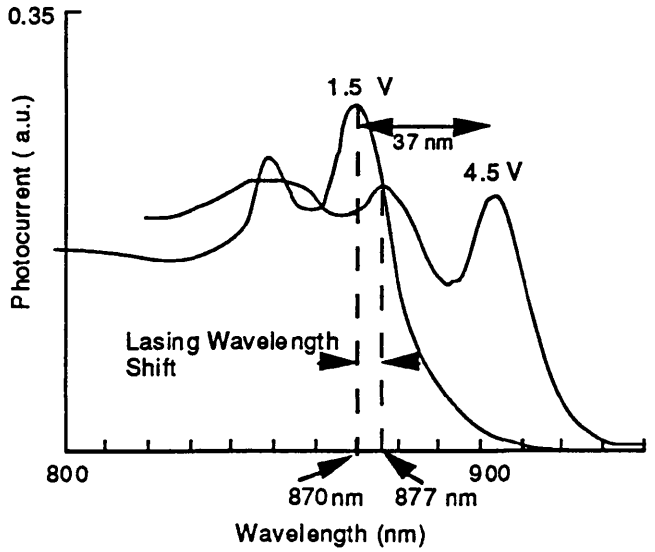

Fig. 5.19b Electroabsorption model illustrating the shift in exciton peak due to a change in reverse bias across the saturable absorber, 870nm is the lasing wavelength at 1.5 V and 877nm is the lasing wavelength at 4.4 V.

5.3. CW Measurements.

CW results were taken using the laser test rig illustrated in Fig. 5.20 The peltier controller temperature was set at 15 °C, and the laser was left running for ten minutes to stabilise before taking results.

During self-pulsation, a strong spectral peak was observed in the frequency domain, with further harmonics occuring at higher frequencies. The first two self-pulsating harmonics are shown in Fig. 5.20, the fundamental self-pulsating frequency of 1.5 GHz and its second harmonic at 3.0 GHz. The two-section laser in this case was driven with a cw current of 80 mA with 1.6 V reverse bias present across the saturable absorber.

The width of the spectral peak of the fundamental harmonic, measured 3 dB down from the peak, was found to be 1 MHz and the amplitude of the second harmonic was also measured and was approximately 10 dB below that of the fundamental self-pulsating line.

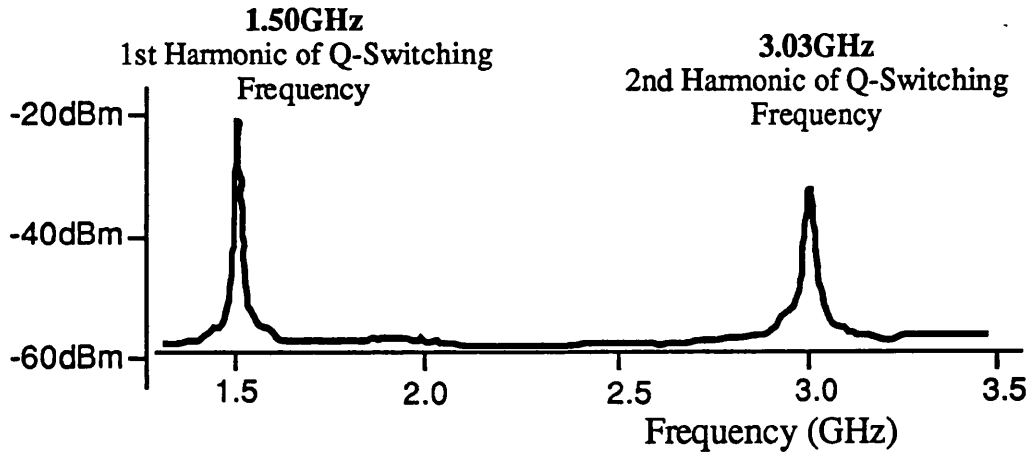

Fig. 5.20. Frequency spectrum of self-pulsating laser.

Of the few devices that were tested cw, the maximum repetition rate observed was 4.5 GHz driven with an injected current of 95 mA, and 0.7 V reverse bias present across the saturable absorber. Fig. 5.21 shows the result of a device measured using the cw laser rig. The reverse bias was kept constant at 0.7 V while the drive current was varied from 25 to 85 mA. From the results, there appears to be a quadratic relationship between the injected current and the self-pulsating frequency which was also the case in the quasi-cw measurements (Fig. 5.13).

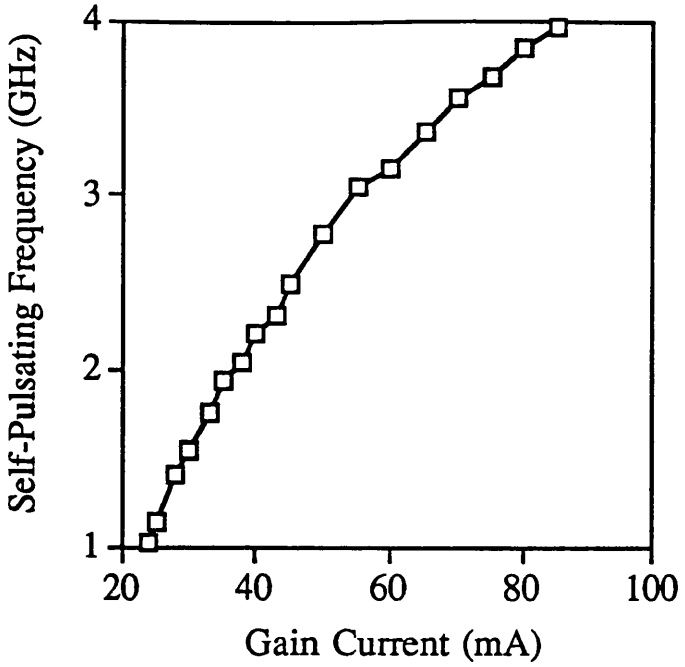

Fig. 5.21. Injected current against self-pulsating frequency, under a constant 0.7 V reverse bias.

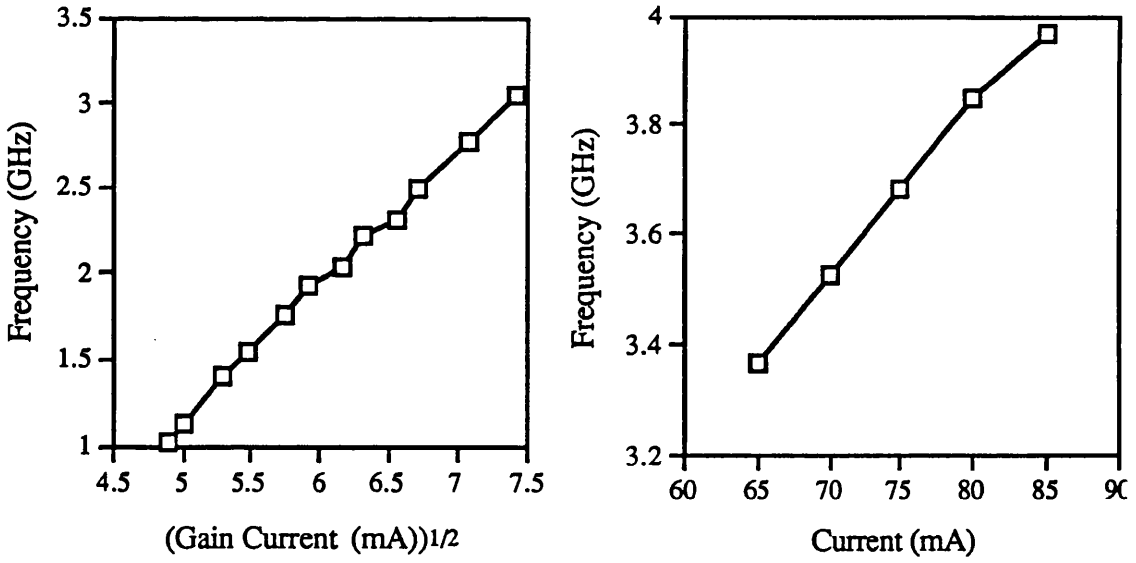

Fig. 5.22. Injected current against self-pulsating frequency, under a constant 0.7 V reverse bias. a) Showing a quadratic relationship between repetition frequency and current. b) Showing a linear relationship between repetition frequency and current.

The same set of data from Fig. 5.21 is plotted in Fig. 5.22, graph (a) is a plot of $\sqrt{\text{Current}}$ against repetition frequency for the current values below 70 mA ($J_{th}/J = 0.3$), illustrating the quadratic dependance the current has on repetition frequency for a small signal analysis, which has been observed observed experimentally [2, 3] and predicted by

Dixon and Joyce [4] in their small signal analysis which describes the self-pulsation repetition frequency dependence on gain current. For a large signal analysis there is a linear dependence of current against repetition frequency which is predicted by equation (3.51). This is illustrated in Fig. 5.22 (b), where the current values above 70 mA are plotted against self-pulsation frequency and a linear dependence is exhibited.

The cw pulse train was also detected in real time using the setup in Fig. 5.23. The electical output from the fast GaAs photodetector was divided in two using an rf splitter and one of the signals was connected to the trigger input the other to the sampling head of the C.S.A.. The maximum frequency of the pulse train was limited to 2 GHz, the bandwidth of the trigger's electronics. The result from a two-section device is shown in Fig. 5.24, the laser was driven by an 80 mA current and had a self-pulsating frequency of 1.45 GHz. Due to electrical reflections from the RF splitter small oscillations are seen in between each pulse.

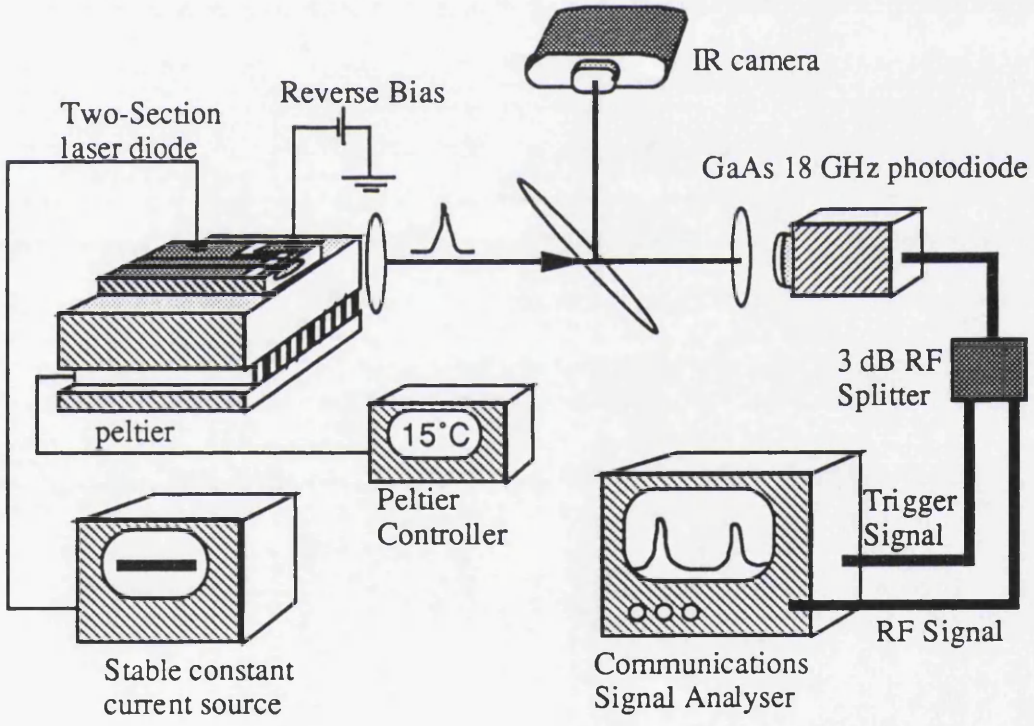

Fig. 5.23. Experimental setup to measure a cw pulse train in real time.

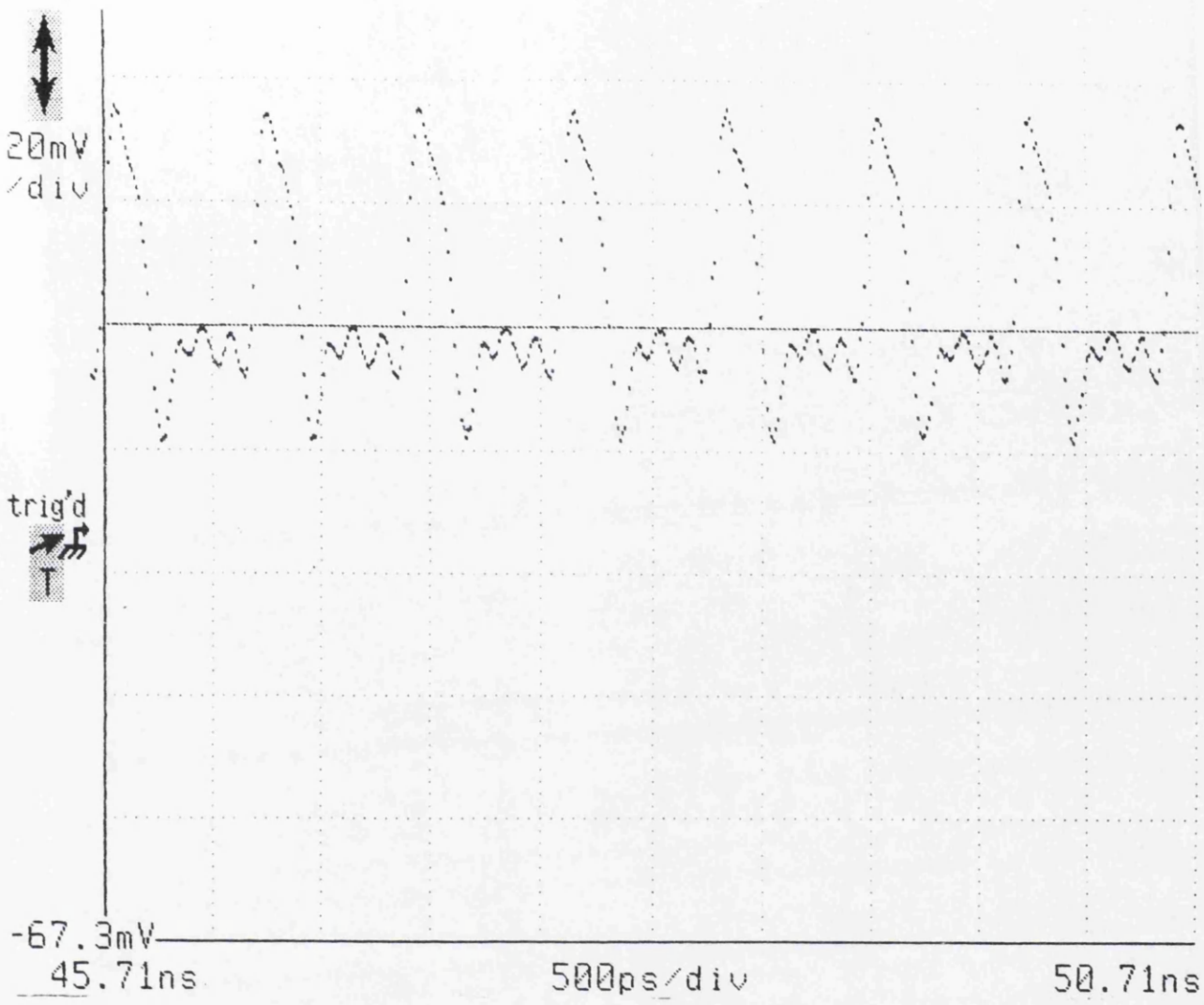

Fig. 5.24. Trace from a communications signal analyser of a 1.45 GHz pulse train.

5.4. Simple Graphical Model

A simple model is proposed to explain the results of saturable absorber length against repetition frequency in Fig. 5.10. The model should help in understanding why there is a optimum value of saturable absorber length.

As the current (I) increases, the steady state gain increases logarithmically. The gain saturation of quantum well lasers can be described according to the equation

$$\gamma = \gamma_o \ln(I/I_T)$$

where γ is the gain coefficient, γ_o is the QW gain parameter and I_T is the transparency current. As illustrated in Fig. 5.25, the shorter the absorber the shorter the photon lifetime

of the saturable absorber (3.37) and therefore the smaller the unsaturated loss becomes, according to equation 3.39. We know, from the description of gain and loss dynamics of self-pulsating lasers, in chapter 3 (Fig. 3.6), that after an optical pulse there is a build up of carriers and the gain increases with time until it exceeds the unsaturated loss, there is net gain in the cavity and the leading edge of the next pulse is formed. We can see from the Fig. 5.25 the shorter the absorber the lower the value of unsaturated loss, the gain will therefore reach the lower value of unsaturated loss in a faster time period than the higher value of unsaturated loss. Therefore, long saturable absorber will give a lower repetition rate than a short absorber

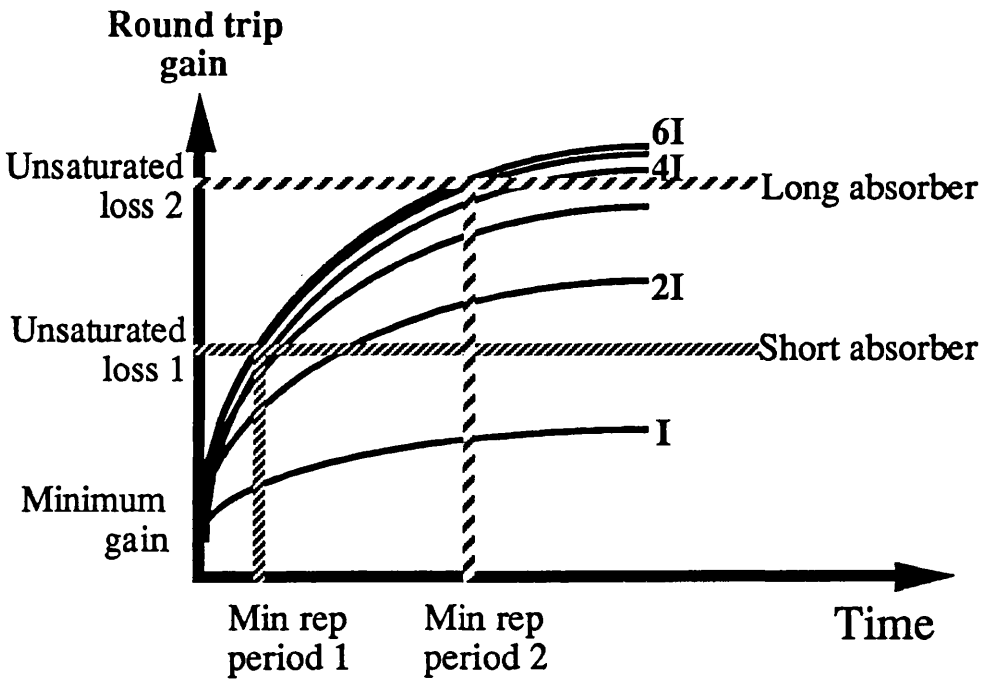

Fig. 5.25. Model showing the increase in the round trip gain against time.

If however the volume of the saturable absorber is too small then the absorber will not fully recover to its unsaturable loss value and lasing occurs in between the pulses loss, further decreasing the length of the saturable absorber the laser will eventually emit a cw optical signal. This is illustrated in fig. 5.26 a modified version of fig 3.6 where a large current injection results in a high repetition rate.

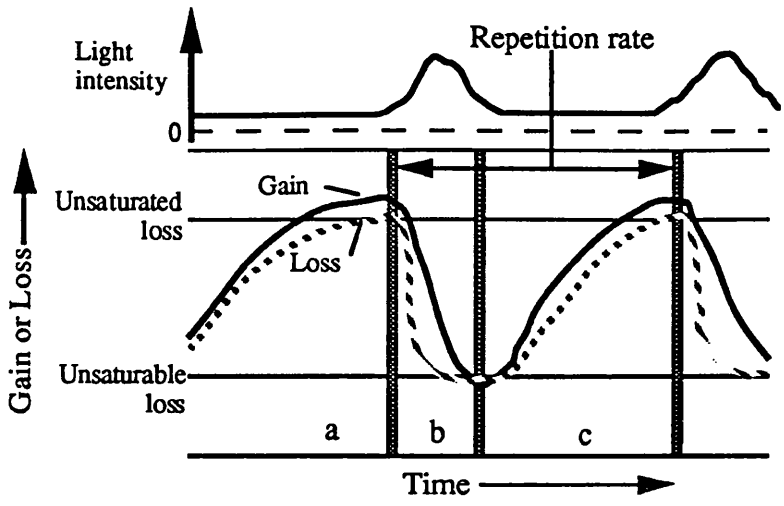

Fig. 5.26. Modified model of self pulsation with a small saturable absorber.

The loss in this case, cannot recover as fast as the gain and the pulses are superimposed on a cw background. This phenomenon can be seen in the streak camera traces of Fig 5.11, where the repetition rate increases with injected current until at a high value the pulses become no longer become fully resolved. This simple model explains the results obtained in Fig. 5.10, a theoretical model is being produced to describe this phenomenon fully.

5.5. References

1 E. Yablonovitch, and E. O. Kane, "Reduction of lasing threshold current density by lowering of valence band effective mass," *IEEE J. Lightwave Technol.*, vol. LT-4, pp. 504-506, 1986.

2. R. W. Dixon, and W. B. Joyce, "A possible model for sustained oscillations (pulsations) in (Al, Ga)As double-heterostructure lasers," *IEEE J. Quantum Electron.*, vol. QE-15, pp. 470-474, 1979.

3. P. E. Barnsley, H. J. Wickes, G. E. Wickens, and D. M. Spirit, "All-optical clock recovery from 5 Gb/s RZ data using a self-pulsating 1.56 μm Laser diode," *IEEE Photon. Technol. Lett.*, vol. 3, pp. 942-945, 1991.

4. S. Olvadia *et al*, "Low- frequency relative intensity noise in self-pulsating ridge waveguide quantum well lasers," *IEEE Photon. Technol. Lett.*, vol. 4, pp. 336-338, 1992.

5. A. M. Fox, *et al*, "Quantum well carrier sweep out: Relation to electroabsorption and exciton saturation," *IEEE J. Quantum Electron.*, vol. QE-27, pp. 2281-2294, 1991.

Chapter 6

Two-Photon GaAs/AlGaAs Autocorrelator

6.1. Introduction

Autocorrelation techniques have been used for some years to measure the duration of ultra-short pulses [1,2]. Previous measurements of the temporal profiles of ultra-short pulses were made by means of second harmonic generation (SHG), or two-photon fluorescence. Recently two-photon-induced photoconductivity (TPC) in commercial photodiodes has been used as the non-linear mechanism to measure pulse widths [3].

In this chapter the use of TPC in a reverse-biased GaAs/AlGaAs waveguide is demonstrated as an autocorrelator detector. The advantage of using TPC rather than conventional SHG as the non-linear process in an autocorrelator is that TPC is relatively wavelength insensitive. Photons of any energy between $E_g/2$ andE_g can be used to obtain an autocorrelation trace, whereas, if a SHG crystal is used, the crystal must be polished at the correct angle to achieve phase-matching at the appropriate wavelength. The waveguide structure also offers the advantage of having greater sensitivity than a simple photodiode structure and allows much greater opportunities for integration. Using a waveguide, however, has the disadvantage that some temporal resolution is lost due to dispersion.

The TPC autocorrelator was initially used to measure the pulse width of a modelocked Nd^{3+}:YAG laser, and a 1.3 μm Q-switched laser. Intensity autocorrelation measurements were then taken of a self-pulsating two-section laser which was designed and fabricated by myself, and then finally initial interferometric autocorrelations were made. The Nd^{3+}:YAG laser measurements were carried out by Dr Frances Laughton [4], the 1.3 μm Q-switched laser measurement was performed by myself and Dr Laughton, the two-section laser autocorrelation measurement was made by myself, and the interferometric autocorrelation was carried out by myself and Mehdi M. Karkhanehchi.

6.2. Two-Photon Absorption

Two-photon absorption (TPA) is a nonresonant nonlinear optical process [5, 6], which occurs for photons with energy hν greater than half the semiconductor energy gap $E_g/2$. It also occurs for photons with an energy greater than E_g however the two-photon process is swamped by single photon absorption. In the energy range between $E_g/2$ and E_g there is very little single photon absorption, since the photon energy is less than the energy band gap of the semiconductor material. However, if the beam of light irradiating the

semiconductor is of a certain intensity, an electron can be excited from the valence band to the conduction band by the absorption of two photons. Because of the high intensity of light needed to perform such a transition, TPA was not observed until the invention of the laser and was first observed by Braunstein and Ockman in CdS, using a ruby laser [7], despite having been predicted 30 years earlier [8].

For TPA to occur an electron has to be excited from the valence band to the conduction band via an intermediate virtual state, as shown in Fig. 6.1. There are three different routes the electron can take [9]. The electron can be excited from the valence to the conduction band by the first photon it then interacts with a second photon in the conduction band (1). In the second route the electron interacts with a photon in the valence band and a second photon excites the electron into the conduction band (2). The final transition the electron can take occurs through the coupling of the two valence bands so that the electron is excited from the light hole to the heavy hole or from the heavy hole to the light hole by the first photon and then up to the conduction band through the interaction of the second photon (3). During the first transition to the intermediate state, momentum is conserved and the electron can only remain in this state for a time governed by the Uncertainty Principle [10].

$$\Delta E \cdot \Delta t \approx h \tag{6.1a}$$

If the second photon is absorbed within the time, Δt, the electron undergoes a second transition to reach the final energy state. For the entire TPA process energy is conserved.

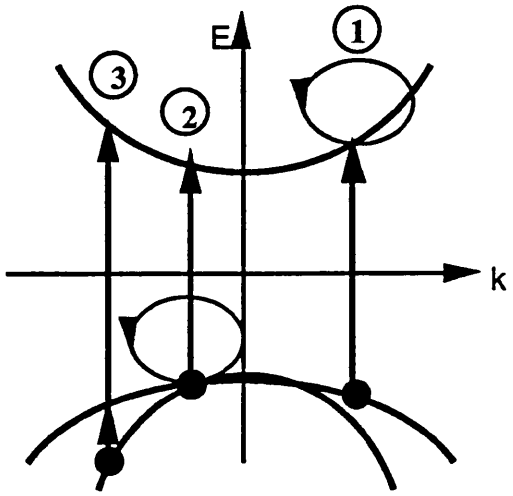

Fig. 6.1. E-k diagram of two-photon absorption.

The change in intensity (I) as the light propagates in the z direction is described by the equation,

$$\frac{dI}{dZ} = -\alpha_1 I - \alpha_2 I^2 \qquad (6.1b)$$

where α_1 is the single photon absorption coefficient and α_2 is the two photon absorption coefficient.

The value of the single photon absorption coefficient for photon energies less than E_g, but greater than $E_g/2$, is very small, therefore it follows that there will also be very few real carriers generated. However, a large population of real carriers can be generated by means of TPA, which can be measured as a photocurrent. Due to the nonlinear nature of TPA, the measured photocurrent will be a quadratic function of the light intensity, and therefore this mechanism can be used as the basis for an autocorrelation technique. We can therefore use a standard p-i-n semiconductor waveguide structure in place of a SHG crystal and photomultiplier tube as the nonlinear element in an autocorrelation measurement. An autocorrelation measurement of a laser pulsewidth is possible by measuring the photocurrent due to TPA as a function of the delay time between the two pulses.

6.3. Initial Autocorrelation Measurements.

In order to be able to use a nonlinear optical effect for pulsewidth measurements, the response time of the nonlinearity must be much less than the pulsewidth to be measured. This section describes the initial experiments carried out by Dr F. Laughton to show that TPA is an almost instantaneous effect (Δt), and therefore suitable for pulsewidth measurements.

Absorption modulation measurements due to TPA were made in a GaAs/AlGaAs Multiple Quantum Well ridge waveguide, in order to investigate the dynamics of the nonlinear processes [11]. Orthogonally polarised pump probe pulses with a FWHM of about 90 ps from a modelocked Nd^{3+}:YAG laser at 1.06 μm were endfire coupled into a 10 mm long waveguide, and the transmission of the probe pulse was measured as a function of the pump-probe delay time.

The results showed a maximum absorption modulation of about 30 % at the point where the pump and probe exactly overlapped. The strength of the modulation became negligible for pump-probe delay times greater than 100 ps. The measurement of the absorption modulation was found to be 83 ps, which was in close agreement with pulsewidth measurements using a conventional autocorrelator (89 ps). It was found that the

width of the absorption plot is related to the laser pulse width and not the carrier lifetime, therefore TPA is an almost instantaneous effect.

However, limitations to this method were seen at higher powers of peak pump intensity, with significant absorption modulation observed when the pump and probe were widely separated temporally. At high pump intensities free carrier absorption (FCA) plays a significant role in the absorption modulation. However, the speed of response of absorption modulation due to FCA is related to the carrier lifetime (measured to be 35 ns in this case), therefore now the width of the modulation graph is no longer related solely to the laser pulsewidth.

If the intensity of the pulse used for the absorption modulation measurements is too high, there will be an additional slow effect of FCA, and the measurement of the pulsewidth will be inaccurate. Therefore an accurate method of pulsewidth measurement needs to be sensitive to instantaneous nonlinearities, such as TPA, but insensitive to the effects of slower nonlinearities, such as FCA.

This can be achieved by measuring the two-photon-induced photoconductivity (TPC), i.e. the photogenerated carrier density in the waveguide. TPA can be detected by an increase in photocurrent because it produces a real carrier population, but FCA does not result in any change in the carrier density, and so is not directly detected. As the light propagates through the waveguide it is attenuated by FCA and also single-photon absorption; this reduction in intensity results in a second-order error, which can be minimised by reducing the length of the waveguide to about 1 mm. Using a shorter waveguide also results in a greater measured photocurrent density, and hence an increase in sensitivity, because the beam is less attenuated and the peak intensity is higher throughout the waveguide. Increasing the photocurrent density also increases the sensitivity of the device by reducing the relative effect of dark current.

6.4. Material Design and Fabrication of a TPA Waveguide.

Two types of material were designed and grown by MBE in the university department. The first p-i-n waveguide structure consisted of a GaAs guide region surrounded by $Al_{0.15}Ga_{0.85}As$ cladding regions, as shown in Fig. 6.2a. This device was used to measure pulsewidths with a wavelength greater than 950 nm. Secondly, a p-i-n waveguide structure with a $Al_{0.2}Ga_{0.8}As$ guide region surrounded by $Al_{0.3}Ga_{0.7}As$ cladding was used for measuring pulsewidths with wavelengths greater than 840 nm, Fig. 6.2b.

p^+ GaAs		$5*10^{18}$	500 Å
p	$Al_{.15}Ga_{.85}As$	$5*10^{17}$	0.6μm
i	$Al_{.15}Ga_{.85}As$		0.4μm
i	GaAs		0.6μm
i	$Al_{.15}Ga_{.85}As$		0.4μm
n	$Al_{.15}Ga_{.85}As$	$5*10^{17}$	4μm
n^+GaAs substrate			

(a)

p^+ GaAs		$5*10^{18}$	500 Å
p	$Al_{.3}Ga_{.7}As$	$5*10^{17}$	0.6μm
i	$Al_{.3}Ga_{.7}As$		0.4μm
i	$Al_{.2}Ga_{.8}As$		0.6μm
i	$Al_{.3}Ga_{.7}As$		0.4μm
n	$Al_{.3}Ga_{.7}As$	$5*10^{17}$	4μm
n^+GaAs substrate			

(b)

Fig. 6.2(a+b). Structure of GaAs/AlGaAs p-i-n waveguide material.

Both material structures were left undoped in the parts of the cladding region where there was expected to be significant optical overlap, in order to reduce losses due to FCA in the p and n regions.

The dimensions of the ridge waveguides were calculated using F-Wave, a vector finite difference computer program, so that 980 nm light would propagate along the guide in a zero order optical mode. Ridge waveguides 3 μm wide were then dry etched in the GaAs/AlGaAs semiconductor material using $SiCl_4$ gas, to a depth of 0.8 μm. Once the waveguides were formed, a wet etch was used to mesa between the ribs and electrically isolate the individual devices, as shown in Fig. 6.3. The individual devices were etched to a depth of about 5 μm which reduced the dark current to about -90 pA at 5 V. (It is important that the dark current is as small as possible in order to increase the sensitivity of the autocorrelator, i.e. decreasing the dark current improves the noise performance.)

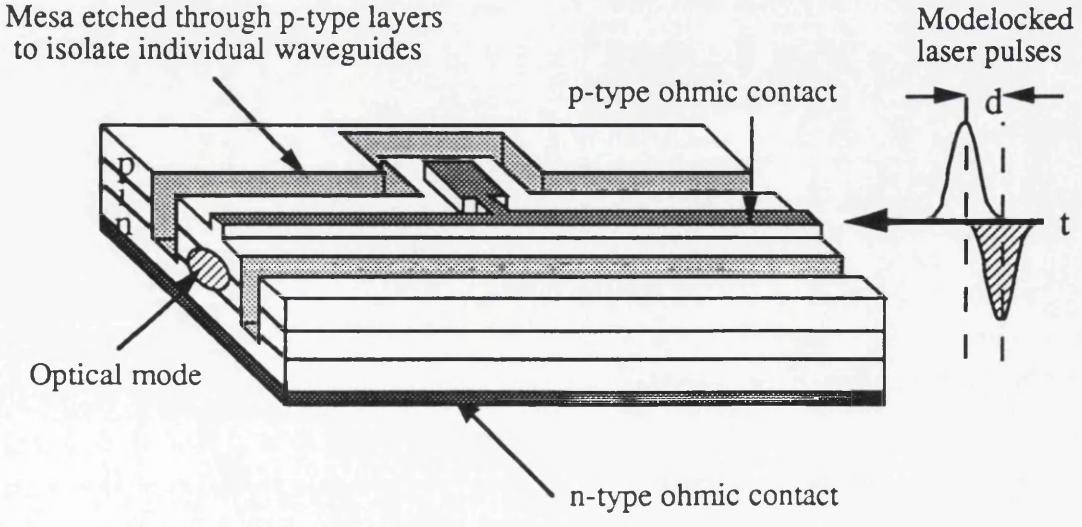

Fig. 6.3. Schematic of a TPA waveguide autocorrelator.

A photocurrent spectrum was taken of the p-i-n material with a $Al_{0.2}Ga_{0.8}As$ guide region surrounded by $Al_{0.3}Ga_{0.7}As$ cladding. The material was tested to ensure that the aluminium fraction of the guide region was correct and the absorption edge of the material was not too near the wavelength of the pulses being measured. Light from a 1 m scanning spectrometer with a tungsten light source was focused onto a sample of p-i-n material at room temperature. The sample was reverse biased so that any photocurrent produced by electroabsorption could be measured. The wavelength of the incident light was scanned from 660 nm to 760 nm and the corresponding photocurrent was measured as a function of the incident wavelength. The photocurrent spectrum trace is shown in Fig. 6.4; from the graph it can be seen that the bandedge of this material is about 735 nm.

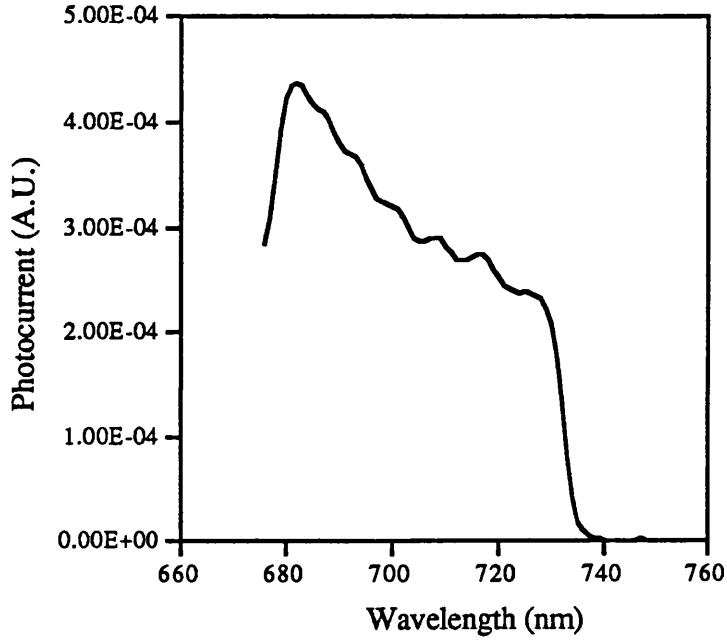

Fig. 6.4. Photocurrent spectrum of a p-i-n structure showing a band edge of 735 nm. This structure was used for measuring TPA at wavelengths greater than 735 nm.

6.5. Initial Experiments using a Nd^{3+}:YAG Laser

6.5.1. Intensity-Dependence of the Photocurrent for Single Beam Measurements

In order to test whether the device was operating correctly, Dr Laughton initially carried out single-beam experiments with the autocorrelator. A single beam from a cw modelocked Nd^{3+}:YAG laser at 1.06 μm was end-fire coupled into the waveguide, which was reverse-biased by 4.5 V. The photocurrent produced by the TPA was found by measuring the voltage across a 10 Ω resistor placed in series with the waveguide. The photocurrent, which was measured using a lock-in amplifier, was found to be extremely sensitive to the degree of coupling into the waveguide, and also the quality of the modelocked pulse. Measurements were taken of the intensity-dependence of the photocurrent for cw and modelocked operation of the Nd^{3+}:YAG laser, Fig. 6.5.

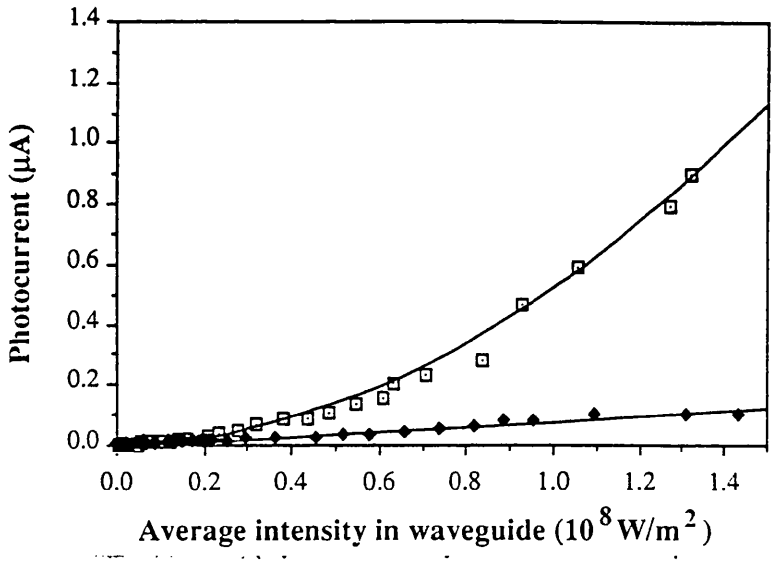

Fig. 6.5. Plot of the intensity- dependence of the photoconductivity of the waveguide. The solid points are experimental data for a CW Nd^{3+}:YAG laser and the open points are for the same modelocked laser.

The difference between the shape of these plots can be easily explained. For a cw beam, the carrier photogeneration rate is given by

$$\left(\frac{dN}{dt}\right)_{ave} = \frac{\alpha}{h\upsilon} I_{ave} + \frac{\beta}{2h\upsilon} I_{ave}^2 \qquad 6.2$$

where hν is the photon energy, I_{ave} is the average intensity of the beam, β is the two-photon absorption co-efficient and α is the single-photon absorption co-efficient, which is that

fraction of the total waveguide propargation loss resulting from the generation of electron-hole pairs by single photons.

As we have already mentioned, the light propagating through the waveguide is attenuated by FCA and single-photon absorption and, if the waveguide were long then the average intensity of the light would decay significantly along the guide. The carrier photogeneration rate would therefore have to be integrated with respect to the distance along the guide. However by making the length of the waveguide 1 mm long, we make the simplifying assumption that the intensity, and hence the average carrier density, remains constant throughout the length of the waveguide. To make this assumption we have to assume that the pulse width being measured is greater than ~20 ps FWHM (the path length of 1 mm corresponds to ~10 ps in GaAs). The average photocurrent due to a cw beam is therefore

$$\left(J_{ph}\right)_{cw} = e\Omega\left(\frac{\alpha}{h\upsilon}I_{ave} + \frac{\beta}{2h\upsilon}I_{ave}^2\right) \qquad 6.3$$

where e is the electronic charge and Ω is the volume in which the photogenerated carriers are created.

To calculate the average photocurrent for a modelocked laser beam, we assume the modelocked pulses have a Gaussian intensity profile, given by

$$I(t) = I' \exp\left(\frac{-2t^2}{T^2}\right) \qquad 6.4$$

where I' is the peak intensity of the modelocked pulse, related to the average intensity by

$$I' = I_{ave}\sqrt{\frac{2}{\pi}}\frac{t_p}{T} \qquad 6.5$$

The measured photocurrent has been averaged over a period of time much longer than the laser pulsewidth. Therefore the carrier generation rate must be integrated over the time between laser pulses, t_p, to calculate the photocurrent for a modelocked beam. The average photocurrent, in the modelocked case is

$$\begin{aligned}\left(J_{ph}\right)_{ml} &= \frac{e\Omega}{t_p}\int_{-\infty}^{\infty}\frac{dN}{dt}dt \\ &= \frac{e\Omega}{t_p}\int_{-\infty}^{\infty}\left(\frac{\alpha}{h\upsilon}I(t) + \frac{\beta}{2h\upsilon}I^2(t)\right)dt \qquad 6.6 \\ &= e\Omega\left(\frac{\alpha}{h\upsilon}I_{ave} + \frac{\beta t_p}{2\sqrt{\pi}h\upsilon T}I_{ave}^2\right)\end{aligned}$$

In both the modelocked and cw expressions for photocurrent, the linear terms are identical, while the quadratic terms differ only by a constant factor.

6.5.2. Sensitivity of two-photon -induced Conductivity

The efficiency of the two-photon-induced conductivity (TPC) was measured using the Nd^{3+}:YAG laser. The coupling of the light into the waveguide was adjusted to maximise the average photocurrent, which was 0.8 mA (corresponding to a peak photocurrent of about 0.11 A) for an average input power of about 300 mW before the waveguide. If we take the reflection coefficient at the input facet to be 0.32 and assume that 20 % the light is then coupled into the guide mode, then the maximum peak intensity in the waveguide is about 6 W.

We define the efficiency of the TPC process as the ratio of the number of photogenerated electron-hole pairs to the number of photons, that is

$$\eta = \frac{J_{ph}' h\upsilon}{eP'} \qquad 6.7$$

where J_{ph}' is the peak photocurrent, and P' is the peak power in the guided mode.

We can then obtain a lower limit on the efficiency of TPC in the waveguide as $\eta \approx 1.6 \times 10^{-4} \times P'$ (where P' is measured in Watts), which compares very favourably with the equivalent estimate of $\eta \approx 2.2 \times 10^{-12} \times P'$ for the efficiency of the two-photon autocorrelator using a photodiode [3]. Because of the increase in efficiency of the waveguide autocorrelator it is much more suitable for applications where the power levels are lower, such as for semiconductor lasers. Part of the improvement in efficiency (a three times order of magnitude) is most likely attributed to the enhancement of non-linear effects in waveguides over normal planar photodiodes, because of the greater interaction length.

6.5.3. Theoretical Behaviour of the Two-photon Absorption Autocorrelator

To calculate the theoretical photocurrent as a function of the time delay, consider two modelocked Gaussian pulses travelling through a waveguide, orthogonally polarised so they do not interfere, separated temporally by t_d, and having a peak intensity I'. The instantaneous intensity in the waveguide is

$$I(t) = I' \exp\left(\frac{-2t^2}{T^2}\right) + I' \exp\left(\frac{-2(t-t_d)^2}{T^2}\right) \qquad 6.8$$

The average carrier generation rate is therefore given by

$$\left(\frac{dN}{dt}\right)_{ave} = \frac{1}{t_p}\int_{-\infty}^{\infty}\left(\frac{\alpha}{h\upsilon} I(t) + \frac{\beta}{2h\upsilon} I^2(t)\right) \qquad 6.9$$

and hence the average photocurrent as a function of the time delay between pulses is

$$J_{ph}(t_d) = e\Omega\left(\frac{2\alpha}{h\upsilon} I_{ave} + \frac{\beta t_p I_{ave}^2}{\sqrt{\pi} h\upsilon T}\left(1 + \exp\left(\frac{-t_d^2}{T^2}\right)\right)\right) \qquad 6.10$$

It can be seen from the expression, that for Gaussian pulses, the average photocurrent has the same Gaussian dependence on the time delay between the two beams as a conventional SHG autocorrelator. Therefore any autocorrelation trace obtained from this method should be divided by $\sqrt{2}$ to obtain the true pulse width.

To calculate the signal ratio of correlation peak to background, we can see that as the pulses overlap ($t_d = T$) the photocurrent is

$$J_{ph}(t_d) = e\Omega\left(\frac{2\alpha}{h\upsilon} I_{ave} + \frac{2\beta t_p I_{ave}^2}{\sqrt{\pi} h\upsilon T}\right) \qquad 6.11$$

and when the time delay between pulses is greater than the pulse width $(t_d > T)$,

$$J_{ph}(t_d) = e\Omega\left(\frac{2\alpha}{h\upsilon} I_{ave} + \frac{\beta t_p I_{ave}^2}{\sqrt{\pi} h\upsilon T}\right) \qquad 6.12$$

which if we assume that single photon absorption is negligible gives a ratio of correlation peak to background of 1:2.

6.5.4. YAG Laser Autocorrelation

Autocorrelation results were taken of a pulse train from a modelocked Nd^{3+}:YAG laser using the two-photon autocorrelator. These pulse width autocorrelation measurements were the first, to our knowledge, using a p-i-n semiconductor waveguide. The experimental arrangement is illustrated in Fig. 6.6. The set-up is very similar to a conventional autocorrelator; the first half of the arrangement is a standard Michelson interferometer which splits the pulse train into two equal beams and recombines them with a known time delay. However the second half of the experimental set-up differs in the way the intensity of the light is measured– the SHG crystal and photomultiplier tube have been replaced by the reverse-biased p-i-n semiconductor waveguide. One of the 'arms' of the Michelson interferometer had a quarter waveplate so that the two pulses were orthogonally polarised to reduce any interference effects in the waveguide. By orthogonally polarising the two pulses an intensity autocorrelation was obtained, however, in later experiments, when the pulses had the same polarisation, an interferometric autocorrelation was produced.

As the time delay between the two pulse varied, the instantaneous peak intensity in the waveguide, and hence the carrier density generated by TPA, also changed. A pulse width measurement was therefore made by altering the time delay t_d between the two pulses and measuring the photocurrent produced from the waveguide as a function of the time delay.

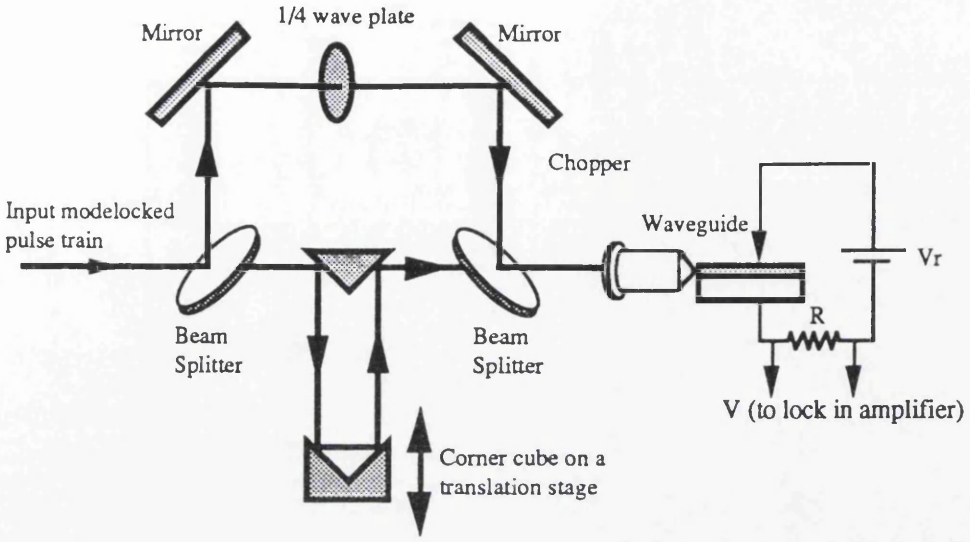

Fig. 6.6. Schematic of an experimental set-up for an intensity autocorrelation measurement of a Nd^{3+}:YAG laser.

The autocorrelation trace obtained for the modelocked Nd^{3+}:YAG laser at 1.06 μm is shown in Fig. 6.7. The average input power of each of the laser pulses immediately before the waveguide was measured to be about 150 mW, which gave a maximum average photocurrent of about 1 mA. Readings of the photocurrent were taken every 1 mm moved by the translation stage, which corresponded to a time delay of 6.66 ps. The solid line in the autocorrelation trace is a Gaussian best fit to the experimental data, from which the FWHM of the laser pulse was calculated to be 83 ps. This result corresponds well with both the specification of the laser and a conventional autocorrelation measurement performed previously (89 ps).

The ratio of the correlation peak to the background in Fig. 6.7 is not 2:1, as predicted by Equation 6.10, but only about 1.7:1. We attribute this to either the polarisation dependance of two-photon absorption in GaAs [6] or residual single photon absorption at this wavelength.

Although this autocorrelation trace is not background-free, this could be obtained if wished using standard heterodyne detection techniques. By placing two choppers of different frequencies in either arm of the Michelson interferometer, and measuring the photocurrent with a frequency equal to the sum or difference of the two chopper frequencies, the background would be eliminated.

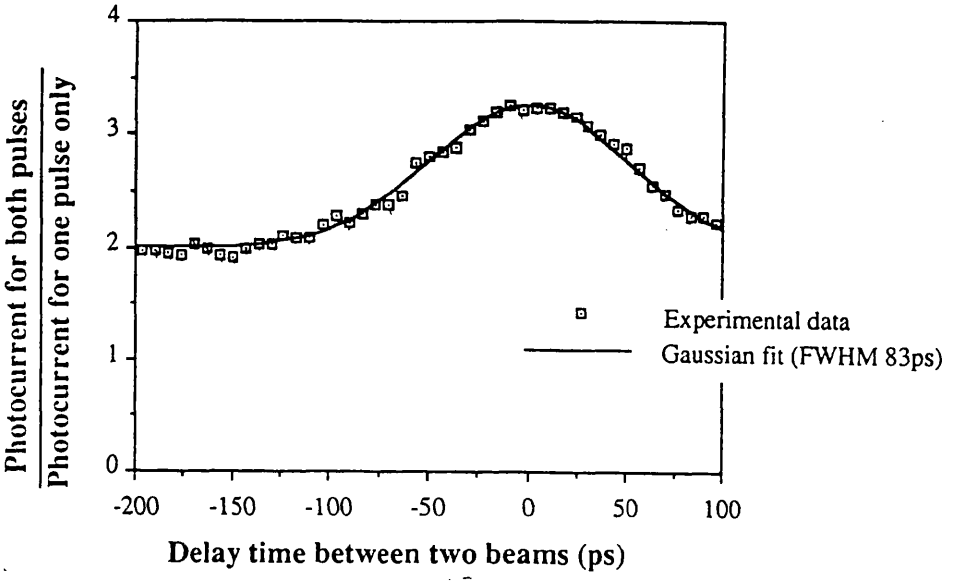

Fig. 6.7 Experimental TPA autocorrelation trace for a mode-locked Nd^{3+}:YAG laser in a GaAs/AlGaAs reverse biased waveguide. The solid line is a Gaussian fit to the experimental points.

6.6. Experiments using a Semiconductor Laser

6.6.1. Introduction

After measuring the pulse width of the modelocked Nd^{3+}:YAG laser, autocorrelation measurements were made on Q-switched semiconductor lasers to further test the sensitivity of the TPA autocorrelator. The experiments were carried out using the Q-switched InGaAsP/InP double heterostructure stripe laser emitting at 1.3 μm, described in chapter 3. Before any autocorrelation measurements were taken, the TPA p-i-n waveguide was directly tested to see if it was sensitive enough to produce a photocurrent from the low average pulse powers emitted from the semiconductor laser.

6.6.2. Intensity-Dependence of the Photocurrent for Single Beam Measurements

Initially single beam experiments were carried out on the p-i-n waveguide to ensure the device was sensitive enough to detect laser diode Q-switched pulses. The experimental arrangement is shown in Fig. 6.8. The pulse train from the semiconductor laser was end-fire coupled directly into the ridge waveguide, which was reverse-bias by 4.5V. The photocurrent produced was then found by measuring the voltage across a 1 kΩ resistor in series with the waveguide. To measure the peak intensity of the Q-switched pulse, about 10 % of the pulse train was split from the main beam and focused onto a fast InGaAs photodetector connected to a sampling oscilloscope.

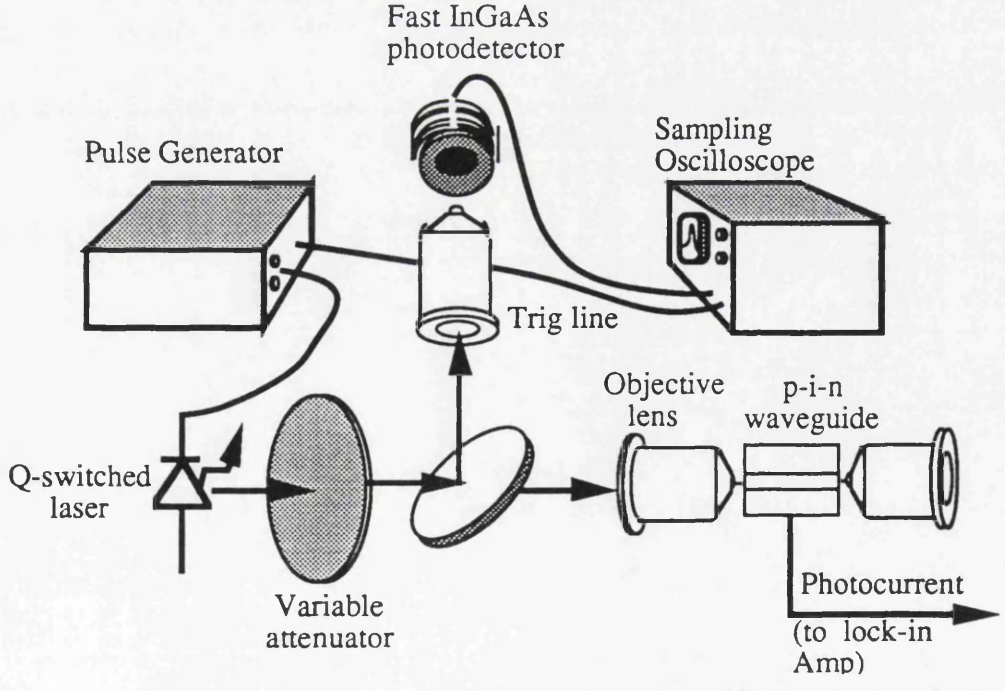

Fig. 6.8. Schematic of an experimental set-up to measure TPA against intensity in a Q-switched laser.

A variable attenuator was used to vary the peak intensity of the pulse, which was directly measured from the sampling oscilloscope.

Proportional values of peak intensity against photocurrent were taken, Fig.6.9, and both photocurrent against peak intensity and the square root of the photocurrent against peak intensity are plotted. It can be seen that, as expected, there is an approximate quadratic relationship between the photocurrent and the peak intensity of the pulse. This again verifies that the conductivity is governed by the two photon effect and the waveguide has the sensitivity to measure extremely low average powers.

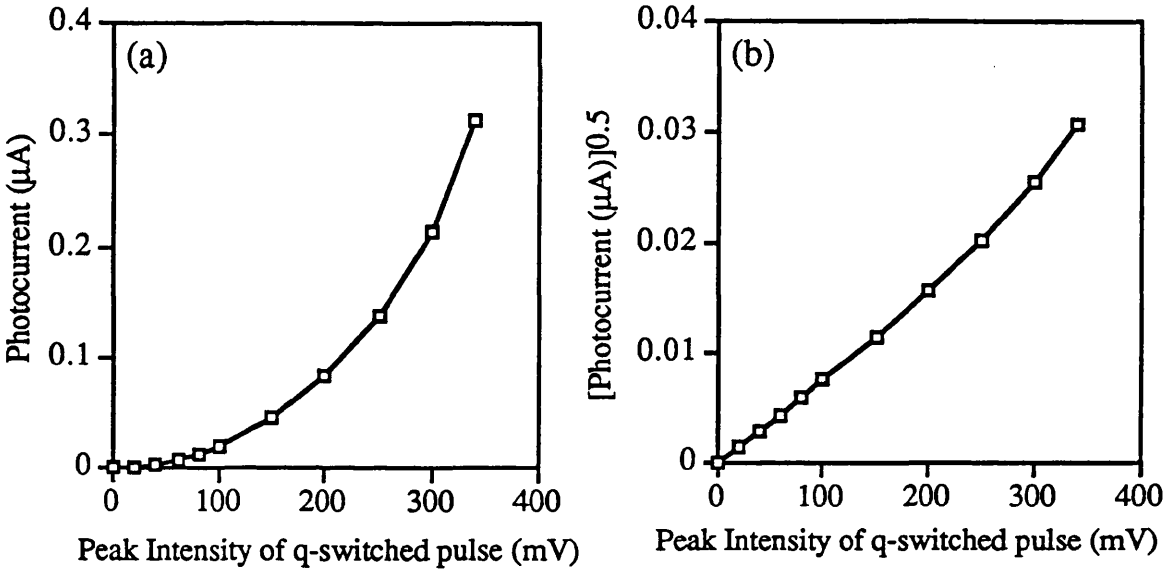

Fig. 6.9. Intensity dependence of the waveguide using a Q-switched semiconductor laser; plot (b) shows the square root of the photocurrent against intensity, illustrating the quadratic dependence.

6.6.3. Intensity Autocorrelation of an Ion-implanted Q-switched Semiconductor Laser.

Initial intensity autocorrelation measurements were made on a Q-switched InGaAsP/InP double heterostructure stripe laser with an ion implanted 'fast' saturable absorber. The laser was driven with short electrical pulses of 1 ns duration at a repetition frequency of 100 kHz. The amplitude of the drive current was reduced to about 200 mA so that one Q-switched pulse was produced for every electrical pulse. The peak optical power from the laser was about 1 W and, immediately before entering the waveguide, the average power in each beam was about 2 μW.

As illustrated before, Fig. 6.10, a Michelson interferometer with a quarter waveplate in one arm was used for the correlation measurements. The two aligned beams were then passed through an optical chopper and end fired into one end of the p-i-n waveguide. An infra-red camera was placed at the other end of the waveguide to aid alignment and to ensure that the light guided through the waveguide was in the zeroth order optical mode. The reverse biased waveguide provided the signal input to the lock-in amplifier and the reference signal came from the chopper. All the experiments were carried out in complete darkness which reduced the noise current to about 5 nA and gave a signal to noise ratio of around 50:1.

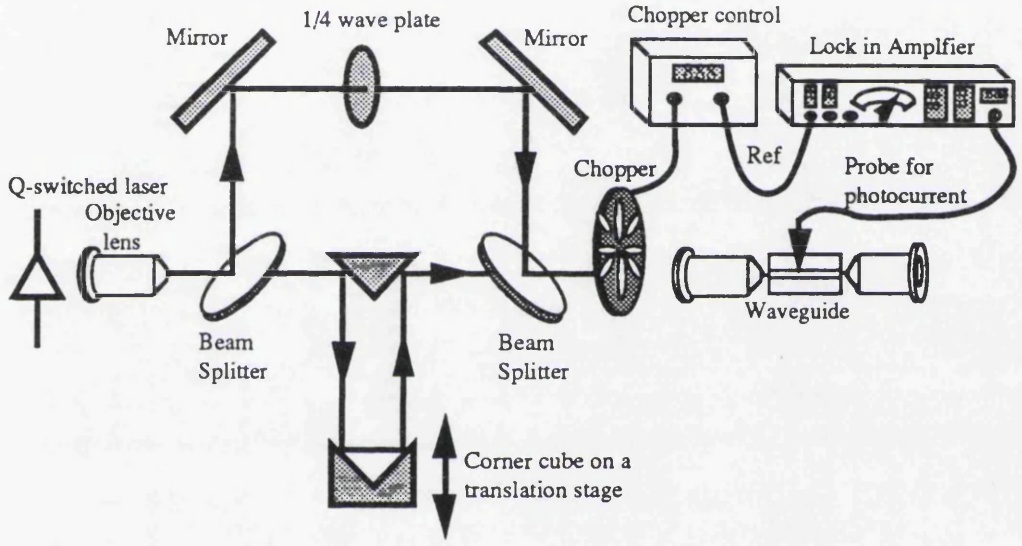

Fig. 6.10. Schematic of an experimental arrangement for an intensity TPA autocorrelator.

From the autocorrelation trace shown in Fig. 6.11, the FWHM of the semiconductor laser pulses was calculated to be about 13 ps. This result corresponds very closely with a streak camera measurement of the optical pulse of this laser, taken at the Ioffe Institute.

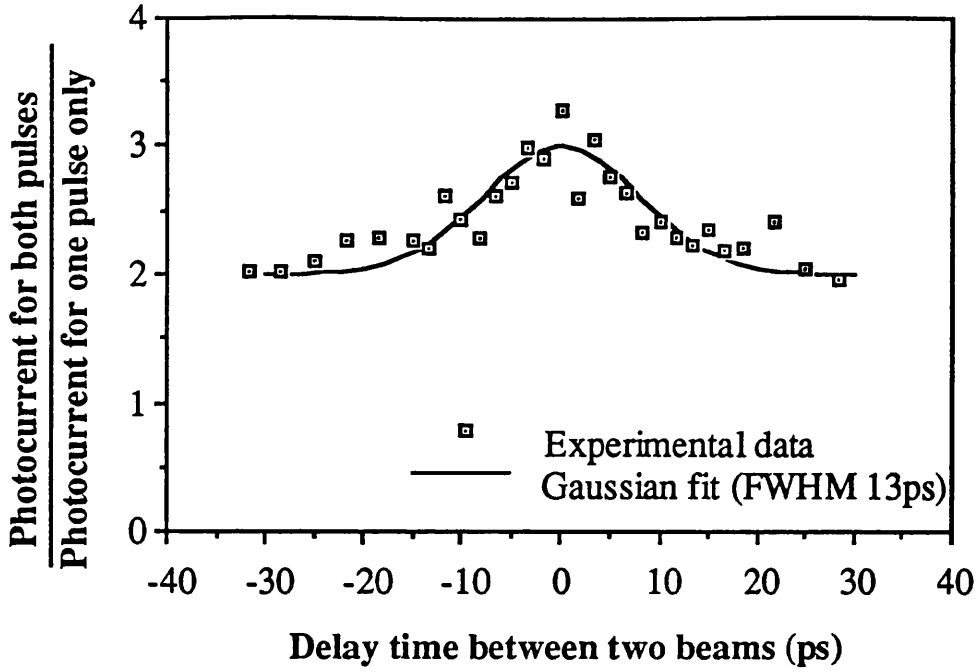

Fig. 6.11. Autocorrelation trace of the Q-switched InGaAsP/InP laser.

It should be noted that there had been previous attempts (at Bell Laboratories) to obtain a conventional autocorrelation trace of this laser using a SHG crystal, however these had been unsuccessful due to the low power of the laser.

6.6.4. Intensity Autocorrelation of a Two-section Semiconductor Laser.

The pulsewidth of a two-section InGaAs/GaAs strained double quantum well laser was measured using a TPA waveguide autocorrelator. The lasing wavelength of this device was 960 nm. The experimental set-up was identical to the previous pulsewidth measurement of a InGaAs/InP semiconductor laser. To produce effective Q-switching, the laser had a reverse bias of 1.5 V across the saturable absorber and a forward drive current of about 100 mA. The gain section of the laser was driven with short electrical pulses of 1 ns duration at a repetition frequency of 100 kHz. Again the amplitude of the drive current was reduced so that one Q-switched pulse was produced for every electrical pulse. For this particular device the peak optical power was about 0.2 W and, immediately before entering the waveguide, the average power in each beam was about 0.5 μW.

The autocorrelation trace is shown in Fig. 6.12, and the pulsewidth was found to be 35 ps FWHM. Assuming a Gaussian pulse and dividing by $\sqrt{2}$ a pulse width of 25 ps is obtained. The jump in the data points is due to a coherence spike.

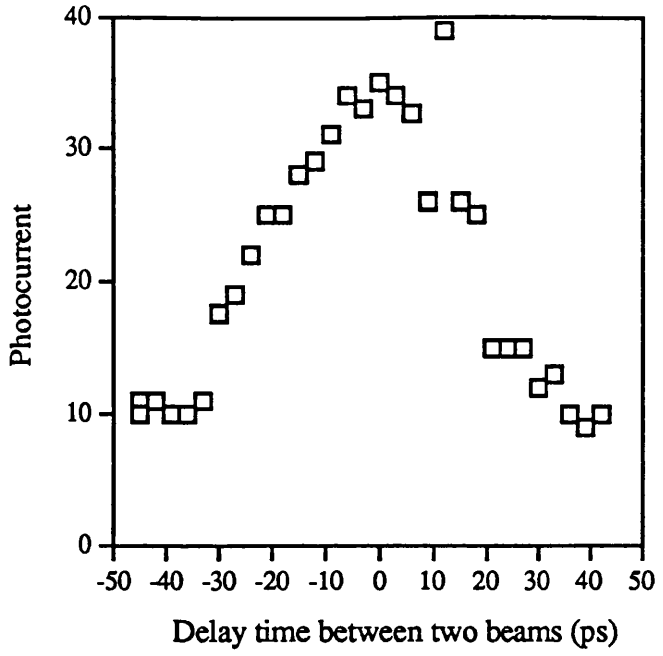

Fig. 6.12. Autocorrelation trace of a two-section laser, showing a pulsewidth of 25 ps.

6.7. Interferometric Autocorrelation of a Nd^{3+}:YAG laser

Interferometric autocorrelation measurements were also made of the modelocked pulses from a Nd^{3+}:YAG laser using the TPA waveguide autocorrelator. As in previous waveguide autocorrelation measurements, a Michelson interferometer was used for the correlation measurements, Fig. 6.13. The two aligned beams were then end fired into a reverse biased p-i-n waveguide where the corresponding photocurrent was measured. The main difference between the intensity and the interferometric experiment is that, in the interferometric experiment, the two beams have the same polarisation which causes interference effects along the waveguide between the two pulses. To measure the interference effects between the two pulses, the movement of the translation stage has to be controllable to within at least 0.1 μm. However, the resolution of the translation stage was not adequate to move in such small increments, and so another method was used. Instead of the translation stage, the corner cube prism was attached to, and coaxial with, the cone of an audio speaker.

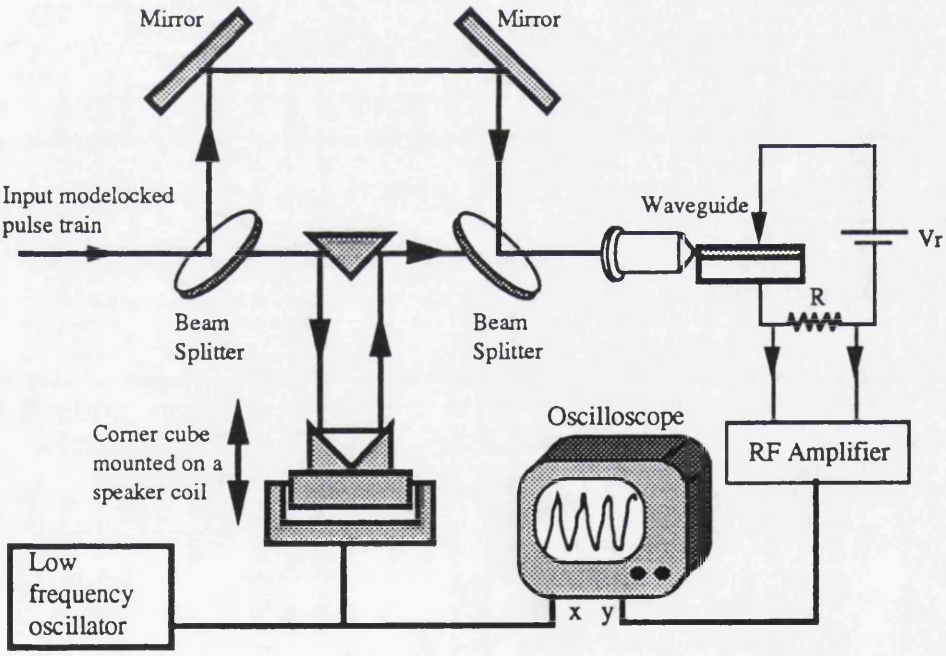

Fig. 6.13. Schematic of an experimental arrangement of an interferometric TPA autocorrelator.

The 6 in diameter speaker was driven through a 75 Ω series resistor by an audio sine wave generator at a frequency of 20 Hz. The maximum stroke obtainable with this particular speaker, after the corner cube was mounted, was 2 mm (peak-to-peak travel)

corresponding to a maximum temporal measurement range of 13 ps. This meant that only a small portion of the Nd^{3+}:YAG laser pulse could be measured interferometrically. The acquisition time of the lock-in amplifier was not fast enough to measure the changing photocurrent from the p-i-n waveguide so it was replaced with an amplifier. The signal from the amplifier was applied directly to the y axis of a digital storage oscilloscope and the x axis of the display was driven by a signal from the sine wave oscillator.

Before the results were taken, the speaker cone was motionless, and the two pulses were checked to see they overlapped identically in the waveguide. An interferometric autocorrelation trace was obtained of the central part of the optical pulse, Fig. 6.14a. As expected for an autocorrelation trace, the peak-to-baseline:baseline-to minimum ratio was measured to be 8:1. However, the trace shows a region with a slightly negative differential. This is possibly due to the sinusoidal motion of the speaker and mirror. At the edges of the trace, where the mirrors velocity is slowest, the sampling rate is high this therefore means that the outer edges of the trace are resolved better than the central part. This problem could be solved by using a lower driving frequency or a shorter mirror movement Fig. 6.14b illustrates the part of the pulse that the trace was obtained from.

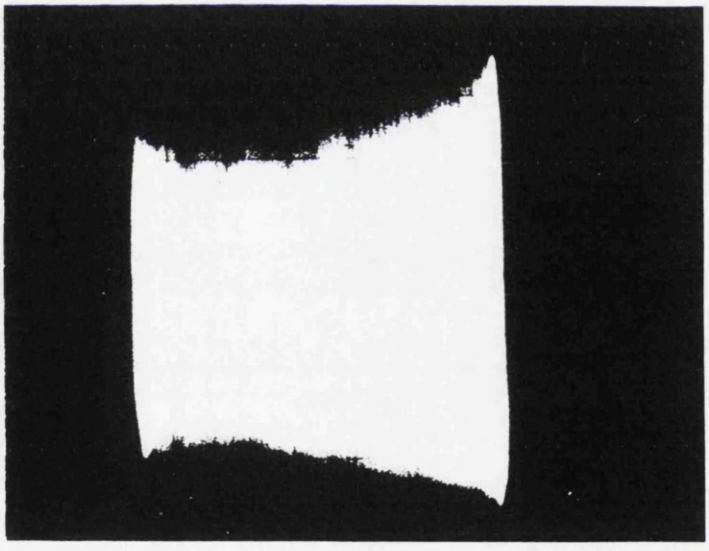

Fig. 6.14a. An interferometric autocorrelation trace of a Nd^{3+}:YAG laser pulse

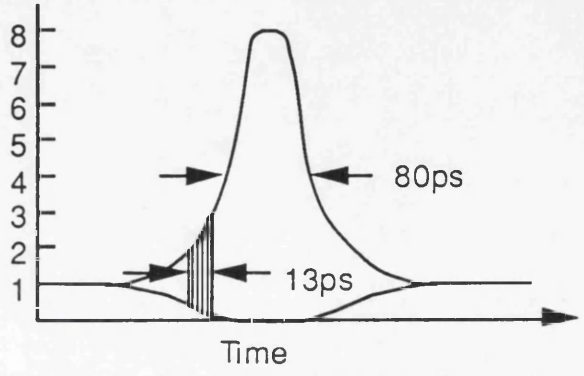

Fig. 6.14b. An illustration of the interferometric trace.

6.8. Temporal Resolution of the Two-Photon Waveguide Autocorrelator

TPA is an ultrafast effect, and as has already been explained, its transition time from the valence to the conduction band, which is governed by the uncertainty principle, is almost instantaneous, i.e. in the order of femtoseconds. Therefore TPA itself does not present any resolution problems for the autocorrelator. The resolution is also not dependant on the sweep-out time of the carriers from the intrinsic region of the waveguide, since an autocorrelation is a relatively slow measurement and an interferometric autocorrelation measurement is rarely taken at more than 1 kHz.

There are however several other constraints on the temporal resolution of the TPA waveguide autocorrelator. As with all conventional autocorrelators they cannot determine the pulse shape of a laser pulse. As this will determine the conversion factor relating the width of the autocorrelation trace to the laser pulsewidth, if the shape is not known large inaccuracies in the measurement of a pulse width can arise. The pulse shape must therefore be assumed or found by some other means.

For all the autocorrelation measurements so far, we have assumed gaussian pulses for both the semiconductor and Nd^{3+}:YAG lasers. The width of the autocorrelation trace was therefore divided by $\sqrt{2}$ to obtain the true pulsewidth. The other conversion factors for $sech^2$, Lorentzian or asymmetrical exponential profiles are given in appendix (1).

Intensity autocorrelations require the two beams to be orthogonally polarised inside the waveguide, This leads to dispersion between the two pulses and can affect the resolution of the TPA autocorrelator. The effective refractive indices, n_{eff}, of the waveguide for TE- and TM-polarised light depend on the material design, and waveguide dimensions. The effective refractive indices for both TE-and TM- polarisations were calculated using a vector finite difference program, and it was found that $(n_{eff})_{TE} - (n_{eff})_{TM} \approx 1 \times 10^{-3}$, which results in a difference in propagation time through the waveguide of about 3 fs. This value is negligible when considering measuring pulses of greater than 10 ps. Even measuring pulses in the order of femtoseconds, the dispersion factor does not become significant since the cavity length of the waveguide would be reduced correspondingly.

Material dispersion in the waveguide could cause problems with ultra-short pulses, due to the wavelength dependence of the refractive index. A shortening of the pulse width has an inverse effect on the spectral bandwith, giving an increase in the spectral bandwidth which will cause an increase in dispersion through the waveguide and therefore broaden the pulse. If we were measuring an ultra short pulse (500 fs) with a high bandwidth time product (~6), a spectral bandwidth of 15 nm is possible. The refractive index of GaAs at 860 nm is ~3.71, and the refractive index of GaAs at 875 nm is ~3.66, which results in a difference in propagation time through a 1 mm waveguide of ~100 fs. Even if the waveguide length was reduced to 200 μm, pulse broadening of 20 fs would have to be taken

into account. However, this is a worse case scenario and spectral bandwidths of 2 nm are more probable.

The only other foreseen problems in resolution could be caused by linear and nonlinear absorption, as the laser pulses will be attenuated as they propergate through the waveguide. Because the peak intensity is not constant along the length of the guide, neither will the photogenerated carrier density. This will cause a loss in resolution which is a function of the peak intensity of the pulses in the waveguide.

6.9. Multicontact autocorrelator

Another novel device, a TPA waveguide multicontact autocorrelator, was designed and fabricated to measure pulsewidths without needing to alter the time delay between the two pulses. The multicontact autocorrelator consists of a reverse biased p-i-n ridge waveguide similar in design to the autocorrelator previously reported. Along the length of the waveguide are a series of contacts electrically isolated from each other. The contacts are spaced every 50 μm along the waveguide which corresponds to about one every 500 fs, the approximate resolution of this particular device, Fig 6.15.

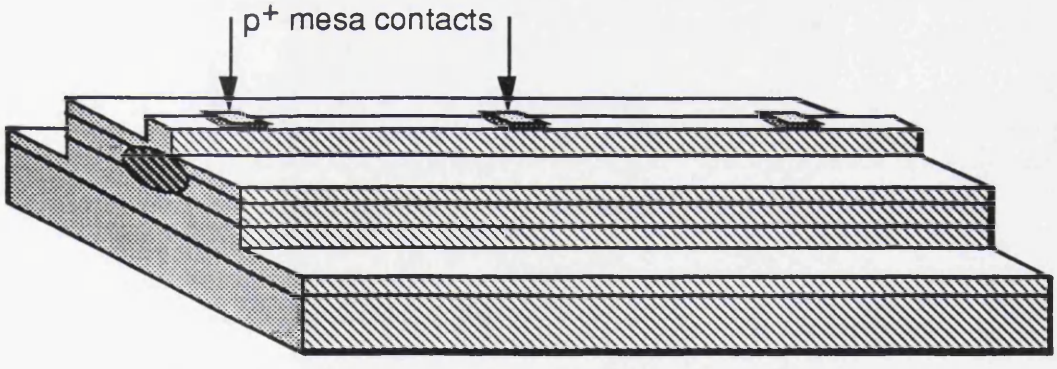

Fig. 6.15. Schematic of the multicontact autocorrelator.

To obtain a pulsewidth measurement using the multicontact autocorrelator, the pulse train is split into two beams and then end fired into either end of the waveguide. The pulses then propagate through the waveguide from both ends where they form an interference wave pattern which is measured by the change in photocurrent along the waveguide.

6.9.1. Fabrication of the Multicontact Autocorrelator

The 3 μm ridge waveguides were dry etched using $SiCl_4$ and the contacts were mesaed by etching 0.6 μm through the upper cladding layer to the intrinsic waveguide layer, which isolated them electrically. However the mesas were found to change the

refractive index along the ridge waveguide, which caused dispersion of the light and stopped it from guiding. This problem was solved by just etching the top p^+ GaAs contact layer using a GaAs/AlGaAs selective dry etch technique. An SEM micrograph of the 3 μm waveguide; Fig. 6.16, illustrates the etched p+ contact pad on top of the waveguide, the original design of the p+ contact pad was square but, due to resolution limits of the photolithography, difraction has rounded the corners. The measured resistance between the contacts was found to be around 10 kΩ and the guiding was not affected by the mesa contacts.

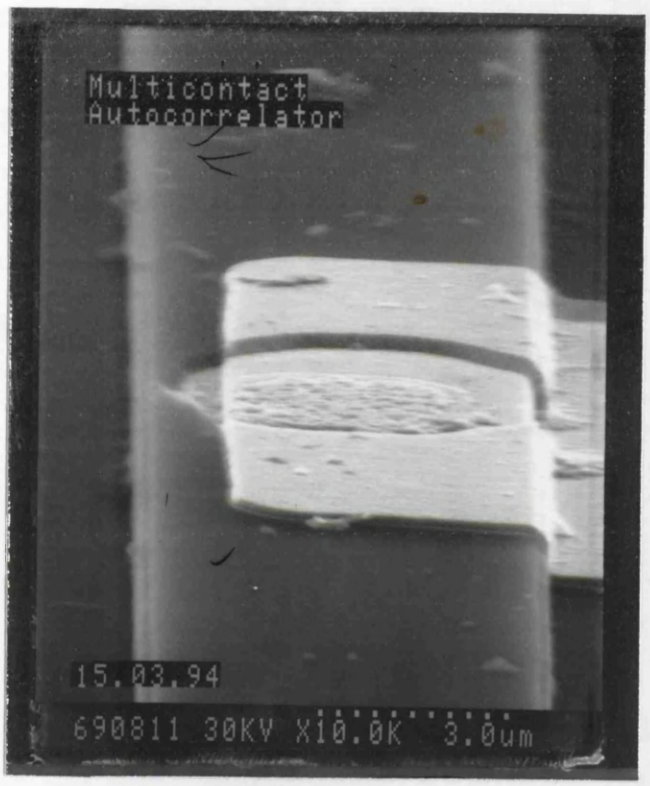

Fig. 6.16. SEM micrograph of a multicontact autocorrelator illustrating the etched p+ contacts on top of the waveguide.

A passivation layer of SiO_2 was deposited onto the device and contact windows were then opened up over the p+ GaAs pads using a wet etch. P-type metal contacts were then deposited and patterned using lift off. An SEM micrograph of the final device, Fig. 6.17(a) shows the patterned metal contacts on the waveguide, and the picture taken from a microscope shows a larger magnification.

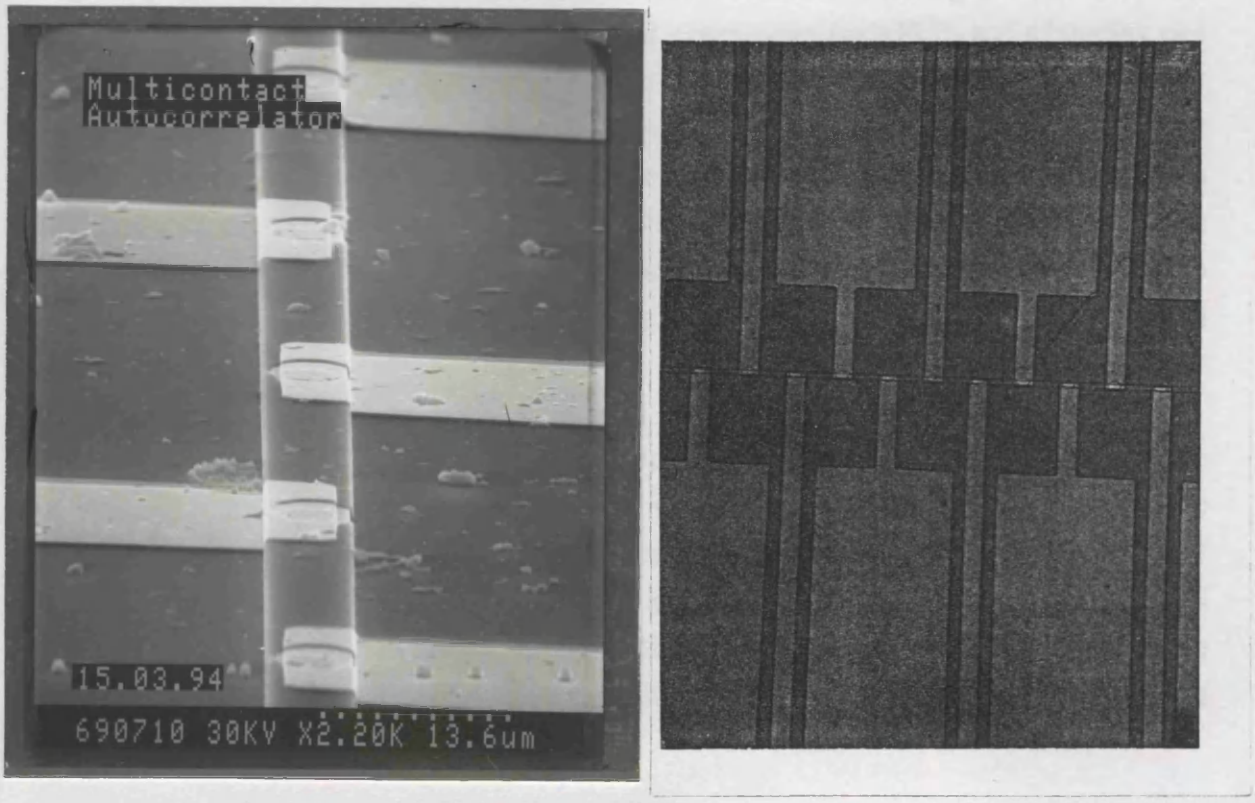

Fig. 6.17. a) SEM micrograph of a multicontact autocorrelator. b) Microscope picture of the same device.

Fig. 6.18. SEM micrograph of a multicontact autocorrelator.

Fig. 6.18 shows the completed multicontact autocorrelator illustrating the etched trench used for isolation. A multi contact bonding pad, constructed from PCB, and a bonding pad holder (appendix 5,6) was designed for mounting onto and bonding to the device while leaving access for an objective to end-fire the pulse train into the device. The multicontact autocorrelator was mounted onto the PCB and wire bonds were made from the 50 contacts on the device to each of the channels on the bonding pad. The fanning out of the channels enabled better access for probing the contacts of the device. There have been no measurements of pulse lengths taken to date, this is due mainly to lack of time and difficulty in completing all the bond contacts.

The main advantage of this device is that the path lengths of both pulses do not have to be varied and, therefore, the coupling into the waveguide can be kept constant. The device also gives greater possibilities for integration by butt coupling fibres to either end of the waveguide, reducing the loss due to optical alignment and making it cheap, portable and simple to use. The optical losses in the Michelson interferometer were found to reduce the power of the pulse to a fifth of its original value which can be significant when working with low power semiconductor lasers.

6.10. Further Experiments that could be Performed

One of the main disadvantages with conventional autocorrelators is that they give no information on the symmetry of a pulse. The pulses propargate through the SHG crystal travelling in the same direction, when a delay between the pulses is produced the pulses are correlated against each other. This correlation, however is between the leading edge of one pulse aginst the trailing edge of the other. The resulting temporal profile is an average product and is purely symmetrical. A streak camera trace reveals asymmetry, however its resolution is limited to measuring pulses greater than about 5 ps FWHM. The advantage of a waveguide autocorrelator is that the pulses can be end-fired into either end of the waveguide, Fig 6.19 so that they propagate through the waveguide in opposite directions. An autocorrelation where the two pulses overlap and meet from opposite directions means that the front-end of the optical pulse is correlated with the front-end and the back-end is correlated with itself. This method will detect asymmetry in an optical pulse shape. The distribution of the energy in a optical pulse can be an important factor especially when using ultra-short pulses for sensitive diagnostic measurement techniques and would also lead to a greater understanding of ultra-short pulse generating techniques.

Further work in this field should be used to produce an all fibre autocorrelator. The waveguide could be fully integrated by coupling either end of the device to an input and output fiber and then wire bonded and packaged.

Fig. 6.18 shows the completed multicontact autocorrelator illustrating the etched trench used for isolation. A multi contact bonding pad, constructed from PCB, and a bonding pad holder (appendix 5,6) was designed for mounting onto and bonding to the device while leaving access for an objective to end-fire the pulse train into the device. The multicontact autocorrelator was mounted onto the PCB and wire bonds were made from the 50 contacts on the device to each of the channels on the bonding pad. The fanning out of the channels enabled better access for probing the contacts of the device. There have been no measurements of pulse lengths taken to date, this is due mainly to lack of time and difficulty in completing all the bond contacts.

The main advantage of this device is that the path lengths of both pulses do not have to be varied and, therefore, the coupling into the waveguide can be kept constant. The device also gives greater possibilities for integration by butt coupling fibres to either end of the waveguide, reducing the loss due to optical alignment and making it cheap, portable and simple to use. The optical losses in the Michelson interferometer were found to reduce the power of the pulse to a fifth of its original value which can be significant when working with low power semiconductor lasers.

6.10. Further Experiments that could be Performed

One of the main disadvantages with conventional autocorrelators is that they give no information on the symmetry of a pulse. The pulses propargate through the SHG crystal travelling in the same direction, when a delay between the pulses is produced the pulses are correlated against each other. This correlation, however is between the leading edge of one pulse aginst the trailing edge of the other. The resulting temporal profile is an average product and is purely symmetrical. A streak camera trace reveals asymmetry, however its resolution is limited to measuring pulses greater than about 5 ps FWHM. The advantage of a waveguide autocorrelator is that the pulses can be end-fired into either end of the waveguide, Fig 6.19 so that they propagate through the waveguide in opposite directions. An autocorrelation where the two pulses overlap and meet from opposite directions means that the front-end of the optical pulse is correlated with the front-end and the back-end is correlated with itself. This method will detect asymmetry in an optical pulse shape. The distribution of the energy in a optical pulse can be an important factor especially when using ultra-short pulses for sensitive diagnostic measurement techniques and would also lead to a greater understanding of ultra-short pulse generating techniques.

Further work in this field should be used to produce an all fibre autocorrelator. The waveguide could be fully integrated by coupling either end of the device to an input and output fiber and then wire bonded and packaged.

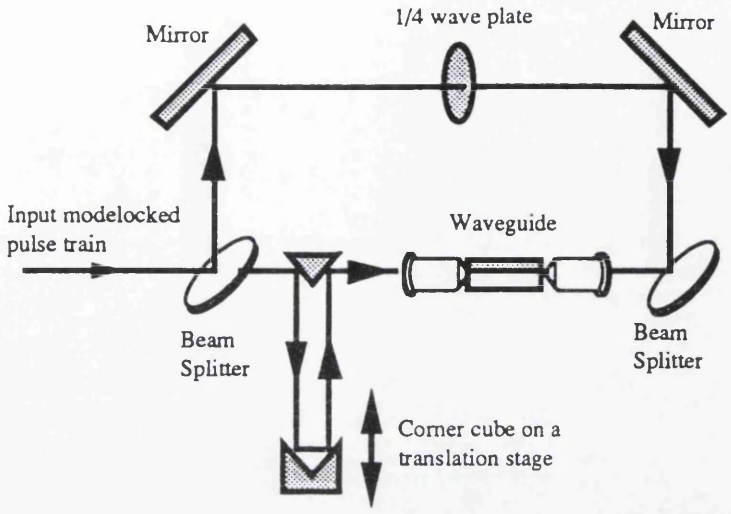

Fig. 6.19. Schematic of a TPA autocorrelator for measuring asymmetric pulses.

The Michelson interferometer could be made up completely in fibre from a 3 dB fibre splitter, to divide the pulse train into two paths, two polarisation control fibres and a fibre stretcher, in one arm of the interferometer, Fig. 6.20. The fibres could then be recombined and connected to the packaged autocorrelator. The output of the autocorrelator could be connected to a polarisation filter and then an additional piece of test equipment (sampling scope, spectrum analyser). The maximum available stretch from an optical fibre is 1% which gives a path difference of 290 ps for 6 m of fibre making this method very feasible.

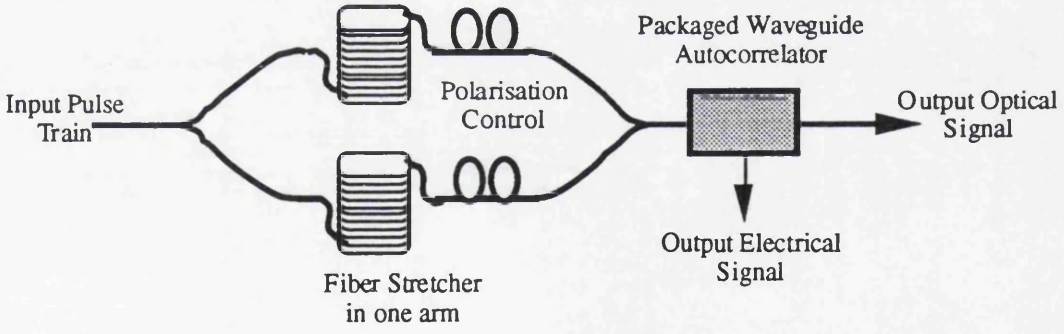

Fig. 6.20. Schematic of an all fibre autocorrelator.

6.11. References

1. H. P. Weber, "Method for pulsewidth measurement of ultrashort light pulses generated by phase-locked lasers using non-linear optics," *J. Appl. Phys.*, vol. 38, pp. 2231-2234, 1967.

2. J. A. Armstrong, "Measurement of picosecond laser pulse widths,",*Appl. Phys. lett.* , vol. 10 (1), pp. 16-18, 1967.

3. Y. Takagi, T. Kobayashi, K. Yoshihara, and S. Imamura, "Multiple and single shot Autocorrelator based on two-photon conductivity in semiconductors," *Opt. Lett.*, vol. 17, pp. 658-660, 1992.

4. F. R. Laughton, J. H. Marsh, and A. H. Kean, "A very sensitive two-photon absorption GaAs/AlGaAs waveguide detector for an autocorrelator,"

5. D. C. Hutchings, and B. S. Wherrett, "Theory of anisotropy of two-photon absorption in Zinc-blende semiconductors," *Phys. Rev. B,* vol. 49, pp. 2418, 1994.

6. D. C. Hutchings, and B. S. Wherrett, "Theory of polarisation dependence of two-photon absorption in Zinc-blende semiconductors," *J. Mod. Optics,* vol. 41, pp. 1141, 1994.

7. Braunstein. *N. Phys. Rev. A,* 134, 1964, pg 499

8. M. Goppert-Mayer,"Über Elementarakte mit zwei Quantensprüngen", *Ann. Phys. (Leipz.),* vol. 9, pp. 273-294, 1931.

9. H. N. Spector, "Two-photon absorption in semiconducting quantum-well structures", *Phys. Rev. B,* vol.35, pp. 5876-5879, 1987.

10. A. Miller, D.A.B. Miller and S.D. Smith, "Dynamic nonlinear optical processes in semiconductors", *Advances in Phys.*, vol. 30, pp. 697-800, 1981.

11. F.R. Laughton, J.H. Marsh and C. Button, "Time resolved nonlinear absorption modulation in GaAs/AlGaAs multiple-quantum-well waveguides at 1.06 μm", *IEEE Phot. Tech. Lett.*, vol. 4, pp. 863-866. 1992.

Chapter 7

Optoelectronic Frequency Mixing in Semiconductor Lasers

7.1. INTRODUCTION.

Frequency mixing, along with signal generation and amplification, is one of the basic functions of electronics. However, in present-day optoelectronic systems, the production and use of amplitude-modulated optical signals, has not yet been fully exploited. Optolectronic mixers, in which an amplitude-modulated optical signal and an electrical signal are mixed in an optical detector, has been demonstrated in several forms, however all the optoelectronic mixers proposed to date produce an *electrical* intermediate-frequency (IF) output [1]. Since high-frequencies can be handled easily optoelectronically, it suggests that a mixing element should be developed which provides its output in the form of an amplitude-modulated *optical* signal.

A proposed block scheme of such an optoelectronic downconverter is shown in Fig. 7.1. The local oscillator signal is a train of optical pulses emitted, for example by a modelocked semiconductor laser at a high repetition frequency, f_{LO}. This signal is coupled into the laser-mixer along with an electrical high-frequency input signal, f_S. The electrical signal causes high-frequency oscillations in the modal gain of the laser-mixer. The output optical signal is therefore at an intermediate frequency which is the sum and difference of the signal and local oscillator (LO) frequencies.

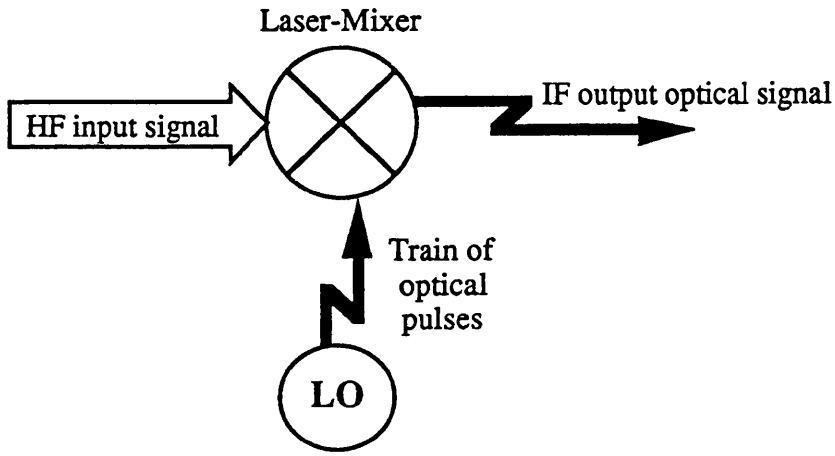

Fig. 7.1. Proposed block schematic of an optoelectronic downconverter.

In this chapter, we propose the use of a semiconductor laser as both a local oscillator and mixer. We shall concentrate on technologically simple monolithically integrated versions of the laser-mixer, for example, a four-terminal laser with dual (current and confinement) modulation [2,3]. Alternatively, the laser could contain a saturable absorber within the cavity [4-9] to achieve either high frequency Q-switching or mode-locking to provide oscillations of the photon and electron densities at a local oscillator frequency f_{LO}. Oscillation of the modal gain at the signal frequency f_S may be achieved in the latter two cases by modulation of either the pumping current (for the Q-switching range of frequencies) or the carrier confinement or photon lifetime (at higher mode-locking frequencies). Mixing of the local oscillator and the signal in all three cases occurs due to parametric effects since the induced recombination rate depends on the product of the modal gain and photon density.

The mixing schemes we propose are attractive for very high frequencies. Indeed, it has been shown theoretically that efficient very high-frequency modal gain modulation can be achieved in a 4-terminal semiconductor laser structure [2,3]. Q-switching produces an easily tunable repetition frequency up to about 20 GHz and passive mode-locking can generate picosecond optical pulses at even higher repetition rates, moving from hundreds of GHz [4] to the terahertz range as new techniques [5,6] are introduced, the average powers available being up to hundreds of mW [7].

The chapter consists of two main sections. In the first the theoretical model, developed mainly by Dr Eugene A. Avrutin and Dr V. B. Gorfinkel, is described. In the second section the theoretical model confirmed experimentally using two-section Q-switched lasers. This work was carried out by myself and Dr Ian Thayne.

7.2. THEORY.

7.2.1. Laser with saturable absorber: passive Q-switching.

The device used in this theoretical model is based on a passively Q-switched two-section laser similar to the one used in previous experiments (chapter 4+5) and the one illustrated in Fig. 7.2. The natural self-pulsating frequency of the laser diode provides the local oscillator signal of the laser-mixer and the carrier frequency comes from a high frequency electrical signal supplied to the gain section of the two-section laser.

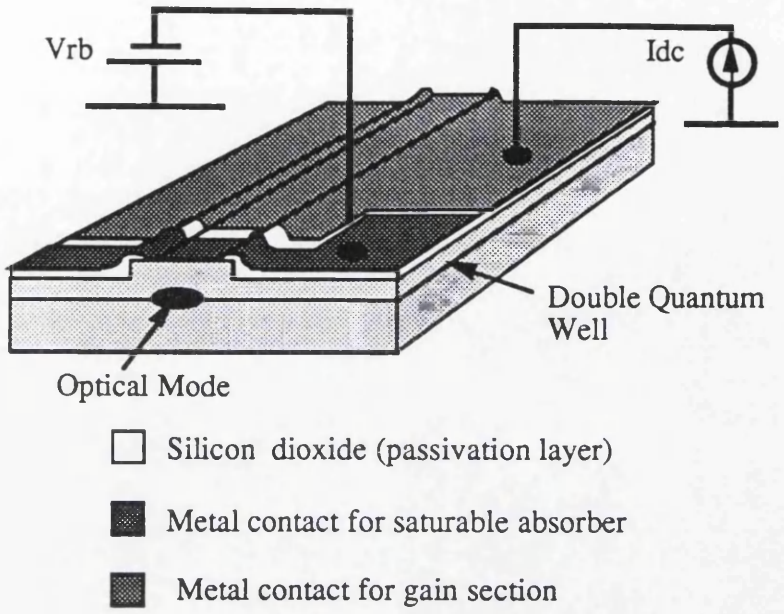

Fig. 7.2. Two-section laser schematic.

To describe a passively Q-switched laser, the standard system of rate equations are completed by an equation describing the carriers in the (slow) saturable absorber; these equations (3.19-3.21) are described in chapter 3 and so the equation for light is modified accordingly to obtain [9] :

$$\frac{dN_g}{dt} = J_g - \frac{N_g}{\tau_N(N_g)} - gP_g$$

$$\frac{dN_a}{dt} = J_a - \frac{N_a}{\tau_a} + aP_a \qquad (7.1a\text{-}c)$$

$$\frac{dP}{dt} = \left[\Gamma\left(r_g g - r_a a\right) - \frac{1}{\tau_p}\right]P + \beta\,\frac{N_g}{\tau_N(N_g)}$$

where N_g and N_a are the carrier densities in the gain and absorber sections of the laser cavity, respectively; r_g and r_a denote the volume fractions occupied by corresponding sections; a is the saturable absorption coefficient in the corresponding section and g is the gain in the gain section. S_g and S_a are the photon densities averaged through these respective sections (to a first approximation, $S_a = S_g = S$, although this assumption is not made in our model which uses simple formulae for S_g and S_a, as derived in [9]).

The numerical calculations are performed here for a tandem laser structure consisting of adjacent gain and absorber sections within a common cavity, the same laser configuration

studied in [9]. The parameter values used in the model are listed in Appendix 7 and chosen so as to correspond approximately to the experimental situation described hereafter (Section 7.3); namely, the geometry of the laser was chosen to be close to that studied in the experiments and the parameters of the saturable absorber fitted to provide

a) similar increase in threshold due to implementation of the SA ($J_{th}/J_{th(0)}$=1.8) and

b) similar Q-switching frequency at given current level (f_{LO}=1.5 GHz at $J/J_{th(0)}$=4). The signal is applied in the form of a sinusoidal modulation of the pumping current in the gain section: $J_g = J_{g0} + \Delta J_g \sin(2\pi f_s t)$.

We now study the behaviour of the laser under external modulation at a constant frequency f_S and increasing amplitude ΔJ_g. Fig. 7.3 shows examples of the calculated time-dependent profiles of the Q-switched pulses without (Fig. 7.3(a)) and with (Fig. 7.3(b)) external modulation.

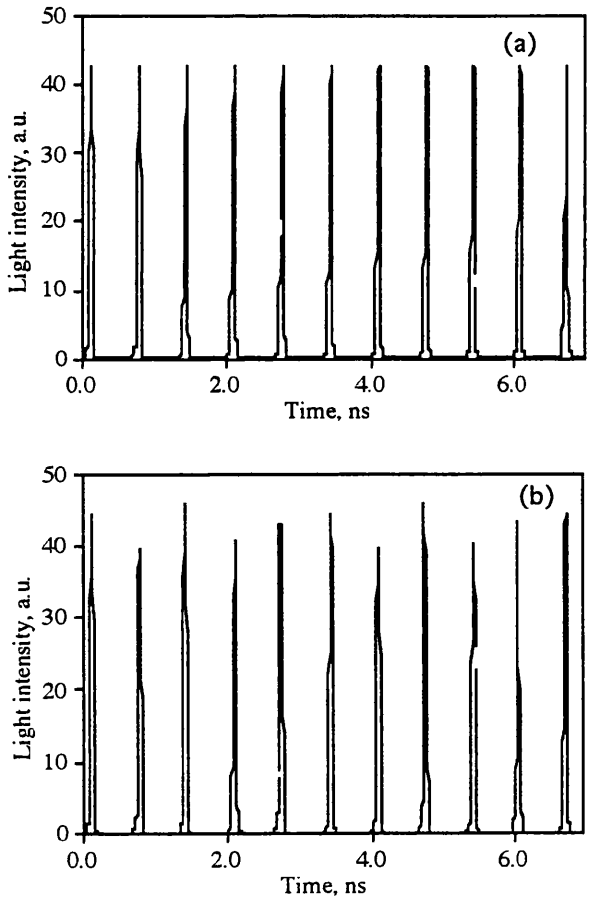

Fig. 7.3(a+b). (a) Fragment of a pulse train emitted by a free-running Q-switched laser diode; parameters as in Appendix 7, pumping current $J/J_{th(0)}$= 4 (self-pulsing frequency f_{LO} = 1.5 GHz). (b) Same as in Fig. 7.3(a), under current modulation of an amplitude $\Delta J_g/J_{th(0)}$= 0.1 applied to gain section.

The modulation imposes a slow envelope on the pulse train which is, in general, of a non-sinusoidal form. To understand the effect of the modulation more quantitatively, we

perform Fourier transforms of the observed light signals, so obtaining the RF spectra. The low-frequency parts of these spectra are illustrated in Fig. 7.4, where Fig. 7.4(a) and Fig. 7.4(b) correspond to Fig. 7.3(a) and Fig. 7.3(b) respectively. Fig. 7.4(a), with $\Delta J_g = 0$, shows the spectrum of clear self-pulsation, which, as expected, consists of a set of narrow lines (of which only the first two are shown) at the frequency f_{LO} and its integer harmonics.

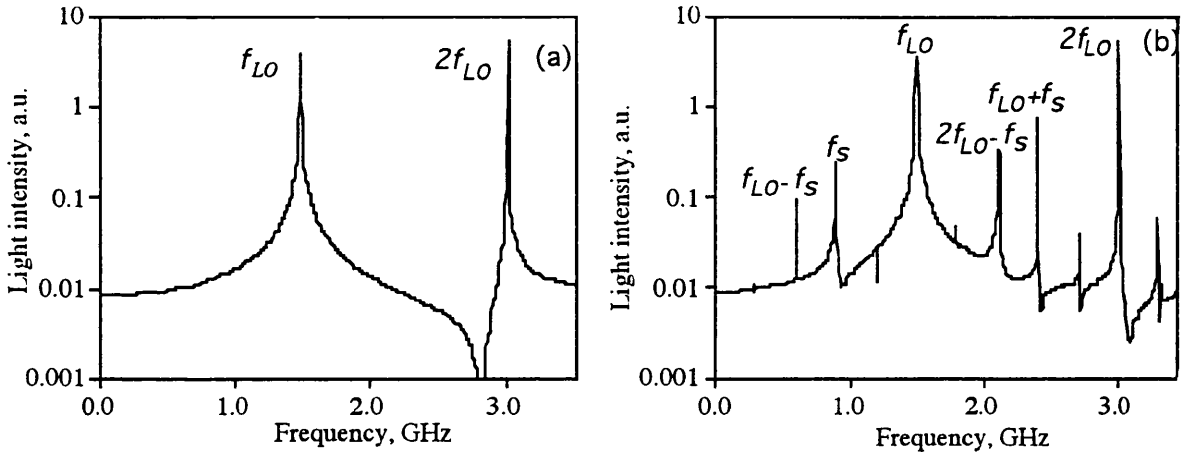

Fig. 7.4 (a+b): (a) Part of the RF spectrum of a free-running Q-switched laser diode; parameters as in Appendix 7, pumping current $J/J_{th(0)}$=4 (spectrum of signal shown in Fig. 7.3(a)); (b) The low-frequency part of the spectrum of the same laser, under current modulation at f_S= 0.9 GHz with an amplitude $\Delta J_g/J_{th(0)}$= 0.1 applied to gain section (spectrum of the signal shown in Fig. 7.3(b))

As one applies a weak RF modulation at f_S (Fig. 7.4(b)), spectral lines appear at the difference beat frequency $|f_s - f_{LO}|$ and at the sum beat frequency $|f_s + f_{LO}|$ thus showing that both down-and up-conversion are taking place. Another line can be seen at $2f_{LO} - f_s$, which, at least for low modulation amplitudes, may be regarded as the result of the mixing between the signal at f_S and the second harmonic of f_{LO}. As the modulation amplitude is increased, the intensities of the beat frequency lines increase as well. We use these intensities to evaluate the efficiency of up-and down conversion, defined as

$$\eta = \Theta \frac{P_2}{P_s} \qquad (7.2)$$

where the factor $\Theta \approx (1-R)/2$, R being the facet reflectivity, approximately relates the average intensity in the laser, used in (7.1), to the intensity emitted through one of the two facets. P_2 is the optical power at the difference frequency $f_2 = f_{LO} \pm f_s$ calculated from the RF spectra of the variable S computed through (7.1), and P_s is the input signal power estimated as $P_s = \hbar\omega \cdot \Delta I_g \cdot V$, V being the active layer volume. Fig.7.4(c) (solid lines)

shows these efficiencies versus the amplitude of the modulation current, measured as a fraction of the threshold current $J_{th(0)}$ of a fully forward biased laser. One sees that the efficiencies, particularly that of up-conversion, are of a respectable order of magnitude even for the modest LO intensities studied. Increasing the modulation amplitude, as is seen in Fig. 7.4(c), results in some saturation in conversion efficiency. It also leads to the emergence of a whole set of sidebands around f_{LO} and its harmonics, and also to the generation of a set of additional lines, arising from mixing between different first- and second-order frequencies, the latter signals being no longer negligible in amplitude.

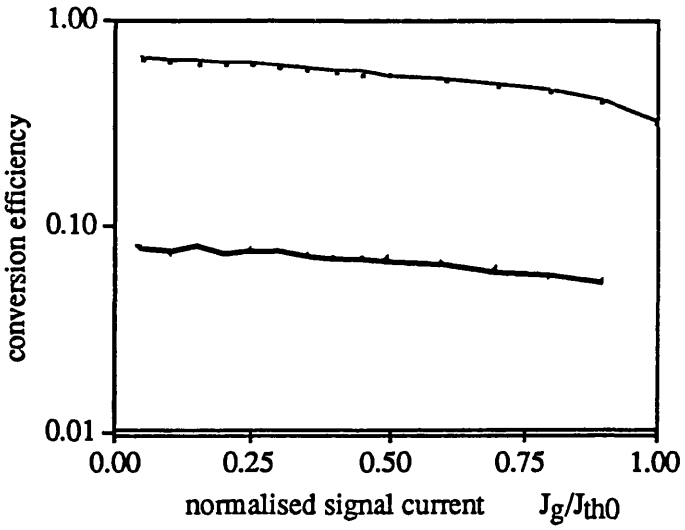

Fig. 7.4(c). Calculated efficiencies of up- and down-conversion vs modulation current. Parameters of the laser and pumping regime as in Fig 7.3, 7.4(a,b).

Some such lines, for example at $2f_S$-f_{LO}~0.3GHz and at $2f_S$=1.8 GHz, are already present, with a small amplitude, in Fig. 7.4b; and at $\Delta J_g / J_{th(o)} \approx 0.4-0.5$, the spectra become highly complex. The increase in modulation is also accompanied by a gradual pulling of the LO frequency towards that of the signal (by approximately 100 MHz within the limits of Fig. 7.4c), and if the modulation amplitude were to be increased further, above a certain threshold value ($\Delta J_g / J_{th(o)} \approx 1.4$ in our case), abrupt frequency locking will occur and the spectrum will once more be a set of narrow lines, but now at harmonics of the signal frequency f_S. Such features, i.e. the generation of various combination frequencies (which is in fact a manifestation of the onset of increasingly complicated nonlinear dynamics, which may lead finally to optical chaos [10]), as well as frequency pulling, are clearly undesirable and will impose some limitations on the practical use of Q-switched lasers for optoelectronic frequency mixing. Other important limitations arise from the fact that the upper frequency

limit of Q-switching, even with all the latest improvements in Q-switching schemes [11], does not exceed several tens of GHz, and from the vulnerability of the regime to noise-induced jitter [9]. Passive mode-locking, for which firmly stabilised repetition frequency is an essential feature, may be expected to be more free of such limitations. Therefore, having established in this section the general principle of frequency mixing in laser diodes, we now proceed to studying this last regime, which we consider to be the most important for very high frequency applications.

7.2.2. Laser with saturable absorber: passive mode-locking.

Model

The device used in this theoretical model is based on a passively mode-locked monolithic extended-cavity laser with electroabsorption-modulated saturable absorber similar to the one fabricated in chapter (9). The device, Fig. 7.5 consists of a gain section, a passive section which has been disordered and a saturable absorber. The passive mode-locked frequency of the laser diode provides the local oscillator signal in the laser-mixer and the electrical carrier signal is supplied to the saturable absorber section of the device.

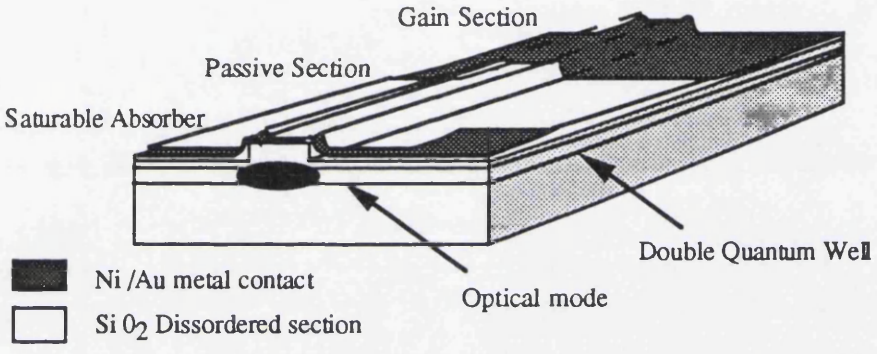

Fig. 7.5. Schematic of a proposed integrated laser-mixer, a monolithic extended-cavity laser with electroabsorption-modulated saturable absorber

For a mathematical description of passive mode-locking we use a model, similar in its main features to those of [12] and [13], in which the light propagation in the cavity is described by a propagation equation of the form

$$\pm\frac{1}{v_g}\frac{\partial E_{R,L}}{dz}+\frac{\partial E_{R,L}}{dt} = \Gamma(\hat{g}E_{R,L}+i\alpha g E_{R,L})+F_{rand} \qquad (7.3)$$

where $E_{R,L}$ are properly normalised complex amplitudes of the field of the light wave propagating to the right and to the left respectively, and the operator $\hat{g}$ includes a digital filter simulating gain dispersion [13]: $\hat{g}E = g\cdot\Delta\Omega_g\cdot\int_0^{\infty}E(t-\tau)\exp(-\Delta\Omega_g\cdot\tau)d\tau$ where $\Delta\Omega_g$ is the gain linewidth and g is the usual gain value used in the previous subsection. The last term in (7.3) represents a random noise source [13] and is essential for running the model. A self-induced grating (self-colliding-pulse effect) was also included in the calculations but did not affect the results significantly for our (uncoated-facet) structure. The dynamics of the carrier density are described by equations which are similar to 7.1(a) but are treated as local equations with

$S = |E_R|^2 + |E_L|^2$:

$$\frac{\partial N(z,t)}{\partial t} = \frac{J(z,t)}{ed} - \frac{N}{\tau_N(z)} - g(N)(|E_R(z,t)|^2 + |E_L(z,t)|^2) \qquad (7.4)$$

Within the saturable absorber sections the same equation holds, except that g becomes $-a$ and the recombination time $\tau(z)$ is adjusted accordingly (see Appendix 7). Although the mode-locking regime is inherently capable of operating up to hundreds of GHz, in the bulk of this Subsection we concentrate on the monolithic extended cavity laser construction, which includes a passive section in tandem with the gain and saturable absorber (SA) sections. The device is therefore designed to emit a pulse train at a moderate repetition frequency (20 GHz in our case), mainly to simulate realistically the parameters of one of the constructions we planned to use in the experimental studies. Our laser would be made of QW material, with the passive waveguide fabricated using QW intermixing techniques [14]. The parameters are therefore chosen to correspond to a QW device and the signal is introduced as a direct modulation of the unsaturated absorption in the SA. In the experiment such modulation will be realised by modulating the reverse bias voltage applied to the SA section of the QW. This modulation technique is essentially a modulation in the photon lifetime, so, it should [8] be more advantageous in the frequency range $f_s >> f_{res}$ than modulation of the pumping current.

Down-conversion:

Fig. 7.6 shows the effect of external modulation on mode-locking spectra for the case of down-conversion.

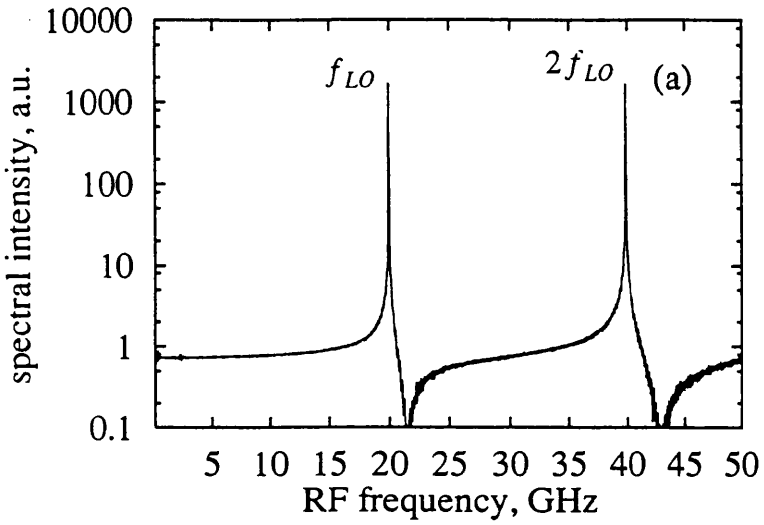

Fig. 7.6(a). Part of the RF spectrum of a free-running mode-locked extended cavity laser emission; parameters as in Appendix 7, pumping current J/J_{th}=4.5

The qualitative similarity with the results obtained for Q-switching is clear, emphasising the point made in Section 7.2.1 that, whichever effect is used to provide the LO, the fundamental physics of frequency mixing is essentially the same. However, there are some differences between the two regimes as well. In particular, since mode-locking is a much more "stiff" regime than Q-switching and the repetition frequency is firmly fixed by the optical length of the cavity, the ranges over which frequency locking by external signal can occur are extremely narrow [15,16]. Therefore, frequency mixing is possible for quite small frequency detuning (of the order of 0.1% of the repetition frequency) without the risk of pulling [15,16]. Also, besides showing well-developed peaks at difference frequency and its harmonics, the spectra also contain additional small noise-like peaks, which may be associated with relaxation oscillations in the system at the frequency f_{res} (all calculated spectra, exhibit also some general baseline intensity but this is due to numerical limitations; its level decreases with increased simulation time). One therefore expects that the conversion efficiency will be maximised if the local oscillator and signal frequency are resonantly adjusted so that $f_s - f_{LO} = f_{res}$.

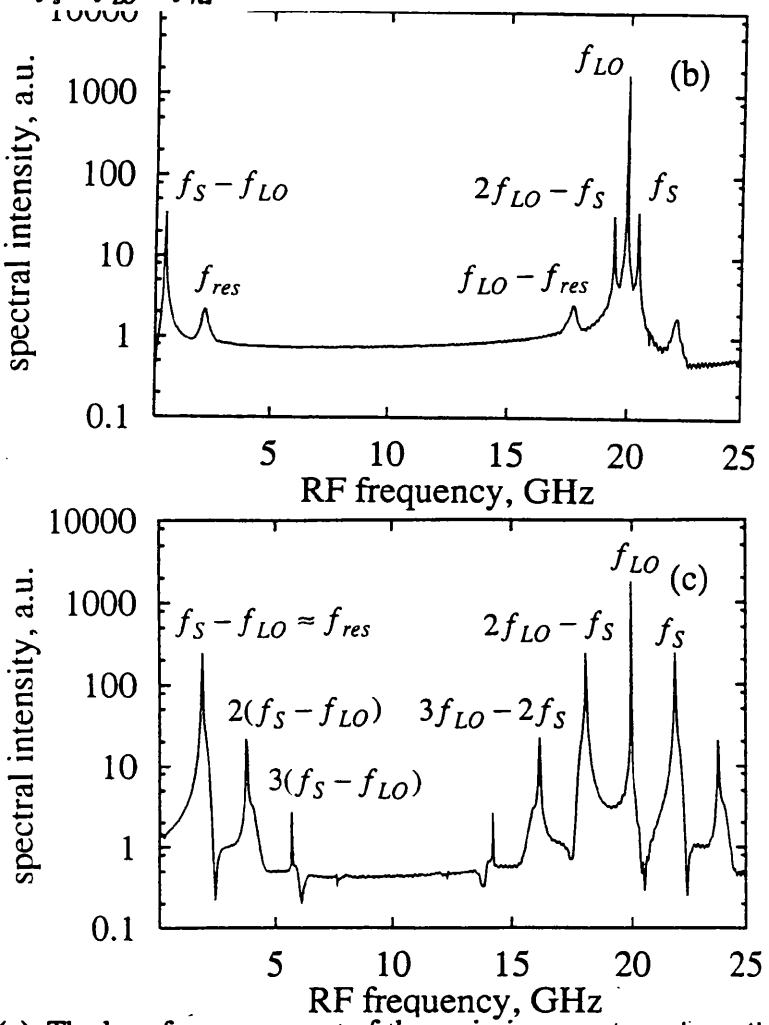

Fig. 7.6(b)-(c). The low-frequency part of the emission spectrum from the mode-locked laser, under direct modulation of the unsaturated absorption of an amplitude $\Delta a / g_{th} = 0.06$. Modulation frequency (b):f_S= 20.5 GHz, (c):f_S= 22.2 GHz

This is indeed confirmed by comparing Fig. 7.6(b) and 7.6(c); in the latter figure, this resonance condition is fulfilled approximately and the conversion efficiency is more than an order of magnitude higher than in the non-resonant case. However, as in the case of Q-switching, efficient conversion is accompanied by generation of multiple harmonics of the intermediate frequency, which is clearly undesirable in many applications. Problems with down-conversion at frequencies close to the resonance condition may also arise because there will be a strong frequency dependence of the conversion efficiency. We have therefore studied the frequency dependence of the down-converted signal amplitude (or conversion efficiency), keeping all other parameters fixed. To quantify the conversion efficiency, we suppose that the power necessary for controlling the absorber is negligible, and the RF power applied to the system is due to the variation of the threshold current by the absorber modulation. We then estimate the efficiency using (7.2) and supposing $P_s = \hbar\omega \cdot \Delta I_{th} \cdot V$. The result is shown in Fig.7.7.

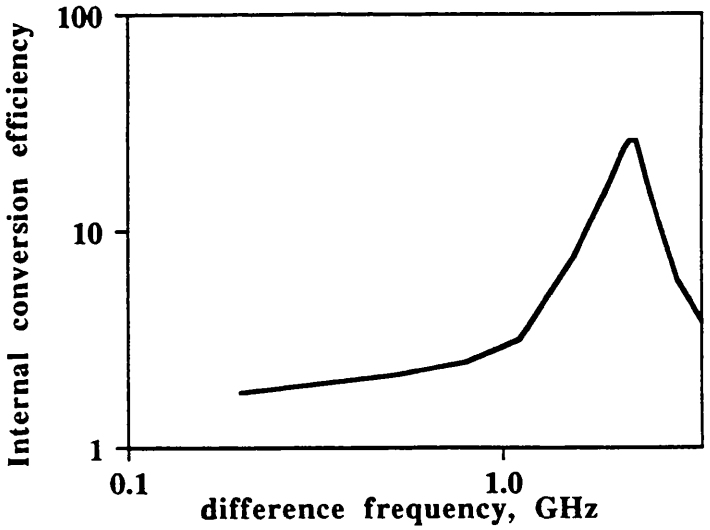

Fig. 7.7. Difference frequency dependency of the intensity of the fundamental down-converted line in the spectra of the same laser shown in Fig. 7.6.

It is clear that this curve is similar to the well-known current modulation characteristics [17] of semiconductor lasers. Besides exhibiting a sharp resonance in the vicinity of f_{res}, the curve in Fig. 7.7 also contains a relatively flat section at frequencies $f < f_{res}$. The former frequency regime should therefore be advantageous for down-conversion of narrowband modulated signals, and the latter for broadband modulated signals.

Up-conversion:

In all the cases so far considered, sum frequencies are always generated along with difference frequencies, i.e. up-conversion always accompanies down-conversion. As can be seen in Fig. 7.8(a), which simply shows a higher frequency section of the spectrum of Fig. 7.6(c), the intensity of the up-converted signal is approximately the same as that of the down-converted signal. The high absolute value of the up-converted intensity is due to the system being close to the resonance condition.

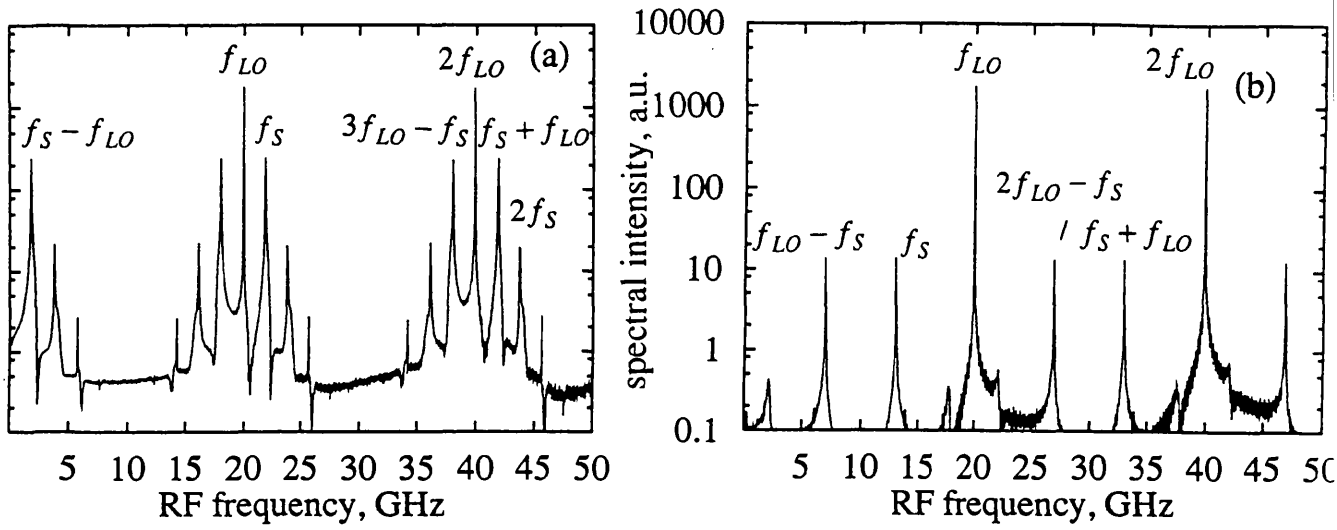

Fig. 7.8. Part of emission spectra from the same laser as in Fig. 7.6-7.7, modulated with the same amplitude $\Delta a / g_{th} = 0.06$, at frequencies: (a) $f_S = 22.2$ GHz, (b) $f_S = 13.0$ GHz.

Fig. 7.8(b) illustrates a more isolated case of up-conversion, in which $f_{res} < f_s < f_{LO} - f_{res}$. One notices that even in this case, clearly the least advantageous being far from of all possible resonant conditions, the intensity of the up-converted line still reaches a significant value of about -40 dB with respect to the main f_{LO} line. One can therefore anticipate that this principle of up-conversion, when combined with the latest achievements in ultrahigh-frequency mode locking [5,6], may be useful in generating millimetre-wave amplitude modulated optical signals. Besides the up-converted peak at 33 GHz $= f_{LO} + f_s$, Fig. 7.8 also contains a peak at 27 GHz $= 2f_{LO} - f_s$. In order to observe up-conversion more clearly, it would be desirable if the initial mode-locking signal (the local oscillator) were to contain only one frequency component, i.e. to be a sinusoidal signal. This is often the case in high-frequency mode-locking schemes [5,6], when only two or three longitudinal cavity

modes are observed in the mode-locked spectra. The analysis of this situation has not yet been carried out, however, a detailed investigation into the high-frequency case is being reserved for future studies.

7.3. EXPERIMENTAL.

As has been shown above, the fundamental physics of frequency mixing is essentially the same regardless of the regime (Q-switching or mode-locking) and the range of frequencies involved. Therefore, in order to demonstrate the feasibility of optoelectronic up- and down-conversion, experiments performed so far have been carried out using signals in the range 1-2 GHz from a passively Q-switched QW laser diode. Two experiments were set up to confirm the feasibility of optoelectronic up- and down-conversion where the frequency mixed train of pulses were observed both temporally using a sampling oscilloscope and spectrally using a spectrum analyser. All the work carried out in these experiments were performed by myself and Dr Ian G. Thayne, using two-section lasers fabricated by myself in the department.

7.3.1 Device Fabrication

The passively Q-switched laser used in the experiment was the same type as the device tested cw in chapter 4, which was based on a ridge waveguide structure with a ridge width of 3.5 μm. The active region consisted of two 6 nm thick strained InGaAs wells separated by 2 nm thick GaAs barriers giving an operating wavelength of 960 nm. The total cavity length of the device was 400 μm (Fig. 7.2). The *p*-type contact was separated into two sections, one of which formed a contact to the gain section, and the other to an electroabsorption loss modulator (the saturable absorber). The two contacts were electrically isolated by selectively etching a 20 μm gap in the GaAs p^+ contact layer to give an isolation resistance between the two regions of 2 kΩ. The length of the saturable absorber was 30 μm and the threshold current of the device with both sections in forward bias was 20 mA.

7.3.2 Measurement System

The self pulsation and intermediate frequency of the laser mixer was observed using both an RF spectrum analyser, Fig. 7.9(a), and a sampling oscilloscope, Fig. 7.9(b). The cw train of optical pulses was collimated then focused onto a fast InGaAs photodetector with a bandwidth of 20 GHz. An infra red camera was used to image the small area photodetector and therefore aid alignment of the focused pulse train onto the photodiode. In the spectral experiment the electrical signal from the photodiode was connected to a RF spectrum analyser (Tektronics 492) with a spectral resolution of 100 kHz and a bandwidth of 20 GHz.

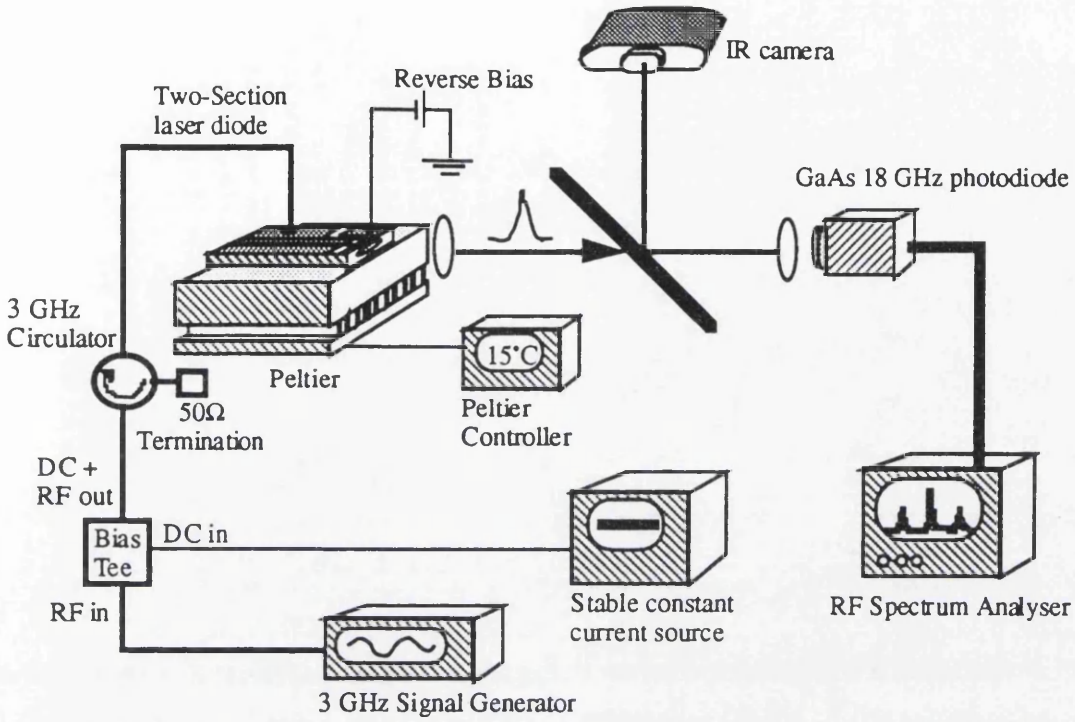

Fig. 7.9(a). Schematic of the experimental arrangement to measure the RF intermediate frequency spectrally from the two-section laser mixer.

The electrical signal supplied to the gain section of the two-section laser comprised of both a DC and RF signal. The DC forward biased the gain section so that self-pulsation occured, the LO signal. The rf signal is the frequency signal to be mixed, f_S . The DC signal came from a stable constant current source (± 5 μA) and the RF signal was supplied by a 3 GHz signal generator, the two signals were connected to the inputs of an 18 GHz bias tee and the output to the laser. High frequency (18 GHz) SMA cabling was used throughout the experiment to handle the high frequency signals. The electrical reflections from the RF signal were reduced by connecting an SMA connector directly to the laser mixer, a 3 GHz circulator was also connected in series, in betwen the bias tee and the laser, so that any reflected power was absorbed by a 50 Ω termination and not reflected back into the laser mixer.

Spectral Measurement.

In the spectral experiment, Fig. 7.9(a), the electrical signal from the photodiode was connected to a RF spectrum analyser (Tektronics 492) with a resolution of 100 kHz and a bandwidth of 20 GHz.

Temporal Measurement.

In the temporal experiment, Fig.7.9(b), the electrical output from the fast GaAs photodetector was divided in two using an RF splitter and connected to a sampling oscilloscope. One of the signals was used as a trigger; the other was connected to the sampling head of a communications signal analyser (sampling oscilloscope).

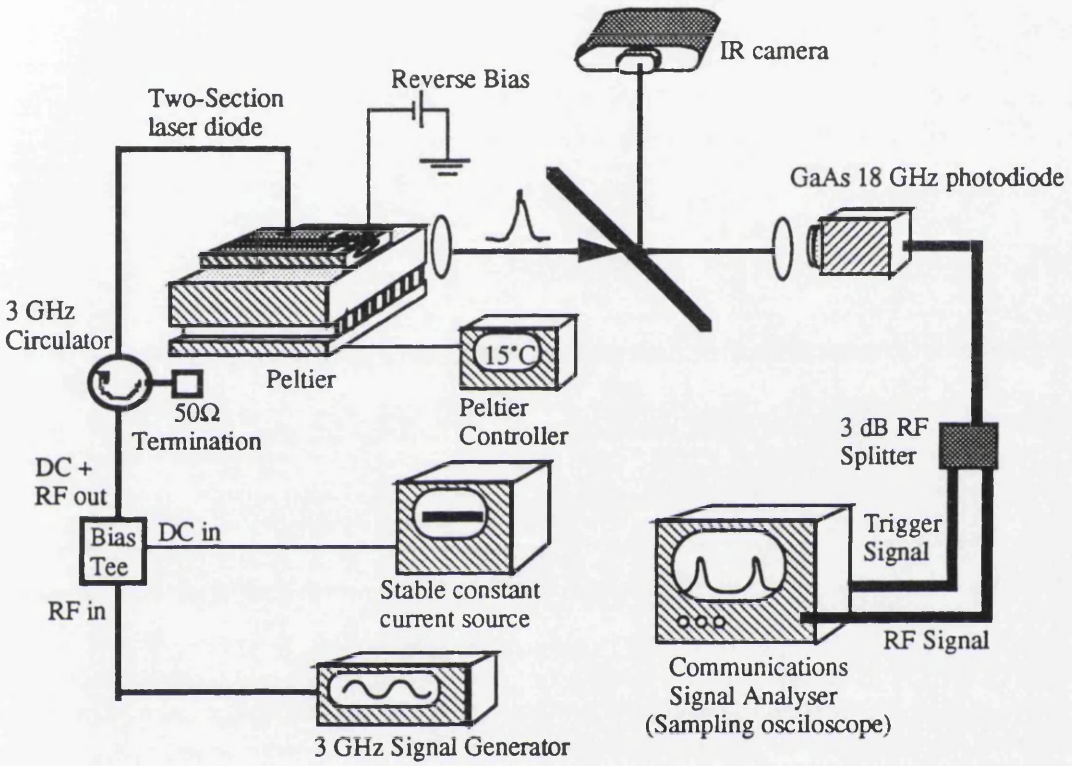

Fig. 7.9(b). Schematic of the experimental arrangement to measure the RF intermediate frequency temporally from a two-section laser mixer.

7.3.3 Experimental Results

Spectral Results.

When driven with a cw current of 80 mA through the gain section and 1.6 V reverse bias across the saturable absorber, the two-section laser demonstrated Q-switching operation, as shown in Figure 7.10(a). The Q-switched pulses result in a number of spectral peaks in the frequency domain. The (fundamental) Q-switching frequency of around 1.5 GHz and its second harmonic at 3.0 GHz are shown in Fig. 7.10(a). Further harmonics were observed at higher frequencies, up to 18 GHz, the bandwidth of the photodiode. Note that the amplitude of the second harmonic is approximately 10 dB below that of the fundamental Q-switching line, which shows that the pulses generated are not far

from sinusoidal, the measurement system being unlikely to introduce distortions at frequencies measured.

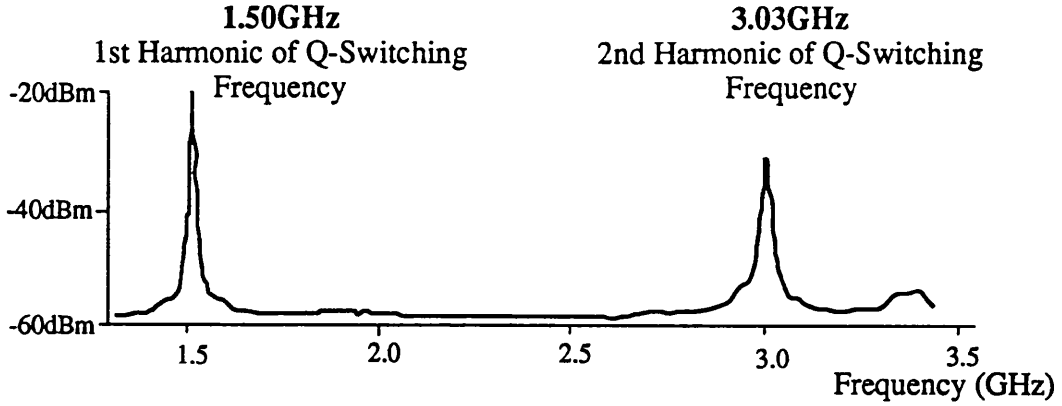

Fig. 7.10(a). Frequency spectra of a two-section laser with no RF signal applied.

The addition of an RF signal to the gain section of the laser alters radically the RF spectrum of the optical output. Figure 7.10(b) shows the result of applying a -14.3 dBm, 1.47 GHz RF signal to the gain section. The first point to note is that for -14.3 dBm applied RF power, the Q-switching (local oscillator) frequency is not pulled towards the RF signal frequency. In the course of these experiments, the Q-switching frequency varied through the range 1.45 to 1.55 GHz with no applied RF signal, which we attribute to temperature drift, hence the change in Q-switching frequency between Figures 7.10(a) and 7.10(b).

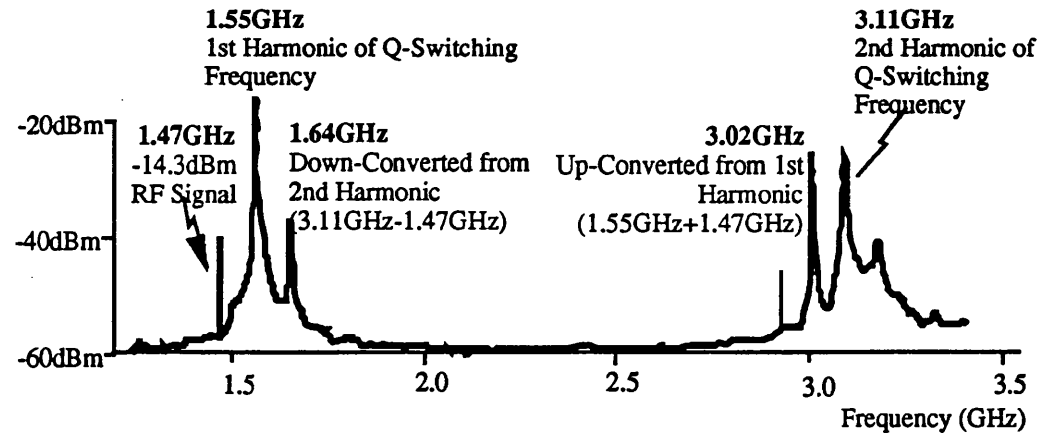

Fig. 7.10(b). Frequency spectra of a two-section laser with 1.47 GHz applied RF signal.

The most pronounced influence of the application of the RF signal are the additional spectral peaks at 1.64 GHz and 3.02 GHz. The first of these peaks can be attributed to mixing of the applied RF signal with the 2nd harmonic of the Q-switching frequency. The peak at 1.64 GHz is the *down-converted* signal resulting from the mixing process (3.11 GHz

-1.47 GHz). The second peak can be ascribed to mixing of the applied RF signal with the fundamental Q-switching frequency. The peak at 3.02 GHz is the *up-converted* signal resulting from the mixing process (1.55 GHz+1.47 GHz).

This demonstrates that both up- and down-conversion processes occur, and that mixing occurs not only between the signal and the fundamental frequency of the laser, but also with the harmonics of the laser LO frequency.

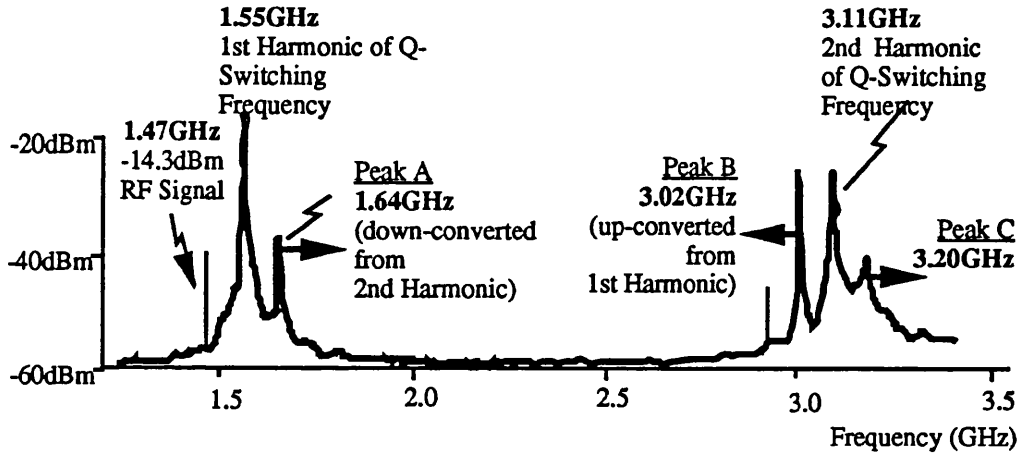

Fig. 7.11(a). Frequency spectra of two section laser with 1.47 GHz RF signal applied to the gain section.

Further evidence that the spectral peaks arising from the addition of an RF signal are due to up- and down-conversion can be obtained by changing the frequency of the applied RF signal. In Fig. 7.11(a), the signal frequency is again 1.47 GHz, whilst in Fig. 7.11(b), the signal frequency is reduced to 1.40 GHz. In both cases, the applied signal is at a power of -14.3 dBm, and the DC bias conditions of the two-section laser are 80 mA drive current to the active section and 1.6 V reverse bias across the saturable absorber. Consider first Peak A, which occurs at 1.64 GHz, in the spectrum of Fig. 7.11(a). We have postulated that this peak is the down-converted signal resulting from mixing of the applied RF signal and the 2nd harmonic of the Q-switched frequency.

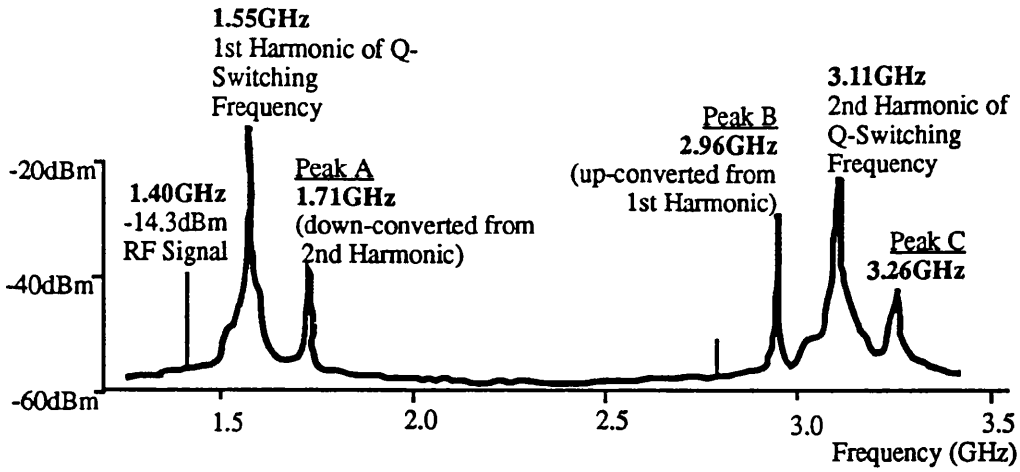

Fig. 7.11 (b). Frequency spectra of two section laser with 1.40 GHz RF signal applied to the gain section.

Reducing the frequency of the applied RF signal from 1.47 GHz to 1.40 GHz causes Peak A to increase from 1.64 GHz to 1.71 GHz, as expected if this spectral peak were the result of a down-conversion process. Similarly, reducing the signal frequency causes Peak B (3.02 GHz in Figure 7.11(a)) to decrease to 2.96 GHz (Figure 7.11(b)), as would be expected if this spectral peak were the up-converted signal resulting from mixing of the signal frequency and the Q-switching LO frequency.

Yet more evidence that mixing is occurring can be found by studying the dependence of the measured RF spectra of the optical output of the laser on the power of the applied signal. Figure 7.12 shows these spectra in the frequency range 1.2 GHz to 3.5 GHz for increasing applied signal powers. Note that in the range -25 dBm to -10 dBm, the fundamental Q-switched LO frequency is essentially independent of the signal power. For -25 dBm applied signal power, there is some evidence of the up-conversion occurring from mixing between the signal frequency and the Q-switching LO. As the RF power is increased to -16 dBm, the down-converted signal from mixing between the signal and the 2nd harmonic of the Q-switching LO becomes apparent. At -10 dBm, the up-converted and 2nd harmonic signals have similar magnitude. For applied powers of greater than -5 dBm, the Q-switching frequency starts to be pulled towards that of the applied RF signal.

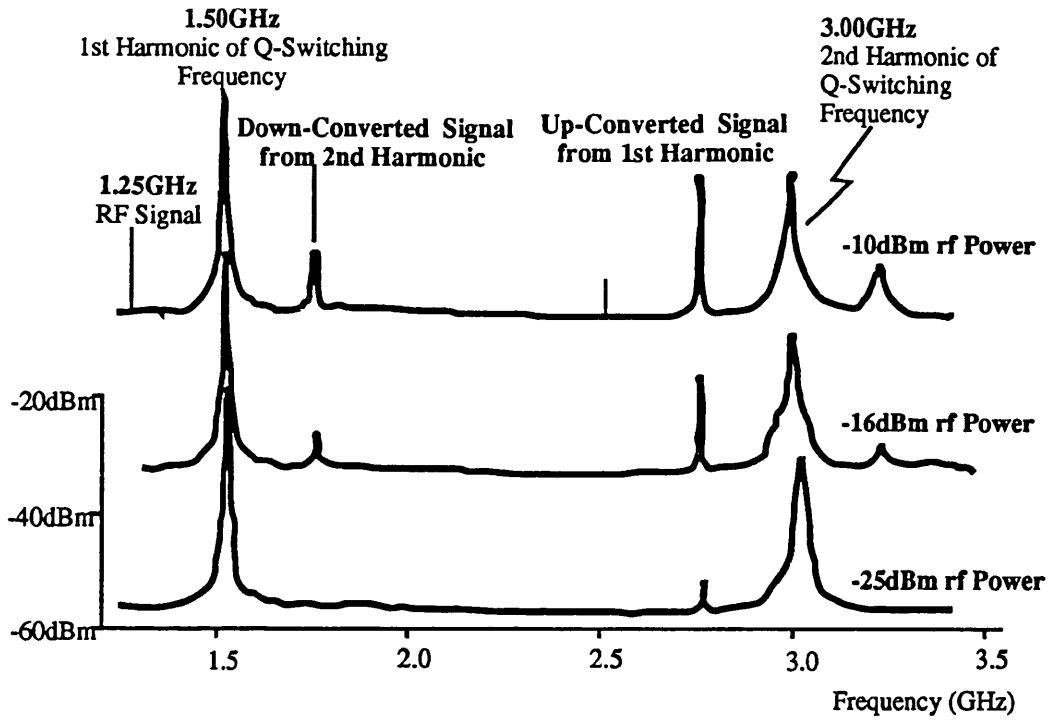

Fig. 7.12. Frequency spectra of two-section laser with 1.25 GHz RF signals of (a) power -25 dBm, (b) -16 dBm and (c) -10 dBm applied to gain section

Figure 7.13(a) shows the output RF spectrum around the fundamental Q-switching frequency in the frequency range 0.5 GHz to 2.5 GHz for no applied RF signal. Again, the DC conditions are 80 mA cw drive current through the gain section, and 1.5 V reverse bias across the saturable absorber. Figure 7.13(b) shows the same frequency range with a -14.3 dBm, 0.5 GHz signal applied to the gain region of the laser. Both the up- and down-converted signals resulting from mixing of the RF signal and the Q-switching are apparent at 1.005 GHz and 2.004 GHz respectively.

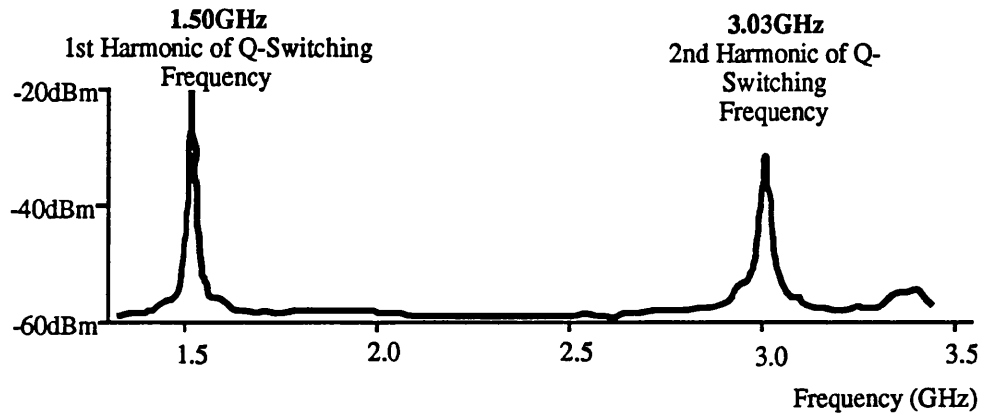

Fig. 7.13 (a). Frequency spectra of two-section laser with no RF signal applied to gain section.

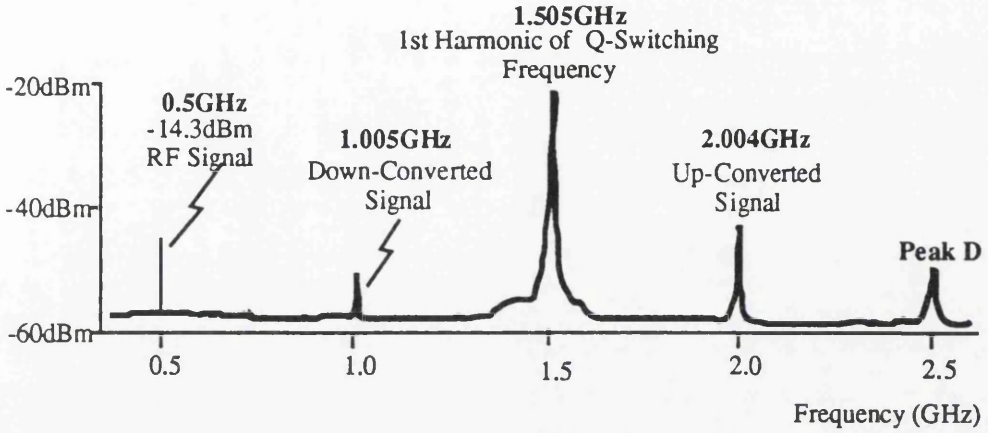

Fig. 7.13 (b) Frequency spectra of two-section laser with with 0.5 GHz applied RF signal

Temporal Results.

The two-section laser was again driven with a cw current of 80 mA through the gain section and 1.6 V reverse bias across the saturable absorber. The Q-switching frequency of 1.45 GHz is observed in time, Fig. 7.14. The filled in line at the bottom of the pulse train indicates the zero signal level taken when the light is blocked from the photodetector. The oscillations in between the pulses are due to internal electrical reflections caused by the RF splitter.

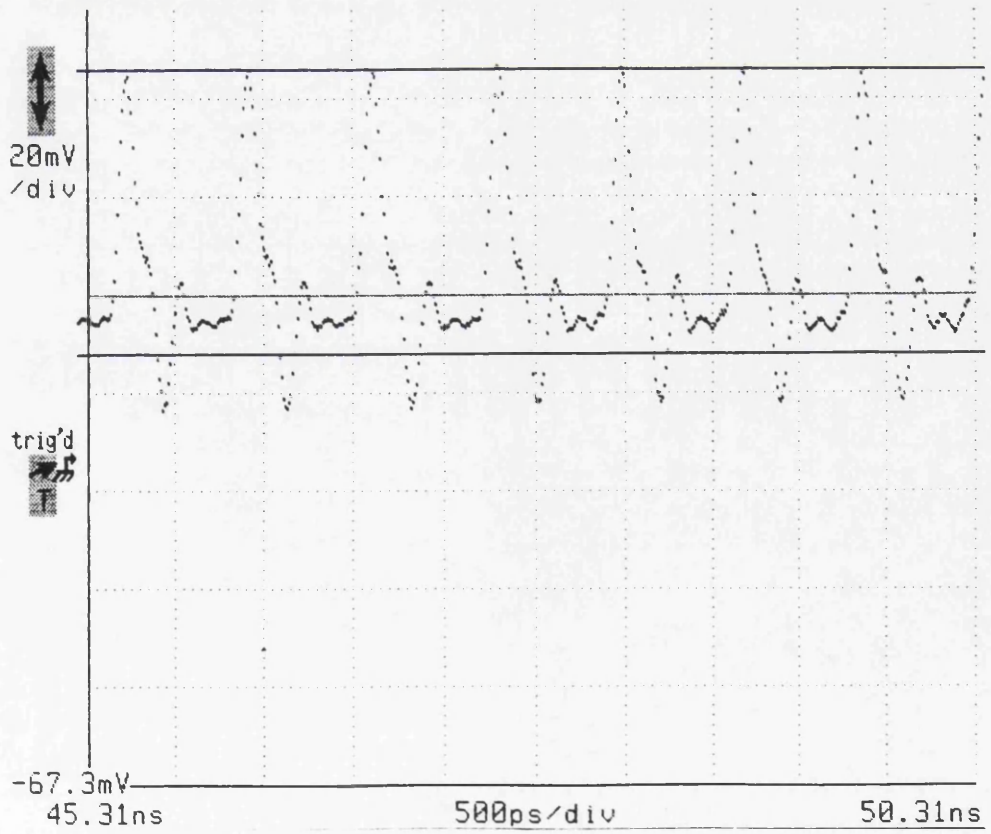

Fig. 7.14. A pulse train emitted by a free-running Q-switched laser at a frequency of 1.45 GHz with no applied RF.

The addition of an RF signal to the gain section of the two-section laser alters the time-dependent profiles of the Q-switched pulses. As proposed in the theory (section 7.1), the external RF modulation imposes a slow envelope on the pulse train, identical to the time-dependant profiles plotted in Fig. 7.3(a). Time-dependent profiles of the two-section laser were taken with an 0.5 GHz RF signal. Fig. 7.15(a) shows the result of applying a -6 dBm, 0.5 GHz signal to the gain section and Fig. 7.15(b) shows the same signal with an applied RF power of -3 dBm. The increase in RF signal power from Fig. 7.15(a) to Fig. 7.15(b) shows an increase in the effect the slow envelope imposes on the pulse train. The envelope imposed onto the pulse train becomes larger with an increase in RF power altering the peak amplitudes of the optical pulses.

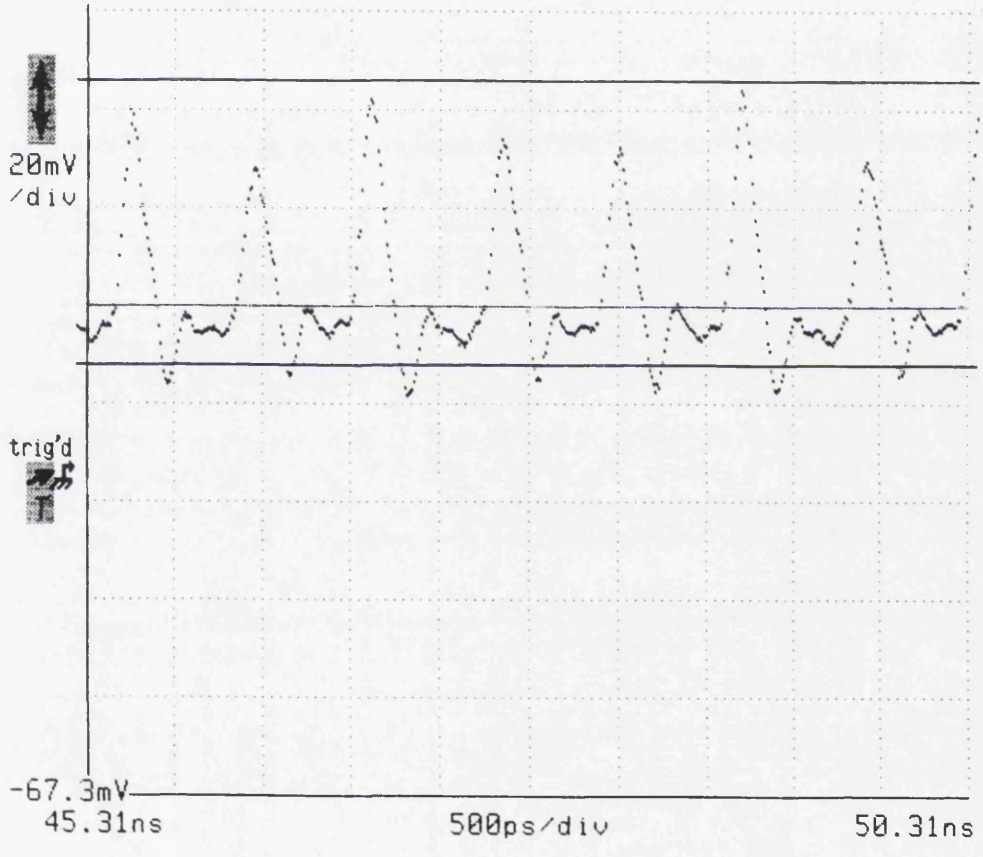

Fig. 7.15(a). A pulse train emitted by a free-running Q-switched laser at a frequency of 1.45 GHz with an applied rf signal of 0.5 GHz at -6 dBm.

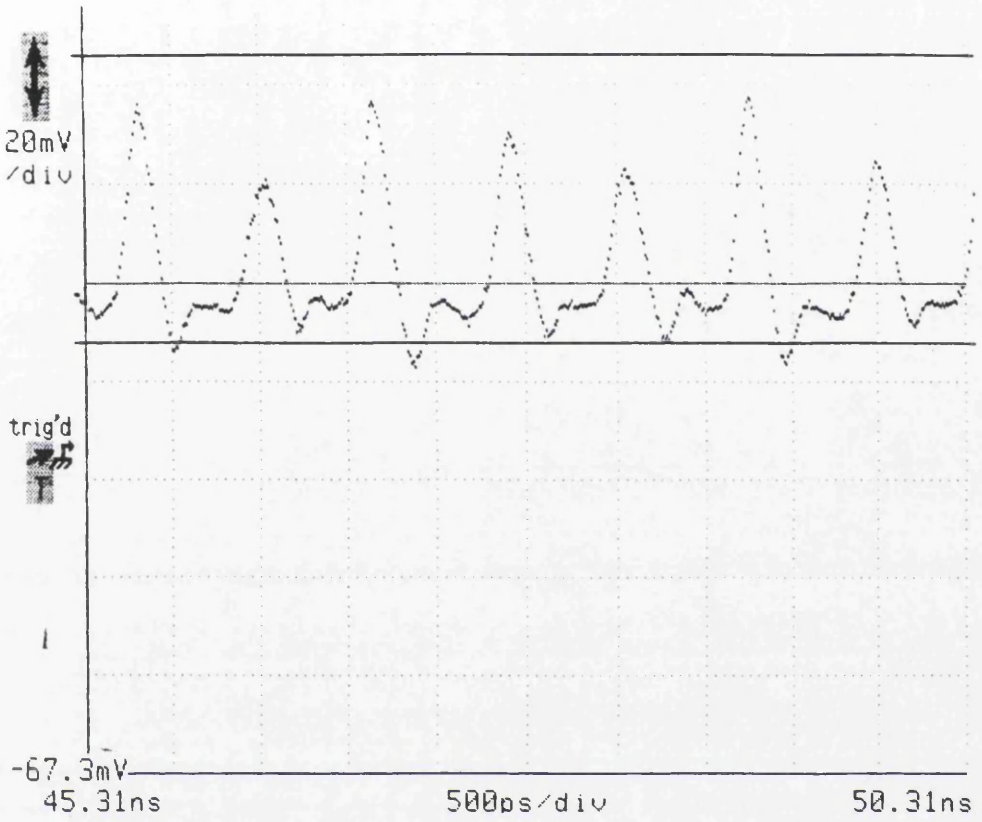

Fig. 7.15(a). A pulse train emitted by a free-running Q-switched laser at a frequency of 1.45 GHz with an applied rf signal of 0.5 GHz at -3 dBm.

7.3.4 Determination Of Conversion Efficiencies

As discussed in section 7.1 (eqn 7.2), when acting as a mixer, the optical conversion efficiency of the laser can be defined as

$$\eta_{opt} = \frac{P_{2opt}}{P_{sopt}} \qquad 7.5$$

where P_{2opt} is the optical output power at the sum and difference frequencies $f_2 = f_{LO} \pm f_s$, and P_{sopt} is the input optical signal power. The electrical conversion efficiency can be defined as

$$\eta_{elec} = \frac{P_{2elec}}{P_{selec}} \qquad 7.6$$

where P_{2elec} is the electrical power measured at the spectrum analyser at the sum and difference frequencies $f_2 = f_{LO} \pm f_s$, and P_{selec} is the absorbed input power of the laser. We can find a simple relationship between the two efficiencies. If we say

$$P_{2elec} = I_{pd}^2 R_{sp-a} \qquad 7.7$$

where R_{sp-a} is the input resistance of the spectrum analyser and I_{pd} is the current from the photodetector which is $I_{pd} = \frac{e}{\hbar\omega} P_{2opt}$. We can also say

$$P_{selec} = \Delta I_{fs} R_{las} \qquad 7.8$$

where ΔI_{fs} is the input modulated current to the laser and R_{las} is the laser resistance which is approximately equal to the laser contact resistance. Therefore substituting (7.8) and (7.7) into (7.6) we get

$$\eta_{elec} = \frac{R_{sp-a}}{R_{las}} \frac{\left(\frac{e}{\hbar\omega}\right)^2 P_{2opt}^2}{\Delta I_{fs}} \qquad 7.9$$

which gives

$$\eta_{elec} = \frac{R_{sp-a}}{R_{las}} \eta_{opt}^2. \qquad 7.10$$

To determine the electrical power at the sum and difference frequencies, the total laser output power, corresponding to the integrated intensity of all peaks in the frequency spectrum, was first measured from the spectrum analyser. The integrated intensity of individual up or down converted peaks was then evaluated and compared with the total integrated intensity from all spectral peaks, giving the electrical power in the sum and difference signals. The magnitude of the microwave signal into the laser was determined by measuring the microwave reflection coefficient of the laser whilst accounting for losses in the system. This also permitted the magnitude of the rf input current to be determined.
These measurements were performed on a two-section laser with a self-pulsation frequency of 1.5GHz when driven with a current of 80mA, and a 0.9GHz rf signal applied to the gain section. Figure 7.16 shows the experimental electrical conversion efficiency of both the up- and down-conversion processes due to mixing of the first harmonic of the Q-switching frequency with the applied rf signal, as a function of input rf current (normalised to the threshold current of the device when fully forward biased). Theoretical values of both conversion efficiencies, derived in Section 7.1, are also plotted in Figure 7.16 using the relationship in equation 7.10 to plot the electrical conversion efficiency from the optical efficiency. In both experimental and theoretical cases, up-conversion is observed to be more efficient than the down-conversion process by approximately an order of magnitude. This is due to a combination of AM and FM components in the mixed signal.

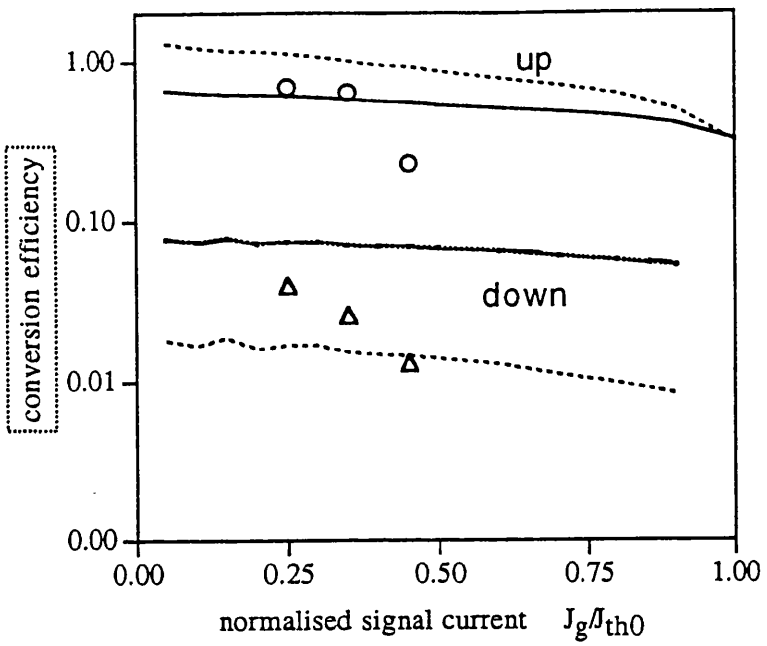

Fig. 7.16. Comparison of experimental and theoretical up- and down-conversion "optical" (solid) and "electrical" (dashed) efficiencies for mixing of first harmonic of Q-switching frequency and input rf signal.

7.4. CONCLUSIONS.

Optoelectronic mixing of very high-frequency amplitude modulated signals in semiconductor lasers has been studied theoretically. Three possible constructions have been proposed for a laser-mixer capable of working simultaneously as a local oscillator and a mixing element. These constructions include four-terminal lasers with dual (pumping and confinement) modulation, and both externally modulated passively Q-switched and externally modulated passively mode-locked lasers. The laser mixers provide their output in the form of an optical signal modulated at sum and difference of the local oscillator and signal frequencies. It has been shown that the fundamental physics of frequency mixing is based on parametric effects and is essentially the same for all the three cases studied. For the case of dual modulation, analytical estimates for the conversion efficiency have been obtained in the small-signal approximation. For the case of a passively mode-locked laser, the frequency dependence of the down conversion efficiency has been studied numerically and shown to be of a resonant type similar to the modulation response of a laser diode. Additional spectral lines have been shown to arise due to mixing with higher harmonics of the local oscillator, and the use of mode-locked lasers with spectral properties engineered to

provide nearly sinusoidal mode-locked pulses suggested as a way of avoiding the generation of these lines. A sinusoidal optical output can be realised through the use of selective spectral gratings within the modelocked laser cavity. Selecting a couple of optical modes and pasively locking them together will produce an optical sinusoidal output signal. An experimental confirmation of the feasibility of the laser-mixer was obtained using a Q-switched laser diode and theoretical values of conversion efficiencies of both up- and down-conversion process have been compared closely with experimental values. Future work will concentrate on experimental and theoretical studies of frequency-mixing at submillimetre frequencies using short-cavity mode-locked lasers; other matters reserved for future studies are to line-narrow the microwave spectrum of the LO for practical applications and to measure the absolute conversion efficiency and phase noise.

7.5 REFERENCES.

1. A.J. Seeds, "Microwave optoelectronics", Opt. and Quantum Electron., vol. **25**, pp. 219-229, 1993

2. V.B. Gorfinkel, G. Kompa, M. Novotny, S.A. Gurevich, G.E. Shtengel, I.E. Chebunina, "High-frequency modulation of a QW diode laser by dual modal gain and pumping current control". Proceedings of the International Electronic Device Meeting /IEDM'93/ , p.933,1993.

3. V.B. Gorfinkel, S.A. Gurevich, I.E. Chebunina, M.S. Shatalov, G.E. Shtengel. " High-frequency operation of heterostructure diode laser modulated by dual optical confinement factor and pumping density control". Submitted to IEEE J. Quantum Electron.

4. E.L.Portnoi, A.V.Chelnokov, "Passive mode-locking in a short cavity diode laser". Digest 12th IEEE International Semiconductor Laser Conference, Davos, Switzerland, p.140-141, 1990.

5. J.M. Martins-Filho, E.A. Avrutin, C.N. Ironside, " High repetition rate by multiple colliding pulse mode-locked operation of a semiconductor laser", Digest, 14th IEEE Semiconductor Laser Conference, 1994, paper M2.3; *IEEE J. of Selected topics in QE.*, Vol. 1, pp. 539-551, 1995.

6. Shin Arahira, Saeko Oshiba, Yasuhiro Matsui, Tatsuo Kunii, Yoh Ogawa, "Terahertz-rate optical pulse generation from a passively mode locked semiconductor laser diode", Optics Letters, vol. **19**, pp. 834-836, 1994.

7. J.H.Zarrabi, E.L.Portnoi, and A.V.Chelnokov, "Passive mode-locking of a multistripe single quantum well GaAs laser diode with an intra-cavity saturable absorber". Appl.Phys.Lett., vol. **59**, pp. 1526-1528, 1991.

8. E.A. Avrutin, V.B. Gorfinkel, S. Luryi, K.A. Shore, "Control of surface-emitting laser diodes by modulating the distributed Bragg mirror reflectivity: small-signal analysis", Appl. Phys. Letters, Vol. **63**, pp. 2460-2462, 1993

9. E.A. Avrutin, "Spontaneous emission and noise in self-pulsing semiconductor lasers". IEE Proc. Pt.J., vol. **140**, pp. 16-20, 1993

10. K.A. Shore, M. W. McCall. "Nonlinear and quantum optics in semiconductor lasers", Prog. Quant. Electron., vol. **14,** pp. 63-127, 1991

11. U. Feiste, M. Moerle, B. Sartorius, J. Hoerer, R. Loeffler. "12 GHz to 64 GHz continuous frequency tuning in selfpulsating 1.55 μm quantum well DFB lasers". Digest, 14th IEEE Semiconductor Laser Conference, 1994, paper Th2.3

12. A. G. Weber, M. Schell, G. Fischbeck, D. Bimberg. "Generation of single femtosecond pulses by hybrid mode locking of a semiconductor laser. IEEE J. Quantum Electron., vol. QE-28, pp. 2220-2229, 1992.

13. M. Schell, A.G. Weber, E. Schoell, D. Bimberg, "Fundamental limits of sub-ps pulse generation by active mode locking of semiconductor lasers: the spectral gain width and the facet reflectivities. IEEE J. Quantum Electron., vol. QE-27, pp. 1661-1668, 1991.

14. J.H. Marsh, "Quantum-well intermixing", Semicond. Sci. Technol., vol. **8,** pp. 1136-1155, 1993

15. E.A. Avrutin, V.B. Khalfin, J.M.Arnold, J.H.Marsh."Time-and frequency domain theory of externally synchronised operation of a passively mode locked laser diode". Technical Digest, Conference on Lasers and Electro-Optics Europe, 1993. paper CTuE6, p. 76.

16. V.B. Khalfin, J.M.Arnold, J.H.Marsh, "Synchronisation of a mode-locked laser with an external pulse stream", *IEEE J. of Selected topics in QE.,* Vol. 1, pp. 523-527, 1995.

17. See for example R. G. Hunsperger. Integrated optics: theory and technology. Springer, 1991, p.241.

Chapter 8

Field Distribution Measurements in Q-Switched Semiconductor Lasers

8.1. INTRODUCTION

The dynamic behaviour of transverse modes in Q-switched stripe geometry laser diodes has been reported previously [1] using sub-nanosecond pulse modulation. Here, however, we report experimental investigations of the transient behaviour of the fundamental and higher order transverse modes in ultrafast Q-switched lasers. This particular experiment evolved from early investigations into ultrafast Q-switching of ion implanted Q-switched semiconductor lasers supplied by the Ioffe Institute in St Petersburg. The investigations have shown that the first pulse in a train of pulses emitted from the Q-switched gain guided laser always exhibits a Gaussian profile similar to a TE_{00} mode distribution, but later pulses display higher order modes. The aim of this work is to control the variation in lateral field pattern to aid future work in modelocking semiconductor lasers. This technique can also be used to screen devices intended for high power operation, which exhibit a TE_{00} mode at low to medium powers, but at high power start to exhibit higher mode operation.

8.2. EXPERIMENT

8.2.1. Device Fabrication.

The lasers used in this experiment were GaAs/AlGaAs lasers with a lasing wavelength of 860 nm which were fabricated at the A.F Ioffe Physico-Technical Institute, Russia. The devices were gain guided oxide stripe, double heterostructure semiconductor lasers, where the stripe width was ~20 μm and the device length was 200 μm long. The laser contained an ultrafast intracavity saturable absorber formed by deep implantation of heavy ions (18 MeV nitrogen ions) into both facets of the laser diode giving an implantation depth of ~10 μm, these lasers are described in detail in chapter 3.

8.2.2. Measurement System

The time-dependent profile of the Q-switched pulse train was observed by focusing the collimated train of pulses onto a fast InGaAs photodetector connected to the sampling head of a sampling oscilloscope, a similar arrangement to that used in previous experiments (chapter 4). The InGaAs photodetector had a small detection area (8000 μm^2) and a risetime of 45 ps and the sampling head had a 30 ps risetime. The overall risetime of the detection system was estimated to be 55 ps. An infra red camera was used to image the small area photodetector and therefore aid alignment of the focused pulse train onto the photodiode. The experimental setup is illustrated in Fig. 8.1.

The Q-switched laser was driven by a pulse generator at a frequency of 100 kHz and a drive current of between 200 and 500 mA, depending on the optical pulse repetition frequency required. The electrical pulse from the pulse generator had a rise time of 150 ps and a pulse width of between 0.4 and 2 ns. The semiconductor laser produced a train of Q-switched pulses on every electrical pulse from the pulse generator; these pulses had a pulse width of 17 ps (FWHM) and a repetition rate of 3 to 8 GHz depending on the drive current. The peak optical power of the laser was about 1 W.

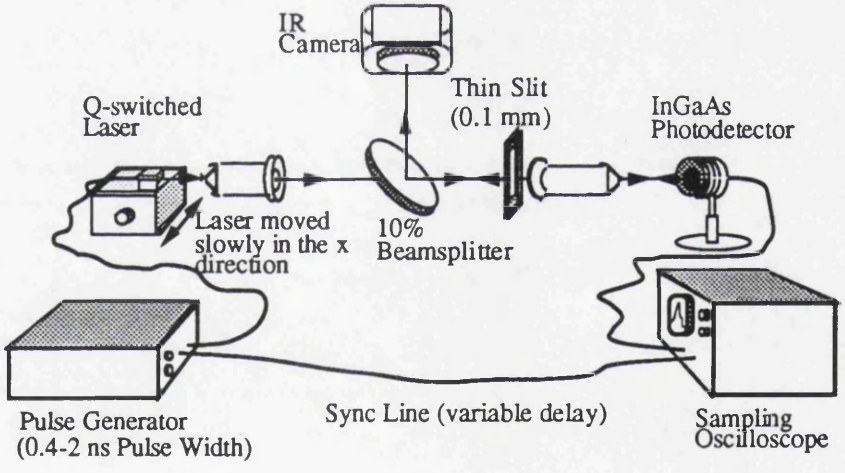

Fig. 8.1. Experimental arrangement for determining lateral distribution of optical pulse energy.

The near field emission from the laser was imaged onto a slit (width 100 μm) in front of the photodetector and the laser was slowly scanned across the slit along the *x*-axis. The optical intensity of the transverse field distribution could then be sampled in small cross sections as the near field image moved across the slit. The displacement of the laser was measured using a linear variable differential transformer (LVDT) and the optical field

intensity was measured from the peak amplitude of the pulse on the sampling oscilloscope. A plot of pulse amplitude against displacement could then be recorded to give the transverse field distribution pattern at a particular time delay. By varying the delay time, field distribution patterns of particular pulses in the pulse train could be measured and, therefore, the temporal behaviour of the transverse field distribution could then be built up.

8.2.3. Experimental Results

The transverse field distributions are shown in Fig. 8.2 for one of the Q-switched lasers. The first pulse of the pulse train is in the TE_{00} mode while the following three pulses contain a substantial fraction of their energy in higher order modes. The transverse field patterns for the consecutive pulses varies from pulse to pulse, however it was found that after approximately 1 ns the field distribution became constant for consecutive pulses. The width of the transverse field profile also changes between consecutive pulses, the first pulse has a pulse width of 18 μm (FWHM) and the forth pulse widens to 28 μm (FWHM).

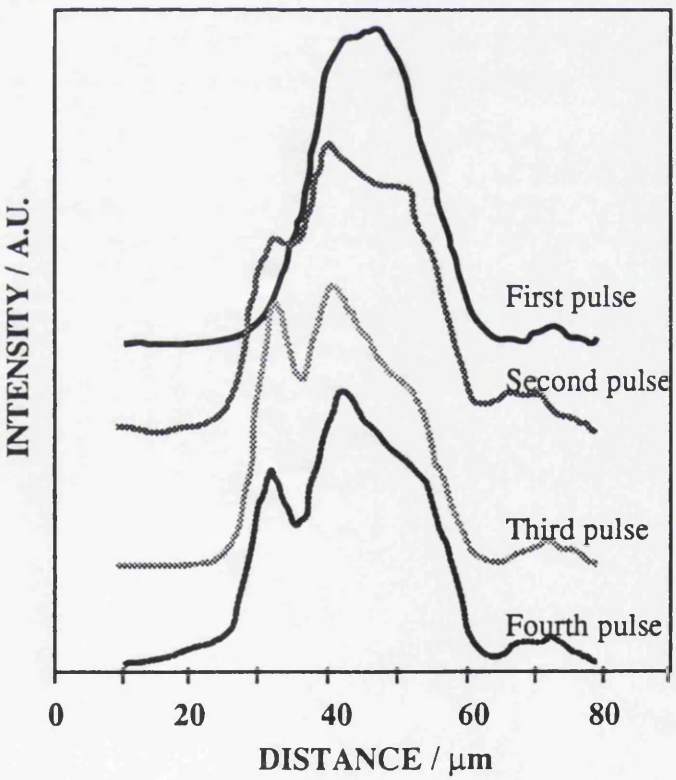

Fig. 8.2. Lateral distribution of pulse energy emitted by an integrated Q-switched laser (102). The laser drive current was ~400 mA and the pulses were separated by 225 ps.

Another transverse field distribution pattern of a different Q-switched laser with a narrower oxide stripe (15 μm) is shown in Fig. 8.3(a+b). Fig. 8.3(a) illustrates a field distribution pattern taken at a low drive current, ~ 250 mA and in Fig. 8.3(b) at a high pulse amplitude ~ 500 mA. All the pulses in the pulse train exhibit a TE_{00} mode, however it can be seen that there is a change in the width of the field distribution pattern between consecutive pulses and in the near field profile at low and high drive currents. In the low drive current regime, the initial pulse has a near field profile width of 14 μm which widens to 20 μm for the fourth pulse; with an increase in drive current (500 mA) the first pulse has a near field width of 17 μm and the final pulse of 30 μm.

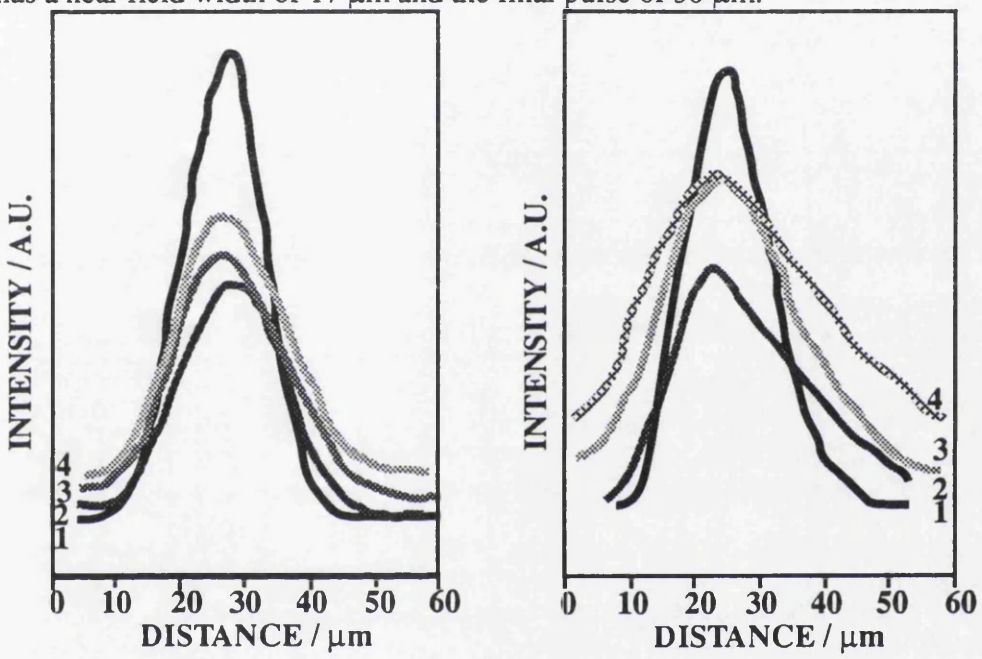

Fig. 8.3. Lateral distribution of pulse energy emitted by an integrated Q-switched laser (022). The laser drive current was a)~250 mA and b)~500 mA.

The transverse field distributions of a set of consecutive pulses from a Q-switched InGaAsP/InP laser, lasing wavelength 1.3 μm, are shown in Fig. 8.4(a+b). The laser is identical to the ion-implanted GaAs/AlGaAs lasers used previously, except the oxide stripe is narrower (5μm).

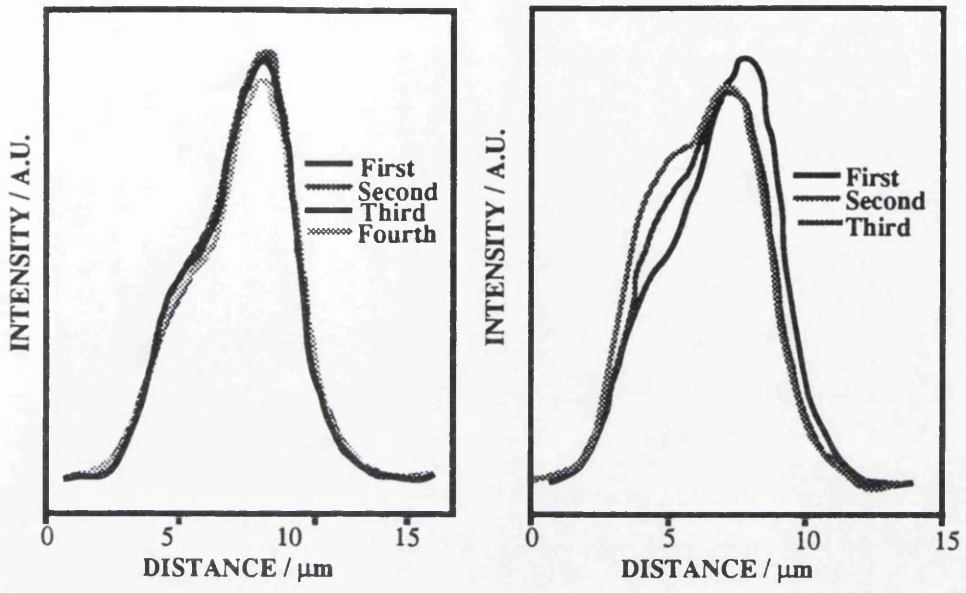

a) b)

Fig. 8.4. Lateral distribution of pulse energy emitted by an integrated 1.3 μm Q-switched laser (068). The laser drive current was a) ~250 mA and b) ~500 mA .

Fig. 8.4(a) illustrates the field distribution pattern observed at a low drive current, ~250 mA and Fig. 8.4(b) observed at a high drive current ~500 mA. For this particular device, at a low drive current, the transverse mode profiles are identical for consecutive pulses with a constant mode profile width of 4.5 μm (FWHM). At the high drive current there is a small increase in mode profile width, from 5 μm (FWHM) for the first pulse to 6 μm (FWHM) for the third.

8.3. Analysis of Results

The results show an increase in the mode profile width with time for both the GaAs/AlGaAs lasers. They also show that the pulse train from the wider striped laser exhibits a transition from a TE_{00} mode for the first pulse to a higher order mode for subsequent pulses. An explanation of these phenomenom is as follows and is illustrated in Fig. 8.5. Prior to the first pulse, a uniform gain distribution builds up across the width of pumped stripe. This favours the formation of a Gaussian distribution in the transverse direction, which is reinforced by the saturable absorber becoming transparent in the region of greatest optical intensity i.e. at the centre of the transverse distribution. The first pulse is then released which depletes the gain in the region of highest optical intensity which is at the centre of the transverse mode. The recovery time [2,3] of the saturable absorber (20 ps) is faster than the rate at which the injected carriers can build up the gain—this is confirmed by the way in which the drive current determines the self-pulsation frequency. Because of the spatial burning of carriers at the centre of the transverse mode caused by

the first pulse, the gain builds up towards the sides of the stripe. Therefore, in the narrower striped Q-switched lasers this is seen in the widening of the transverse field profile. However in the wider striped laser there is effectively a depletion in gain around the centre of the stripe. This gain distribution causes the subsequent pulses to exhibit higher order transverse modes for the wider striped laser.

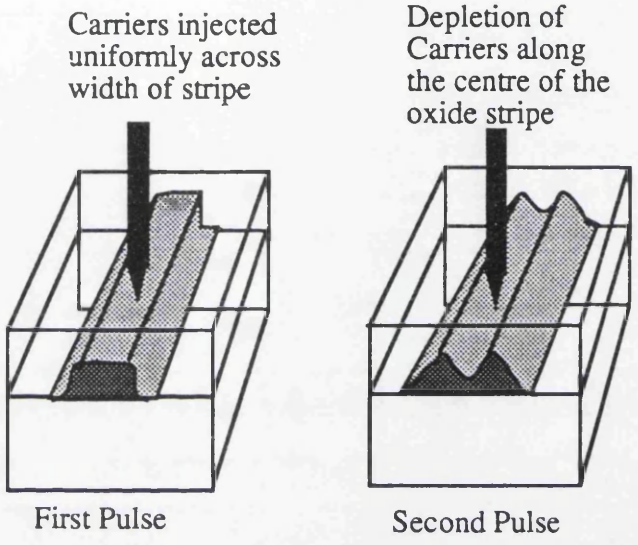

Fig. 8.5. Model illustrating the change in distribution of carrier concentration with time.

8.4. CONCLUSIONS

A simple method of determining the transverse mode distribution of semiconductor lasers has been described. The technique has been applied to lasers containing a saturable absorber so that they can be Q-switched. The same technique, however can equally well be applied to gain-switched lasers and can also be used to study higher order modes which would normally only propagate at high drive currents. The development of unwanted high order modes is a particular problem in high power lasers intended for pumping erbium fibre amplifiers, for example.

The behaviour of the pulse stream from Q-switched lasers has been studied. It is found that the first pulse in a stream generally favours the lowest order transverse mode, but that subsequent pulses have a larger fraction of their energy in higher order modes. This phenomenom is observed particularily in wider stripe gain guided lasers which would be more likely to form higher order modes. This behaviour can be understood in terms of lateral spatial hole burning caused by the first pulse and the nonuniform way in which the gain recovers across the width of the pumped stripe.

8.5. REFERENCES

1. F. Mengel, and V. Ostoich, "Dynamics of longitudinal and transverse modes along the junction plane in AlGaAs stripe lasers," *IEEE J. Quantum Electron.*, vol. 13, pp. 359-363, 1977.

2. E.L. Portnoi, N.M. Stel'makh and A.V. Chelnokov, *Sov. Tech. Phys. Lett*, vol. **15**, p. 432, 1989.

3. E.A. Avrutin and M.E. Portnoi, *Sov. Phys. Semicond.*, vol. **22**, p. 968, 1988.

Chapter 9

Modelocked and Extended Cavity Lasers

9.1. Introduction

The monolithic integration of active laser and passive waveguide sections is an essential step towards the complete fabrication of photonic integrated circuits (PICs), optoelectronic integrated circuits (OEICs) and integrated mode-locked lasers. To achieve these goals the passive waveguide sections need to be compatible with laser structures in terms of geometrical dimensions and fabrication processes. One method that provides nearly ideal optical mode matching in the passive and active waveguide sections is an intermixing processs of the quantum wells (QW) with the barriers to form an alloy semiconductor. The bandgap of the intermixed alloy is larger than that of the original QW structure and can therefore form a low-loss waveguide and, compared to other methods such as regrowth [1] or growth on patterned substrates [2], QW disordering has the advantage of reduced resonant losses independant of waveguide dimensions. Therefore, the waveguide can be continuous from the active to the transparent passive section, allowing negligible coupling loss and virtually no optical reflections at the interface between the two sections. A number of intermixing techniques have been reported, of which the most notable are impurity induced disordering (IID) [3,4], laser induced disordering [5] and impurity-free vacancy diffusion (dielectric cap annealing) [6]. Of the three techniques, dielectric cap annealing was chosen to form the passive waveguide because it was the simplest to use, requires no extra expensive machine processing such as ion implantation or laser annealing and was compatible with the fabrication processes used to produce lasers. In this chapter we propose fabricating and testing a low loss extended cavity laser using impurity-free vacancy diffusion. The extended cavity laser will be fabricated with an intracavity saturable absorber so that the device can be modelocked, and used in the frequency mixing experiments described in section 7.2.

9.2. The Impurity-Free Vacancy Diffusion Process

Impurity-free capless thermal annealing has been used for layer disordering and the accompanying shift of the recombination radiation to a higher energy. The process is carried out by annealing a sample at high temperatures (850°C, 20 h). Since no impurity is involved in the process, carrier concentrations in the annealed quantum well material are not necessarily altered to a large extent from the as-grown wafer. This process,

however, is not selective, and intermixing occurs uniformly across the whole sample. Therefore, an impurity-free selective intermixing process was needed.

Dielectric encapsulation had been investigated as a means of preserving surface stoichiometry, maximising impurity activation, and limiting the redistribution of implanted impurity profiles during high temperature annealing of ion-implanted GaAs material [3]. More recent experiments have studied the effects of dielectric encapsulation on Al-Ga interdiffusion in as-grown AlGaAs/GaAs quantum well heterostructures [6]. It was found that the Al-Ga interdiffusion rate was significantly different in the case of Si_3N_4 versus SiO_2- encapsulated regions of the same QW material, and that the activation energy for Al-Ga interdiffusion was smaller for dielectric-encapsulated samples (~ 3.5 eV) than for capless samples (~ 4.7 eV). The Al-Ga interdiffusion coefficient ($D_{Al\text{-}Ga}$) was also observed to be almost an order of magnitude smaller for Si_3N_4 -encapsulated samples than for either capless or SiO_2- encapsulated samples ($800 \leq T \leq 875$ °C).

An explanation of these observations is that the three types of encapsulation (Si_3N_4, capless and SiO_2) establish different surface conditions for the introduction of vacancies into the crystal. The Si_3N_4 encapsulant effectively seals off the crystal surface and, consequently is not a rich source of vacancies. In contrast, SiO_2 encapsulant is porous to Ga out-diffusion and, as a result, provides column-III vacancies for Al-Ga interdiffusion. The creation of Ga vacancies at the surface of the QW material therefore causes Al diffusion from the barrier to the well and an increase in the Al concentration within the well itself.

Stress and Si diffusion can also significantly influence the interdiffusion process. Stress due to mismatch of the thermal expansion coefficients of the two dielectrics, when used in conjunction, is responsible for a decrease in activation energies of $D_{Al\text{-}Ga}$. Si diffusion into the QW material causes Si impurity induced disordering and occurs at the SiO_2-GaAs interface. Therefore the GaAs surface layer must be relatively thick ($\geq$ 1000 Å) to "screen" effectively Si diffusion from the SiO_2 "source" itself and, thereby, prevent Si IID. Recent work in the Department [4] has found that SrF_2 is a better encapsulant than Si_3N_4 for sealing the crystal surface and hence creating fewer column-III vacancies. SrF_2 and SiO_2 were therfore used to intermix the quantum well material selectively and form the extended passive sections in the mode locked laser.

9.3. Material Design and Device Fabrication

Mode-locked lasers were made in GaAs/AlGaAs material (QT 418). The 860 nm semiconductor material structure was grown by metal organic chemical vapour deposition (MOCVD) at Sheffield, and contained four quantum wells. The device structure was

sequentially grown on a (100) n^+-GaAs substrate orientated 3 degrees off and doped to 2 x 10^{18} cm^{-3}; a 0.1 μm n^+-GaAs buffer layer (4 x 10^{18} cm^{-3}); a 1.5 μm n-$Al_{0.42}Ga_{0.58}As$ cladding layer (Si- 5.5 x 10^{17} cm^{-3}); a 0.1 μm $Al_{0.20}Ga_{0.80}As$ undoped waveguide layer; an undoped active region consisting of four 100 Å GaAs quantum wells separated by 100 Å $Al_{0.20}Ga_{0.80}As$ barriers; a 0.1 μm $Al_{0.20}Ga_{0.80}As$ undoped waveguide layer; a 0.9 μm p-$Al_{0.42}Ga_{0.58}As$ upper cladding layer (C- 3.3 x 10^{17} cm^{-3}); and a 0.1 μm p^+-GaAs contact layer (Zn- 8 x 10^{18} cm^{-3}). Four quantum wells structure was used because it was found to intermix better than the double quantum well material.

The masks were designed by myself and written onto a chrome mask using an electron beam writer. They are illustrated in Appendix 8. The dimensions of the waveguide (4 μm wide by 0.9 μm deep) were calculated using a vector finite difference computer program created by Mr M. Taylor, F-Wave, so that 860 nm light would propagate through the guide in the zero order optical mode. The cavity of the device was designed to be 2.5 mm in length. This length corresponds to a natural modelocking frequency of 17 GHz, the resolution limit of the photodetector used with the high frequency sampling scope.

9.3.1. Fabrication of the passive section

The first step of fabrication process defined the alignment marks in the semiconductor material. The sample was cleaned and a 1000 Å layer of SiO_2 was deposited on the p-type side of the semiconductor by a plasma enhanced chemical vapour deposition machine (PECVD). The sample was patterned and the silica removed where intermixing was not needed. A 1500 Å layer of SrF_2 was then deposited over the whole of the sample in an evaporator at a vacuum pressure of $2x10^{-6}$ t. Localised intermixing was then accomplished by rapid thermal annealing (RTA) at temperatures between 920 and 940 °C for 30 s. A piece of undoped GaAs substrate was placed over each sample as a proximity cap during each RTA.

PL Measurement Results from Intermixing

Photo-luminescent (PL) spectroscopy measurements were taken, at 77 K using the 514 nm line of an argon ion laser, of the SiO_2 capped and uncapped regions before subsequent processing. The at 77 K using the 514 nm line of an argon ion laser. The intermixed areas on the sample being fabricated were large enough (2.5x5 mm) to make direct PL measurements possible. This meant we could directly control the degree of intermixing before the next stage of laser fabrication. For comparison, control samples were measured, which had not been subjected to IFVD.

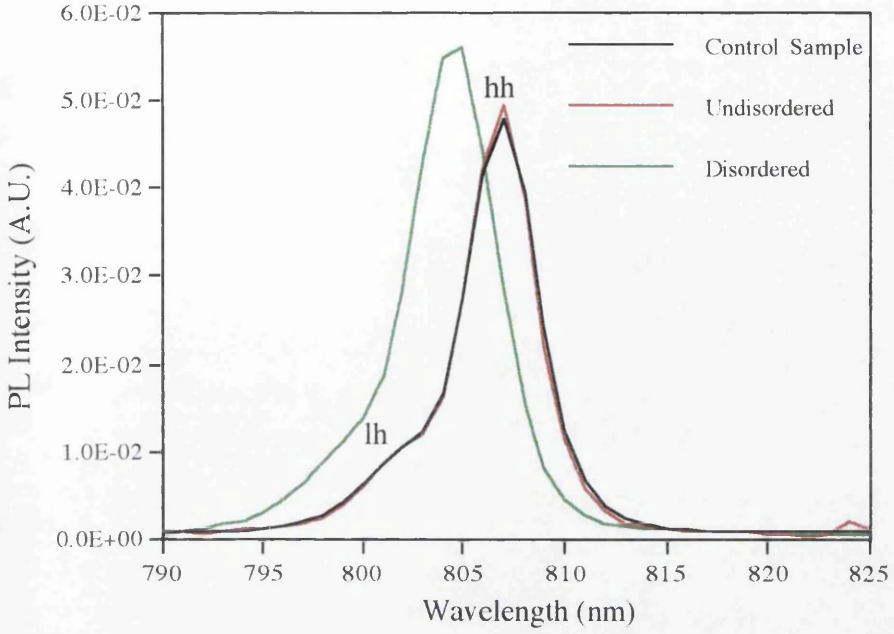

Fig. 9.1. Photoluminescence spectrum of an uncapped and SiO_2 capped MQW sample following RTA at 920 °C for 30 s.

The PL spectrum from the non-SiO_2 region after RTA exhibited a peak at 807 nm which was unaltered from the the control sample, Fig. 9.1. In contrast, the PL spectum in the SiO_2 capped region was shifted to a lower wavelength (804 nm) following RTA at 920 °C for 30 s, which can be attributed both to a decrease in the effective width of the quantum wells and an increase in the aluminium fraction within the quantum wells. The PL spectrum also exhibited faintly separable n=1 heavy hole (hh) and light hole (lh) exciton transitions for the region not capped with SiO_2 again identical to the control sample. However, the intermixed region exhibited less well resolved hh and lh peaks and a broadening of the excitonic peak from 4.5 nm to 5.5 nm (FWHM). The blue shift in wavelength of 3 nm for this sample was too small to form a passive waveguide. Therefore another sample was subjected to RTA at a higher temperature of 940 °C for 30 s; Fig. 9.2 shows the result of the PL measurement.

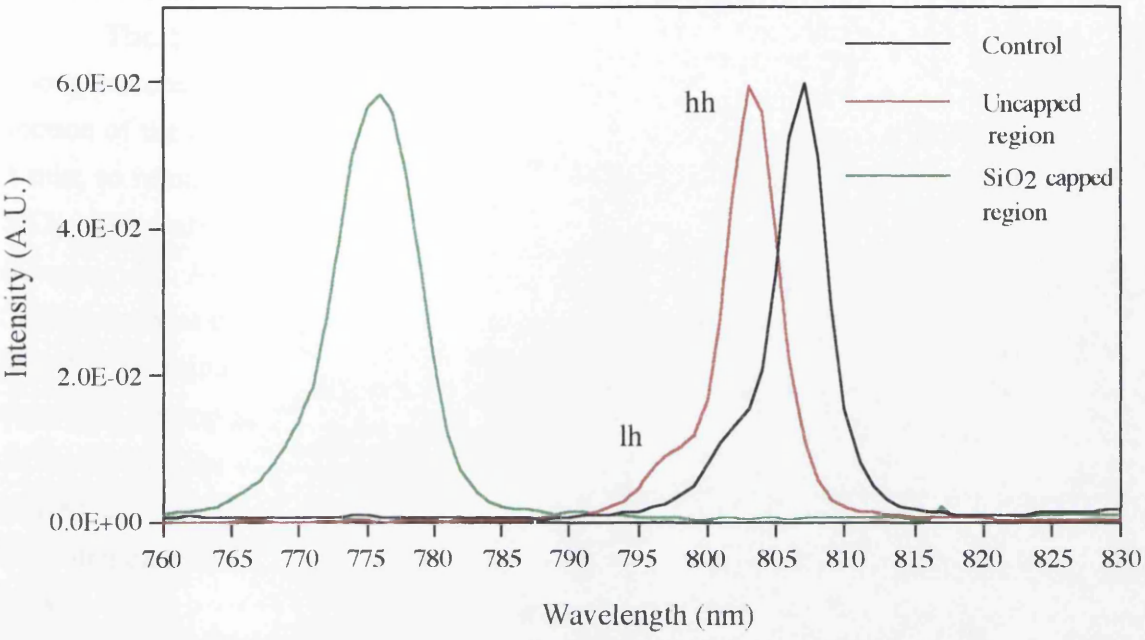

Fig. 9.2. Photoluminescence spectrum of an uncapped and SiO_2 capped MQW sample following RTA at 940 °C for 30 s.

The PL spectrum for the non-SiO_2 region following this higher temperature RTA, exhibited a small blue shift of 4 nm from its original excitonic peak; from 807 nm to 803 nm. This shift was probably due to a small degree of thermal intermixing. The exciton transitions in the region capped with SiO_2 shifted to a lower wavelength after the annealing cycle, Fig. 9.2. The exciton peak was centered at 776 nm which gave a total blue shift of 27 nm (46 meV) between the capped and uncapped regions. The PL spectrum for the non-SiO_2 region still exhibited faintly resolved heavy hole and light hole exciton transitions, whereas the capped region exhibited only a broad excitonic peak after the 940 °C anneal. The spectrum was also seen to broaden from 5 nm in the uncapped region to 7 nm in the SiO_2 capped area.

The mechanisms to which the broadening of the exciton transitions can be attributed are (1) grading of the well/barrier interfaces, which can lead to a substantial variation of Al composition and well depth (exciton confinement energy) within the volume of the exciton, and (2), a probably less substantial effect, variation in the degree of intermixing across the thickness of the four quantum wells, which will give rise to some finite range of effective quantum well widths.

9.3.2. Fabrication of the Active Section

The blue shift of 27 nm between the capped and uncapped section was large enough to create a passive section; processing was therefore continued to form the active section of the device. The dielectric caps were removed by etching the sample in HCl for 1 min, to remove the SrF_2, and then a solution of HF for another minute to remove the SiO_2. The wafer was then processed as normal to form ridge-waveguide lasers 4 μm wide (Chapter 4). After dry etching to a depth of 0.9 μm, the wafer was examined under a SEM to look at the surface damage caused by the intermixing process. The damage was found to be minor with the heavier damage being inflicted on the SrF_2 capped surface, shown in the top of the SEM micrograph, Fig. 8.5. This was probably due to the large difference in the expansion coefficient between SrF_2 and the GaAs. Further studies carried out since by Dr S. Ayling and myself have found that a thinner SrF_2 layer deposited on a heated sample at 200 °C causes minimal surface damage to the sample after RTA.

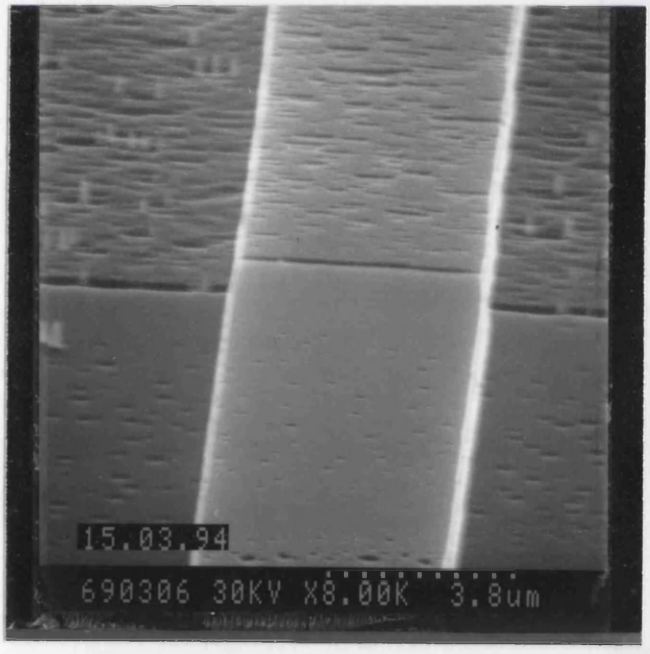

Fig. 9.3. SEM micrograph of a waveguide 4.5 μm wide, the top half was capped with SrF_2 and the bottom capped with SiO_2.

After the waveguides were formed, 2000 Å of SiO_2 was deposited over the sample and a window on top of the waveguide was opened in the SiO_2 using a wet etch solution. A p-type metal (Ni/Au) was evaporated over the sample and then the metal was lifted-off to leave a contact area over just the active region. The active region comprised two sections: a 500 μm or 250 μm gain section and a 15 μm saturable absorber. The wafer was thinned and the n-type contact (mikohm, appendix 4) deposited. The final process step was a selective dry etch of the p^+-GaAs contact between the gain and saturable

absorber sections. The resistance between the two sections increased from 800 Ω to 2 kΩ after the selective etch. The p^+-GaAs contact above the passive section was also selectively etched to stop current spreading from the gain section into the intermixed area which would have the effect of increasing the threshold current. The devices were optically cleaved into 2.5 mm lengths ready for testing, Fig. 9.4.

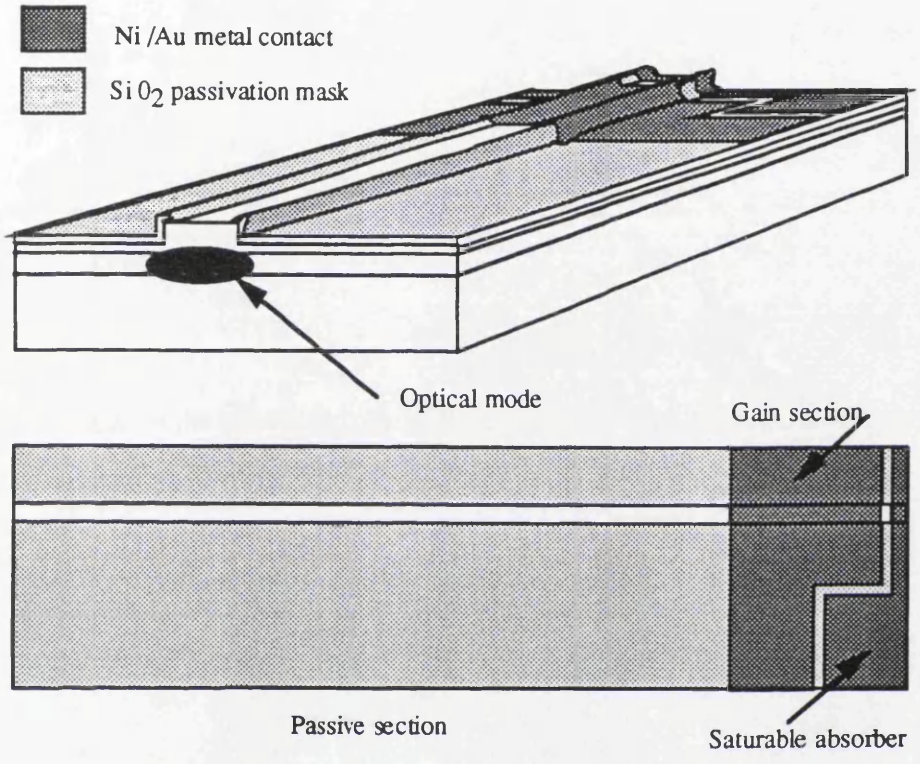

Fig. 9.4. Schematic of the integrated modelocked laser, showing passive and active sections.

9.4. Experimental Results

9.4.1. Light Current Test

The light current (*L-I*) characteristic, of the device were tested using the same experimental arrangement as the one used to test two-section lasers, section 4.4.1. The pulsed threshold current was 18 mA for external cavity lasers with 250 μm and 500 μm gain sections. The threshold currents of lasers with no external cavity was 14 mA. Light power versus current curves, Fig. 9.5, exhibited sharp turn-on characteristics not, however, as sharp as for lasers with no external cavity. Most devices had an differential quantum efficiency of 20 % per facet. Lasers made previously from this material (QT 418, section 5.1) exhibited a current threshold of 12 mA; the increase in threshold is possibly due to the annealing process.

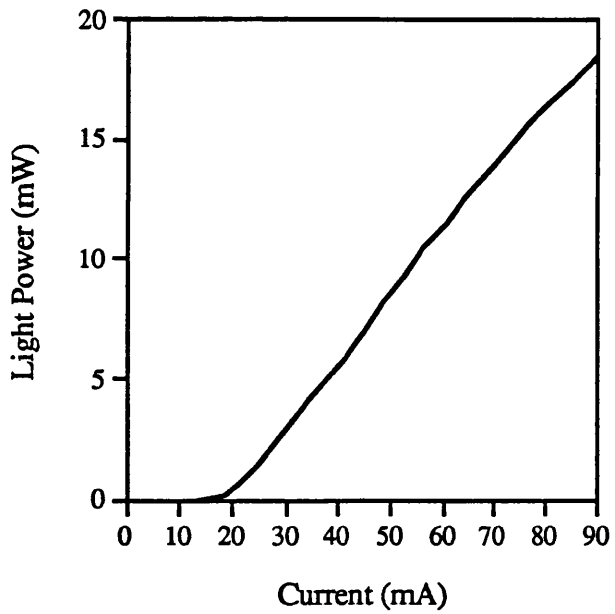

Fig. 9.5. Light current characteristic for an extended cavity laser.

9.4.2. Far Field Results

Far field measurements were taken using the experimental arrangement described in section 4.4.2. The far field was examined from the extended cavity facet of the device. The plot in Fig. 9.6 shows the far field profile of an extended cavity laser at pulsed drive currents of 40 and 60 mA. The shape of the plots show a close approximation to a zero order transverse field profile, however they are not perfect gaussian shaped modes. The mode width for this device was measured to be 8° (FWHM) for both pulsed drive currents.

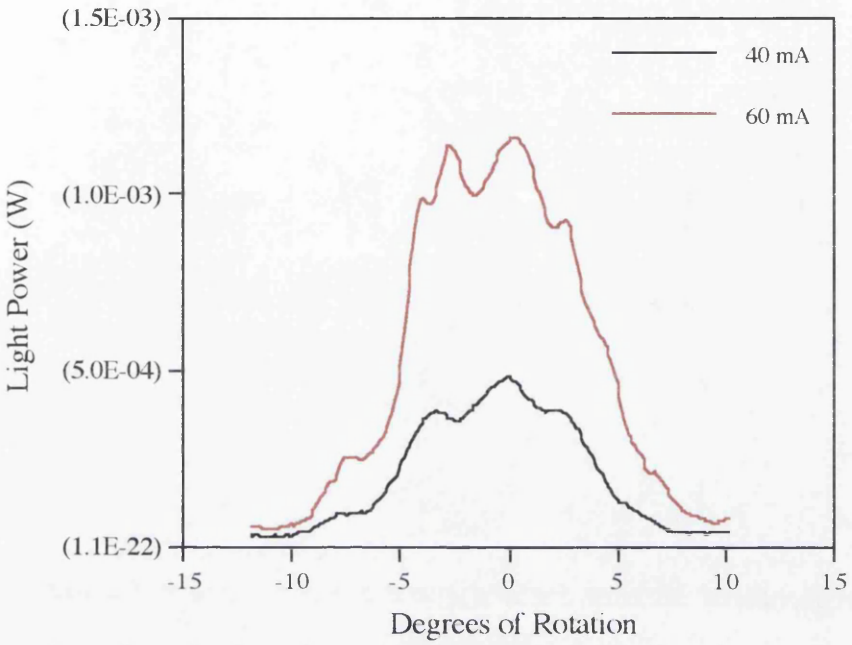

Fig. 9.6. Far field plot of an extended cavity laser at a pulsed drive currrent of 40 mA and 60 mA.

9.4.3. Waveguide Loss Measurements of Extended Cavity

The modal loss of the passive waveguide at the lasing wavelength (858 nm) was examined. An extended cavity laser with an initial passive waveguide length of 2 mm and gain section length of 0.25 mm was used in the experiment. During the experiment the length of the active section (L_a) was fixed while the passive section was cleaved to certain cavity lengths (L_p) and light current characteristics measured. Four measurements were made cleaving the passive cavity from 2 mm to 0.25 mm. Fig. 8.9 compares the threshold current of an extended cavity laser against the length of the extended cavity, L_p. The initial threshold current with L_p= 2 mm was 19.8 mA and the final threshold current value with no external cavity (L_p= 0) was 14 mA.

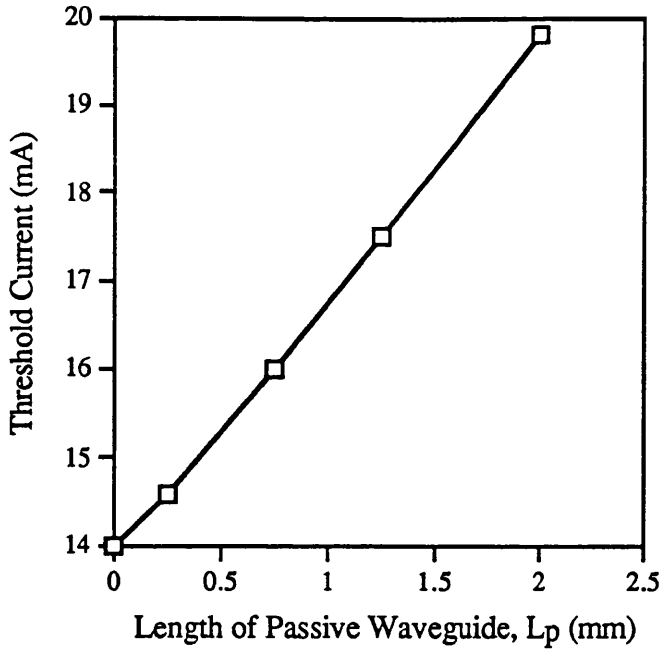

Fig. 9.9. A plot of threshold current against passive section length of an extended cavity laser.

If we take a logarithmic dependence of the QW gain on the current density we would expect a linear dependence of ln[I_{th}/I_{th} (L_p=0)] vs L_p /L_a, if the gain parameters of the active section do not change. Since there is little shift in lasing wavelength between the extended cavity laser and the same laser with no extended cavity, we can assume that the gain parameters of the active section do not change. The slope of this linear dependence is then proportional to the coefficient of the total modal loss per QW in the passive section. Figure 9.10 compares the logarithm of the normalised threshold current for an extended cavity laser with diferent lengths L_p and a fixed length L_a. The threshold current was normalised to the threshold current of the laser with no extended cavity (L_p=0). The cavity-length dependence of the threshold current I_{th} can be modeled using a gain versus current relation that accounts for the gain saturation in MQW lasers [6],

$$g(J) = n\Gamma_w G_o(J/J_T) \tag{9.1}$$

where g is the modal gain, J is the effective current density per well, J_T is the transparent current density per well, G_0 for this particular material is calculated to be 840 cm^{-1} [7], and the optical confinement factor per well is 0.025 [8], and n is the number of wells, which is four. Therefore, balancing the cavity gain and loss then yields

$$\ln\left[{}^{I_{th}}\!/_{I_{th}(L_p=0)}\right]=\frac{\alpha_p\left(L_p/L_a\right)+\left(1/L_a\right)\ln\left(\frac{1}{\kappa}\right)}{n\Gamma_w G_0} \qquad (9.2)$$

where α_p is the modal loss coefficient in the passive section and κ is the fraction of optical power that couples from the active into the passive section. Assuming κ is ~1 and the calculated slope of Fig. 9.10 is 0.045 then α_p is ~ 3.8 cm^{-1}. When compared to the wavelength independent waveguide loss (due to scattering and free-carrier absorption) which is between 5-3 cm^{-1}, then the actual wavelength dependent resonant modal loss is negligible. This is due to the absorption edge of the passive section being at a much lower wavelength than the lasing wavelength of the active region.

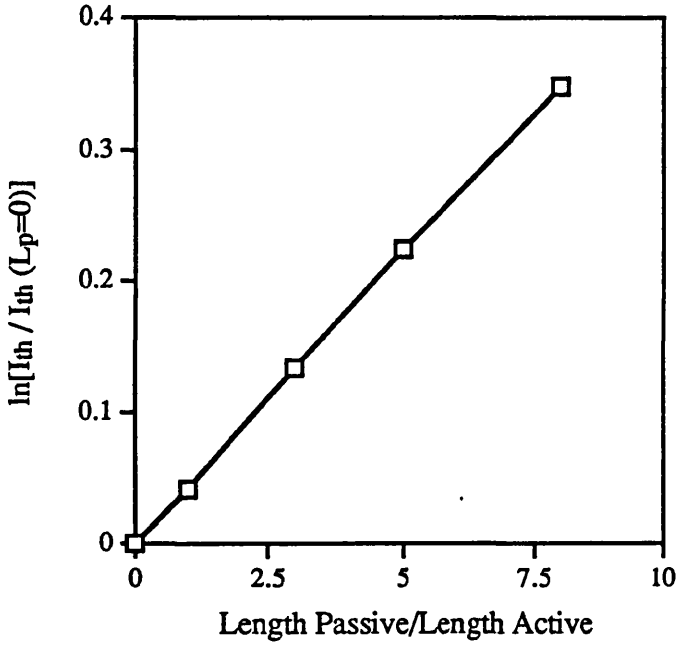

Fig. 9.10. Logarithm of the normalised threshold current vs the passive to active section length ratio for an extended cavity laser. The threshold current is normalised to a laser threshold current of a laser with $L_p = 0$. The length of the active section is constant. Slope is 0.045.

9.4.4. Modelocked Testing

The integrated lasers were tested for evidence of modelocking by observing the wavelength spectrum at different values of saturable absorber bias. One of the integrated lasers with the best light-current characteristics was mounted onto a heat-sink and both the gain and saturable absorber sections wire bonded. A cw current from a stable constant

current source was guided to the gain section of the integrated laser and a reverse bias connected to the saturable absorber. The light output from the extended cavity end of the integrated laser was connected to a spectrum analyser and optical spectra were recorded at corresponding values of reverse bias. All through the experiment the gain section was driven with a constant 50 mA current and the device temperature was kept at 15 °C using a peltier cooler. The spectra are plotted in Fig. 9.11 and have been scaled accordingly (values of scaling are shown next to spectra). Initially the optical spectrum at zero volts reverse bias (saturable absorber short circuited) is centered at 854.2 nm and has a FWHM spectrum width of 0.4 nm. Since the resolution of the spectrum analyser is only 0.2 nm this is not an accurate value of the spectrum width of the integrated laser. With an increase in reverse bias to 0.3 V the optical spectrum widens to 1 nm (FWHM) and the peak shifts to 854.9 nm, the peak power of the spectrum drops as the light energy of the laser is dispersed into other longitudinal modes as well as some absorbed by an increase in absorption of the saturable absorber. At 0.6 V reverse bias, the spectrum widens to a maximum value of 4 nm (FWHM) with a peak centered at 854 nm. The peak power is about 1/15 of the initial value at 0 V.

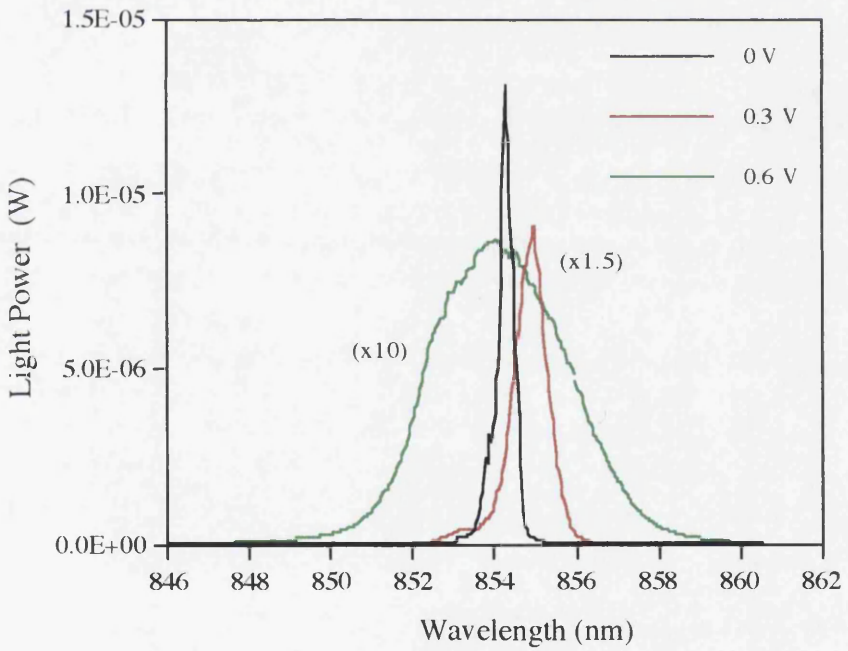

Fig. 9.11. Optical spectra of a integrated modelocked laser at various values of reverse bias, scaled units next to spectrum.

The optical spectrum remains unaltered from 0.6 to 1 V reverse bias. At 1 V a substructure of noise appears superimposed on top of the optical spectrum, Fig. 9.12.

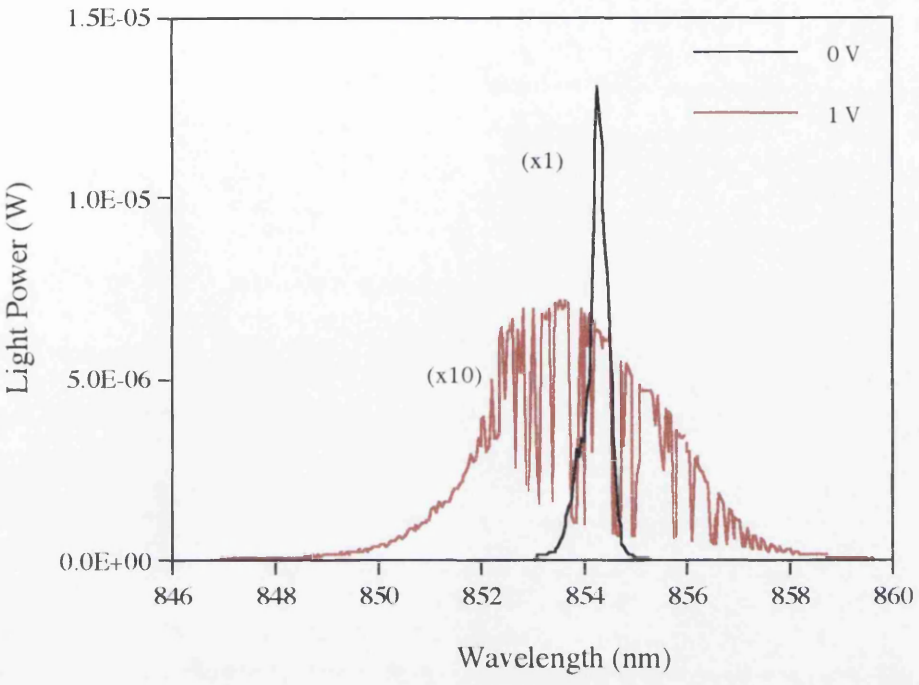

Fig. 9.12. Optical spectra of a integrated modelocked laser at 0 and 1 V reverse bias, scaled units next to spectrum.

9.5. Analysis of Modelocked Results

The results show that there is a dramatic change in the optical spectra with an increase in reverse bias across the saturable absorber. The FWHM width of the lasing spectrum increases from 0.4 nm at 0 V to 4 nm at 0.6 V reverse bias. We propose that this increase in width is due to modelocking occuring at between 0.6 and 1 V reverse bias, where the narrowing of the modelocked pulses corresponds inversely to an increase in the spectral width (inverse fourier transform theorem). The spectral width of 4 nm corresponds to $\Delta\nu$ =1.64 Thz. If we assume that the laser is modelocked and the pulses are transform limited then the corresponding pulse width which would be emitted from this device is 0.6 ps. The noise exhibited in Fig. 9.12 for the device reverse biased at 1 V is probably the device going from a mode-locked state to a Q-switching regime. Unfortunately further investigations to confirm modelocking could not be carried out, the saturable absorber of this particular device broke down while measuring the optical spectra and there was no time to fabricate any more devices. However work is being continued on these devices so that they can be used as optical high frequency mixers to be used in further mixed frequency experiments.

9.6. References

1. R. L. Thornton, W. J. Mosby, and T. L. Paoli, *J. Lightwave Technol.* vol. 6, pp. 786-791, 1989.

2. K. Y. Liou, U. Koren, *et al, Appl. Phys. Lett.* vol. 54, pp. 540-542, 1989.

3. D.G. Deppe and N. Holonyak, Jr, "Atom diffusion and impurity-induced layer disordering in quantum well III-V semiconductor heterostructures", *J. Appl. Phys.* vol. 64 (12), pp. R93-R113, 1988.

4. J. H. Marsh, S. I. Hansen, A. C. Bryce, R. M. De la Rue, "Applications of neutral impurity disordering in fabricating low-loss optical waveguides," *Optical Quantum Electron.,* vol. 23, pp. S941-S957, 1991.

5. J. D. Ralston *et al, ,Appl. Phys. Lett.* vol 50, pp.1817-1819, 1987.

6. L. J. Guido, N. Holonyak, Jr., *et al* "Effects of dielectric encapsulation and As overpressure on Al-Ga interdiffusion in AlGaAs-GaAs quantum well heterostructures"', *J. Appl. Phys.* vol. 61, pp. 1372, 1987.

7. R. M. Malbon, D. H. Lee, and J. M. Whelan, *J. Electrochem. Soc.* vol. 123, p. 1413, 1976.

8. P. W. A. Mc Ilroy, a. Kurobe and Y. Uematsu, "Analysis and appplication of theoretical gain curves to the design of multi-quantum-well lasers", *IEEE J. of Q.E.*, vol. 21, pp 1958, 1985.

Chapter 10

Conclusions and future work

10.1. Ultra-short pulse measurement

In this thesis we have described the main ultrashort pulse measurement techniques commonly used. Examining both direct and indirect methods of temporal optical pulse characterisation. Techniques such as optical chronography and fast photodiodes, that give direct temporal measurement and indirect methods such as linear and non-linear correlation have been discussed. The resolution of each method has been compared examining the suitability of each technique for particular applications. Three of these methods were used later on in the thesis to measure the repetition frequency and optical pulse width of a generated optical pulse train.

A novel technique of using two photon conductivity (TPC) in a reverse-biased GaAs/AlGaAs waveguide as an autocorrelator detector is demonstrated. We have shown that a standard p-i-n waveguide structure can be used in place of a SHG crystal and photomultiplier tube as the non-linear element in an autocorrelation measurement. The advantage of this method over the other conventional correlation technique which uses second-harmonic generation, is that it is at least as sensitive, operates over a very wide range of wavelengths, and could be easily adapted in order to be integrated. It has been demonstrated that the photocurrent measured from a p-i-n waveguide has an almost quadratic dependence on the intensity of the incident light, as expected for a two photon effect.

We have demonstrated the practical use of the two-photon autocorrelator by obtaining autocorrelation traces for a modelocked Nd^{3+}:YAG laser at 1.06 μm, a passively Q-switched semiconductor laser at 1.3 μm and a passively Q-switched two-section semiconductor laser at 980 nm.

10.2. Ultra-Short Pulse Generation

Short pulses (25 ps) at high repetition rates (18 GHz) have been generated through the passive Q-switching of two-section lasers. We have shown that a high frequency optical pulse train can be produced by forward biasing a long section of the laser cavity to provide the gain and reverse biasing a short section of the cavity to form a saturable absorber. It has been demonstrated that the self-pulsating repetition rate is controlled by varying the current to the gain section and that for a small signal analysis the frequency is proportional to $I^{1/2}$. We have shown that there is an optimum value of saturable absorber/cavity length which was found to be 0.07. We have also proposed a simple

model to explain these results. The absorption of the saturable absorber for quantum well material is observed to have a non-monotonic dependence to the applied reverse bias. This relationship is explained by a shift in exciton peak with reverse bias, from light hole to heavy hole, due to the quantum confined Stark effect.

A monolithically integrated extended cavity modelocked laser has been fabricated by impurity free vacancy disordering of the quantum well structure. Low loss waveguides were formed using this technique, which were found to have a loss of 3 to 4 cm^{-1}. An increase in spectral width was observed with increasing reverse bias, indicating modelocking of the device. These pulses were theoretically calculated to be ~0.6 ps at a modelocking frequency of 17 GHz.

Optoelectronic mixing of very high-frequency amplitude modulated signals in semiconductor lasers has been studied theoretically. It has been demonstrated experimentally in Q-switched two-section lasers and we have shown that optical frequency mixing is possible at frequencies up to 1.5 GHz.

10.3. Future Work

Work is to be carried out in future on an all-fibre two-photon autocorrelator. Interest has been raised over an autocorrelator for measuring asymmetric short optical pulses suggested in section 6.10 however no proposals for future work have been planned.

Future work on two-section lasers will involve fabrication of the devices in strained p-doped MQW semiconductor material, and further optimisation of the device parameters to achieve higher self-pulsation repetition rates.

Future work on the monolithically integrated passively modelocked laser will be to integrate the device further with an optical grating to pick out two longitudinal modes. Beating of these two modes together in the cavity will form a high frequency sinusoidal signal. This device can then be used as a local oscillator in further mixed frequency experiments.

APPENDIX 1

Table of time bandwidth, autocorrelation values against pulse shape.

I(t)	$\Delta t\Delta\nu$ Time bandwidth (K)	$G_0^{\,2}(\tau)$ Autocorrelation Trace	τ_p/τ_G Pulse width / autocorrelated width
Parabolic $I(t)=\begin{cases}1-x^2 & ;\lvert t\rvert \le T\\ 0 & ;\lvert t\rvert > T\end{cases}$	0.7276	$\begin{cases}1-\frac{5}{4}y^2+\frac{5}{8}\lvert y\rvert^3-\frac{1}{32}\lvert y\rvert^5 & ;\lvert\tau\rvert\le 2T\\ 0 & ;\lvert\tau\rvert>2T\end{cases}$	0.8716
Gaussian $I(t)=e^{-x^2}$	0.4413	$e^{-y^2/2}$	0.7071
Hyperbolic sech $I(t)=\sec h^2 x$	0.3148	$\frac{3}{\sinh^2 y}[y\coth y-1]$	0.6482
Lorentzian $I(t)=\frac{1}{1+x^2}$	0.2206	$\frac{1}{1+(y/2)^2}$	0.5000

APPENDIX 2

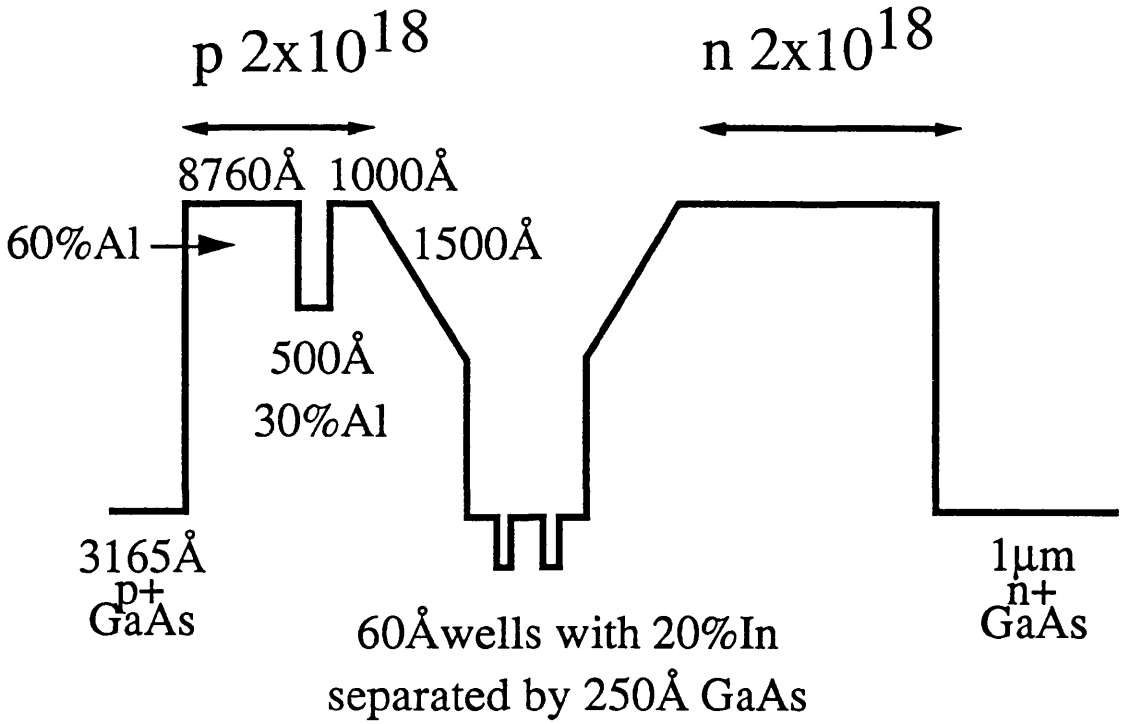

Energy-Band diagram for 980 nm laser material

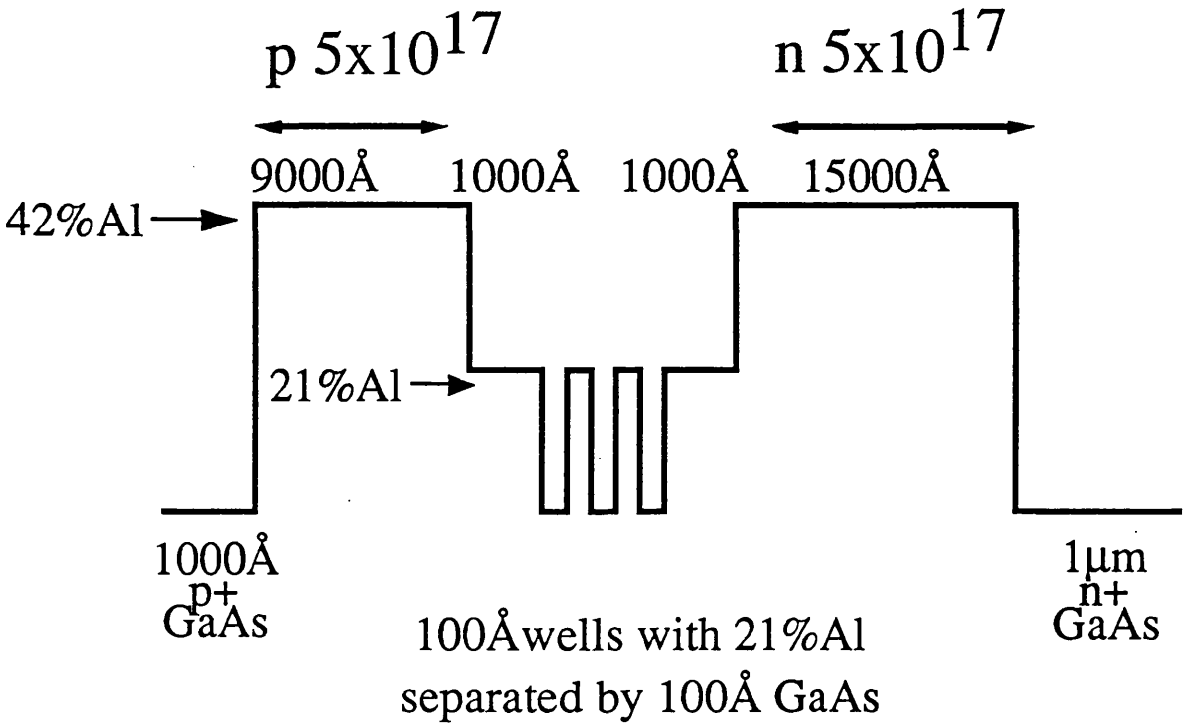

Energy-Band diagram for 860 nm laser material.

APPENDIX 3

Two-Section Lithography Masks

Ridge-waveguide Mask

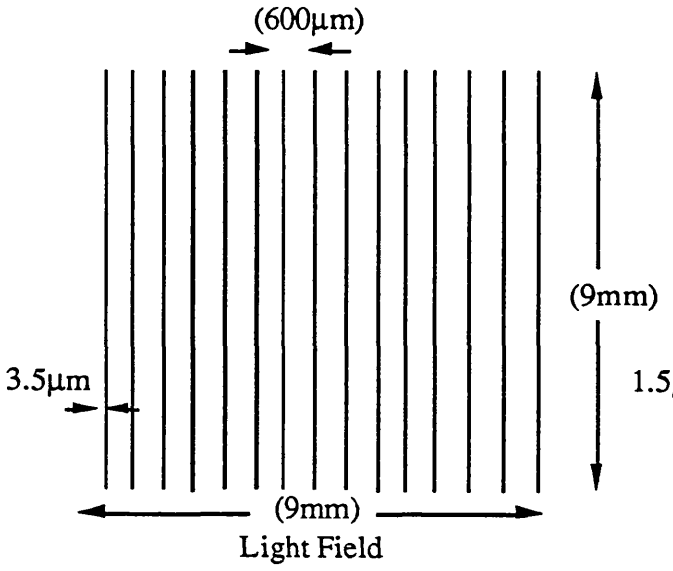

Contact-window Mask

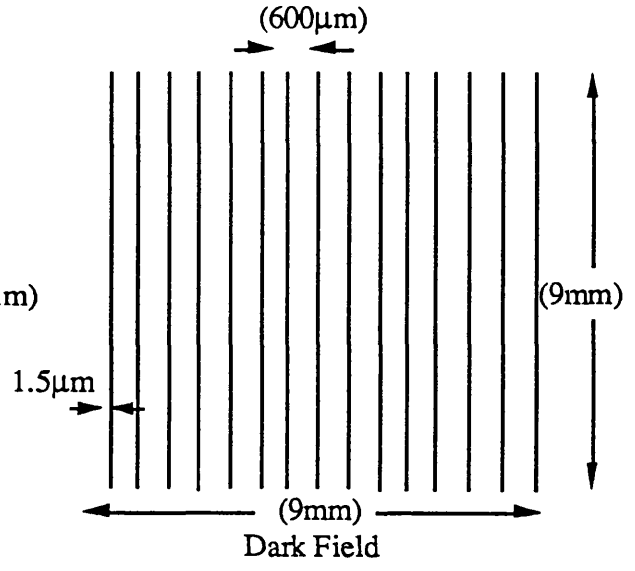

Metal Mask

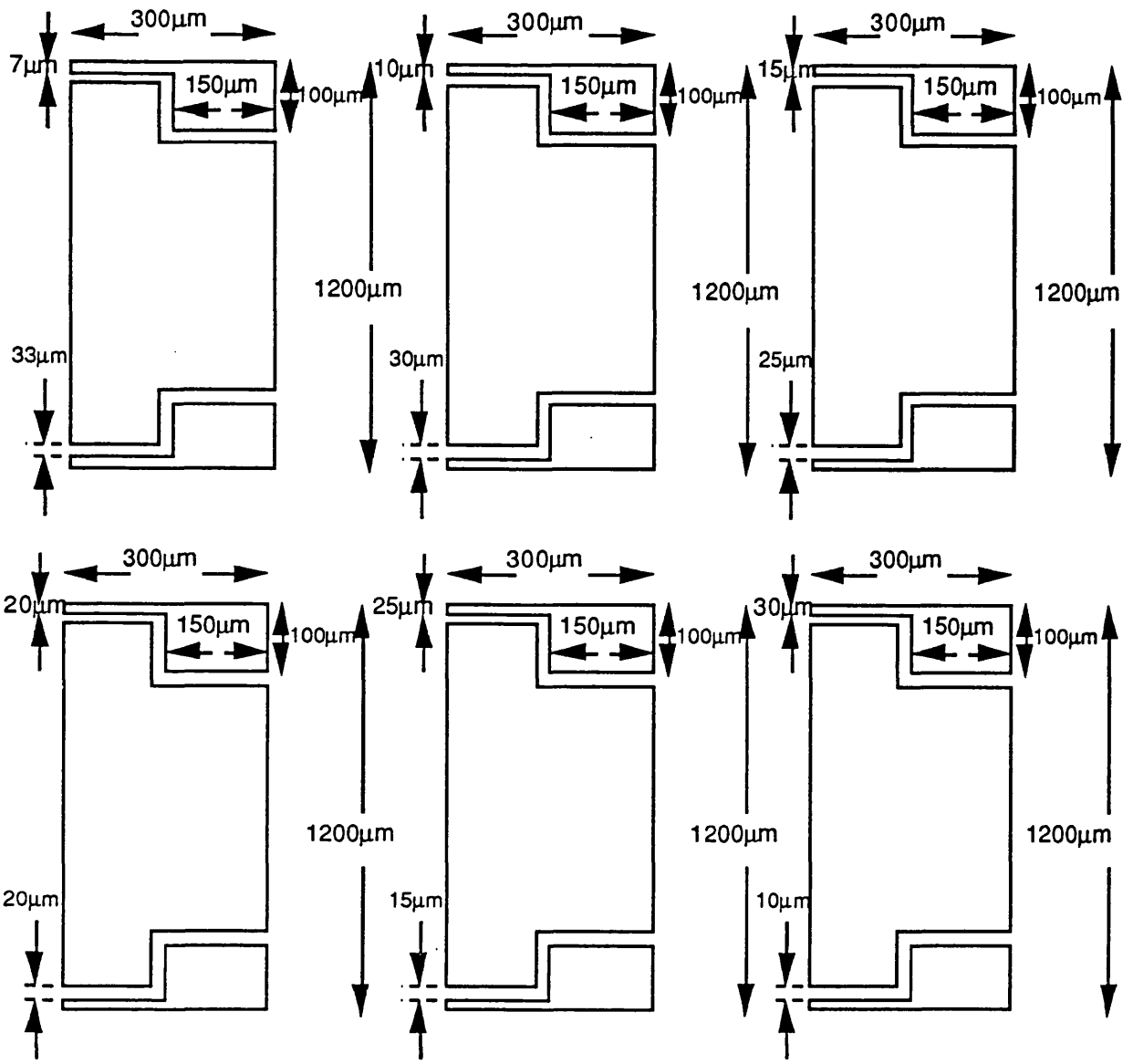

APPENDIX 4

Mikohm n-type contact Recipe

First layer	
Au	14 nm
Ge	14 nm
Au	14 nm
Ni	11 nm
Au	240 nm

APPENDIX 5

Multi-contact Autocorrelator Bond-pad Design.

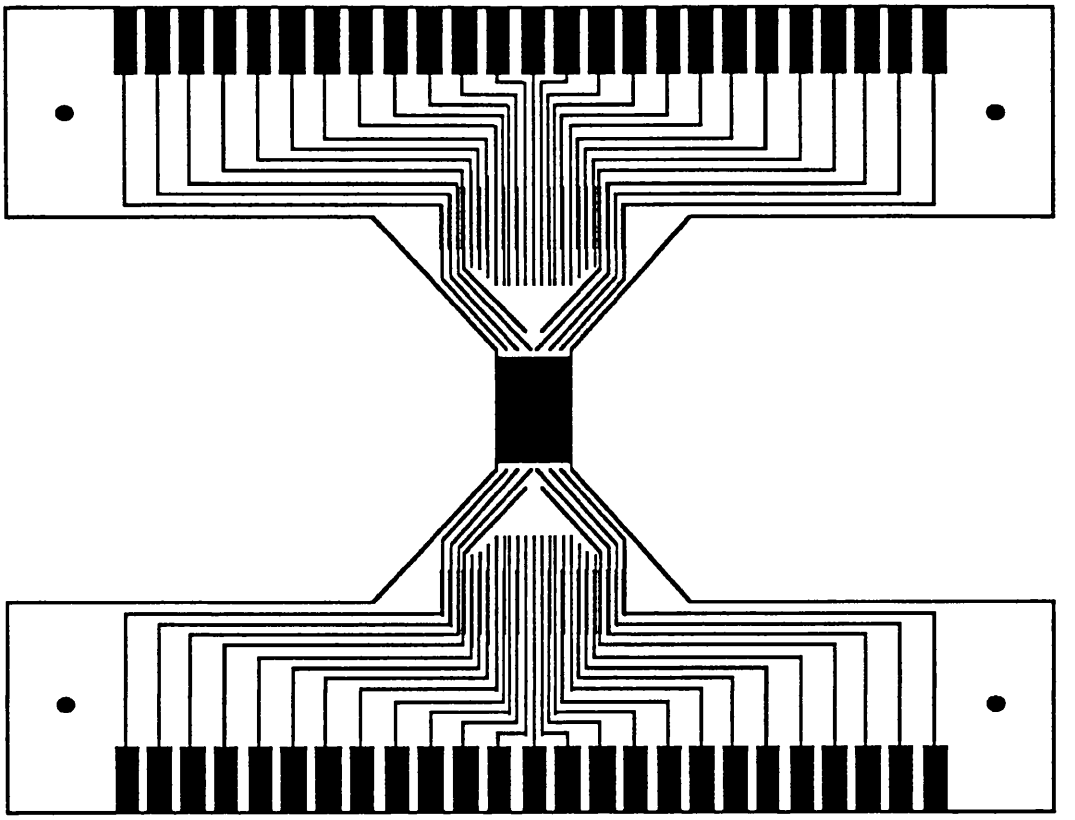

APPENDIX 6

Multicontact Autocorrelator Holder.

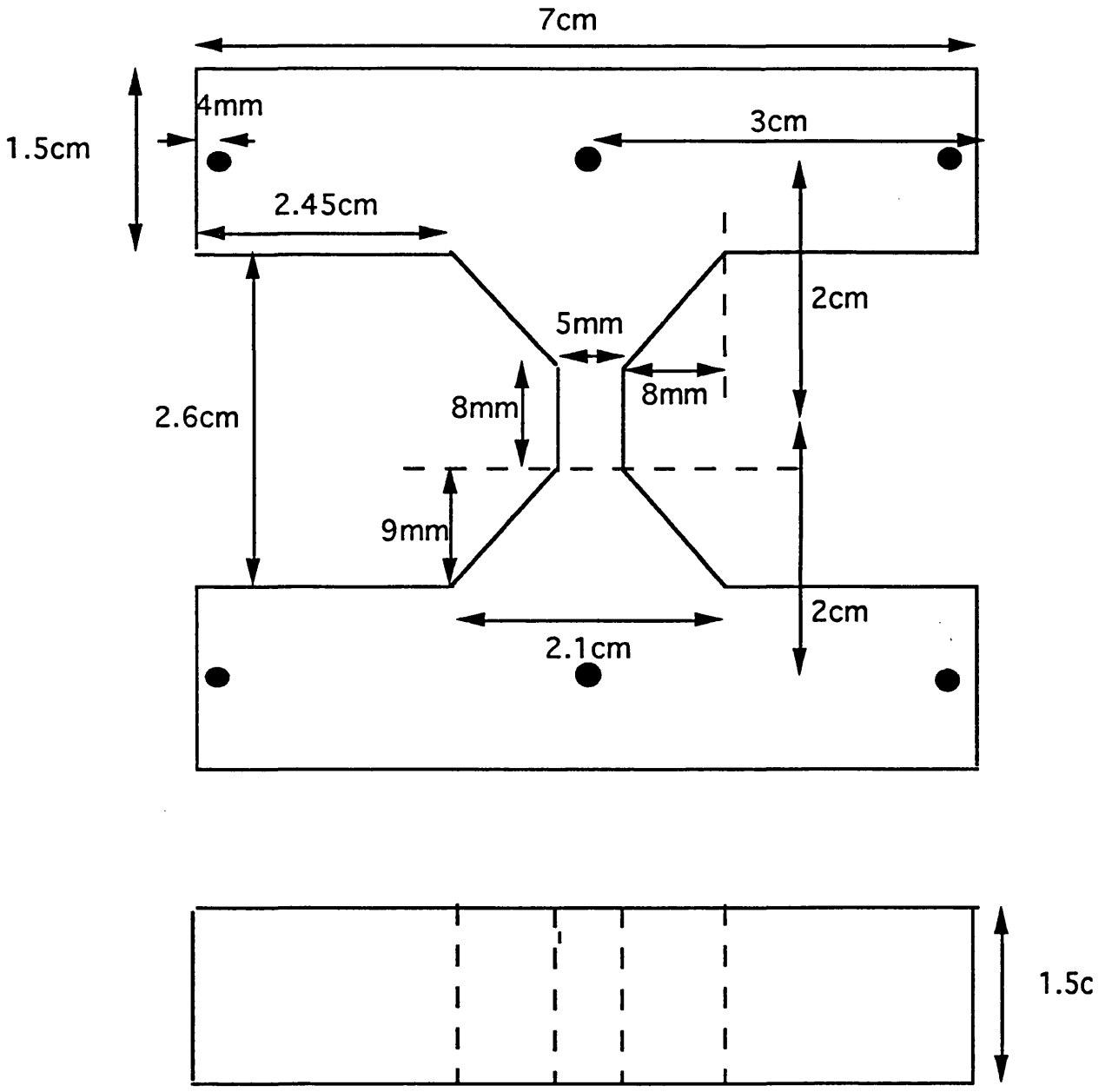

DESIGN FOR MULTICONTACT HOLDER MADE OUT OF BRASS

APPENDIX 7. Laser diode parameters used in computations

Parameter	Symbol	Value in Subsection 2.2	Value in Subsection 2.3	Unit
gain (in gain section)	g	$v_g A_g (N-N_{0g}) (1-\varepsilon_g S)$		1/s
absorption (in saturable absorber section)	a	$v_g A_a (N_{0a}-N) (1-\varepsilon_a S)$		1/s
electron lifetime (in gain section)	τ_N	$1/BN$		s
photon lifetime	τ_{ph}	$2L/(v_g \ln(1/R))$		s
pumping current in gain section	J_g			
pumping current in saturable absorber section	J_a	0		
active layer thickness	d			
bimolecular recombination coefficient	B	$1.5*10^{10}$		cm^3/s
spontaneous emission factor	β_{sp}	10^{-4}		
recombination time in saturable absorber section	τ_a	0.01		ns
group velocity of light	v_g	$0.75*10^{10}$		cm/s
confinement factor	Γ	0.08	0.05	
saturable absorber (SA) length fraction	r_a	0.088	0.037	
gain length fraction	r_g	$1-r_a$	0.336	
gain cross section	A_g	$4*10^{-16}$		cm^2
SA cross section	A_a	$10*10^{-16}$	$16*10^{-16}$	cm^2
effective transparency carrier density, gain section	N_{0g}	$1.2*10^{18}$		cm^3
effective transparency carrier density, SA section	N_{0a}	$2.6*10^{18}$	$1.2*10^{18}$	cm^3
gain suppression coefficient	ε_g	$5*10^{-18}$		cm^3
saturable absorption suppression coefficient	ε_a	$5*10^{-18}$		cm^3
intensity reflection coefficients (both sides)	R	0.36		
linewidth enhancement factor	α		2	
gain linewidth	$\Delta\Omega_g$		$2*10^{13}$	1/s
laser cavity length	L	400	1875	μm

APPENDIX 8 . Schematic of Modelocked Optical Masks

Alignment Mask

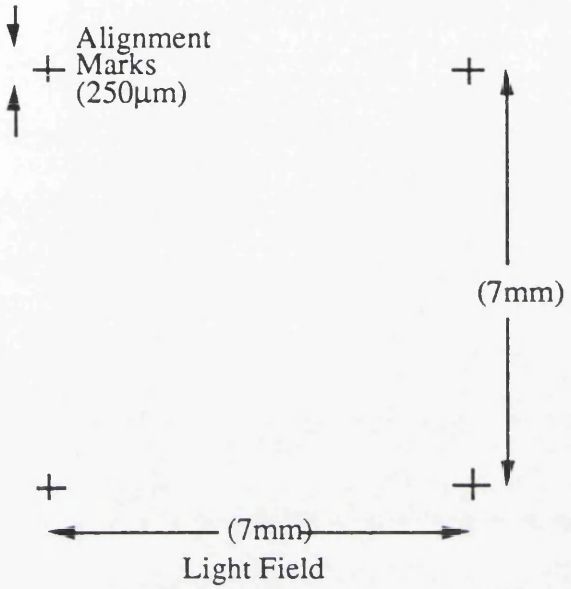

Intermixing Mask

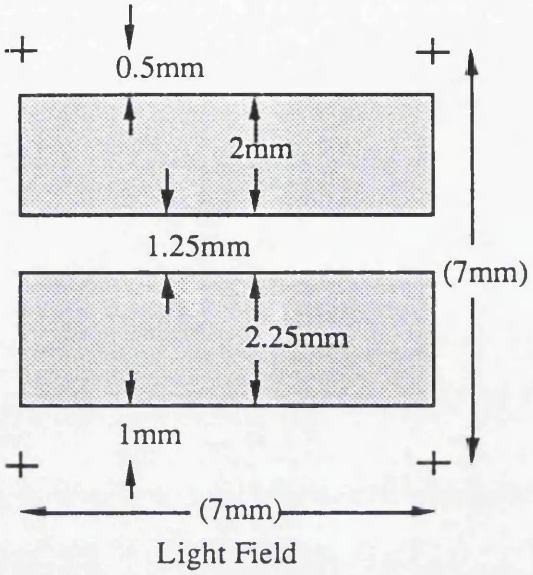

Ridge-waveguide Mask

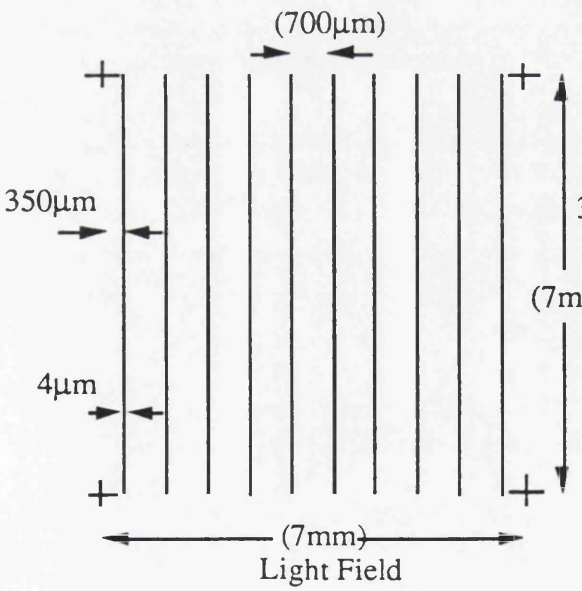

Contact-window Mask

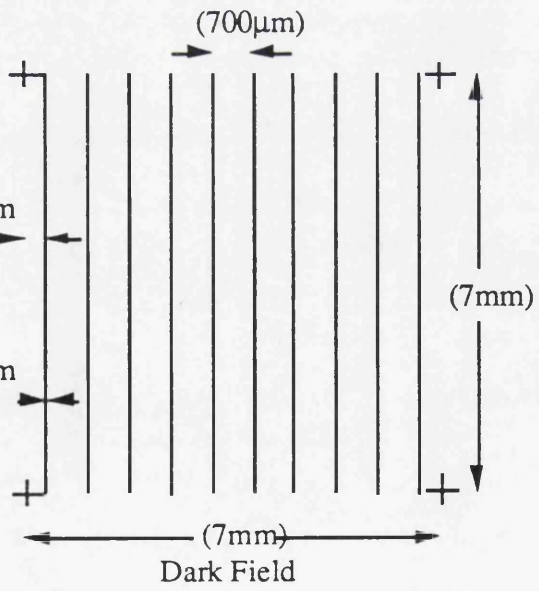

Metal Mask

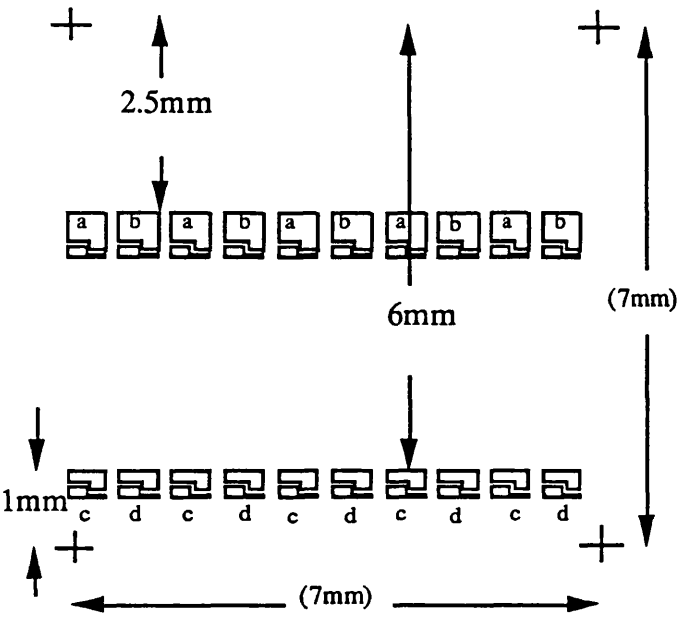

Dark Field

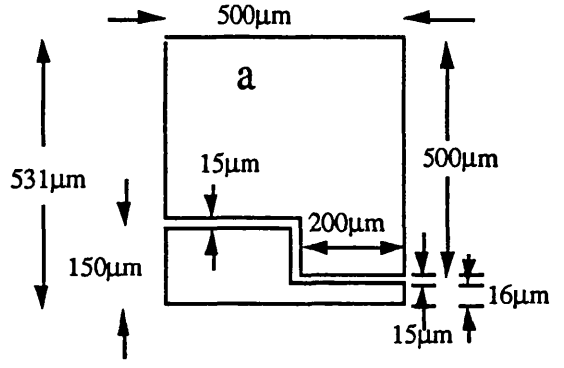

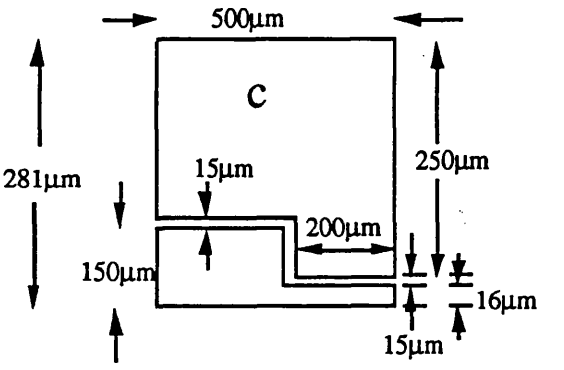

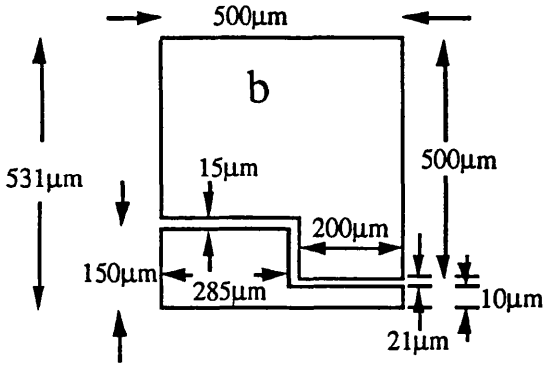

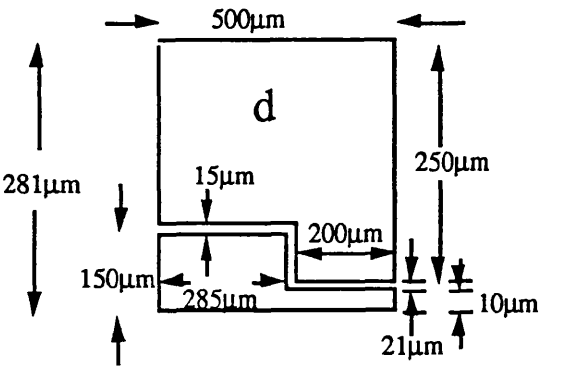

Publications

1. F.R. Laughton, J.H. Marsh, D.A. Barrow and E.L. Portnoi : "The two-photon absorption semiconductor waveguide autocorrelator"—*IEEE J Quantum Electronics*, **30**, 838-845, (1994).

2. E.L. Portnoi, V.B. Gorfinkel, E.A. Avrutin, I. Thayne, D.A. Barrow, J.H. Marsh, S. Luryi : "Optoelectronic microwave-Range frequency mixing in semiconductor lasers"—*IEEE J of Selected Topics in Quantum Electronics*, (1995).

3. E.L. Portnoi, V.B. Gorfinkel, D.A. Barrow, I.G. Thayne, E.A. Avrutin, J.H. Marsh : "Semiconductor lasers as integrated optoelectronic up/down-converters"—to appear in *Electronics Letters*, (1995).

4. F.R. Laughton, J.H. Marsh, D.A. Barrow, A.H. Kean and E.L. Portnoi : "Demonstration of the use of two-photon absorption waveguide detector as an autocorrelator"—IEE Colloquium "Measurements on Optical Devices", London, 19 November 1992—*IEE Conf Digest* **1992/210** pp 10/1-10/4 (1992).

5. D.A. Barrow, J.H. Marsh and E.L. Portnoi : "Field distribution measurements in Q-switched semiconductor lasers"—IEE Colloquium "Measurements on Optical Devices", London, 19 November 1992—*IEE Conf Digest* **1992/210** pp 8/1-8/4 (1992).

6. F.R. Laughton, D.A. Barrow, J.H. Marsh and E.L. Portnoi : "Generation and Detection of 13 ps Q-Switched Pulses from a 1.3 μm Semiconductor Laser Containing a Saturable Absorber"—Fifth International Conference on Indium Phosphide and Related Materials, Paris, France, 18-22 April 1993. *Proceedings of the Fifth Intl. Conf. on InP and Related Materials*, (IEEE Publishing Services, New York) pp 624-626 (1993)

7. E.L. Portnoi, Yu.M. Shernjakov, G.B. Venus, B.S. Yavich, J.H. Marsh and D.A. Barrow : "Gain modulation at millimeter wave frequencies in strained QW lasers"—International Symposium on Nanostructures: Physics and Technology, St Petersburg, Russia, 3-18 June 1993.

8. J.H. Marsh, D.A. Barrow, F.R. Laughton and E.L. Portnoi : "Generation and detection of Q-switched pulses from two-section semiconductor lasers"—IEE Tutorial Colloquium "Ultra-Short Optical Pulses", London, 3 November 1993—*IEE Conf Digest* **1993/202** pp4/1-4/6 (1993).

9. D.A. Barrow, F.R. Laughton, M.M. Karkhanehchi, J.H. Marsh : "Two photon absorption semiconductor autocorrelators for ultra-short pulse measurements —CLEO/Europe, Amsterdam, 28 Aug-2 Sep 1994. *Technical Digest, Conference on Lasers and Electro-Optics Europe, Amsterdam, The Netherlands, 1994.* (IEEE Publishing Services, New York), paper CThM5, pp.366-367 (1994).

10. D.A. Barrow, J.H. Marsh, E.L. Portnoi : "Q-switched pulses at 16 GHz from two-section semiconductor lasers"—CLEO/Europe, Amsterdam, 28 Aug-2 Sep 1994. *Technical Digest, Conference on Lasers and Electro-Optics Europe, Amsterdam, The Netherlands, 1994.* (IEEE Publishing Services, New York), paper CTuE4, p.75 (1994).

11. E.L. Portnoi, E.B. Venus, A.A. Khazan, V.B. Gorfinkel, G. Kompa, J.H. Marsh, E.A. Avrutin, I. Thayne and D.A. Barrow : "Monolithically integrated optoelectronic downconvertor (MIOD)"—14th International Semiconductor Laser Conference, Maui, Hawaii, 19-23 Sep 1994.

12. E.L. Portnoi, G.B. Venus, A.A. Khazan, V.B. Gorfinkel, G. Kompa, J.H. Marsh, E.A. Avrutin, I. Thayne and D.A. Barrow : "Monolithically integrated optoelectronic downconvertor (MIOD)"—9th meeting on Optical Engineering in Israel, Tel-Aviv, Israel, 25-26 Oct 1994. *Digest of the 9th Meeting on Optical Engineering in Israel,* pp.13-14 (1994).

13. D.A. Barrow, I.G. Thayne, A. Avrutin, J.H. Marsh, E.L. Portnoi, V.B. Gorfinkel : "Semiconductor lasers as integrated optoelectronic up/down convertors"—EDMO'94 (2nd Intl Workshop on High Performance Electron Devices for Microwave and Optoelectronic Applications), London, 14 Nov 1994. *Conference proceedings,* (IEEE, UK and Republic of Ireland Section, London) pp110-115 (1994).